

This item was submitted to Loughborough University as a PhD thesis by the author and is made available in the Institutional Repository (<https://dspace.lboro.ac.uk/>) under the following Creative Commons Licence conditions.



For the full text of this licence, please go to:
<http://creativecommons.org/licenses/by-nc-nd/2.5/>

3-D Antenna Array Analysis using the Induced EMF Method

by

Norun Farihah Abdul Malek

Doctoral Thesis

Submitted in partial fulfillment of the requirements for the award of
Doctor of Philosophy of Loughborough University
2013

© By Norun Farihah Abdul Malek, 2013

ABSTRACT

The effect of mutual coupling between elements plays a crucial role to the performance of the antenna arrays. The radiation patterns of antenna arrays will be altered by the coupling effect from the adjacent elements thus reducing the accuracy and resolution in direction finding application. This research developed and validated the novel 3-D Algorithm to calculate the far-field pattern of dipole arrays arranged in three dimensions and in any configuration (both in straight and slanted position). The effect of mutual coupling has been accounted using the Induced EMF method. The computation is performed on 2x2 parallel dipoles and 12 dipoles arranged at the edge of a cube. The results are validated with other electromagnetic techniques such as Method of Moment (MoM) and Finite Difference Time-Domain (FDTD). Then, a 2x2 dipole array is chosen for beam steering and experiment validation due to its ease of implementation and feeding network. The array optimisation to control the pattern is performed using a genetic algorithm. The far-field pattern computed using the 3-D algorithm might be less accurate than other 3-D electromagnetic techniques but its array optimisation is faster and efficient. The simulation and measurement results are in good agreement with each other confirmed the validity of the 3-D algorithm.

Keywords: Mutual coupling, antenna arrays, steerable beam, Induced EMF Method, genetic algorithm.

ACKNOWLEDGEMENTS

I would like to thank Mr. Rob D. Seager, who has served many years as my adviser for my Masters and PhD degrees. Mr. Rob D. Seager provided invaluable advice and support throughout the work on this dissertation. Without his guidance, support and patience, I would not have completed my thesis. I would like to thank Dr. James A. Flint for the additional assistance on the work presented in this dissertation. Many hours of discussions we have been spent on the ideas that were very enlightening. Both Rob and James enabled me to develop a good understanding of the subject and how to do research in overall perspective.

I would also like to express my gratitude to all those who gave me the possibility to complete this thesis. I want to thank the School of Electronic, Electrical and Software Engineering of Loughborough University for giving me the opportunity to commence this thesis in the first instance, to do the necessary research work and to use school equipment. My deepest thanks go to John Brister, Dr. Alford, Chandrakant B. Mistry and Terry West for their assistance in making the measurement set up successful. Furthermore, I would like to thank my friends Mr. Nidal A. Qasem, Miss Emma Kowalczyk, Miss Chinwe Njoku, Mr. Ajit Yadav, and many others who are not named here for their stimulating support.

I also would like to thank my university (IIUM) and Malaysian government for giving me the financial support for all these years.

Especially, I would like to give special thanks to my husband Zulfadli and my son for being extremely supportive and patient during my graduate work. Last but not least, I am grateful to my family, in-laws and friends for giving me support throughout these years.

PUBLICATIONS

1. N. A. Malek, R. D. Seager, “3D Reconfigurable antenna”, in Loughborough Antennas & Propagation Conference, 2010, © IEEE. doi: 10.1109/LAPC.2010.5666796
2. N. A. Malek, R. D. Seager, J. A. Flint, “ Pattern synthesis using combination of the induced EMF method and a genetic algorithm” Loughborough Antennas & Propagation Conference, 2011, © IEEE. doi: 10.1109/LAPC.2011.6114077
3. N. A. Malek, R. D. Seager, J. A. Flint, “3-D antenna array using the Induced EMF method”, IEEE Trans. Antennas and Propagation, 2013 (working paper).

CONTENTS

ABSTRACT	ii
ACKNOWLEDGEMENTS	iii
PUBLICATIONS	iv
CONTENTS	v
LIST OF FIGURES	viii
LIST OF TABLES	xv
LIST OF SYMBOLS	xvii

CHAPTER 1:

Introduction to Research

1.1 Research Background	1
1.2 Problem Statement	4
1.3 Research Contributions	6
1.4 Thesis Outline	7

CHAPTER 2:

Basics of Antenna Arrays

2.1 Introduction	13
2.2 Basics of Element and Array Antenna	13
2.2.1 Array Element: Half wavelength Dipole	14
2.2.2 Antenna Array	16
2.2.3 Ideal Array Theory: Element and Array Factor	19
2.3 Analysis of Mutual Coupling Effects in Antenna Arrays	20
2.3.1 Mutual Coupling between Elements	21
2.4 Self- and Mutual Impedance	29
2.4.1 Self Impedance using the Induced EMF Method	29
2.4.2 Mutual Impedance using the Induced EMF Method	30
2.5 Conclusions	37

CHAPTER 3:

Numerical Methods and Optimisation Techniques

3.1 Introduction	43
3.2 Electromagnetic Modelling	43
3.2.1 Numerical Methods	45
3.2.2 Analytical Method	51
3.3 Optimisation Techniques	65
3.4 Conclusions	69

CHAPTER 4:

Computational and Modelling Details of Dipole Antenna Arrays

4.1 Introduction	74
4.2 Background Theory and Algorithm using Induced EMF Method	75
4.2.1 2-D Algorithm	75
4.2.2 3-D Algorithm	77
4.3 Pattern Multiplication Method (without mutual coupling)	88
4.4 Numerical Modelling using MoM and FDTD	89
4.4.1 MoM	89
4.4.2 FDTD	90
4.5 Results of the 3-D algorithm.	91
4.5.1 Mutual impedance	91
4.5.2 Impedance matrix, Z for four parallel dipoles	93
4.5.3 Impedance matrix for twelve dipoles in various configurations	94
4.5.4 3-D Far-Field Patterns	96
4.6 Conclusions	110

CHAPTER 5:

Pattern control of a Four Dipole Antenna Array using a Genetic Algorithm

5.1 Introduction	114
5.2 Introduction to Genetic Algorithms	115
5.2.1 Initialisation and Coding	118
5.2.2 Reproduction	119
5.2.3 Generation Replacement	122
5.2.4 Termination Criteria	123
5.3 Radiation Pattern Control using a Combination of the 3-D (based on the Induced EMF Method) and a Genetic Algorithms	123
5.3.1 Computation of the Far-Field Radiation Pattern	123
5.3.2 GA Specifications	124
5.3.3 Desired Pattern	126
5.3.4 Fitness Function	127
5.4 Results of Pattern Control Using Genetic Algorithm	128
5.4.1 Steerable Main Beam at 100°	128
5.4.2 Steerable Main Beam at 110°	131
5.4.3 Steerable Main Beam at 120°	132
5.4.4 Steerable Main Beam at 130°	134
5.4.5 Steerable Main Beam at 140°	135
5.5 Computational Run Time of 3-D Algorithm and Other Numerical Techniques	136
5.5 Discussion	138
5.6 Conclusion	141

CHAPTER 6:

Measurement

6.1 Introduction	145
6.2 The Description of the Array Hardware.....	145
6.2.1 The Dipole Antenna	147
6.2.2 Wilkinson Power Divider.....	148
6.2.3 Phase Shifter and Attenuation Circuit.....	149
6.2.4 Vector Network Analyser	150
6.2.5 Voltage Supply.....	150
6.3 Simulation, Fabrication and Measurement Results.....	152
6.3.1 Dipole Antennas.....	152
6.3.2 Four-way Wilkinson Divider	155
6.3.3 Phase Shifter and Attenuator Circuit.....	162
6.4 Measurement Set-up	167
6.4.1 Anechoic Chamber.....	167
6.4.2 Transmitter and Receiver Set-up.....	168
6.4.3 Device under Test: 2x2-Dipole Array with a Feed Network	171
6.4.4 Simulation and Measurement Results.....	174
6.5 Conclusion	192

CHAPTER 7:

Final Conclusions

7.1 Summary of Research	196
7.2 Future Study	200

Appendix A: 3D Algorithm for 2x2 Dipole Arrays.....	202
--	------------

Appendix B: 3D Algorithm for 12 Dipole Arrays arranged at the edge of Cube	215
---	------------

Appendix C: 3D Algorithm (2x2 dipole arrays) with Genetic Algorithm..	223
--	------------

Appendix D: Effects of Element Spacing and Orientation on the Far-field Pattern of Four Dipole Antenna Arrays.....	230
---	------------

D.1 Parameters Variation.....	230
D.2 Design Sample used in Measurement Study	231
D.3 Calculation of the Array Factor of Four Dipoles	232
D.4 Effect of varying spacing in parallel on the pattern	234
D.5 Effect of Varying the Spacing in Echelon on the Pattern	235
D.6 Effect of Varying the Spacing (Skewed) on the Pattern	238

LIST OF FIGURES

1-1	a) A four element monopole switched-parasitic antenna array on a ground plane b) Four radiation pattern when one monopole is active while others remain passive at four different positions.....	3
1-2	(a) Four (or 2x2) dipole antenna arrays, (b) Twelve dipole antenna arrays arranged at the edge of a cube (or known as cubic arrays).....	6
1-3	Flowchart of the thesis.....	10
2-1	The coordinate system for far-field pattern analysis from Balanis.....	15
2-2	Far-field pattern of antenna array (in dB).....	18
2-3	(a) Two ports network and (b) its T-network equivalent.....	23
2-4	The circuit conditions defining the impedance: a) Antenna 1 transmitting and antenna 2 receiving, b) Antenna 2 is transmitting and antenna 1 is receiving.....	23
2-5	Free Excitation Model where V_s and Z_s is the source excitation and impedance respectively	25
2-6	The equivalent circuit of free excitation model. It is for an element n driven by a Thevenin source in an array.....	26
2-7	Geometry of a uniform N -element linear array where V_1, V_2, \dots, V_N are excitation voltages for each element and d is the spacing between element.....	28
2-8	Defining geometry for the active element pattern of a uniform N -element array.....	29
2-9	Configuration of two dipoles where l is the length of dipole, d is the spacing between two dipoles along y -axis and h is the distance between end point of dipole 1 and dipole 2 along z -axis: (a) Side-by-side, (b) Collinear, (c) Parallel.....	31
2-10	Mutual coupling between two dipoles along z -axis.....	33
2-11	Mutual coupling between two dipoles arranged along vector t	34
2-12	Horizontal components of the electric field may be broken down into E_x and E_y using a trigonometric function (top view).....	35
2-13	Resolution of electric field intensity.....	35
3-1	FDTD (Yee) Cell.....	50
3-2	Non uniform amplitude arrays of even and odd number of elements. Reproduction from Balanis	53
3-3	Pascal's Triangle.....	54
3-4	Unit circle for an array.....	57
3-5	Linear and planar array geometries.....	59
3-6	Geometry of an N -element circular array.....	60

3-7	Methods that employ active element pattern.....	64
3-8	Building block of an optimization routine.....	66
4-1	Four half-wavelength dipoles with spacing of 0.08 m.....	75
4-2	Flowchart of the modified 2-D algorithm.....	77
4-3	Flowchart of the novel 3-D algorithm.....	80
4-4	Transformation technique and Euler angle.....	81
4-5	An array of 12 dipoles at the edge of a cube.....	82
4-6	The relationship between Cartesian and spherical coordinates.....	83
4-7	Feed and antenna coordinate systems.....	86
4-8	2x2 dipoles arranged in circular configuration.....	89
4-9	Arrays of (a) four and (b) twelve dipoles at 2.45 GHz from 4NEC2++.....	90
4-10	Arrays of (a) four and (b) twelve dipoles at 2.45 GHz from Empire XCcel.....	90
4-11	Mutual impedance vs spacing (x -axis) for two parallel half-wavelength antennas, non-staggered.....	92
4-12	Mutual impedance vs spacing (y -axis) for two parallel half-wavelength antennas, non-staggered.....	92
4-13	Mutual impedance vs spacing (x -axis) for two parallel half-wavelength antennas in echelon, staggered by $0.25\lambda_0$	92
4-14	Mutual impedance vs spacing (y -axis) for two parallel half-wavelength antennas in echelon, staggered by $0.25\lambda_0$	92
4-15	Mutual impedance vs spacing (x -axis) for two parallel half-wavelength antennas in echelon, staggered by $0.5\lambda_0$	92
4-16	Mutual impedance vs spacing (y -axis) for two parallel half-wavelength antennas in echelon, staggered by $0.5\lambda_0$	92
4-17	Mutual impedance vs interior angle for two half-wavelength antennas in a V configuration (along x -axis).....	93
4-18	Mutual impedance vs interior angle for two half-wavelength antennas in a V configuration (along y -axis).....	93
4-19	Mutual impedance vs interior angle for two half-wavelength antennas in a V configuration ($\varphi = 45^\circ$).....	93
4-20	Diagram showing the position of each dipole on the xy plane.....	96
4-21	2-D azimuth far-field pattern at $\theta=90^\circ$	97
4-22	2-D elevation far-field pattern at $\varphi = 0^\circ$	97
4-23	3-D far-field pattern calculated via Induced EMF Method from this thesis (3-D algorithm).....	97

List of Figures

4-24	3-D far-field pattern of a circular array calculated using pattern multiplication method.....	97
4-25	The 3-D far-field pattern from Empire XCcel.....	98
4-26	Far-field pattern at $\theta=90^\circ$	99
4-27	Far-field pattern at $\phi=100^\circ$	99
4-28	3-D far-field pattern calculated via Induced EMF Method from this thesis (eqn 4-46).....	99
4-29	3-D far-field pattern of a circular array calculated using pattern multiplication method (eqn 3-36).....	99
4-30	The 3-D far-field pattern from simulation (Empire XCcel).....	100
4-31	Far-field pattern at $\theta=90^\circ$	102
4-32	Far-field pattern at $\phi=284^\circ$	102
4-33	3-D far-field pattern calculated via Induced EMF Method from this thesis (eqn 4-46).....	102
4-34	3-D far-field pattern of a circular array calculated using pattern multiplication method (eqn 3-36).....	102
4-35	3-D Far-field pattern from Empire XCcel.....	102
4-36	Far-field pattern at $\theta=84^\circ$	103
4-37	Far-field pattern at $\phi=6^\circ$	103
4-38	3-D far-field pattern calculated via Induced EMF Method from this thesis (eqn 4-46).....	104
4-39	3-D far-field pattern calculated using pattern multiplication method (eqn 3-36).....	104
4-40	3-D far-field pattern from Empire XCcel.....	104
4-41	Far-field pattern at $\theta=90^\circ$	106
4-42	Far-field pattern at $\phi=100^\circ$	106
4-43	3-D far-field pattern calculated via Induced EMF Method from this thesis (eqn 4-46).....	107
4-44	3-D far-field pattern calculated using pattern multiplication method (view from yz plane.....	107
4-45	3-D far-field pattern from Empire XCcel.....	107
4-46	E far-field pattern at $\theta=90^\circ$	108
4-47	E far-field pattern at $\phi=280^\circ$	108
4-48	3-D far-field pattern calculated via Induced EMF Method from this thesis (eqn 4-46).....	109
4-49	3-D far-field pattern calculated using pattern multiplication method.	109
4-50	3-D Far Field pattern from Empire XCcel.....	109

List of Figures

5-1	Block diagram of a simple genetic algorithm optimiser.....	117
5-2	Stochastic universal sampling.....	121
5-3	Crossover operation.....	122
5-4	Antenna elements (blue dots) are placed in 3-D coordinates with same spacing.....	124
5-5	Flowchart of the genetic algorithm and Induced EMF Method.....	126
5-6	A cosine shaped main beam pattern directed towards 120° with side-lobe level of -10dB.....	127
5-7	Performance of GA when steering at 100°	130
5-8	Comparison between the GA optimised and desired pattern.....	130
5-9	Comparison between the GA optimised and circular array pattern....	130
5-10	Amplitude excitation versus number of elements of dipole antennas	130
5-11	Phase excitation versus number of elements of dipole antennas.....	130
5-12	Performance of GA when steering at 110°	131
5-13	Comparison between the GA optimised and desired pattern.....	132
5-14	Comparison between the GA optimised and circular array pattern....	132
5-15	Amplitude excitation versus number of elements of dipole antennas	132
5-16	Phase excitation versus number of elements of dipole antennas.....	132
5-17	Performance of GA when steering at 120°	133
5-18	Comparison between the GA optimised and desired pattern.....	133
5-19	Comparison between the GA optimised and circular array pattern....	133
5-20	Amplitude excitation versus number of elements of dipole antennas	133
5-21	Phase excitation versus number of elements of dipole antennas.....	133
5-22	Performance of GA when steering at 130°	134
5-23	Comparison between the GA optimised and desired pattern.....	134
5-24	Comparison between the GA optimised and circular array patterns..	134
5-25	Amplitude excitation from GA for each dipole element.....	135
5-26	Phase excitation from GA for each dipole element.....	135
5-27	Performance of GA when steering at 140°	135
5-28	Comparison between the GA optimised and desired pattern.....	136
5-29	Comparison between the GA optimised and circular array pattern....	136
5-30	Amplitude excitation versus number of elements of dipole antennas	136
5-31	Phase excitation versus number of elements of dipole antenna.....	136
5-32	Script code (MATLAB) to calculate the run time for 3-D algorithm.	137

6-1	Block diagram of a phased array antenna (on the transmitting side)..	146
6-2	(a) The unbalanced coaxial line without a balun, (b) The circuit of balanced system with a balun.....	147
6-3	The schematic of a wide band balun.....	148
6-4	a) Two-way Wilkinson divider in microstrip form. b) Equivalent transmission line circuit.....	149
6-5	Wilkinson divider, phase shifter and attenuation circuit at 2.45 GHz	150
6-6	DC voltage supplies for JPHPS 2484+ and EVA 3000+.....	151
6-7	Battery supplies and voltage regulator circuit.....	151
6-8	A model of a dipole antenna and its far field pattern using Empire XCcel.....	153
6-9	Four fabricated dipole antennas with balun.....	153
6-10	Simulated and measured return loss for dipole 1.....	154
6-11	Simulated and measured return loss for dipole 2.....	154
6-12	Simulated and measured return loss for dipole 3.....	155
6-13	Simulated and measured return loss for dipole 4.....	155
6-14	The design of a 4:1 Wilkinson Divider using Empire XCcel.....	156
6-15	Fabrication of the 4:1 Wilkinson divider and its S_{21} measurement...	157
6-16	Measurement of the S_{11} parameter using VNA.....	157
6-17	Simulation (black line) and measured results (red-dotted) of S_{11}	158
6-18	Simulated (magenta line) and measured (blue line) magnitude of S_{21} are on the left axis (L) while the simulated (red line) and measured (green line) angle of S_{21} are on the right axis of the graph	159
6-19	Simulated (magenta line) and measured (blue line) magnitude of S_{31} are on the left axis (L) while the simulated (red line) and measured (green line) angle of S_{31} are on the right axis of the graph	160
6-20	Simulated (magenta line) and measured (blue line) magnitude of S_{41} are on the left axis (L) while the simulated (red line) and measured (green line) angle of S_{41} are on the right axis of the graph	160
6-21	Simulated (magenta line) and measured (blue line) magnitude of S_{51} are on the left axis (L) while the simulated (red line) and measured (green line) angle of S_{51} are on the right axis of the graph	161
6-22	The current distribution of the 4:1 Wilkinson divider at 2.45 GHz using Empire XCcel.....	161
6-23	Points where phase and amplitude errors may be introduced in each branch of a phased array antenna.....	162
6-24	Feed network characteristics measurement.....	163
6-25	Four-way Wilkinson divider, phase shifter and attenuator circuit.....	164

6-26	Phase shift characteristics for each port versus voltage control of the phase shifter, V_p	165
6-27	Insertion loss for each port versus voltage control of the phase shifter, V_p	165
6-28	Phase shift characteristics for each port versus the control voltage of the attenuator, V_{att}	166
6-29	Insertion loss for each port versus the control voltage of the attenuator, V_{att}	166
6-30	Wiring diagram of Loughborough University's anechoic chamber...	168
6-31	Measurement set-up in an anechoic chamber for dipole antenna arrays (transmitter) with the feed network.....	169
6-32	The feed network is connected to the batteries, which act as control voltages for the surface mounted attenuator and phase shifter.....	170
6-33	Measurement set-up of a horn antenna (1-18 GHz) at the receiving side in an anechoic chamber.....	170
6-34	Four dipole antennas with the feed network.....	171
6-35	Trial 1 of a 2x2-dipole antenna array.....	172
6-36	The set-up of the dipole antenna array with SMA (M-M) straight coaxial cable, worms and tape to hold the four dipoles together.....	173
6-37	Four slots were added to Trial 1 to allow the set-up of straight SMA connectors, worms and semi-flexible coaxial cables.....	173
6-38	Top view of the dipole array with ferrite rings.....	174
6-39	Side view of the dipole array with ferrite rings.....	174
6-40	Measured S_{11} of Trial 1.....	175
6-41	Magnitude of S_{21}, S_{31}, S_{41} and S_{51} (in dB) at 2.45 GHz of the feed network.....	177
6-42	Phase of S_{21}, S_{31}, S_{41} and S_{51} (in degrees) at 2.45 GHz of the feed network.....	177
6-43	The 3-D algorithm simulated (red) and measured (blue) plots for the co-polar pattern at 2.45 GHz.....	178
6-44	The 3-D algorithm simulated (red) and measured (blue) plots for the cross-polar pattern at 2.45 GHz.....	179
6-45	Amplitude of S_{21}, S_{31}, S_{41} and S_{51} (in dB) at 2.56 GHz of the feed network.....	180
6-46	Phase of S_{21}, S_{31}, S_{41} and S_{51} (in degrees) at 2.56 GHz of the feed network.....	180
6-47	The 3-D algorithm simulated (red) and measured (blue) plots for the co-polar pattern at 2.56 GHz.....	181

List of Figures

6-48	Measured S_{11} for Trial 1 with sample #2.....	182
6-49	Sample #2's magnitude of S_{21}, S_{31}, S_{41} and S_{51} (in dB) at 2.45 GHz.....	183
6-50	Sample #2's phase of S_{21}, S_{31}, S_{41} and S_{51} (in degrees) at 2.45 GHz.....	183
6-51	Sample #2's co-polar 3-D algorithm simulated (red) and measured (blue) plots at 2.45 GHz.....	184
6-52	Sample #2's cross-polar 3-D algorithm simulated (red) and measured (blue) plots at 2.45 GHz.....	185
6-53	Measured S_{11} of Trial 2.....	186
6-54	Magnitude of S_{21}, S_{31}, S_{41} and S_{51} (in dB) at 2.54412 GHz of the feed network.....	187
6-55	Phase of S_{21}, S_{31}, S_{41} and S_{51} (in degrees) at 2.54412 GHz of the feed network.....	188
6-56	The 3-D algorithm simulated (red) and measured (blue) plots for the co-polar pattern at 2.54 GHz.....	189
6-57	Magnitude of S_{21}, S_{31}, S_{41} and S_{51} (in dB) at 2.56 GHz of the feed network.....	190
6-58	Phase of S_{21}, S_{31}, S_{41} and S_{51} (in degrees) at 2.56 GHz of the feed network.....	190
6-59	The 3-D algorithm simulated (red) and measured (blue) plots for the co-polar pattern at 2.56 GHz.....	191

LIST OF TABLES

1	Comparison between numerical and analysis softwares.....	45
2	Comparison between method of moments and finite-difference time-domain method.....	50
3	The position of dipole elements in rectangular coordinates (x, y, z) and Euler angle (α, β, γ).....	82
4	The impedance matrix, [Z], for four parallel dipoles.....	94
5	The impedance matrix, [Z], for 12 dipoles.....	95
6	Comparison on the far-field pattern.....	98
7	Excitation values with uniform amplitude and different phases.....	99
8	Comparison on the far-field pattern.....	100
9	Excitation values with different amplitude and phases.....	101
10	Comparison on the far-field pattern.....	103
11	Comparison on the far-field pattern.....	105
12	Excitation values with the same amplitude but different phases.....	106
13	Comparison on the far-field pattern.....	107
14	Excitation values with the different amplitude but phases.....	108
15	Comparison on the far-field pattern.....	109
16	Genetic Algorithm terminology.....	115
17	GA control parameters using different methods.....	125
18	Parameters for the genetic and 3-D algorithms.....	125
19	Run time comparison for 2x2 dipole antenna arrays.....	138
20	The length and diameter of four dipole antennas.....	153
21	Voltage control of sample#1 applied to attenuator and phase shifter..	176
22	The magnitude and phase applied at each dipole antenna in the 3D algorithm.....	178
23	The magnitude and phase applied at each dipole antenna (at 2.56 GHz) in the 3D algorithm.....	181
24	Voltage control of sample#2 applied to attenuator and phase shifter..	182
25	The magnitude and phase applied at each dipole antenna in the 3D algorithm.....	184
26	Voltage control of sample#1 applied to attenuator and phase shifter..	186
27	The magnitude and phase applied at each dipole antenna (at 2.54 GHz) in the 3D algorithm.....	188
28	The magnitude and phase applied at each dipole antenna (at 2.56	191

GHz) in the 3D algorithm.....

LIST OF SYMBOLS

Symbols	Description	Units
E_θ	Electric field (or far-field) component along θ direction	V/m
H_ϕ	Magnetic field component along ϕ direction	A/m
η	Wave impedance (120π)	Ω
λ	Wavelength	m
P_{rad}	Radiated power	W
D_0	Maximum directivity	
I_0	Maximum current (rms)	A
k	Number of wavelength	
r	Distance from any point on the source to the observation point	
$C_i(x)$	Cosine integral	
$S_i(x)$	Sine integral	
C	Euler's Constant	
l	Length of dipole	m
l_1	Length of dipole 1	
l_2	Length of dipole 2	
R_r	Real component of impedance	Ω
X_m	Imaginary component of impedance	Ω
AF	Array factor	
$F_e(\theta)$	The active element pattern (AEP)	
$f_0(\theta)$	The isolated element pattern	
m, m_1, m_2	Angle between the axis of dipole towards the observation points.	
A_n	Amplitude excitation for n^{th} element	V
d	Spacing between elements	m
θ	Elevation angle	$^\circ$
ϕ	Azimuth angle	$^\circ$
N	Number of total elements	
E_{21}	Electric field radiated by antenna 1 to antenna 2	
E_z	Electric field component along z axis	
E_ρ	Electric field component along ρ axis	

List of Symbols

Z_a	Active input impedance	Ω
Z_{mn}	Mutual impedance at port m due to current at port n (with port m open-circuited) and $m \neq n$	
Z_{mm}	Self impedance when $m=n$	
Z	Impedance matrix consists of self and mutual impedance	Ω
Z^g	Generator impedance (it has been assumed 50Ω)	Ω
Z^s	Source impedance ($Z^s = Z^g$)	Ω
V^s	Voltage source	V
I	Terminal current vector	A
ψ	The angle between x, y axis for E_x and E_y components	$^\circ$
Re and Im	Real and imaginary part of electric field E	
C	Array phase function	
α_n	Phase excitation for n^{th} element	$^\circ$
(θ_0, ϕ_0)	Beam peak occurred at angle θ_0 and ϕ_0	$^\circ$
χ	Progressive phase shift	$^\circ$
a_n	Excitation coefficient (amplitude and phase) for n^{th} element	
b	The distance from the origin to the n^{th} element in circular array (radius).	
ϕ_n	Angular position of n^{th} element on x-y plane	$^\circ$
\mathbf{E}	Electric field vector	
R_n	the distance from each dipole (x_n, y_n, z_n) to the far-field observation point (r, θ, ϕ)	m
\mathbf{B}	Transformation matrix.	
$\{\mathbf{c}\}$	Primary Cartesian coordinate system	
$\{\mathbf{c}'\}$	Secondary Cartesian coordinate system	
$\{\mathbf{s}\}$	Primary spherical coordinate system	
$\{\mathbf{s}'\}$	Secondary spherical coordinate system	
(x, y, z)	Components in primary Cartesian coordinate system	m
(x', y', z')	Components in secondary Cartesian coordinate system	m
(α, β, γ)	Euler angles	$^\circ$
(r, θ, ϕ)	Components in primary spherical coordinate	(m, $^\circ$, $^\circ$)

List of Symbols

	system	
(r', θ', ϕ')	Components in primary spherical coordinate system	$(m, ^\circ, ^\circ)$
$({}^s T^c)$	Transformation from Cartesian to spherical components.	
$({}^c T^s)$	Transformation from spherical to Cartesian components.	
S_{d_i}	Desired radiation pattern for $i=1, 2, \dots, Q$ sampling points.	
S_{c_i}	The far-field pattern calculated using the 3-D algorithm	
(x_i, y_i, z_i)	Position of dipole i ($i=1, 2, \dots, 4$) in x, y, z components.	m
D_i	Dipole element where $i=1, 2, \dots, 4$	
θ_i	The slanted angle in elevation plane for i^{th} dipole element ($i=1, 2, \dots, 4$)	$^\circ$
Z_c	The impedance of balun	
C_n	Coarse adjustment of variable voltage at the attenuator and phase shifter ($n=1, 2, 3, \dots, 7$)	
F_n	Fine adjustment of variable voltage at the attenuator and phase shifter ($n=1, 2, 3, \dots, 7$)	
Phase n	Phase shifter of $n=1, 2, 3$.	
Att n	Attenuator of $n=1, 2, \dots, 4$	
V_{att}	Voltage assigned at attenuator.	V
V_p	Voltage assigned at phase shifter	V

CHAPTER 1:

Introduction to Research

1.1 Research Background

Phased array antennas are in high demand due to certain applications such as in radar development that require radiation pattern control. They have the ability to shape or electronically steer the radiation pattern by proper element excitations without the need to mechanically rotate. Electronic beam steering is preferable compared to mechanical steering due to the rapid and flexible electronic phasing for each element. In the 1950s, many industrial companies, government laboratories and academic institutions developed various methods of electronic beam steering, as summarized by Fowler [1] from the 1950s to date.

The Special Radar Group in Lincoln Laboratories, Massachusetts was one of the major contributors to the phased array radar development project in 1958. The group began with the application in satellite surveillance, and later developing the Millstone Hill radar, one of the few radar instruments existed at that time with satellite detection and tracking capability [2]. In 1959, the group led by John L. Allen developed the technology of phased arrays for military purposes. As a result, the laboratory produced a series of reports [3-5] entitled ‘Phased-Array Radar Studies’. The reports highlighted the development of array theory to hardware implementation to obtain reliable and low-cost array components, a variety of beam scanning techniques and a good understanding of the array theory.

Early works on phased array antennas concentrated on the dipole antenna, as it is the simplest type [3-5]. However, one of the primary challenges in designing a phased array is the existence of mutual coupling between elements in the antenna array. Mutual coupling is the interaction of microwave power transmitted by one element that can be received by other elements surrounding

that element in an array. It can affect the performance of the antenna array. Allen [6] investigated the effects of mutual coupling by comparing the measured H-plane pattern of a 16-dipole antenna array with and without the effect of mutual coupling. The measured H-plane pattern is in closer agreement by taking the mutual coupling effect into account rather than neglecting it.

The effect of mutual coupling between elements plays a crucial role in the direction-finding performance of the adaptive antenna arrays. The radiation patterns of antenna arrays will be altered by the coupling effect from the adjacent elements thus reducing the accuracy and resolution of direction finding system. Gupta [7] considered the mutual coupling effect into account by using the concept of mutual impedance to derive the open-circuit voltages from the terminal voltages. From there, the steady state output signal-to-interference noise ratio (SINR) has been derived as a measured performance for the adaptive arrays. It was shown that its performance is lower compared to that obtained without the mutual coupling effect. On the other hand, Hui [8] introduced a new definition of mutual impedance by taking the actual measured current on the antenna element. The result is used as input in Multiple Signal Classification (MUSIC) algorithm [9] where the algorithm is used to provide unbiased estimation of the direction of arrival (DoA) of signals at the antenna array. The combination of both methods enabling them to accurately predicts the direction-of-arrival's of two signals at angle 30° and 57° better than open-circuit voltages [7]. Other than accurately predict DoA, the mutual coupling also affects the nulls which is also important to steer the nulls in undesired direction [10].

Preston [11, 12] demonstrated the switched-parasitic antenna array in a direction-finding system for the tracking of base stations in mobile communications. The author presents three modes of direction-finding solution for both single- and multiple-signal detection by using a switched four-element parasitic array with the four patterns as shown in Figure 1-1. One way to track the single incident signal is by detecting the field strength sequentially at q_1 , q_2 , q_3 and q_4 . The maximum value is determined and the antenna is switched to the position that gives the maximum signal until a further update is required.

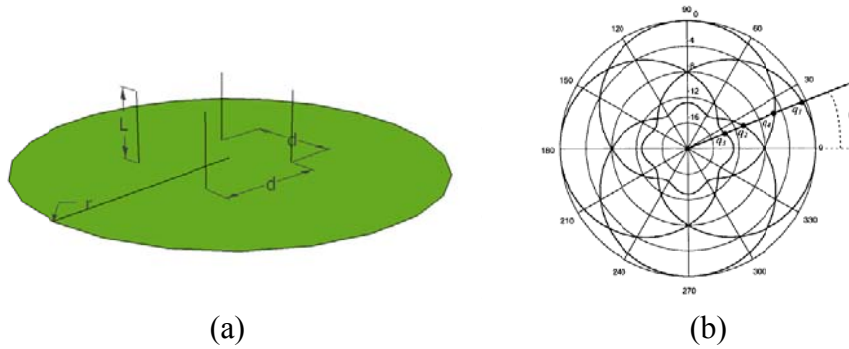


Figure 1-1: a) A four element monopole switched-parasitic antenna array on a ground plane with d is spacing between elements, L is the length of monopole and r is the radius of the ground plane. The dimensions are as follows, $d=0.27\lambda$, $L=0.25\lambda$ and $r=0.625\lambda$. b) Four radiation pattern when one monopole is active while others remain passive at four different positions [11].

A few methods are available to analyze the mutual coupling effect in antenna arrays either using numerical techniques or closed form solution of the array analysis (such as the pattern multiplication and the input impedance methods). The accuracy of numerical analysis of antenna characteristics received tremendous improvements in the last few decades [13]. Examples of popular antenna analysis methods that utilize numerical techniques to solve Maxwell's equations are the method of moments (MoM), the finite element method (FEM) and the finite-difference time-domain method (FDTD). These methods have evolved substantially and they have now become very accurate and reliable commercial numerical analysis tools. Moreover, several factors such as an increase in computational speeds, reduction in computer hardware costs, improvements in numerical analysis methods and the availability of numerous commercial software packages allow electrical engineers to analyse antennas of various geometries rapidly and easily.

On the other hand, there is also substantial progress in array analysis methods due to the advancement of computational software. As the complexity of array antennas increased, improved techniques became necessary for the understanding of array characteristics. The conventional pattern characteristics of antenna arrays can be determined by the principle of pattern multiplication of array and element factors. However, it does not include mutual coupling among the array elements and assumes identical element radiation patterns. It can be a useful tool in understanding the basic principles of antenna arrays, but

inadequate for detailed analysis. Therefore, it has been compensated with many thorough array analysis existed nowadays.

1.2 Problem Statement

The mutual coupling effect plays a significant role in the array environment and should be taken into consideration, especially in small antenna arrays. It is always desirable to achieve a small antenna array due to its flexibility and cost effectiveness. However, small antenna arrays incorporate small spacing which leads to high coupling between antenna elements.

One of the well-known array analyses that include the mutual coupling effect is the active element pattern [14]. The pattern of a fully excited (scanned) phased array is the product of the active element pattern and array factor. The active element pattern (or known as AEP) of a phased array is defined as the radiation pattern of the array when one radiating element is driven and all others are terminated with matched loads. The method is accurate for infinite arrays and approximately true for finite but large arrays. However, in small arrays, it might be inaccurate since the mutual coupling change in edge elements may be neglected. The coupling of edge elements behaves differently with each other and its change should not be ignored.

Many papers discuss array analysis techniques that include the mutual coupling effect between elements in small antenna arrays. However, they are lacking in 3-D, where the elements can be placed in any configuration and orientation, which is useful for conformal, cubic or spherical arrays. Conformal arrays are array antennas on curved surface and are usually integrated on vehicles such as cars, aircraft and satellite bodies. Cubic arrays are the arrangement of all the antenna elements (such as dipoles and slots) at the edge of cube structure as presented in [15, 16]. One of the reasons is due to the increasing complexity of the analysis as the dimensions increase.

Accurate and fast calculations of the antenna radiation patterns are essential for optimisation methods to generate antenna arrays. Full-wave analysis takes long computation and requires large memory. Numerical technique such as method of moment (MoM) considers coupling between elements. It directly

applies Maxwell's equation and computes the unknown current distribution from a set of known voltage excitation with the proper selection of basis and weighting functions. On the other hand, the calculation of the far-field pattern without the mutual coupling effect (such as pattern multiplication) resulting inaccurate decisions by the optimisation method. Pattern multiplication is a conventional technique which is the product of the array factor and the element pattern. The array factor does not consider the mutual coupling between elements because it depends only on the geometry of antenna elements and the current distribution is directly proportional to the voltage excitation of the antenna elements. Other technique tends to remove the effect of the mutual coupling by increasing the element spacing, d as in Figure 1-1. However, the technique might produce higher side-lobe levels and grating lobes.

Optimization techniques have evolved tremendously in recent years to ease computational burden in optimizing antenna arrays. Dolph-Chebyshev [17] and Taylor [18] are a few conventional ways to find the best weighting amplitude for low side lobe levels. Using high-speed computers, iterative and evolutionary methods such as genetic algorithm (GA) [19], particle swarm optimization (PSO) [20], least-mean square (LMS) [21] are widely used in pattern synthesis. On the other hand, there are new hybrid techniques [22] which sometimes offer greater performance compared to iterative and evolutionary methods. Criteria in determining good performance depends on computational efficiency, not trapped in local extremums, capability to optimize multi objectives (PARETO) function, complex problems and large variables. Hybrid methods combine more than one method thus providing more capabilities compared to single optimization technique.

Realising the importance of mutual coupling effect in 3-D array, its effect in dipole antenna arrays is investigated. It can be applied to elements arranged in any locations and configurations, such as in aperiodic, cubic or spherical arrays. As a result, a novel 3-D array analysis has been developed considering the mutual coupling effect between elements. The analysis has been demonstrated both on four (or known as 2 by 2 dipoles arranged in x and y -axis) and cubic dipole arrays (or known as twelve dipoles arranged at the edge of cube as shown in Figure 1-2). A 2x2 dipole array can be categorized as 2-D array while cubic

dipole array can be categorized as 3-D array. Then, the synthesis pattern of four dipole arrays was performed using a combination of this new array analysis and a genetic algorithm. The realization of the dipole antenna array was then performed using a four-dipole antenna with a feed network. The purpose is to validate the new array analysis considering the mutual coupling effect with measured results of a dipole array; this is elaborated in detail in this thesis.

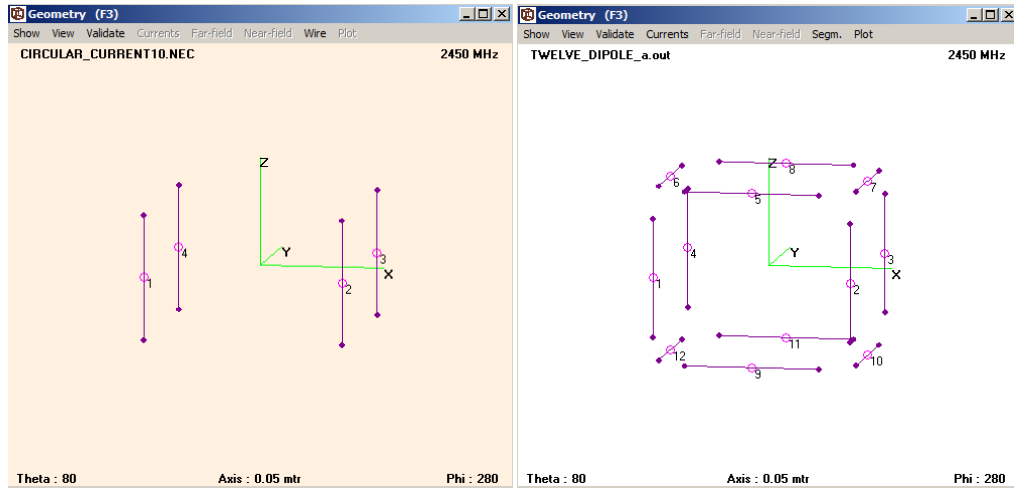


Figure 1-2 (a) Four (or 2x2) dipole antenna arrays, (b) Twelve dipole antenna arrays arranged at the edge of a cube (or known as cubic arrays).

1.3 Research Contributions

The principal aim of this thesis is to develop a 3-D antenna analysis employing mutual coupling effect between elements for direction finding application. At this stage, a few research contributions are achieved:

- *The development of new array analysis for dipole antenna arrays considering the mutual coupling effect using the Induced EMF method in three dimensions.*

The above point is the major and novel contribution of this dissertation. The new 3-D algorithm developed is applicable to elements arranged in any configuration; 1-D, 2-D, or 3-D. The model takes into account the mutual coupling effect between the elements, giving more accurate results compared to conventional pattern multiplication, especially in the side-lobe and null regions. The method was compared with other full wave modelling software such as FDTD (Empire XCcel) and MoM (4NEC2++). The results show that the 3-D

algorithm is more than 75% in agreement with other techniques, especially with FDTD.

- *The optimisation to find the 'best fit' to the desired pattern using a combination of the 3-D algorithm and a genetic algorithm.*

The 3-D algorithm was developed from scratch, allowing a greater flexibility to control the pattern by considering the mutual coupling effects into account. One way to demonstrate it by using a genetic algorithm (GA) to vary the amplitude and phase excitations of each element in order to obtain the desired pattern. The pattern can be steered sequentially in order to determine the strength of the signal in direction finding application. The results from the 3-D algorithm might be less accurate compared with other 3-D electromagnetic software but faster and efficient where the simulation runs simultaneously and does not need to be exported to the genetic algorithm.

- *The validation of the 3-D algorithm with experimental work using a 2x2 dipole antenna array and a feed network consists of phase shifter and attenuator.*

Last but not least, the validation of 3-D algorithm is performed with the experimental work using a 2x2 dipole array. A good agreement between them proves the 3-D algorithm comprising of mutual coupling effect is accurate, fast and efficient, especially for small antenna arrays.

1.4 Thesis Outline

The second chapter of this thesis presents an introduction and the mathematical background related to the characteristics of antennas' elements and arrays. A conventional pattern multiplication for antenna arrays and the mutual coupling effect between elements are also included. Other methods such as the active input impedance and the active element pattern to account for the mutual coupling effect in antenna arrays are briefly introduced. The mathematical concept of self and mutual impedances is also discussed in detail in this chapter.

Numerical methods and array analysis are described in Chapter Three. The numerical techniques such as method of moment (MoM) and finite-

difference time-domain (FDTD) method are briefly explained. A review of previous works related to array analysis in 1-D (linear), 2-D (planar or circular) and 3-D (spherical, cube) are also presented. The study is essential in order to develop a new array analysis technique that includes mutual coupling effect for 3-D arrays. Furthermore, a number of array optimisation techniques, include sequential uniform sampling, gradient search, Nelder-Mead simplex, simulated annealing and genetic algorithm, which is used for pattern synthesis, are discussed at the end of this chapter.

Chapter Four provides the development of novel pattern analysis of antenna arrays using the Induced EMF method. This method takes into account the mutual coupling effect between elements. It is applicable for elements arranged in any configuration. The novel 3-D algorithm was tested for 2x2 and twelve dipole arrays arranged at the edge of cubic structure. The result was compared with full wave techniques such as FDTD, MoM and a conventional pattern multiplication method.

The pattern needs to be electronically steered into any desired direction while removing any interference in other directions. This may be achieved using a genetic algorithm by varying the amplitude and phase excitation of each element. The combination of this optimisation technique and the new 3-D Algorithm are explained in Chapter Five. It is demonstrated using a 2x2-dipole array arranged in a rectangular grid with a spacing of $0.9\lambda_0$ between the elements. The obstacles and limitations of this technique are discussed in this chapter.

In Chapter Six, the verification of the novel 3-D algorithm is performed with the experimental setup of 2x2-dipole antenna array. A feed network was designed in order to feed the four-dipole antenna array with different amplitudes and phases. The feed network consists of a Wilkinson Divider, a circuit of surface-mounted voltage control phase shifter and attenuator chips. The dipole array was mounted on Rohacell substrate to make it robust. The entire devices were mounted on the platform in the anechoic chamber for pattern measurement. The measurement setup and results are explained in details within this chapter.

Chapter Seven highlights the conclusions discussed in each chapter. Furthermore, some recommendations for future work are also included. Then,

four appendices are included at the end of this thesis; the former three are the 3-D algorithm for 2x2 and cubic dipole arrays, the genetic algorithm, and last but not least the effect of the element spacing and orientation on the far-field pattern of four dipoles array. Last but not least, Figure 1-3 categorized the content of the whole thesis in a flowchart.

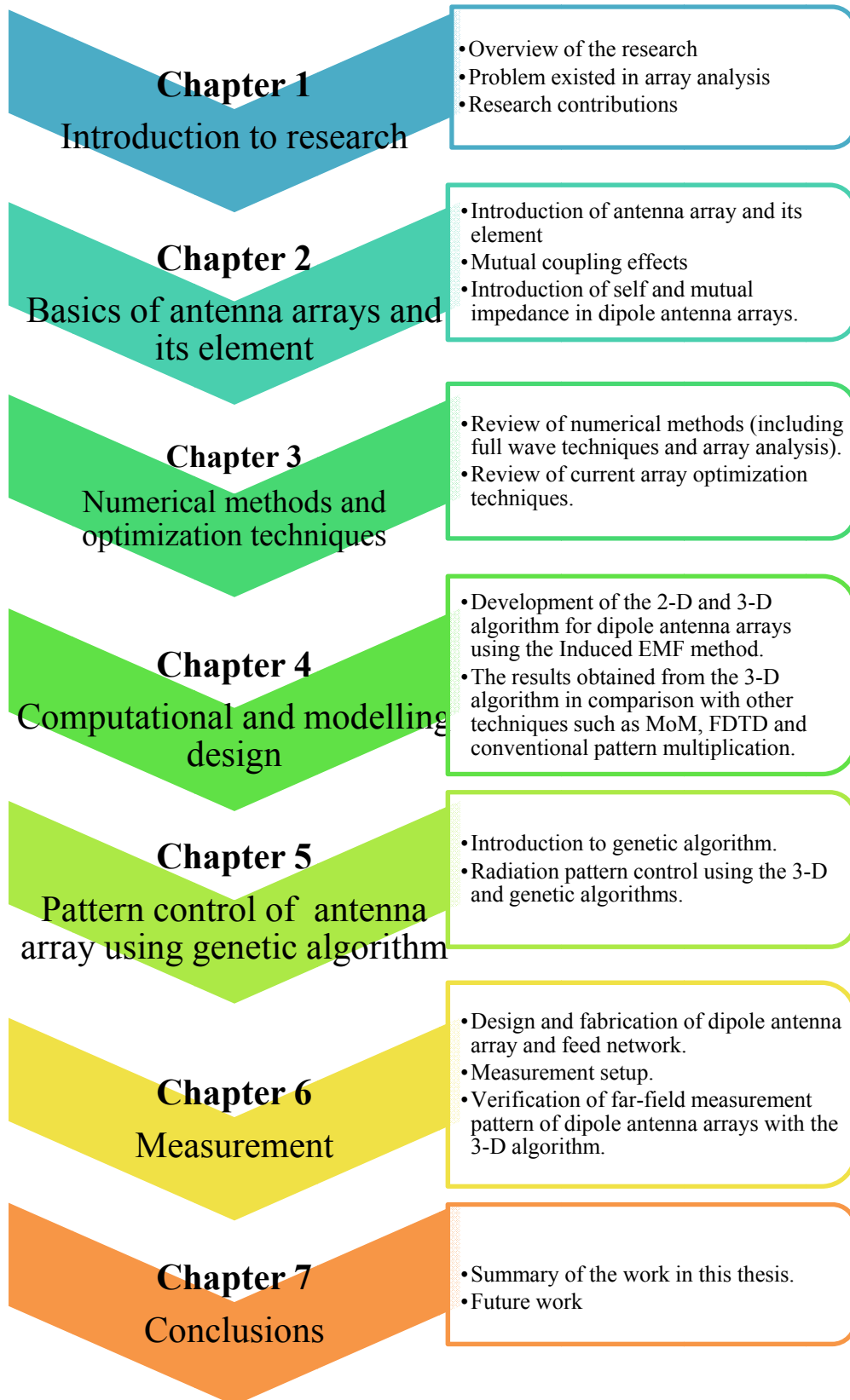


Figure 1-3: Flowchart of the thesis

References

- [1] C. A. Fowler, "Old Radar Types Never Die; They just Phased Array or ... 55 Years of Trying to Avoid Mechanical Scan". *Aerospace and Electronic Systems Magazine, IEEE*, Vol. 13 (9), pp. 24A-24L, 1998.
- [2] A. J. Fenn, D. H. Temme, W. P. Delaney, and W. E. Courtney, "The Development of Phased-Array Radar Technology". *Lincoln Laboratory Journal*, Vol. 12 (2), pp. 321-340, 2000.
- [3] J. L. Allen, L. Cartledge, W. P. Delaney, and J. Dibartolo, "Phased Array Radar Studies, 1 July 1960 to 1 July 1961". Lincoln Laboratory, Lexington, Massachusetts, *Technical Report 236*, 13 Nov. 1961.
- [4] J. L. Allen, D. M. Bernella, W. W. Carpenter, and W. P. Delaney, "Phased Array Radar Studies, 1 July 1961 to 1 January 1963". Lincoln Laboratory, Lexington, Massachusetts, *Technical Report 299*, 20 Feb. 1963.
- [5] J. L. Allen, D. M. Bernella, F. Betts, and L. Cartledge, "Phased Array Radar Studies, 1 January 1963 to 1 July 1964". Lincoln Laboratory, Lexington, Massachusetts, *Technical Report 381*, 31 March 1965.
- [6] J. L. Allen and W. Delaney, "On the effect of mutual coupling on unequally spaced dipole arrays". *IRE Transactions on Antennas and Propagation*, Vol. 10 (6), pp. 784-784, Nov. 1962.
- [7] I. Gupta and A. Ksienski, "Effect of mutual coupling on the performance of adaptive arrays," *Antennas and Propagation, IEEE Transactions on*, vol. 31, pp. 785, sep, 1983.
- [8] H. T. Hui, "Improved compensation for the mutual coupling effect in a dipole array for direction finding," *Antennas and Propagation, IEEE Transactions on*, vol. 51, pp. 2498, sep, 2003.
- [9] R. Schmidt, "Multiple emitter location and signal parameter estimation," *IEEE Transactions on Antennas and Propagation*, vol. 34, pp. 276, Mar., 1986.
- [10] A. Tennant and B. Chambers, "A two-element time-modulated array with direction finding properties," *IEEE Antennas and Wireless Propagation Letters*, vol. 6, pp. 64, 2007.
- [11] S. L. Preston, D. V. Thiel, T. A. Smith, S. G. O'Keefe, and J. W. Lu, "Base-station tracking in mobile communications using a switched parasitic antenna

- array,” *IEEE Transactions on Antennas and Propagation*, vol. 46, pp. 841, June 1998.
- [12] S. L. Preston and D. V. Thiel, “Direction finding using a switched parasitic antenna array,” *Antennas and Propagation Society International Symposium*, vol. 2, pp 1024-1027, 1997.
- [13] K. Takamizawa. "Analysis of highly coupled wideband antenna arrays using scattering parameter network models." PhD Theses, Virginia Polytechnic Institute and State University, Virginia, 2002.
- [14] D. M. Pozar, “The active element pattern”. *IEEE Transactions on Antennas and Propagation*, vol. 42, pp. 1176, aug., 1994.
- [15] L. Nagy, "Modified MIMO Cube for Enhanced Channel Capacity," *International Journal of Antennas and Propagation*, vol. 2012, 2012.
- [16] B. N. Getu and J. B. Andersen, "The MIMO cube - a compact MIMO antenna," *Wireless Communications, IEEE Transactions on*, vol. 4, pp. 1136, may, 2005.
- [17] C. L. Dolph, "A Current Distribution for Broadside Arrays Which Optimizes the Relationship between Beam Width and Side-Lobe Level," *Proceedings of the IRE*, vol. 34, pp. 335-348, 1946.
- [18] T. T. Taylor, ‘ Design of Line Source Antennas for Narrow Beam Widths and Low Sidelobes,’ *IRE AP Trans*, 4.16-28, 1955.
- [19] K-K. Yan, Y. Lu, ‘Sidelobe Reduction in Array-pattern Synthesis using Genetic Algorithm’, *IEEE Trans on Antennas and Propagation*, Vol. 45, No. 7, 1117-1123, 1997.
- [20] P. Koduru, S. Das, and S. M. Welch, “A Particle Swarm Optimization-Nelder Mead Hybrid Algorithm for Balanced Exploration and Exploitation in Multidimensional Search Space”, iee.cugb.edu.cn/WorldComp2006/ICA4682.pdf.
- [21] P. C. Strickland, ‘A Least Mean Square Error Synthesis with Pattern Constraints at Multiple Frequencies’, *IEEE Trans. on Antennas and Propagation*, Vol. 40, No. 4, 463-466, 1992.
- [22] W. Li, S. Liu. X. Shi, Y. Hei, ‘Low-sidelobe Pattern Synthesis of Spherical Array using the Hybrid Genetic Algorithm’, *Microwave and Optical Technology Letters*, Vol. 51, No. 6, 1487-1492, 2009.

CHAPTER 2:

Basics of Antenna

Arrays

2.1 Introduction

This chapter introduces the readers to the background theory of dipole antenna and arrays. One of the advantages of antenna arrays as compared with individual radiating elements is to obtain radiation pattern control. Pattern multiplication technique which is the conventional and idealised method in array analysis is presented. However, there are other effects that influence how elements behave in arrays when compared to individual elements in isolation. The effect, which is known as mutual coupling, brings a significant effect to arrays, which will be explained in this chapter.

There are a few methods to study the effect of mutual coupling between elements, such as the active input impedance and the active element pattern (AEP). Those will be briefly introduced in this chapter. The active element pattern may be performed through simulation software or measurement. On the other hand, the active input impedance can be obtained from numerical computation or measurement. It is based on N -port network and its background theory such as self and mutual impedance is elaborated in details before the concluding remarks in this chapter.

2.2 Basics of Element and Array Antenna

An antenna array is a combination of several single-element antennas (or sources) forming a single antenna in order to achieve an improved performance in comparison to an elementary antenna. The performance may be either to

increase the overall gain, to provide diversity reception, to cancel out interference from a particular set of directions, to steer the array to a desired direction, to determine the direction of arrival of the incoming signal or to maximise the Signal to Interference Noise ratio (SINR). Generally, elements are arranged in a uniform geometrical configuration or matrix, such as in linear, planar and circular. Antenna arrays constructed in this way have received a lot of research interest due to their wide application such as communications and radar.

Usually, one type of antenna is used to form an array. However, the use of different types of antenna in an array is also possible. Monopoles, dipoles, slot-in waveguides and microstrip are types of elements that are generally used in arrays. Factors that influence the selection of the type of antenna include operating frequency, power-handling capability, polarisation, cost, feeding arrangements and mechanical constraints.

There are a few terms to describe the performance of the antenna. Characteristics such as the far-field pattern, directivity and input impedance are discussed in this chapter.

Moreover, the characteristics of antenna array are explained. The total far-field pattern of an array that represents ideal array theory is also described in this section.

2.2.1 Array Element: Half wavelength Dipole

A few elements of dipole antennas were chosen for this study due to their simple characteristics and ease of implementation in array analysis. The half-wavelength dipole is the most common length of antenna used in many applications. The coordinate system that is used in this thesis is taken from [1] (Figure 2-1). A pattern can be referred in polar form as a function of three vectors \mathbf{a}_r , \mathbf{a}_θ and \mathbf{a}_ϕ . The electric and magnetic far-field components of a half-wavelength dipole ($l = \lambda/2$), E_θ and H_ϕ are [1]:

$$E_\theta(\theta, \varphi) \approx \frac{j \eta I_0 e^{-jkr}}{2\pi r} \cdot \frac{\cos(\frac{\pi}{2} \cos \theta)}{\sin \theta} \quad (2 - 1)$$

$$H_\phi(\theta, \varphi) \approx \frac{E_\theta}{\eta} \approx \frac{j I_0 e^{-jkr}}{2\pi r} \cdot \frac{\cos(\frac{\pi}{2} \cos \theta)}{\sin \theta} \quad (2 - 2)$$

where I_0 is the maximum current, η is the wave impedance (120π), k is the number of wavelength, r is the distance from any point on the source to the observation point, θ and φ is the angle calculated from z and x -axis respectively to the any point on the source as shown in Figure 2-1.

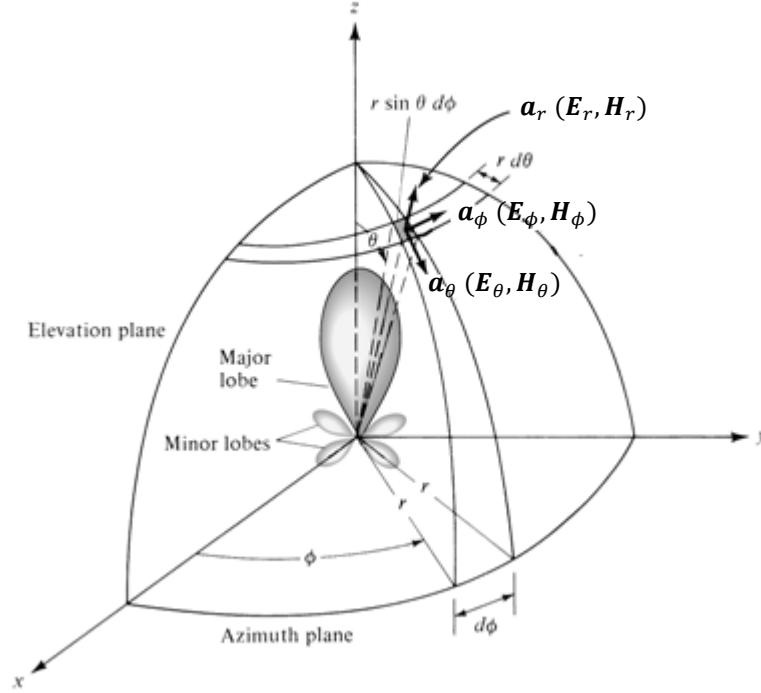


Figure 2-1: The coordinate system for far-field pattern analysis from Balanis [1].

The far-field components are valid when the measurement distance is greater than $2D^2/\lambda$. D is the largest dimension of the antenna and λ is the wavelength.

The total power radiated, P_{rad}

$$P_{rad} = \eta \frac{|I_0|^2}{8\pi} C_{in}(2\pi) \quad (2-3)$$

where $C_{in}(x)$ is derived from the cosine integral $C_i(x)$

$$C_i(x) = \int_{\infty}^x \frac{\cos y}{y} dy \quad (2-4)$$

$$C_{in}(x) = 0.5772 + \ln(x) - C_i(x) \quad (2-5)$$

where $C_i(2\pi)=2.435$ is obtained from Balanis [1].

The maximum directivity of the half wavelength dipole is

$$D_0 = 4\pi \frac{U_{max}}{P_{rad}} \quad (2 - 6)$$

where U_{max} is the maximum radiation intensity of half-wave dipole (occured at $\theta=90^\circ$) and is given by

$$x \approx \eta \frac{|I_0|^2}{8\pi^2} \sin^3 \theta \quad (2 - 6a)$$

Substituting equation 2-3 to 2-5 into equation 2-6 will give:

$$D_0 \approx 1.643 = 2.156 \text{ dB} \quad (2 - 6b)$$

The radiation resistance for a dipole in free space ($\eta \approx 120\pi$) is given by:

$$R_r = \frac{2P_{rad}}{|I_0|^2} = \frac{\eta C_{in}(2\pi)}{4\pi} \approx 30(2.435) \approx 73\Omega \quad (2 - 7)$$

These values are for an infinitely thin dipole and might be different for finite thickness dipole. The imaginary part (reactance) is calculated using the induced EMF method and found to be $j42.5$ for a half-wavelength dipole at resonance [1]. Since the current maximum for a $\lambda/2$ dipole occurs at the input terminals, the radiation resistance and reactance given is also the input impedance of the dipole and equal to:

$$Z_{in} = 73 + j42.5 \quad (2 - 8)$$

Usually, in practice, the length of the antenna is reduced so that the imaginary part of the input impedance decreases to zero at the resonant frequency. The length to be reduced depends on the radius of the wire, around $l = 0.47\lambda$ to 0.48λ . The thinner the wire, the closer the length is to 0.48λ [1].

2.2.2 Antenna Array

There are many advantages of an antenna array including increasing gain and achieving desired radiation pattern. Gain is equal to the product of antenna radiation efficiency and directivity. Antenna radiation efficiency takes into account the conduction and dielectric losses. Directivity is defined as “the ratio

of the radiation intensity in a given direction from the antenna to the radiation intensity averaged over all directions” [2].

The Yagi-Uda antenna is one of the best known dipole antenna arrays with high gain [3, 4]. It consists of a driven element placed between several dipoles that act as directors and a dipole that acts as a reflector. By increasing the number of directors in an array, the gain of the antenna is increased. The technique had been applied widely in radio and television due to its directivity, low wind resistance and low cost.

Another advantage of antenna arrays is the ability to control the radiation pattern. The total radiation field is the summation of the radiation field of each element in that array. Each element in an array can be arranged so that their radiation fields accumulate constructively in the desired direction while interfering destructively (cancelling each other) in other directions. Many works discuss how to shape the pattern of an antenna array according to the designer’s specification, see, for example [1, 8].

There are at least five factors that affect the shape of the radiation pattern of an array of identical elements:

- The geometrical configuration of the overall array (such as linear, rectangular, circular, and spherical).
- The spacing between the elements.
- The excitation amplitude of the individual elements.
- The excitation phase of the individual elements.
- The relative pattern of the individual elements.

For example, the effect of mutual coupling is high for small spacing between elements because of the interaction of energy from its neighbourhood. On the other hand when the spacing is large between elements, another effect called grating lobes will occur. Grating lobes are unintended strong beams radiation that occurred in the other direction away than main lobe that existed in the radiation pattern of the array.

The term ‘phased array’ refers to those antenna arrays with elements that are excited with a few methods such as variable phase shift or time delay control to direct the radiation energy in the desired direction. Phase shift control can be

obtained by varying the phase of the input excitation for each element in an array using phase shifting network [5] while time delay control can be accomplished by switching on-off the elements at different time [6]. The disadvantage of using phase shifting network in antenna array is that they are expensive and complex as the number of elements increased. On the other hand, the time delay control produces unwanted harmonics, or sidebands, at multiples switching frequency and many studies are concentrating on minimizing this effect [7]. Depending on the application, it is sometimes necessary to increase the radiation energy in a particular direction (main lobe signal), suppress the interference in the other directions and block electromagnetic signal(s) approaching from a known direction (nulling signal). These modifications to the radiation pattern can be made through a pattern synthesis process [7].

The characteristic of the far-field pattern of an antenna array is shown in Figure 2-2.

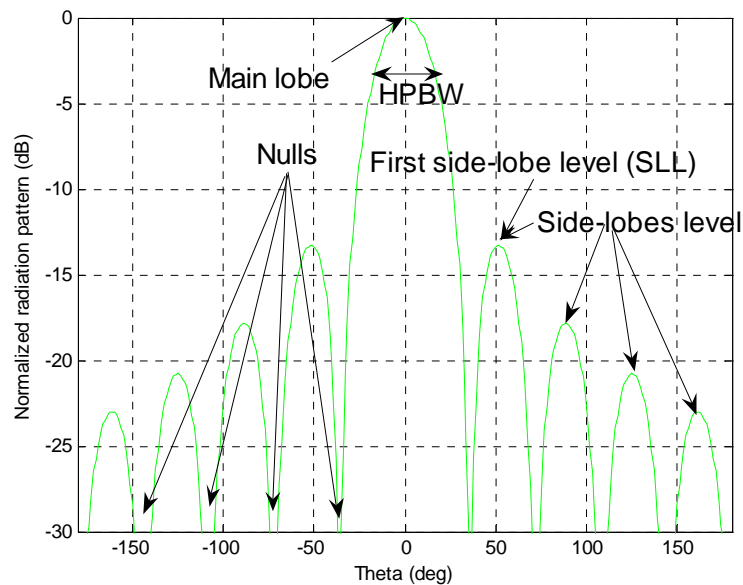


Figure 2-2: Far-field pattern of antenna array (in dB).

Generally, the radiation patterns are plotted for normalised values on a dB scale. The radiation pattern shows the proportion of the electric field or the power directed to a particular direction. This radiation pattern helps to define several important antenna array metrics. The metrics presented in this chapter are used for the array pattern synthesis problems dealt within this work.

Beamwidth refers to the angular width of the main lobe of the radiation pattern. The beamwidth is measured in degrees. It usually refers to 3-dB-

beamwidth (or half-power beamwidth). It is defined as the angular separation between the two points on the main lobe where the power is dropped to 3-dB or the electric field pattern is half from the peak of the main beam (Figure 2-2). Usually, the larger size of the beamwidth indicates the low gain performance of the antenna array.

2.2.3 Ideal Array Theory: Element and Array Factor

The total radiation pattern can be simplified by multiplying the pattern of an individual element (the element factor) positioned at the reference point (or origin) by the pattern due to an array of isotropic sources, called the array factor. This is known as the pattern multiplication rule and applies to identical elements of an array. Generally, an array factor is a function of the number of elements (N), their geometrical arrangement, their relative magnitudes, their relative phases and their spacing. Therefore, the array factor can be calculated by replacing each element with an isotropic (point) source, since it does not depend on the characteristic of the element itself [1]. Many conventional techniques such as Uniform, Binomial, and Chebyshev used the concept of array factor due to its computational efficiencies.

The concept of the array factor can be derived from two half-wavelength dipoles positioned along z-axis. The far-field pattern for a half wavelength dipole is defined in equation (2-1). Thus, the total far-field pattern radiated by array without coupling between elements is equal to the summation of two elements and is given by:

$$E_{total}(\theta, \phi) = E_1(\theta, \phi) + E_2(\theta, \phi) \quad (2 - 9)$$

$$E_{total}(\theta, \phi) = j\eta \left\{ \frac{\cos\left(\frac{\pi}{2} \cos \theta_1\right) I_1 e^{-jkr_1}}{2\pi r_1 \sin \theta_1} + \frac{\cos\left(\frac{\pi}{2} \cos \theta_2\right) I_2 e^{-jkr_2}}{2\pi r_2 \sin \theta_2} \right\}, \quad (2 - 10)$$

where $I_1 = I_2 = Ae^{j\chi/2}$ where χ is the phase difference (or progressive phase) between elements and the amplitude excitation is identical. By using the far-field observation:

$$\theta_1 \simeq \theta_2 \simeq \theta \quad (2 - 11a)$$

$$\left. \begin{aligned} r_1 &\simeq r - \frac{d}{2} \cos \theta \\ r_2 &\simeq r + \frac{d}{2} \cos \theta \end{aligned} \right\} \text{for phase variation} \quad (2-11b)$$

$$r_1 \simeq r_2 \simeq r \text{ for amplitude variation} \quad (2-11c)$$

Equation 2-9 and 2-10 reduce to:

$$E_{total}(\theta, \phi) = \frac{j\eta A}{2\pi r} e^{-jkr} \frac{\cos\left(\frac{\pi}{2} \cos \theta\right)}{\sin \theta} \left\{ e^{j\left(\frac{kd}{2} \cos \theta + \frac{\chi}{2}\right)} + e^{-j\left(\frac{kd}{2} \cos \theta + \frac{\chi}{2}\right)} \right\},$$

$$E_{total}(\theta, \phi) = \frac{j\eta A}{2\pi r} e^{-jkr} \frac{\cos\left(\frac{\pi}{2} \cos \theta\right)}{\sin \theta} \left\{ 2 \cos \left[\frac{1}{2} (kd \cos \theta + \chi) \right] \right\}, \quad (2-12)$$

Therefore, by comparing equation (2-12) and (2-1), it is apparent that the total far-field pattern of the array is equal to the pattern of single half-wavelength dipole antenna (equation (2-1)) multiplied by a factor which is known as the array factor (denoted in the bracket of the equation (2-12)). The normalized array factor for the two-element array of same constant magnitude is given as:

$$AF = \cos \left[\frac{1}{2} (kd \cos \theta + \chi) \right] \quad (2-13)$$

The array factor is as a function of the spacing and the excitation phase. Thus, the total field can be controlled by varying the spacing, d and/or the phase χ between the elements. Thus the total far-field pattern can be summarized as:

$$E_{total} = [E(\text{single element at reference point})] \times [\text{array factor}] \quad (2-14)$$

Equation 2-14 is known as pattern multiplication for arrays of identical elements. The equation is also valid for arrays with any number of identical elements with different excitation amplitudes and phases, and/or spacing between them.

2.3 Analysis of Mutual Coupling Effects in Antenna Arrays

Ideal array theory does not guarantee optimum array pattern synthesis performance. There is another effect known as mutual coupling that changes the radiation pattern significantly, especially in closely spaced antenna arrays. Mutual coupling is the interchange of energy from one element to another when they are placed in close proximity to each other. There are at least three factors that lead to coupling: coupling through a feed network, indirect coupling caused by near-by scatterers and direct space coupling between array elements [8]. Lee

and Chu [9] present an analysis of the mutual coupling effect between a phased array of dipoles and its feed network. Therefore, the mismatch between the radiating elements and the feed network has to be taken into account. Indirect coupling caused by near-by-scatterers such as mounting platform might leads to multipath propagation that affecting the pattern of the antenna array [10, 11]. The multipath propagation causes reflection and refraction to the electromagnetic waves thus may alter the characteristics of antenna. One way to overcome propagation delay is by using multiple antennas or known as MIMO (multiple input multiple output) to combine information from multiple signals improving both speed and data integrity.

Mutual coupling might affect the performance of the antenna arrays. A few papers discussed the mutual coupling effect to the channel capacity in 3-D antenna system such as MIMO cube [12, 13]. Others mentioned that the effect of mutual coupling reduces the channel capacity such as in [14] while a work by Svantesson and Ranheim [15] showed that it enhanced capacity in other situation. The mutual coupling behaviour is complex and therefore should be taken into account especially for closely spaced antenna arrays.

2.3.1 Mutual Coupling between Elements

The amount of mutual coupling between array elements depends on the radiation characteristics of each antenna, the relative separation between the pair of antennas and the relative orientation of each antenna. Conventionally, the mutual impedance was used to measure the mutual coupling effect. Many works [16, 33] describe the concept of mutual coupling assuming the antenna systems consist of two elements with one antenna in transmitting mode connected to a source and another is in receiving mode and open circuited.

Conventional mutual impedance (introduced by Carter [33]) represented two antennas as two port (four terminals) networks (Figure 2-3). Therefore, the current-voltage relationship is given by:

$$V_1 = Z_{11}I_1 + Z_{12}I_2, \quad (2 - 15)$$

$$V_2 = Z_{12}I_1 + Z_{22}I_2, \quad (2 - 16)$$

where Z_{mn} the impedance is the ratio of voltage to current.

$$Z_{11} = \left. \frac{V_1}{I_1} \right|_{I_2=0} \quad (2-17)$$

Z_{11} is the input impedance at port 1 with port 2 open circuited.

$$Z_{12} = \left. \frac{V_1}{I_2} \right|_{I_1=0} \quad (2-18)$$

Z_{12} is the mutual impedance at port 1 due to current at port 2 (with port 1 open-circuited). In a reciprocal network, $Z_{12} = Z_{21}$.

$$Z_{21} = \left. \frac{V_2}{I_1} \right|_{I_2=0} \quad (2-19)$$

Z_{21} is the mutual impedance at port 2 due to current at port 1 (with port 2 open-circuited).

$$Z_{22} = \left. \frac{V_2}{I_2} \right|_{I_1=0} \quad (2-20)$$

Z_{22} is the input impedance at port 2 with port 1 open-circuited. Equations (2-17) and (2-20) stated that the impedances Z_{11} and Z_{22} are the self impedances of antenna 1 and 2 when in isolated environment. The circuit conditions defining the impedances are demonstrated in Figure 2-3(a) and (b). By placing antenna 2 close to antenna 1; a current, I_2 , is induced in antenna 2 due to radiation from antenna 1. Vice versa, current I_2 will also cause radiation from antenna 2 and thus will influence the current on antenna 1 (Figure 2-4). This effect is called mutual coupling.

Knowing the values of self and mutual impedances, the relation may be expanded to a N -element antenna array for which V_1, V_2, \dots, V_N are the input voltages of each element.

$$\begin{aligned} V_1 &= Z_{11}I_1 + Z_{12}I_2 + \dots + Z_{1N}I_N \\ V_2 &= Z_{21}I_1 + Z_{22}I_2 + \dots + Z_{2N}I_N \\ &\vdots \\ V_N &= Z_{N1}I_1 + Z_{N2}I_2 + \dots + Z_{NN}I_N \end{aligned} \quad (2-21)$$

where

$$Z_{mn} = \left. \frac{V_m}{I_n} \right|_{I_i=0, i \neq n} \quad (2-22)$$

The active input impedance Z_a of the n^{th} element in the array (or the driving point impedance), including the effect of mutual coupling, is then

$$Z_a = \frac{V_a}{I_a} = Z_{a1} \frac{I_1}{I_a} + Z_{a2} \frac{I_2}{I_a} + \dots + Z_{aa} + \dots + Z_{an} \frac{I_n}{I_a} \quad (2-23)$$

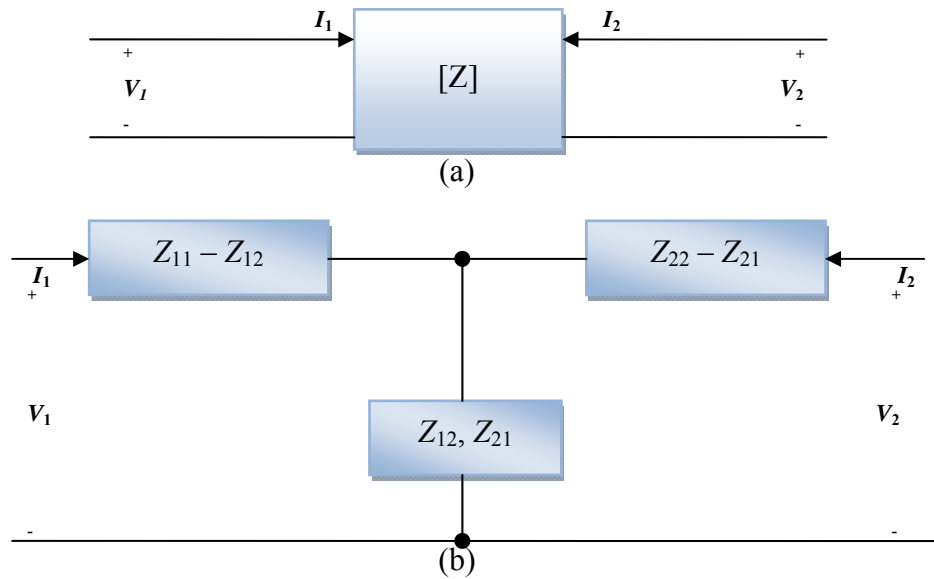


Figure 2-3: (a) Two ports network and (b) its T-network equivalent.

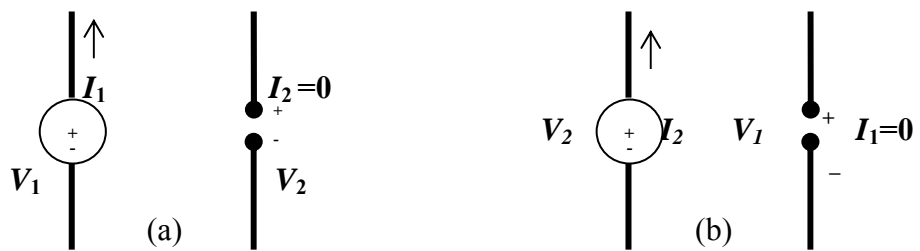


Figure 2-4: The circuit conditions defining the impedance: a) Antenna 1 transmitting and antenna 2 receiving, b) Antenna 2 is transmitting and antenna 1 is receiving.

It is observed (from equation 2-23) that mutual coupling will affect the input impedances of the elements in the array. As the current distribution varies due to the effect of the coupling, the radiation pattern also changes.

The convention of mutual impedance assumes that the same model is applicable in transmitting and receiving mode. However, Hui [17, 18] defines and introduces new concept of mutual impedance in the receiving mode. In receiving mode, the mutual impedance Z_{12} is defined as the ratio of the induced voltage V_1 across the terminal load of antenna 1 to the current I_2 on the terminal load of antenna 2 when the array is excited by an external source.

As a result, the effect of mutual coupling between elements needs to be taken into consideration, since the pattern of isolated elements (a single element with the absence of other array elements) behaves differently compared to when it is placed in an array environment. Several techniques have taken this effect into account, including the active input impedance method and the active element patterns. Other works [19, 20] compensated the mutual coupling effect by designing an inverse coupling network in an antenna array. The coupling matrix may be obtained from the scattering parameters of an array. After the coupling matrix have been compensated, the pattern may be synthesized using conventional methods such as Chebyshev, Taylor, and pattern multiplication method that do not include mutual coupling effects in antenna arrays. The above-mentioned techniques will be explained in the next chapter.

2.3.1.1 The Active Input Impedance Method

The active input impedance treated an N -element array as an N -port network. The array elements may be excited either using a set of individual transmitters or a feed network. For both cases, array excitation may be modelled as a set of Thevenin equivalent voltage sources with source impedances, as shown in Figure 2-5.

There are two concepts by which antenna arrays can be viewed: the forced and the free excitation models. In the forced excitation model, a driving voltage (or current) assumed to be constant is applied to each element when the excitation is phased. When each element has an excitation with a different phase, the active reflection coefficient varies with scan angles and affects the actual gain (or pattern). The active reflection coefficient is related to the active element

impedance (admittance). Nevertheless, the voltage across the element is kept constant by a generator [21, 22].

A different situation occurs with the free excitation method: when the active impedance varies, the voltage drop across the generator impedance, Z^g , varies, thus making the voltage across the element no longer constant. As the voltage across the element is varied according to the conditions, it is termed 'free'. The feeding method in this case is a constant-incident power instead of voltage (Figure 2-6). This method is used practically, since in actual arrays the feed network is based on power. Another reason is that a constant voltage or current source is difficult to maintain or obtain.

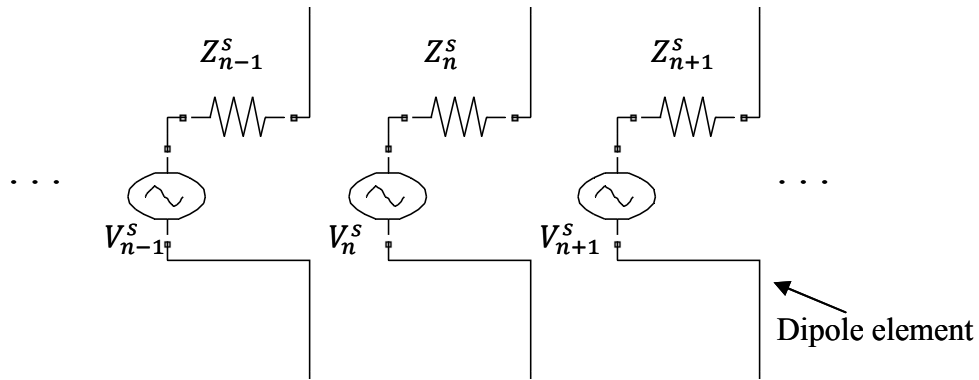


Figure 2-5: Free excitation model where V^s and Z^s is the source excitation and impedance respectively.

The impedance matrix for a total of N elements, Z consists of self and mutual impedances:

$$Z = \begin{bmatrix} Z_{11} & Z_{12} & \cdots & Z_{1N} \\ Z_{21} & Z_{22} & \cdots & Z_{2N} \\ \vdots & \vdots & \ddots & \vdots \\ Z_{N1} & Z_{N2} & \cdots & Z_{NN} \end{bmatrix} \quad (2 - 24)$$

Then, by assuming the array elements are fed by independent Thevenin sources (Figure 2-6), the source impedances are represented by a diagonal matrix (eq. 2-25).

$$Z^s = \begin{bmatrix} Z_{11}^s & 0 & \cdots & 0 \\ 0 & Z_{22}^s & \cdots & 0 \\ \vdots & \vdots & \ddots & \vdots \\ 0 & 0 & \cdots & Z_{NN}^s \end{bmatrix} \quad (2 - 25)$$

As the active element impedances depend on the array excitation with scan angle, the feed current is no longer proportional to the generator voltage. Therefore, if the feed current for each element is phased by α rad, the generator voltage for each element may not be phased by α rad due to mutual coupling. The relationship between terminal current, mutual impedance, source impedance and source voltage is represented as follows [21, 22],

$$\mathbf{I} = \{\mathbf{Z} + \mathbf{Z}^s\}^{-1}\mathbf{V}^s \quad (2 - 26)$$

where \mathbf{I} is the terminal current, \mathbf{Z} is the impedance matrix, \mathbf{V}^s and \mathbf{Z}^s is the source voltage and impedance for N element respectively. Usually, the generator impedance for each element is identical, so for N elements, $Z_{nn}^s = Z^g$ ($n = 1, \dots, N$), where Z^g is the universal generator impedance. If the generator impedance is zero ($Z^g=0$), then the free excitation model reduces to a fixed excitation model. Similarly the voltage terminal is represented as:

$$\mathbf{V} = \mathbf{Z}\mathbf{I} = \mathbf{Z}\{\mathbf{Z} + \mathbf{Z}^s\}^{-1}\mathbf{V}^s \quad (2 - 27)$$

Therefore, the active input impedance is the impedance of an element in an array when all of the elements are fully excited. It is a ratio of terminal voltage and current for each element and defined by:

$$Z_n = \frac{V_n}{I_n}, \quad n = 1, 2, \dots, N \quad (2 - 28)$$

The equivalent circuit for the free excitation model is shown in Figure 2-6.

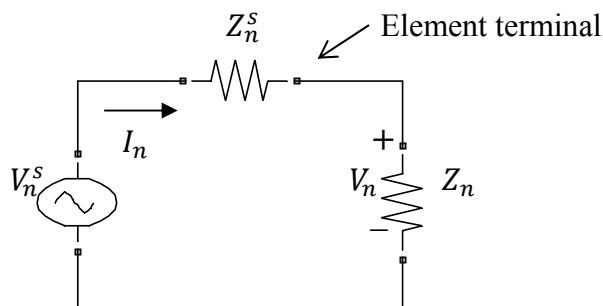


Figure 2-6: The equivalent circuit of free excitation model. It is for an element n driven by a Thevenin source in an array.

There are many techniques to calculate the mutual impedances of dipoles either by measurement (the measurement of self- and mutual impedances) or numerical computation. Numerical computation can be performed using various methods such as the Method of Moments (MoM) [23], the Induced EMF Method [24-27] or the Galerkin Method [28]. Pozar [29] analysed the mutual impedance of a printed dipole array on a substrate using MoM. MoM provides an accurate value for mutual impedance but requires large computation time and storage. The Induced EMF method provides a good approximation and is easy to evaluate, since it gives a closed form solution.

There are a few papers that address the analysis of mutual coupling in parallel or planar arrays using the active input impedance method [9, 35]. However, not many papers address the far-field pattern including mutual coupling effect for elements arranged in any other configurations. Therefore, the method has been expanded into a 3-D antenna array so that it will be useful to analyse the elements in any configuration, i.e. spherical or cubic arrays.

2.3.1.2 The Active Element Pattern Method

Various authors have used the concept of active element pattern such as Pozar and Rudge [30, 31] to predict the scan performance of large phased array antennas. This method takes into account the mutual coupling effect between elements and can be employed in any configuration, such as in a 3-D antenna array. Hansen [32] replaces the terms ‘active element pattern’ and ‘active impedance’ with ‘scan element pattern’ and ‘scan impedance’ respectively. This section provides a definition of the active element pattern, and the next chapter will discuss how this method may be applied in the analysis of antenna arrays.

The derivation begins by considering an N -element uniform linear array of identical elements with its feed as shown in Figure 2-7. Conventional array theory ignores the effect of mutual coupling between elements and derives the pattern radiated by the array as pattern multiplication between the element factor and the array factor. The element factor, $f_0(\theta)$, is the pattern of a single element taken in isolation from the array.

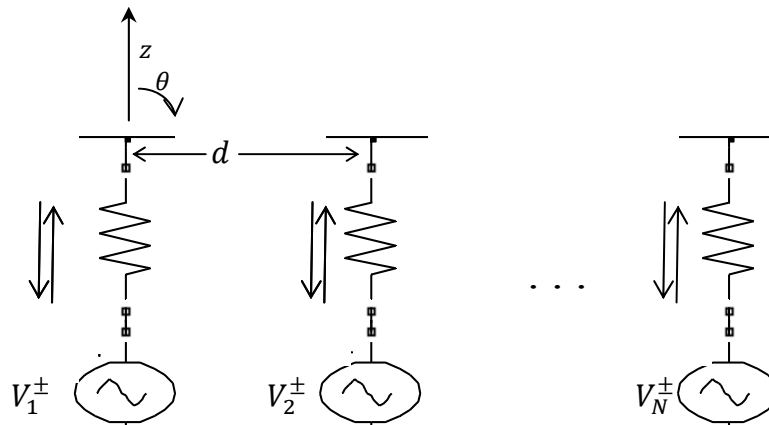


Figure 2-7: Geometry of a uniform N -element linear array where V_1, V_2, \dots, V_N are excitation voltage for each element and d is the spacing between elements.

Then, the array shown in Figure 2-7 has been replaced by the one shown in Figure 2-8 to define the active element pattern, $F_e(\theta)$. N feeds in Figure 2-7 have been replaced with a feed at a single element in the array and terminating all other elements with matched loads (Figure 2-8).

The active element pattern, $F_e(\theta)$, is different from the isolated element pattern, $f_0(\theta)$, because of several reasons:

- The active element pattern consists of radiation from neighbouring elements due to mutual coupling with the feed element.
- $F_e(\theta)$ depends on the location of the feed element in the array: edge elements have a different active element pattern compared to elements at the centre of the array. However, for large arrays, $F_e(\theta)$ can be approximated as equal for all elements in the array since the ratio of edge elements to the other elements is small and may be neglected.

If the active element pattern for all elements can be approximated as equal, then the pattern of the fully excited array in Figure 2-7 is the product of the active element pattern and the array factor. Chapter 3 discusses the pattern of the fully excited array in more detail.

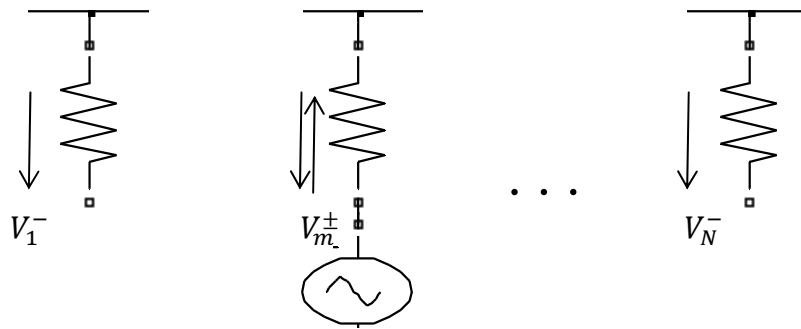


Figure 2-8: Defining geometry for the active element pattern of a uniform N -element array.

2.4 Self- and Mutual Impedance

Through the active input impedance method, it is possible to compute the mutual coupling using the mutual impedance matrix. The mutual impedance matrix may be solved using methods such as the Method of Moments (MoM) or the Induced EMF Method. Carter [33] introduced the concept of conventional mutual impedance using the Induced EMF method from the perspective of a circuit network. It is a first order theory (sinusoidal current distribution) which is usually adequate for dipole arrays. To start with, its application was limited to straight, parallel and in echelon elements only [33, 34, 35]. Subsequently, it was further developed to skew dipoles [26, 27, 36]. The drawbacks of this method are that it does not account for the radius of the wires or the gaps in the feeds. It assumes a very small gap between the upper and lower arms of the dipole. The advantage of this method is that it leads to closed form solutions. It gives an accurate result for an infinitely thin wire but still provides a good approximation for others [1].

2.4.1 Self Impedance using the Induced EMF Method

In general, the radiation resistance for any length, l , of a single dipole is given as [1]:

$$\begin{aligned}
 R_r &= \frac{2P_{rad}}{|I_0|^2} \\
 &= \frac{\eta}{2\pi} \left\{ C + \ln(kl) - C_i(kl) + \frac{1}{2} \sin(kl) [S_i(2kl) - 2S_i(kl)] + \frac{1}{2} \cos(kl) \left[C + \ln\left(\frac{kl}{2}\right) + C_i(2kl) - 2C_i(kl) \right] \right\},
 \end{aligned}
 \tag{2-29}$$

where C is a Euler's constant, where $C=0.5772$, and C_i and S_i are the cosine and sine integrals.

The imaginary part of the impedance is calculated using the EMF Method and given as:

$$X_m = \frac{\eta}{4\pi} \left\{ 2S_i(kl) + \cos(kl) [2S_i(kl) - S_i(2kl)] - \sin(kl) \left[2C_i(kl) - C_i(2kl) - C_i\left(\frac{2ka^2}{l}\right) \right] \right\}, \quad (2-30)$$

Kraus [16] gives the simplified impedance value for a thin linear centre-fed antenna that is an odd number n of half wavelengths long.

$$Z_{11} = R_{11} + jX_{11} = 30(C_{in}(2n\pi) + jS_i(2n\pi)) \quad (2-31)$$

where C_{in} is derived from equation (2-5) and S_i is a sine integral

$$S_i(x) = \int_0^x \frac{\sin(y)}{y} dy \quad (2-32)$$

By substituting $C_i(2n\pi)$ (equation 2-5) into equation (2-29), the simplified self impedance for a thin linear centre-fed antenna of odd number (n) of half wavelengths long is:

$$Z_{11} = 30(0.577 + \ln(2n\pi) - C_i(2n\pi) + jS_i(2n\pi)) \quad (2-33)$$

2.4.2 Mutual Impedance using the Induced EMF Method

There are many methods of calculating the mutual impedance numerically or experimentally. In this case, an Induced EMF Method is employed to calculate the mutual impedance for an array of dipoles arranged in arbitrary configurations. Conventional mutual impedance assumed similar mutual impedance both in transmitting and receiving mode. Hui [18, 19] shows that the receiving mutual impedance and the conventional mutual impedance are quite different, especially when the antenna separation is small and the mutual coupling effect is large. However, the conventional mutual impedance is close to the receiving mutual impedance when the spacing of the antenna is greater than $0.5\lambda_0$.

2.4.2.1 Side by Side, Collinear and Parallel in Echelon Configurations

There are three classic configurations generated by Carter, Brown and others to calculate the mutual impedance between two dipoles [24, 33, 34 and 35]. These configurations are side by side, collinear, and parallel in echelon (Figure 2-9). These expressions are already simplified for two identical elements (the length of both dipole arms are the same) with the length of odd multiples of $\lambda/2$. General expressions for unequal elements are much more complex and can be found in King [35].

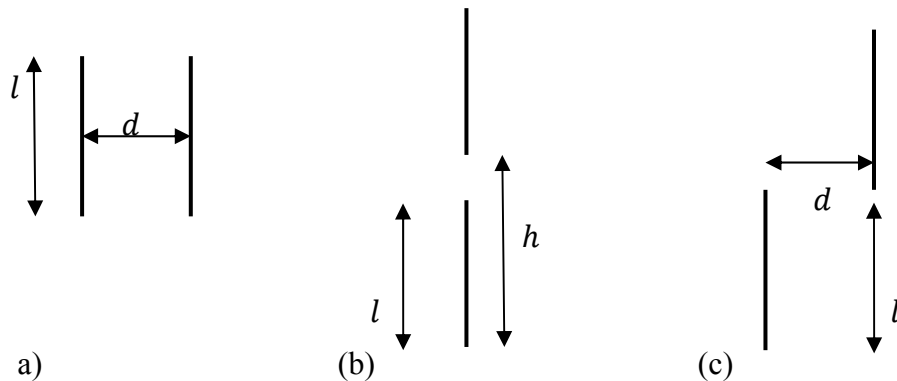


Figure 2-9: Configuration of two dipoles where l is the length of dipole, d is the spacing between two dipoles along y -axis and h is the distance between end point of dipole 1 and dipole 2 along z -axis: (a) Side-by-side, (b) Collinear, (c) Parallel in Echelon.

2.4.2.2 Skew or slanted configuration

The previous section introduces the mutual impedance between two dipoles arranged side by side, collinear and echelon configurations. Other literature extends the work so that the mutual impedance between two dipoles can be calculated no matter what orientation it is placed in [24-27, 36]. Due to its ease of implementation, the method proposed by Baker and LaGrone [27] has been chosen to calculate the far field for dipole arrays. Results obtained from this method have been verified with both published and experimental data for various parallel, echelon and skew cases. It is applicable to the relative geometrical configuration of the two antennas, with arbitrary lengths.

The method is based on the Induced EMF Method. Therefore, the mutual impedance is computed as the ratio of the voltage induced across the open-circuited terminals of antenna 2 to the excitation current flowing through the short-circuited terminals of antenna 1.

$$Z_{21} = \frac{V_{21}}{I_1} \quad (2 - 34)$$

Figure 2-10 shows that the induced open-circuit voltage in antenna 2, V_{21} , with respect to its current at the input terminals, due to the radiation from antenna 1 is given in equation (2-35) [1]. The primary coordinates (x, y, z) refers to coordinates of antenna 1, and secondary coordinates (x', y', z') refer to coordinates of antenna 2. The term dash ($'$) here refers to secondary coordinates of antenna 2. The dipoles length of (l_1, l_2) refer to dipole 1 and dipole 2, the distances (r, r_1, r_2) are measured from the z -axis at the start, middle and end point of dipole 2 to any point along dipole 1, (y_0, z_0) are the displacements (in wavelengths) in the y and z directions between primary and secondary coordinate systems and h is the distance between end point of dipole 1 and dipole 2 along z -axis.

Therefore, the derivation of mutual impedance is derived as follows:

$$V_{21} = -\frac{1}{I_2} \int_{-l_2/2}^{l_2/2} E_{z21}(z') I_2(z') dz' \quad (2 - 35)$$

where $E_{z21}(z')$ is the E-field component radiated by antenna 1, which is parallel to antenna 2. While $I_2(z')$ is the current distribution along antenna 2 (assuming sinusoidal distribution).

Therefore, the mutual impedance is defined as:

$$Z_{21} = \frac{V_{21}}{I_1} = -\frac{1}{I_1 I_2} \int_{-l_2/2}^{l_2/2} E_{z21}(z') I_2(z') dz' \quad (2 - 36)$$

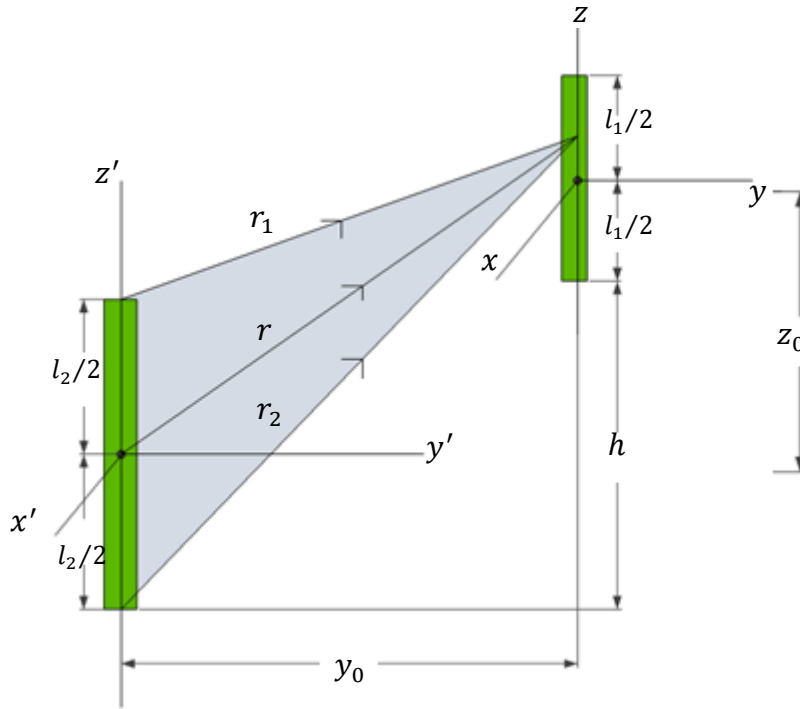


Figure 2-10: Mutual coupling between two dipoles along z-axis.

The mutual impedance given by Balanis [1] is for two parallel dipoles positioned along the z-axis (Figure 2-10). Since the position of the dipoles, in general, is not along the z-axis only, the integration is performed along vector \mathbf{t} (Figure 2-11, 2-12 and 2-13), where \mathbf{t} is the direction of the centre of the secondary dipole toward the end point of antenna 2. Similar nomenclatures as mentioned in Figure 2-10 also applies to Figure 2-11 to 2-13 with a few additional terms: the distance ρ is the radial distance from the z-axis to the point defined by \mathbf{t} , (m, m_1, m_2) are positive angles as shown in Figure 2-11, and dt is an incremental distance along vector \mathbf{t} . Therefore, all the components of the electric field are integrated with respect to \mathbf{t} where the mutual impedance is defined as:

$$Z_{21} = \frac{V_{21}}{I_1} = -\frac{1}{I_1 I_2} \int_{-l_2/2}^{l_2/2} E_{21}(t) I_2(t) dt \quad (2-37)$$

where $E_{21}(t)$ is the E-field component radiated by antenna 1 to antenna 2. While $I_2(t)$ is the current distribution along antenna 2 (assuming sinusoidal distribution).

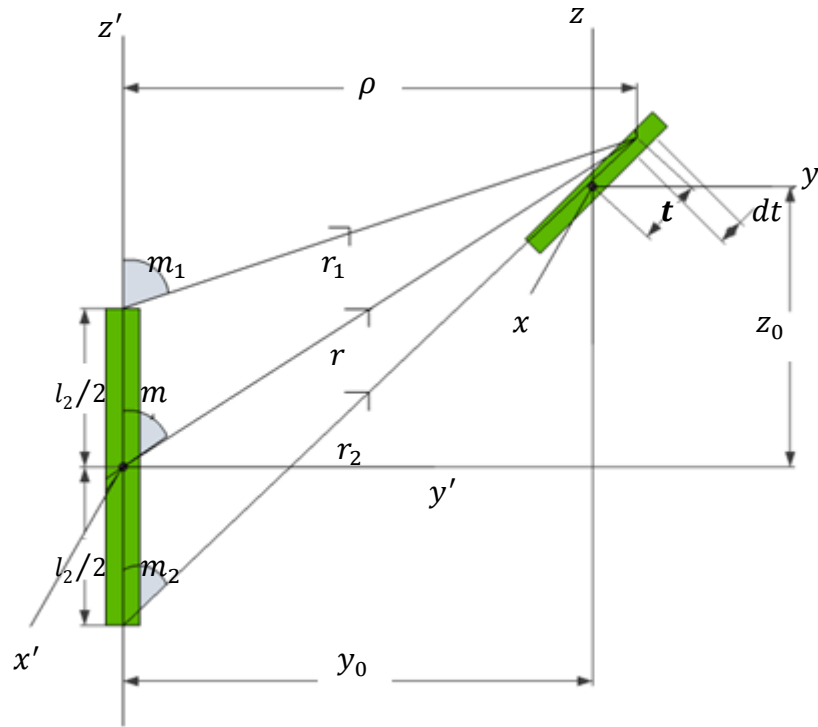


Figure 2-11: Mutual coupling between two dipoles arranged along vector t .

A derivation by Schelkunoff [37] decomposes an electric field vector along t , E_{zz1} , along the z and ρ components.

$$E_z = j30I_1 \left[2 \frac{e^{-2j2\pi r} \cos \pi l_1}{r} - \frac{e^{-j2\pi r_1}}{r_1} - \frac{e^{-j2\pi r_2}}{r_2} \right] \quad (2 - 38)$$

$$E_\rho = j30 \frac{I_1}{\rho} \left[e^{-j2\pi r_1} \cos m_1 + e^{-j2\pi r_2} \cos m_2 - 2 \cos \pi l_1 e^{-j2\pi r} \cos m \right], \quad (2 - 39)$$

E_ρ in Figure 2-12, is a horizontal component of the electric field and can be broken down to x and y components by using a trigonometric function. It has been modified from [27] for this thesis so that it can be employed in 3-D (the x , y and z -axes). The angle ψ is between y -axis to radial ρ and angle γ is between vectors t and E . The components of E_x and E_y are defined as follow:

$$E_x = E_\rho \sin \psi = E_\rho \left(\frac{t_x + x_0}{\rho} \right) \quad (2 - 40)$$

$$E_y = E_\rho \cos \psi = E_\rho \left(\frac{t_y + y_0}{\rho} \right) \quad (2 - 41)$$

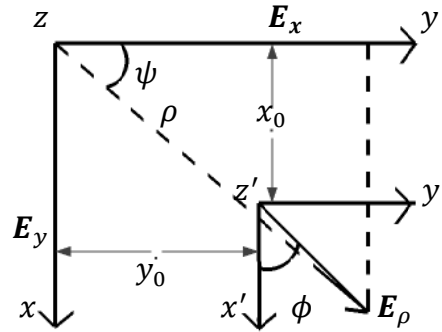


Figure 2-12: Horizontal components of the electric field may be broken down into \mathbf{E}_x and \mathbf{E}_y using a trigonometric function (top view)

Therefore, the magnitude of electric field \mathbf{E}_{21} (Figure 2-13) is defined as follow:

$$E_{21} = |\mathbf{E}| \cos \gamma = \frac{\mathbf{E} \cdot \mathbf{s}}{t} = \frac{E_x t_x + E_y t_y + E_z t_z}{t} = \frac{E_\rho \left[\frac{t_x^2 + t_x x_0 + t_y y_0 + t_y^2}{\rho} \right] + E_z t_z}{t}, \quad (2-42)$$

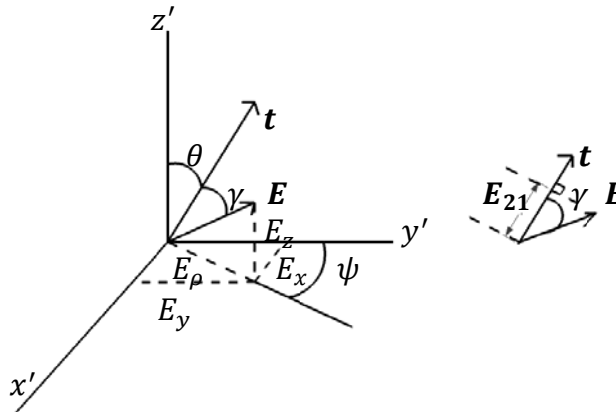


Figure 2-13: Resolution of electric field intensity.

The real and imaginary of the E_z and E_ρ may be separated by multiplying the identity given in equation (2-43) to equations (2-38) to (2-39):

$$e^{ju} = \cos u + j \sin u \quad (2-43)$$

where u is a variable. Therefore, the real and imaginary of the E_z and E_ρ are expanded, as in equations (2-44) to (2-47).

$$\text{Re}(E_z) = 30I_1 \left[2 \frac{(\sin 2\pi r)(\cos \pi l_1)}{r} - \frac{(\sin 2\pi r_1)}{r_1} - \frac{(\sin 2\pi r_2)}{r_2} \right], \quad (2-44)$$

$$Im(E_z) = 30I_1 \left[2 \frac{(\cos 2\pi r)(\cos \pi l_1)}{r} - \frac{(\cos 2\pi r_1)}{r_1} - \frac{(\cos 2\pi r_2)}{r_2} \right], \quad (2-45)$$

$$Re(E_\rho) = \frac{30I_1}{\rho} [(\sin 2\pi r_1)(\cos v_1) + (\sin 2\pi r_2)(\cos v_2) - 2(\cos \pi l_1)(\sin 2\pi r)(\cos v)], \quad (2-46)$$

$$Im(E_\rho) = \frac{30I_1}{\rho} [(\cos 2\pi r_1)(\cos v_1) + (\cos 2\pi r_2)(\cos v_2) - 2(\cos \pi l_1)(\cos 2\pi r)(\cos v)], \quad (2-47)$$

The $I_2(t)$ in equation (2-37) is equal to the product of maximum I_2 with the sinusoidal factor. The factor is:

$$\sin \left[2\pi \left(\frac{l_2}{2} - |t| \right) \right] \quad (2-48)$$

By using equations 2-44 to 2-48 and applying them to E_{Z21} (equation 2-42) and Z_{21} (equation 2-37), the mutual impedance can be derived based on real and imaginary values in integration form, as follows:

$$R_{21} = -30 \int_{t=-l_2/2}^{t=l_2/2} \left\{ \frac{1}{\rho^2} \left([\sin 2\pi r_1] \left[\frac{t_x + z_0 + \frac{l_1}{2}}{r_1} \right] + [\sin 2\pi r_2] \left[\frac{t_x + z_0 - \frac{l_1}{2}}{r_2} \right] - 2[\cos \pi l_1][\sin 2\pi r] \left[\frac{t_x + z_0}{r} \right] \right) [t_x^2 + t_x x_0 + t_y y_0 + t_z^2] \right. \\ \left. + \left[\left(2 \frac{(\sin 2\pi r)(\cos \pi l_1)}{r} - \frac{\sin 2\pi r_1}{r_1} - \frac{\sin 2\pi r_2}{r_2} \right) t_x \right] \left\{ \frac{\sin \left[2\pi \left(\frac{l_2}{2} - |t| \right) \right]}{t} \right\} dt, \quad (2-49a)$$

$$X_{21} = -30 \int_{t=-l_2/2}^{t=l_2/2} \left\{ \frac{1}{\rho^2} \left([\cos 2\pi r_1] \left[\frac{t_x + z_0 + \frac{l_1}{2}}{r_1} \right] + [\cos 2\pi r_2] \left[\frac{t_x + z_0 - \frac{l_1}{2}}{r_2} \right] - 2[\cos \pi l_1][\cos 2\pi r] \left[\frac{t_x + z_0}{r} \right] \right) [t_x^2 + t_x x_0 + t_y y_0 + t_z^2] \right. \\ \left. + \left[\left(2 \frac{(\cos 2\pi r)(\cos \pi l_1)}{r} - \frac{\cos 2\pi r_1}{r_1} - \frac{\cos 2\pi r_2}{r_2} \right) t_x \right] \left\{ \frac{\sin \left[2\pi \left(\frac{l_2}{2} - |t| \right) \right]}{t} \right\} dt, \quad (2-49b)$$

The integration in equations (2-49) is later achieved using Simpson's Rule. Simpson's Rule is a method of numerical approximation of definite integrals. It is employed in order to obtain the real and imaginary values of input impedance. Simpson's equation is based on the following approximation:

$$\int_a^b f(x) dx \approx \frac{b-a}{6} \left[f(a) + \left(\frac{a+b}{2} \right) + f(b) \right] \quad (2-50)$$

However, a Composite Simpson's Rule has been used in this thesis [39]. It is an approximation of integration which is split up into n subintervals with n as an even number. The program will compute n increments between a and b .

$$\int_a^b f(x)dx \approx \frac{h}{3} \left[f(x_0) + 2 \sum_{j=1}^{n/2-1} f(x_{2j}) + 4 \sum_{j=1}^{n/2} f(x_{2j-1}) + f(x_n) \right] \quad (2-51)$$

where

$$\left. \begin{aligned} h &= \frac{b-a}{n} \\ x_0 &= a \\ x_n &= b \\ x_j &= a + jh \end{aligned} \right\} \quad (2-52)$$

Therefore,

$$\left. \begin{aligned} x_{2j} &= a + 2jh \\ x_{2j-1} &= a + (2j - 1)h \end{aligned} \right\} \quad (2-53)$$

In conclusion, the real and imaginary values of mutual impedance between two dipole antennas of different lengths arranged in any configuration may be calculated using the method proposed by Baker [27]. Thus, this will be used to study the effect of mutual coupling in antenna arrays where the elements are arranged in any configuration.

2.5 Conclusions

The first section of this chapter discussed the basic characteristics of the dipole antenna, including its far-field pattern, self-impedance, directivity and gain. The characteristics of antenna arrays were then discussed in detail, due to their ability to increase gain and control the radiation pattern.

This thesis focussed on the latter ability in order to meet the requirement of pattern synthesis in an antenna array. Therefore, the pattern multiplication of antenna arrays which is the ideal theory is briefly discussed. Some other properties that influence the ideal pattern such as coupling from the feed network

and from the adjacent elements are discussed in this chapter. The mutual coupling between elements is investigated through several approaches. There are the active input impedance and the active element pattern (AEP) methods.

The active input impedance observed the mutual impedance through Thevenin's N -ports equation, while the active element pattern contains the mutual coupling effect by exciting one element and terminating the rest with matched loads. In the former method, the mutual impedance may be performed by numerical computation or measurement. Conventionally, the Induced EMF method for an N -port networks provides a good approximation to calculate the self and mutual impedance for dipole antenna arrays. It has been explained thoroughly and can be used to calculate the mutual impedance of thin dipoles arranged side-by-side, collinear and in echelon configurations. Then, the technique was expanded carefully before this section to calculate the mutual impedance between thin dipoles arranged in various configurations.

References

- [1] C. A. Balanis, *Antenna Theory: Analysis and Design*. Canada: Wiley-Interscience, 2005.
- [2] "IEEE Standard Definition of Terms for Antennas." U.S. IEEE Std 145-1983.
- [3] H. Yagi, "Beam Transmission Of Ultra Short Waves," *Proceedings of the IEEE*, vol. 85, pp. 1864-1874, 1997.
- [4] D. M. Pozar, "Beam Transmission Of Ultra Short Waves: An Introduction To The Classic Paper By H. Yagi," *Proceedings of the IEEE*, vol. 85, pp. 1857-1863, 1997.
- [5] R. J. Mailloux, *Phased Array Antenna Handbook*. Artech House, Inc., 2005.
- [6] A. Tennant and B. Chambers, "A two-element time-modulated array with direction finding properties," *IEEE Antennas and Wireless Propagation Letters*, vol. 6, pp. 64, 2007.
- [7] A. Tennant and B. Chambers, "Control of the harmonic radiation patterns of time-modulated antenna arrays," in *Proc. IEEE APS*, San Diego, CA, Jul. 5-12, 2008, pp. 1-4.
- [7] C. A. Olen and R. T. Compton Jr., "A numerical pattern synthesis algorithm for arrays," *IEEE Transactions on Antennas and Propagation*, vol. 38, pp. 1666, Oct. 1990.
- [8] W. L. Stutzman and G. A. Thiele, *Antenna Theory and Design*. John Wiley, 1998.
- [9] K. M. Lee and R. -S. Chu , "Analysis of mutual coupling between a finite phased array of dipoles and its feed network," *IEEE Transactions on Antennas and Propagation*, vol. 36, pp. 1681-1699, Dec. 1988.
- [10] T. Su and H. Ling, "On the simultaneous modeling of array mutual coupling and array–platform interactions," *Microwave Opt Technol Lett*, vol. 33, pp. 167-171, 2002.
- [11] F. Obelleiro, L. Landesa, J. M. Taboada and J. L. Rodriguez , "Synthesis of onboard array antennas including interaction with the mounting platform and mutual coupling effects," *IEEE Antennas Propagation Magazine*, vol. 43, pp. 76-82, Apr. 2001.
- [12] L. Nagy, "Modified MIMO Cube for Enhanced Channel Capacity," *International Journal of Antennas and Propagation*, vol. 2012, 2012.

- [13] B. N. Getu and J. B. Andersen, "The MIMO cube - a compact MIMO antenna," *Wireless Communications, IEEE Transactions on*, vol. 4, pp. 1136, may, 2005.
- [14] R. Janaswamy, "Effect of element mutual coupling on the capacity of fixed length linear arrays," *Antennas and Wireless Propagation Letters, IEEE*, vol. 1, pp. 157, 2002.
- [15] T. Svantesson and A. Ranheim, "Mutual coupling effects on the capacity of multielement antenna systems," in *Acoustics, Speech, and Signal Processing, 2001. Proceedings. (ICASSP '01). 2001 IEEE International Conference 2001*, pp. 2485.
- [16] J. D. Kraus and R. J. Marhefka, *Antennas for all Applications*. United States of America: McGraw-Hill, 2002.
- [17] H. T. Hui and S. Lu, "Receiving mutual impedance between two parallel dipole antennas," in *TENCON 2006. 2006 IEEE Region 10 Conference, 2006*, pp. 1.
- [18] H. T. Hui, "A new definition of mutual impedance for application in dipole receiving antenna arrays," *IEEE Antennas and Wireless Propagation Letters*, vol. 3, pp. 364-367, Dec, 2004.
- [19] H. Steyskal and J. S. Herd, "Mutual coupling compensation in small array antennas," *Antennas and Propagation, IEEE Transactions on*, vol. 38, pp. 1971, dec, 1990.
- [20] P. Darwood, P. N. Fletcher and G. S. Hilton, "Mutual coupling compensation in small planar array antennas," *Microwaves, Antennas and Propagation, IEE Proceedings -*, vol. 145, pp. 1, feb, 1998.
- [21] A. A. Oliner and R. G. Malech, "Mutual coupling in infinite scanning arrays," in *Microwave Scanning Antennas*, R. C. Hansen, Ed. New York: Academic, 1966, pp. 195.
- [22] K. Takamizawa. "Analysis of highly coupled wideband antenna arrays using scattering parameter network models." PhD Theses, Virginia Polytechnic Institute and State University, Virginia, 2002.
- [23] R. F. Harrington, *Field Computation by Moment Methods*. New York: Macmillan Publishing Company, 1993.

- [24] L. Lewin, "Mutual impedance of wire aerials," *Wireless Engineer*, vol. 28, pp. 352-355, 1951.
- [25] K. E. Schmidt, "Simplified mutual impedance of nonplanar skew dipoles," *IEEE Transactions on Antennas and Propagation*, vol. 44, pp. 1298-1299, 1996.
- [26] J. Richmond and N. Geary, "Mutual impedance of nonplanar-skew sinusoidal dipoles," *IEEE Transactions on Antennas and Propagation*, vol. 23, pp. 412-414, 1975.
- [27] H. Baker and A. LaGrone, "Digital computation of the mutual impedance between thin dipoles," *IRE Transactions on Antennas and Propagation*, vol. 10, pp. 172-178, 1962.
- [28] X-D. Cai and G. I. Costache, "Numerical analysis of mutual coupling effects in linear and circular arrays," in *International Symposium Antennas and Propagation Society*, 1992. AP-S. 1992 Digest. Held in Conjunction with: URSI Radio Science Meeting and Nuclear EMP Meeting., IEEE, 1992, pp. 641.
- [29] D. M. Pozar, "Analysis of finite phased arrays of printed dipoles," *IEEE Transactions on Antennas and Propagation*, vol. 33, pp. 1045, Oct, 1985.
- [30] D. M. Pozar, "The active element pattern," *IEEE Transactions on Antennas and Propagation*, vol. 42, pp. 1176, Aug, 1994.
- [31] A. W. Rudge, *The Handbook of Antenna Design*. Stevenage : Peregrinus on behalf of the Institution of Electrical Engineers, 1986.
- [32] R. C. Hansen, *Phased Array Antennas*. New York ; Chichester: New York ; Chichester : Wiley, 1998.
- [33] P. S. Carter, "Circuit Relations in Radiating Systems and Applications to Antenna Problems," *Proceedings of the Institute of Radio Engineers*, vol. 20, pp. 1004, June, 1932.
- [34] G. H. Brown, "Directional Antennas," *Proceedings of the IRE*, vol. 25, pp. 78-145, Jan., 1937.
- [35] H. E. King, "Mutual impedance of unequal length antennas in echelon," *Antennas and Propagation, IRE Transactions on*, vol. 5, pp. 306-313, July, 1957.
- [36] J. Richmond and N. Geary, "Mutual impedance between coplanar-skew dipoles," *Antennas and Propagation, IEEE Transactions on*, vol. 18, pp. 414-416, 1970.

[37] S. A. Schelkunoff, *Electromagnetic Waves*. New York: Van Nostrand, p 371, 1943.

[38] R. L. Finney, M. D. Weir and F. R. Giordano, *Thomas' Calculus*. London: Addison Wesley, 2003.

CHAPTER 3:

Numerical Methods and Optimisation Techniques

3.1 Introduction

This chapter reviews several array numerical techniques including numerical methods and closed form analytical methods. Some of the well-known methods utilize numerical techniques to solve mutual coupling such as the method of moments (MoM) and the finite-difference time-domain method (FDTD) will be discussed. The benefits and drawbacks of both methods are also presented.

Then, the array analysis is investigated in one-, two- and three-dimensions. Many techniques applied in one- and two-dimensions are conventional but useful. Most of them are inaccurate because the mutual coupling effect has not been taken into account such as binomial, Dolph-Chebyshev and Schelkunoff method. However, it works better and faster with the optimisation techniques to meet engineers' specifications.

Later, the optimisation techniques that work with array analysis are reviewed. The techniques are sequential universal sampling, Nelder-Mead, finite difference quasi-Newton method (FDFNLF1), quasi-Newton method, particle swarm optimization (PSO), simulated annealing and genetic algorithm (GA). Finally, the chapter concludes with the method used throughout this thesis and the explanation behind it.

3.2 Electromagnetic Modelling

Antenna arrays play an essential role in many applications, such as in communication, surveillance and radar systems. Many advantages for an array include increasing antenna gain, meeting radiation pattern requirements, beam

steering and multiple beam channels capability such as MIMO. Practically, there is always a need to design an antenna system that meets desired radiation characteristics. Many examples include designing an antenna whose far-field pattern have nulls in certain directions. Other requirements are the pattern needs to have a desired distribution, such as narrow beam width, low side lobes, and so forth.

A few numerical solutions are available to analyze the far-field pattern that includes mutual coupling effect in antenna arrays. The numerical methods can be divided into two equation based on integral or differential form. They are employed in order to solve unknown quantities such as current distribution based on the known quantities such as voltage excitation and boundary values. Full wave numerical techniques (such as method of moments, finite-time difference domain) are extremely accurate, versatile, complex, able to treat single elements, arrays, stacked elements, arbitrary shaped elements and coupling. The model usually employs simulating software to estimate an antenna performance. However, it has drawbacks when working with array optimisation techniques (such as genetic algorithm, least mean square method) because the computation may take longer and in the active element pattern (AEP), results needs to be extracted from the simulating software. It complicates the whole process and in certain cases, the simulation might need to be performed more than once.

The advancement of computer technologies enabled array analysis becomes a reality. The array analysis is an approximation to the integral equation of numerical methods, with the aid of few assumptions and approximations to obtain closed form solution. Analytical methods in arrays are fast and easy to implement with optimisation methods but inaccurate. Most of them are based on array factor and do not take into account mutual coupling (such as Dolph-Chebyshev and Schelkunoff method) and some provide approximations to simplify the methods. Several authors applied the compensation techniques [1, 2] in order to compensate the mutual coupling effect before using the above-mentioned method. These will be reviewed here to gives an understanding of the pros and cons of the methods. Table 1 summarizes the differences between numerical and analysis softwares to compute the characteristics of antenna.

Table 1: Comparison between numerical and analysis softwares.

	Numerical softwares	Analytical softwares
Characteristics	<ul style="list-style-type: none"> ▪ solve Maxwell's equations subject to appropriate boundary conditions. ▪ Requires the user to be very familiar with the software, the limitations of the technique, and the problem being analysed. 	<ul style="list-style-type: none"> ▪ solve specific problems that have pre-defined geometries using closed-form equations. ▪ The user must be able to relate the geometry of the problem being analyzed to a geometry that the software is capable of solving.
Advantages	<ul style="list-style-type: none"> ▪ provides very accurate solutions to well-defined problems. 	<ul style="list-style-type: none"> ▪ provides fast solutions for a limited class of problems.

3.2.1 Numerical Methods

Numerical methods solve Maxwell's equations subject to appropriate boundary conditions. It provides very accurate solutions to well-defined problems. Full-wave numerical methods can be subdivided into integral and differential equation based. Both of them are further divided into frequency domain methods (such as method of moments and finite element method) and time domain methods (such as finite-difference time domain and transmission line method). A good understanding of the principles on which the software is based is necessary in order to set the relevant parameters properly and avoid the misuse and misinterpretation of the results.

3.2.1.1 Method of Moments (MoM)

The basic idea of the method of moments is to transform an integral or differential equation into a set of simultaneous linear algebraic equations (or matrix equation) which may then be solved by numerical techniques. It was first applied to electromagnetic problems in the 1960s by Harrington [3]. It presents a

unified approach to MoM by employing the concepts of linear spaces and functional analysis.

The integral or differential equations may have the form of

$$F(g) = h, \quad (3 - 1)$$

where F is a known linear operator (either integral or differential operator), g is an unknown response function, and h is the source or excitation function. The objective is to find g once F and h are given. The unknown response function g can be expanded as a linear combination of N terms as:

$$g(z') \approx a_1 g_1(z') + a_2 g_2(z') + \dots + a_N g_N(z') = \sum_{n=1}^N a_n g_n(z') \quad (3 - 2)$$

where a_n is an unknown constant and each $g_n(z')$ is a known function usually a basis or expansion function. Substituting equation (3-2) into (3-1) and applying the linearity of the F operator replaces (3-1) into

$$\sum_{n=1}^N a_n F(g_n) = h \quad (3 - 3)$$

The selection of basis function g_n depends on each $F(g_n)$ in equation (3-3) to be solved easily, either in closed form or numerically at least. Every equation of (3-3) leads to N unknown of a_n ($n=1, 2, \dots, N$) constants. N unknown constants can be solved using N linearly independent equations. This can be obtained by evaluating equation (3-3) at N different points (such as the boundary conditions). This technique is known as point-matching (or collocation). Therefore, equation (3-3) takes the form of

$$\sum_{n=1}^N I_n F(g_n) = h_m, \quad m = 1, 2, \dots, N \quad (3 - 4)$$

Equation (3-4) may be represented in matrix form as:

$$[Z_{mn}][I_n] = [V_m] \quad (3 - 5)$$

where

$$Z_{mn} = F(g_n) \quad (3 - 5a)$$

$$I_n = a_n \quad (3 - 5b)$$

$$V_m = h_m \quad (3 - 5c)$$

The unknown coefficients a_n can be obtained by solving equation (3-5) using inverse technique as:

$$[I_n] = [Z_{mn}]^{-1}[V_m] \quad (3 - 6)$$

The point-matching method is a numerical technique where solutions meet the electromagnetic boundary conditions (such as vanishing tangential electric field on the surface of an electric conductor) only at discrete points. However, the boundary conditions might not be satisfied between these points, thus creating a residual (residual= $\Delta E|_{tan}=E(\text{scattered})|_{tan}+E(\text{incident})|_{tan}\neq 0$ on the surface of an electric conductor). Therefore, the method of weighted residual is applied which forces the boundary conditions to be satisfied in an average sense over the entire surface. It minimizes the residual in a way that its overall average over the entire surface approaches zero.

The method of weighted residuals begins by defining a set of N weighting (or testing) functions $\{w_m\}=w_1, w_2, \dots, w_N$ in the range of F . Forming the inner product between this function with equation (3-3) yields to:

$$\sum_{n=1}^N a_n \langle w_m, F(g_n) \rangle = \langle w_m, h \rangle \quad m = 1, 2, \dots, N \quad (3 - 7)$$

Equation (3-7) is written in matrix form as:

$$[F_{mn}][a_n] = [h_m] \quad (3 - 8)$$

where

$$[F_{mn}] = \begin{bmatrix} \langle w_1, F(g_1) \rangle & \langle w_1, F(g_2) \rangle & \dots & \langle w_1, F(g_N) \rangle \\ \langle w_2, F(g_1) \rangle & \langle w_2, F(g_2) \rangle & & \vdots \\ \vdots & \vdots & & \vdots \\ \langle w_N, F(g_1) \rangle & \langle w_N, F(g_2) \rangle & \dots & \langle w_N, F(g_N) \rangle \end{bmatrix} \quad (3 - 8a)$$

$$[a_n] = \begin{bmatrix} a_1 \\ a_2 \\ \vdots \\ a_N \end{bmatrix} \quad [h_m] = \begin{bmatrix} \langle w_1, h \rangle \\ \langle w_2, h \rangle \\ \vdots \\ \langle w_N, h \rangle \end{bmatrix} \quad (3 - 8b)$$

The unknown coefficients a_n may be solved using inversion matrix:

$$[a_n] = [F_{mn}]^{-1}[h_m] \quad (3 - 9)$$

By relating MoM to the antenna theory, the electric field integral equation is written as:

$$E = F(J) \quad (3 - 10)$$

where E is the known electric field, J is the unknown induced current, F is the linear operator.

Steps to be taken to obtain current distribution J is as follows:

1. Expand J as a finite sum of basis function as:

$$J = \sum_{n=1}^N J_n g_n \quad (3 - 11)$$

where g_n is the n^{th} basis function and J_n is an unknown coefficient.

2. Define a set of N linearly independent weighting functions, w_m . Substituting equation (3-11) into (3-10) and performing the inner product on both sides resulting:

$$\langle w_m, E \rangle = \sum_{n=1}^N \langle w_m, F(J_n, g_n) \rangle \quad (3 - 12)$$

where $m=1, 2, \dots, N$

In matrix form, the equation (3-12) is in the form:

$$[E] = [Z_{mn}] J \quad (3 - 13)$$

where

$$[E] = \langle w_m, E \rangle \quad (3 - 13a)$$

$$Z_{mn} = \langle w_m, F(g_n) \rangle \quad (3 - 13b)$$

and J is the current distribution containing the unknown quantities.

Once the current distribution is known, parameters of interest such as field patterns, input impedance, etc. can be calculated by employing the

appropriate formulas. Numerical Electromagnetics Code (NEC) is a user oriented program developed based on method of moment. It is a numerical solution of an integral equation to analyze the interaction of electromagnetic waves of the structure. It is approached by dividing the integration range into discrete steps, thereby turning it into a set of linear equations of matrices. It applies the electric field integral equation (EFIE) for thin wires and magnetic field integral equation (MFIE) for surfaces. There are two possibilities for excitation: applied voltage source or an incident plane wave. The code calculates induced currents and charges, near- and far-zone electric and magnetic fields, radar cross section, impedances or admittances, gain and directivity, power budget, and antenna-to-antenna coupling.

3.2.1.2 Finite-Time Difference Domain (FDTD)

The (FDTD) method is one of grid-based differential time domain numerical modelling methods. It was developed by Yee in 1966 at Lawrence Livermore National Laboratories [4]. The method discretized into many cells (usually square or rectangular), known as Yee cells/lattices (Figure 3-1). The electric and magnetic field components have been decomposed into (x, y, z) components. It discretized the time-dependent partial-differential Maxwell equations (given in equation (3-14)) using central-difference approximations to the space and time partial derivatives. The resulting equations are solved in a leapfrog manner: the electric field vector components in a volume of space are solved initially (assuming the magnetic fields are known), then the magnetic field vector components in the same spatial volume are solved at the next instant in time. This process is repeated until the desired transient or steady-state electromagnetic field behavior is fully evolved. This scheme has proven to be very robust and remains at the core of many current FDTD software constructs. Various modelling tools are developed based on this method including Empire XCcel.

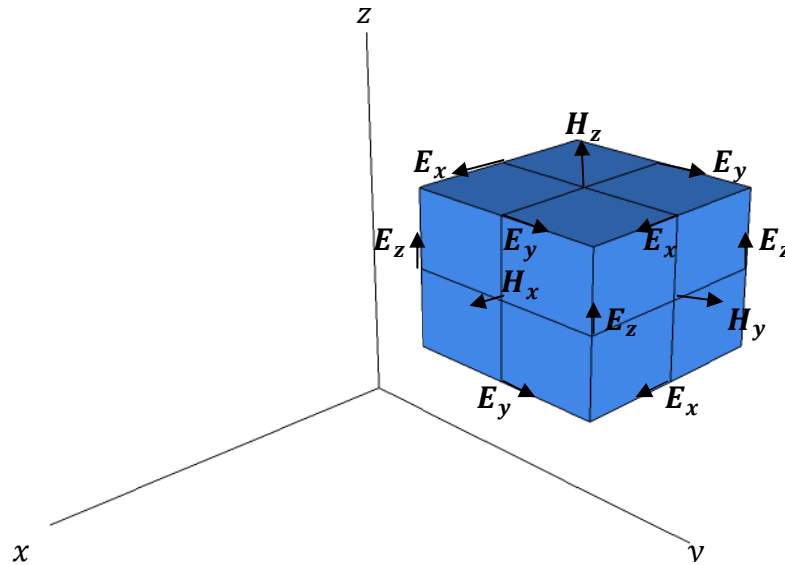


Figure 3-1: FDTD (Yee) Cell

$$\frac{\partial y}{\partial x} + \nabla \times E = 0, \tag{3 - 14a}$$

$$\frac{\partial y}{\partial x} - \nabla \times H = J \tag{3 - 14b}$$

$$B = \mu H \tag{3 - 14c}$$

$$D = \epsilon E \tag{3 - 14d}$$

Table 2: Comparison between method of moments and finite-difference time-domain method.

	Frequency domain method	Time domain method
	MoM	FDTD
Advantages	Fast at single frequency.	Broadband results with one simulation.
	Easily combined with other methods to deal with large problems.	Good for pulse type problem.
Disadvantages	Difficult to deal with pulse-type problem	Not suitable for electrically large systems
Note	Most suitable for wire type antennas.	Need to be careful with the boundary conditions.

3.2.1.2.1 Discretisation

Discretisation or known as meshing is one of the key factors in the accuracy of any numerical modelling. The discretisation in Empire XCcel can be defined in two ways: automatic or manual discretisation. The simulation domain of the structure will be meshed according to the user specification. The automatic

discretisation creates a suitable mesh for the entered structure. It also defines the boundaries of the simulation domain by detecting the objects' extensions and following certain rules as defined from far field definition, excitation response, port size and so on. The automatic discretisation can be optimized depending on information about the object types such as planar, 3D or it can be user defined. The general rule to define the mesh is that the largest cell size of the mesh should be smaller than the tenth of the smallest wavelength. On the other hand, the smallest cell size will determine the time step for the simulation; which means for very small cell size resulting longer computation time.

3.2.2 Analytical Method

Analytical modelling softwares solve specific problems that have pre-defined geometries using closed-form equations. It provides fast solutions for a limited class of problems. This section reviews the array analysis techniques and have been arranged according to complexity of dimension of the array itself, starting with the first-dimension (such as linear array) to three-dimensions. Most of the synthesis techniques of the array analysis are based on the array factor and is explained in this section.

3.2.2.1 1-D Array (Linear array)

A linear array refers to a number of antenna's elements arranged along a straight line. Since the far-field equation in 1-D is not complex, many literatures developed their techniques using the array factor (Section 2.1.2). Balanis [5] has described how an antenna array can produce either a broadside or endfire pattern simply by changing the phase difference between elements. For an array with elements greater than 2, a uniform array excites all elements with the same amplitude and a progressive phase prior to previous element. Binomial and Dolph-Chebyshev implemented amplitude tapering in order to synthesize the pattern [6, 7]. All the above-mentioned method applies to narrow beam patterns and producing low side lobes. Schelkunoff [8] described a technique which is similar to the z transform (used by Hurewicz in developing his pulsed filters [9]) in order to exhibit pattern with nulls in interference direction. All of the above

techniques by default do not take into account the mutual coupling effect between elements. However, a few of the array analysis [1, 2] compensates the mutual coupling effect first before applying the above techniques to control the radiation pattern. All of these will be explained in details within this section.

3.2.2.1.1 Non-Uniform Amplitude, Equispaced Array

In pattern multiplication method, the total field of the array is equal to the field of single element positioned at the origin times a factor which is known as array factor. It is a function of the displacement of the array elements and the excitation phase. By changing either one or both of them, the total field of the array can be controlled.

The array factor for even ($2M$) or odd number ($2M + 1$) of elements can be arranged as follows (Figure 3-2):

$$(AF)_{2M}(\text{even}) = \sum_{n=1}^M A_n \cos[(2n - 1)u] \quad (3 - 15)$$

$$(AF)_{2M+1}(\text{odd}) = \sum_{n=1}^{M+1} A_n \cos[(2n - 1)u] \quad (3 - 16)$$

where

$$u = \frac{\pi d}{\lambda} \cos \theta \quad (3 - 17)$$

The array factor is arranged in the above equation so that the elements can be positioned symmetrically along the z axis.

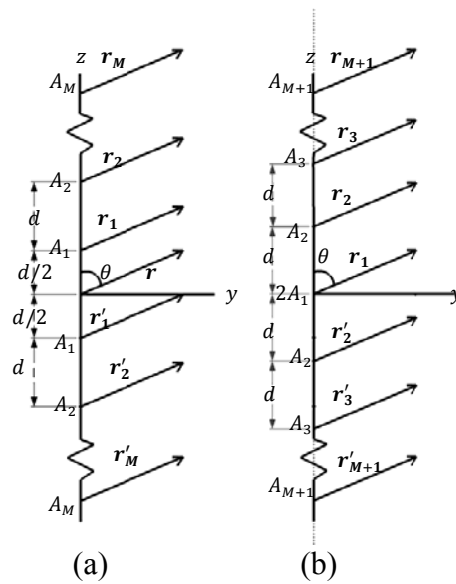


Figure 3-2: Non uniform amplitude arrays of (a) even and (b) odd number of elements where A_n is the amplitude excitation for each element, d is the separation between elements and r is the distance for each element to the observation point.

3.2.2.1.2 Binomial Weight Excitation

Binomial array determined the excitation coefficient of each element from Binomial expansion. It is applicable to an equally spaced array. For an array with N elements, the excitation coefficient is in the form

$$AF = (1 + e^{jc})^{N-1}$$

$$= 1 + (N-1)e^{jc} + \frac{(N-1)(N-2)}{2!}e^{j2c} + \frac{(N-1)(N-2)(N-3)}{3!}e^{j3c} + \dots, (3-18)$$

and

$$c = \alpha + kd \cos \theta \quad (3-19)$$

where c is array phase function, α is phase of excitation coefficients, d is the element spacing, k is wave number and θ is elevation angle. The excitation coefficients for different values of N are (using Pascal's triangle- see Figure 3-3.)

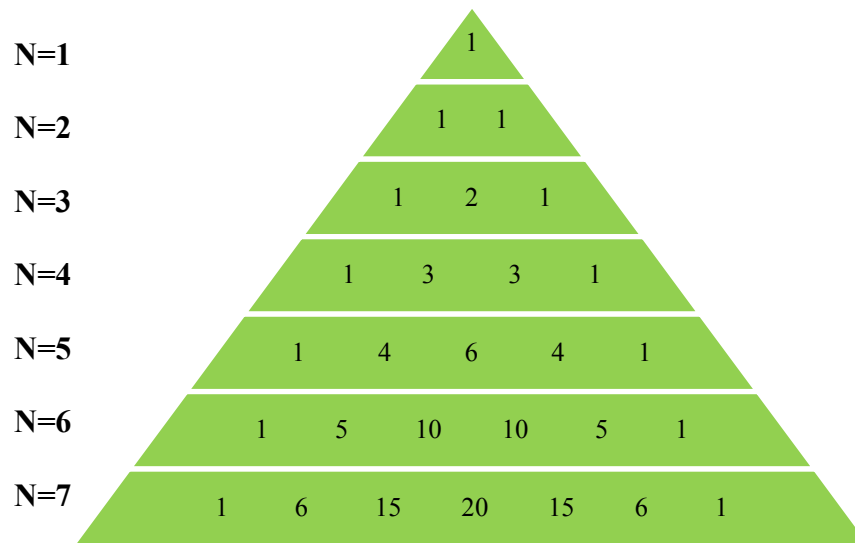


Figure 3-3: Pascal's Triangle.

Thus, for a given number of elements the excitation coefficients can be used to design pattern with low side lobes. In fact, they have no side lobes when the spacing between elements is $\lambda/4$ or $\lambda/2$ [1]. However, even though Binomial weight excitation has the lowest side-lobe level compare to uniform and Dolph-Chebyshev, it has wide variation between the coefficients of the different elements in an array which making it less efficient. For example (Figure 3-3), ($N=7$) the coefficient for first element is 1 and the center element is 20. As the number of elements increase, the amplitude variation between different elements becomes larger. In practice, it is difficult to maintain large amplitude variations between different elements.

3.2.2.1.3 Dolph-Chebyshev

The technique was introduced by Dolph [7] and further developed by others [10-12]. It is a compromise between uniform and binomial arrays. Their side lobe levels are lower than uniform array but higher than the binomial array.

The technique works by applying equation (3-15) and (3-16) to a Chebyshev polynomial. Equation (3-15) and (3-16) is a summation of M (even) or $M+1$ (odd) cosine terms. The largest harmonic of these cosine terms is one less than the total number of elements of the array. The argument for each cosine term is integer multiples of u . It can be rewritten as a series of cosine functions

with u as the argument. It is further expanded into m^{th} order using trigonometric identities.

By following the design procedure as explained by Balanis [5], Hansen [13] and Fourikis [6], the polynomial excitation coefficients can be determined from the given side lobe characteristics.

3.2.2.1.4 Schelkunoff Method

The Schelkunoff method yields the number of elements and their excitation coefficients needed based on the given location and number of nulls in the radiation pattern.

The far-field pattern of a linear array is a summation of the fields radiated by each element with the existence of the other elements. The excitation variable will affect the far-field pattern of linear array. Thus, a far-field pattern is a discrete Fourier transform of the excitation array. The excitation array is represented by [14]

$$F(u) = \sum_{n=1}^N A_n \exp[j2\pi(n-1)u] \quad (3-20)$$

where u is

$$u = \frac{d}{\lambda} \cos \theta - \chi \quad (3-21)$$

A_n is the excitation coefficient, N is the total number of elements, and u is the progressive phase shift, the elevation angle is θ and the element spacing is d .

Schelkunoff [14] elaborates how each element interacts with each other in an array by using the unit circle approach. The exponential factor in equation (3-20) has been replaced with a new variable, z .

$$z = \exp(j2\pi u) \quad (3-22)$$

Therefore, the excitation can be represented as

$$F(z) = \sum_{n=1}^N A_n z^{n-1} = A_1 + A_2 z + A_3 z^2 + \dots + A_N z^{N-1} \quad (3-23)$$

Equation (3-23) has a degree of $(N-1)$ and possesses $(N-1)$ roots. It can be expressed as a product of $(N-1)$ linear terms as

$$F(z) = A_n(z - z_1)(z - z_2)(z - z_3) \dots (z - z_{N-1}) \quad (3 - 24)$$

where $z_1, z_2, z_3, \dots, z_{N-1}$ are the roots. The magnitude of equation (3-24) can be expressed as

$$F(z) = |A_n| |z - z_1| |z - z_2| |z - z_3| \dots |z - z_{N-1}| \quad (3 - 25)$$

The polar angle (or visible region) is $\vartheta = 2\pi u$ and substituting equation 3-21 in the ϑ gives:

$$\vartheta = kd \cos \theta - \chi \quad (3 - 26)$$

where $\cos \theta$ is varied from $[-1: 1]$ thus covering the region unit circle (visible region) between

$$-kd - \chi \leq \vartheta \leq kd - \chi \quad (3 - 26a)$$

As spacing is half-wavelength, z goes over unit circle once. This traverse is called visible region [5]. For spacing of a wavelength, z moves around the unit circle twice and so on. By increasing the spacing will increase the visible region of that array factor. On the other hand, changing progressive phase shift, χ , will rotate the visible region to any side around unit circle. The polynomial in z has $N-1$ roots. The root placement can be real valued (on the unit circle) or a complex value (inside the unit circle). Zeros placed on the unit circle within the visible region creates nulls in the pattern, while zeros inside unit circle may produce pattern minima. Therefore, the pattern is the product of the distance from the observation point in z (on unit circle) to each of the zeros (roots). As z goes around the circle, lobes form and reduced to create null and pattern minima. While, $z=1$ denotes the principal maximum of the pattern (Figure 3-4).

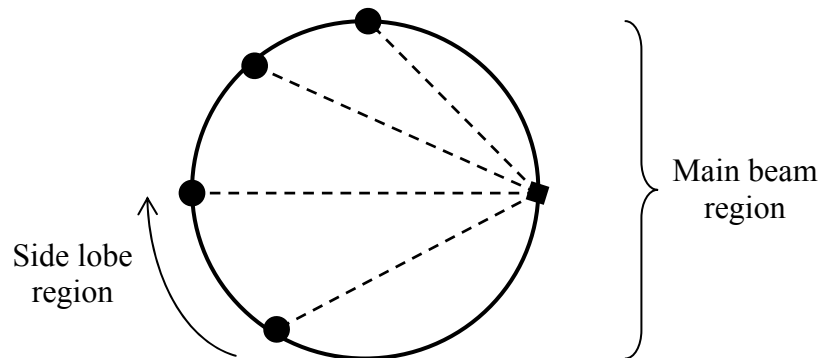


Figure 3-4: Unit circle for an array.

The zeros placed in the visible region on the unit circle will contribute to nulls in the pattern of array factor. If no zeros exist in the visible region of the unit circle, then that particular array factor has no nulls for any value of θ . However, if a given zero lies on the unit circle but not in its visible region, that zero can produce null to the pattern by changing the phase excitation χ so that the visible region can be rotated and cover that root.

Many works have already employed Schelkunoff's method for pattern synthesis. Another important issue is that the choice of the sample point is crucial as if one fails to specify the pattern correctly; some undesirable side-lobe might appear and dominate the regions in interest [19].

3.2.2.2 2-D Array (Planar, Circular)

Geometrically, simple 2-D arrays are described. Examples are the planar and circular arrays. They deal with the array factor and do not incorporate coupling between elements.

3.2.2.2.1 Rectangular (Planar) Array

The elements can be positioned along a square grid to form a 2-D array. Planar arrays give additional parameters and dimension which can be used in beam shaping and pattern control. Therefore, the electric field for this design will be investigated in this section.

Figure 3-5(a) and (b) shows the elements positioned along a linear and rectangular array respectively. The array factor for Figure 3-5a is

$$AF = \sum_{m=1}^M A_{m1} e^{j(m-1)(kd_x \sin\theta \cos\phi + \chi_x)} \quad (3-27)$$

where A_{m1} is the excitation coefficient for each element, d_x is spacing, χ_x is the phase shift between the elements, and M is total number of elements along x axis. For N total number of elements placed in the y -direction, a square array is produced (Figure 3-5b). The array factor for the whole array is

$$AF = \sum_{n=1}^N A_{1n} \left[\sum_{m=1}^M A_{m1} e^{j(m-1)(kd_x \sin\theta \cos\phi + \chi_x)} \right] e^{j(n-1)(kd_y \sin\theta \sin\phi + \chi_y)}, \quad (3-28)$$

where d_y and χ_y is spacing and progressive phase shift between elements along y -axis. The total array factor can also be represented as:

$$AF = S_{xm} S_{yn} \quad (3-29)$$

where

$$S_{xm} = \sum_{m=1}^M A_{m1} e^{j(m-1)(kd_x \sin\theta \cos\phi + \chi_x)} \quad (3-30)$$

$$S_{yn} = \sum_{n=1}^N A_{n1} e^{j(n-1)(kd_y \sin\theta \sin\phi + \chi_y)} \quad (3-31)$$

$$A_{mn} = A_{m1} A_{1n} \quad (3-32)$$

If the amplitude excitation for entire array is uniform ($A_{mn}=I_0$), equation (3-28) can be expressed as

$$AF = I_0 \left[\sum_{m=1}^M e^{j(m-1)(kd_x \sin\theta \cos\phi + \chi_x)} \right] \sum_{n=1}^N e^{j(n-1)(kd_y \sin\theta \sin\phi + \chi_y)}, \quad (3-33)$$

In order to obtain the desired main beam at $\theta=\theta_0$ and $\phi=\phi_0$, the progressive phase shift between the elements in the x - and y -directions is equal to:

$$\chi_x = -kd_x \sin\theta_0 \cos\phi_0 \quad (3-34a)$$

$$\chi_y = -kd_y \sin\theta_0 \sin\phi_0 \quad (3-34b)$$

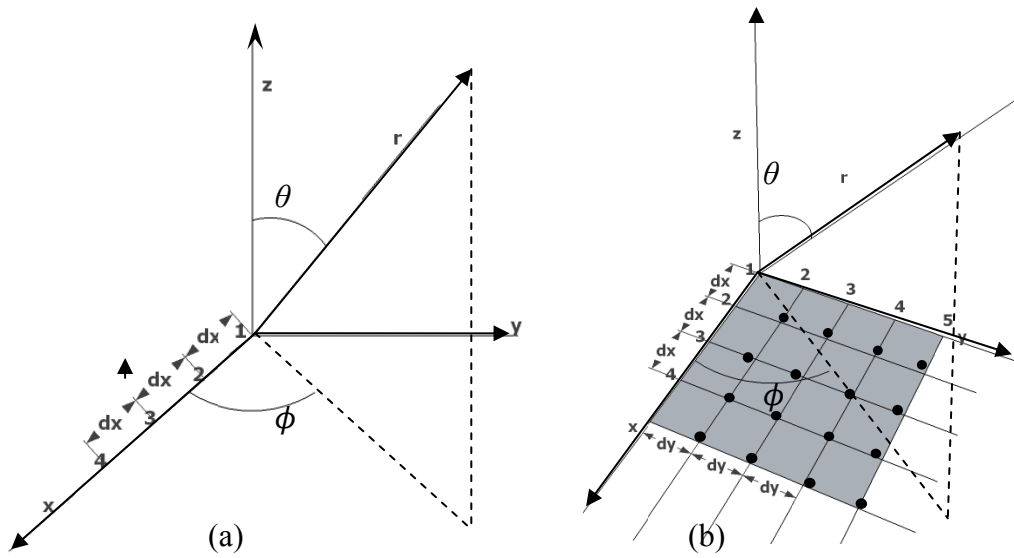


Figure 3-5: (a) Linear and (b) planar array geometries.

3.2.2.2.2 Circular Array

The normalized far-field pattern for an array of N isotropic elements (Figure 3-6) is written as [5]

$$E_n(r, \theta, \phi) = \sum_{n=1}^N a_n \frac{e^{-jkR_n}}{R_n} \quad (3-35)$$

R_n is the distance from the n th element to the observation point.

$$R_n = (r^2 + b^2 - 2br \cos \psi)^2 \quad (3-35a)$$

when $r \gg b$ (3-35a) reduces to

$$R_n \simeq r - b \cos \psi_n = r - b(\mathbf{a}_\rho \cdot \mathbf{a}_r) = r - b \sin \theta \cos(\phi - \phi_n), \quad (3-35b)$$

where,

$$\begin{aligned} \mathbf{a}_\rho \cdot \mathbf{a}_r &= (\mathbf{a}_x \cos \phi_n + \mathbf{a}_y \sin \phi_n) \cdot (\mathbf{a}_x \sin \theta \cos \phi + \mathbf{a}_y \sin \theta \sin \phi + \mathbf{a}_z \cos \theta) \\ &= \sin \theta \cos(\phi - \phi_n) \end{aligned} \quad (3-35c)$$

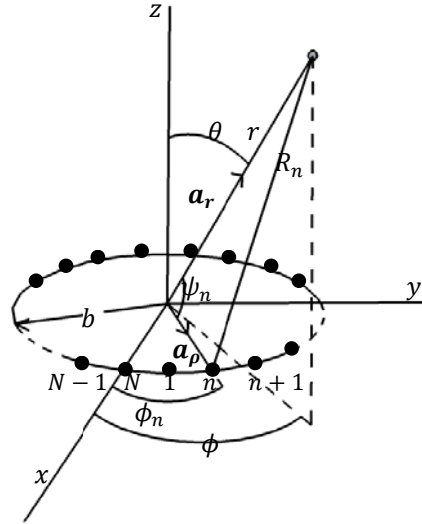


Figure 3-6: Geometry of an N -element circular array.

Thus by assuming $R_n \approx r$ and taking $N = 4$ elements reduces equation (3-35) to

$$E_n(r, \theta, \phi) = \frac{e^{-jkr}}{r} \sum_{n=1}^4 a_n e^{jkb \sin \theta \cos(\phi - \phi_n)} \quad (3-36)$$

where,

a_n is the excitation coefficients (amplitude and phase) of the n^{th} element.

ϕ_n is the angular position of n^{th} element on x-y plane.

The excitation coefficient for the n^{th} element can be represented as:

$$a_n = A_n e^{j\alpha_n} \quad (3-37)$$

where,

A_n is the amplitude excitation of the n^{th} element.

α_n is the phase excitation (relative to the array center) of the n^{th} element (in radians).

To obtain the total far-field for an array of four dipoles, (3-35) becomes

$$E_n(r, \theta, \phi) = 60j \cdot \frac{\cos(\frac{\pi}{2} \cos \theta)}{\sin \theta} \cdot \frac{e^{-jkr}}{r} \sum_{n=1}^4 a_n e^{jkb \sin \theta \cos(\phi - \phi_n)} \quad (3-38)$$

By using (3-37), (3-38) can be written as

$$E_n(r, \theta, \phi) = 60j \cdot \frac{\cos(\frac{\pi}{2} \cos \theta)}{\sin \theta} \cdot \frac{e^{-jkr}}{r} \sum_{n=1}^4 A_n e^{j[kb \sin \theta \cos(\phi - \phi_n) + \alpha_n]}, \quad (3 - 39)$$

where

$$AF(\theta, \phi) = \sum_{n=1}^4 A_n e^{j[kb \sin \theta \cos(\phi - \phi_n) + \alpha_n]} \quad (3 - 40)$$

To direct the peak of the main beam in the (θ_0, ϕ_0) direction, the phase excitation for each element can be selected as

$$\alpha_n = -kb \sin \theta_0 \cos(\phi_0 - \phi_n) \quad (3 - 41)$$

3.2.2.2.3 The active input impedance approaches

The techniques that have been discussed previously are ideal theories which are essential but not adequate to characterise the pattern of antenna array. Therefore, the active input impedance approach has been employed in many literatures by taking a consideration of mutual coupling effect in antenna array. However, many of them are concentrated to 1-D and 2-D antenna arrays [15]. This method has been discussed in chapter 2. It has been developed further into 3-D and will be explained in chapter four in order to observe the effect of mutual coupling to the antenna array.

3.2.3 3-D Array (Cubic, Spherical)

Many authors discussed about 1-D and 2-D array analysis compared to 3-D array due to the 3-D complexity [16]. Now, the advancement of computer technology makes the 3-D analysis and synthesis a possibility. The most popular method that demonstrated the idea by considering mutual coupling effect is the active element pattern (AEP). However, it depends on fixed geometry structure thus make the optimisation process limited to only on the excitation value. There might be issues in order to find the best performance and cost effective of antenna array such as how many elements required and what is the spacing between elements. As a result, there is a need to find a 3-D antenna array which developed from scratch in order to give flexibility in the optimisation process

such as spacing, number of elements and so on. Moreover, the method can be developed in order to include other effect such as the effect from the platform, feed network and array elements to increase its accuracy.

3.2.3.1 The active element pattern method

There are few methods employing the active element pattern (AEP) as shown in Figure 3-7. The unit-excitation AEP represents the pattern radiated by the array when the n th element is excited by a unit voltage with its associated generator impedance Z_n , and the other elements are loaded by their respective generator impedances $\{Z_n\}$. The total radiation pattern can be expressed as [15]:

$$E(\theta, \varphi) = \sum_{n=1}^N V_n g_n^u(\theta, \varphi), \quad (3 - 42)$$

The quantity $g^u(\theta, \varphi)$ is called the unit excitation active element pattern where it represents the pattern radiated by the array when the n th element is excited by a unit voltage with its associated generator impedance Z_n and the other elements are loaded by their respective generator impedances $\{Z_n\}$. V_n is the complex-valued feed voltage applied to the n th element and N is the number of voltage sources applied to the array. Therefore, the array pattern can be computed for any set of feed voltages $\{V_n\}$ using equation 3-28. The set $g^u(\theta, \varphi)$ includes the effect of mutual coupling and since it is calculated or measured once for each element, it is known as the exact active element pattern.

The phase-adjusted unit-excitation AEP is an extension from the previous method by extracting the spatial phase information that contains the element location from the unit-excitation parameter, $g^u(\theta, \varphi)$. By using this method, the total far-field pattern can be computed for arbitrary geometries for once. However, it is not true as the phase-adjusted change whenever the array geometry change [15].

Both of the above methods are exact methods and become complex as the number of elements increased. Therefore, they are suitable for small and finite arrays. In this case, the active element pattern is performed for each element and summed up in order to obtain the total far-field pattern. For large (i.e. infinite)

arrays, the average AEP method, $F_e(\theta)$ provides a better solution since the active element pattern of all elements is identical and used only once. However, the disadvantages are that it doesn't take into account the edge effect and how many number of elements so that it can be classified as an infinite array. The edge effect occurs because the way the central element sees the array environment is different compared to the elements placed at the edge of antenna array. On the other hand, the hybrid AEP is a good solution for medium sized array where it is an intermediate between the average and the unit excitation AEP method. It is suitable for finite array analysis where the edge effects will be taken into account [15].

The active element pattern may be obtained from the simulated or measured patterns of the individual element in the array environment to calculate the pattern of the fully excited array. This method is applicable especially in conformal analysis [16, 17] when classical analysis and numerical techniques failed to do so. Plus, its measurement is much simpler and cheaper compared to the direct measurement of the scanning characteristics of a large phased array antenna, combined with power divider network and phase shifters. The measurement of active element pattern requires only a large antenna array with matched loads on all but one of the elements. Thus, it can be used to locate and correct array design problems and thereby, reduced the risk of a costly design failure. However, this technique only accounts mutual coupling effect between array elements and does not consider the coupling effect between feed networks, mounting platform with array elements. The AEP also does not take into account the mismatch effect in source network. Wang [16] proposed a new method based on the active element pattern that includes mutual coupling and platform effects of conformal array.

Another disadvantage of the AEP method is that it is restricted to fixed structures, frequency and set of generator impedances. Therefore, it is only applicable in order to obtain the best excitation values for the element. There are other issues that need to be considered such as number of elements for an array so that the design will be cost effective, the element spacing to avoid grating lobes and so on. This issue may be solved using array analysis or numerical methods.

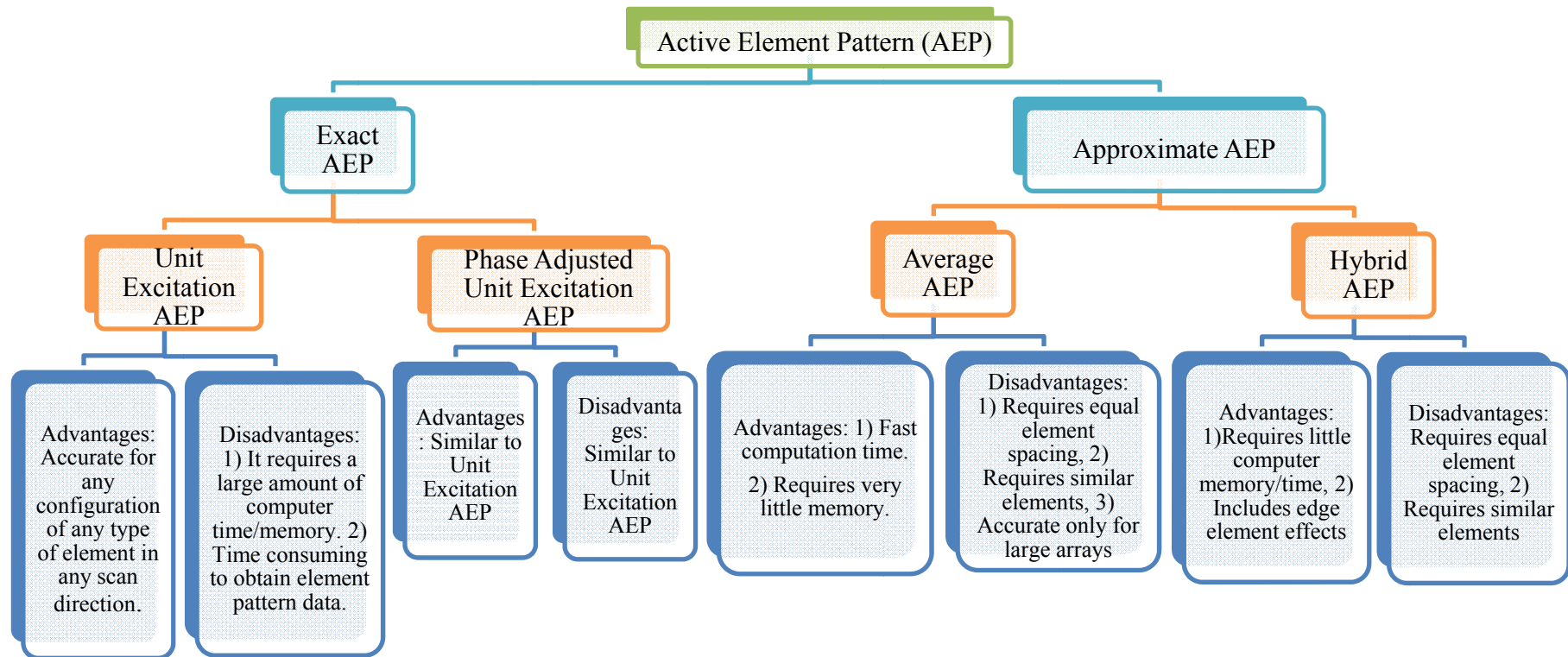


Figure 3-7: Methods that employ active element pattern [15].

3.3 Optimisation Techniques

There are many techniques available to optimize the antenna characteristic so that it meets the designer's specification. The antenna requirements are based on the application. For example, a flat-topped and cosecant shaped beam pattern which has low side-lobe levels and narrow bandwidth are importance in satellite and radar systems. Another application is the use of smart antennas in mobile applications that provide adequate signal strength in designated areas while having a low strength (nulls) in interference area [18].

It is a difficult task to meet the antenna's specification since there are a large number of variables may be involved in the process. Many authors focused on synthesizing the pattern either in one [19] or two-dimensions [20] due to its simplicity. In some cases, the antenna's requirement may not be fulfilled entirely due to other restrictions placed on the antenna itself. However, an optimisation process will lead all the variables toward a compromise solution to the problem.

The building blocks of optimisation process have been illustrated by Thiel and Smith [21] in Figure 3-8. The optimization technique makes a comparison between new calculated optimized antenna design with the 'ideal' performance as required by the designer.

One of the most important factors in any optimization techniques is cost function. A cost function (or objective function or error function) represents how close the optimized design meets the specification. There are a few ways to calculate a cost function. A common way is to define it in terms of the least squared error. If the parameters that need to be optimized are the directivity $D(i)$ dB, the front-to-back ratio $FB(i)$ dB, the beamwidth $\phi(i)^\circ$, and the $S_{11} = S(i)$ dB, then the least squared error cost function, C_{lse} [21] is:

$$C_{lse} = \sum (D_{opt} - D(i))^2 + (FB_{opt} - FB(i))^2 + (\phi_{opt} - \phi(i))^2 + (S_{opt} - S(i))^2, \quad (3-43)$$

where is D_{opt} the desired directivity (dB), FB_{opt} is the desired front-to-back ratio (dB), ϕ_{opt} is the desired beamwidth, and S_{opt} is the desired S_{11} .

Thus, the variables within the cost function are varied until the minimum of C_{lse} is reached. The disadvantage of this definition is that if one variable is

very large in comparison with others, it will dominate the cost function. On the other hand, if it has small value, it has the tendency to be ignored in the optimization process. To overcome this problem, the relative least squared error, $C_{rlse}(i)$ (equation 3-44) has been employed and is given by [21]:

$$C_{rlse}(i) = w_1 \left[\frac{FB_{opt} - FB(i)}{FB_{opt}} \right]^2 + w_2 \left[\frac{\phi_{opt} - \phi(i)}{\phi_{opt}} \right]^2 + w_3 \left[\frac{S_{opt} - S(i)}{S_{opt}} \right]^2, \quad (3 - 44)$$

The weight parameters, w_i has been assigned to prevent one variable from dominating or ignored in the cost function.

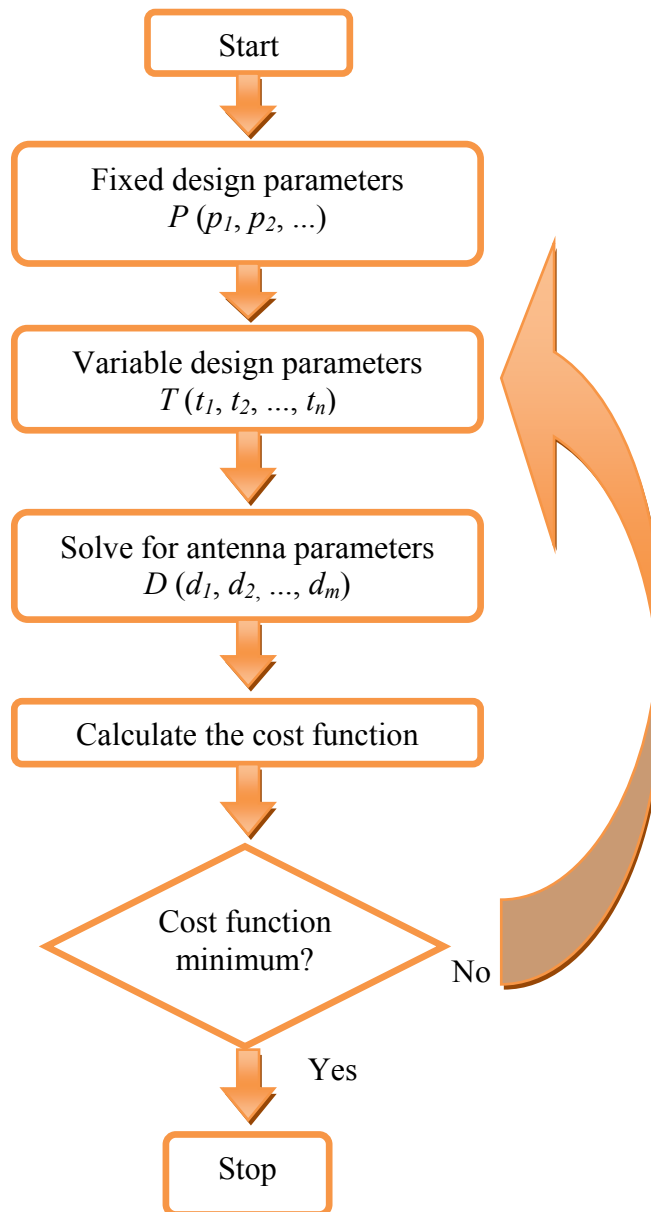


Figure 3-8: Block building block of an optimisation routine [21].

The simplest array optimization technique is the sequential uniform sampling. It calculates the cost function for each possible value of the input variables in the solution space [21]. The step size of the variables determines the number of iterations required for all possible input combination. The advantage of this technique is the ability to locate a number of minimum values for the cost function, increasing a degree of flexibility in the chosen solution. The drawbacks of using this method is that the number of iterations to calculate the cost function increase as the step size decrease (for higher resolution) or the number of variables increase. For example, if there are 64 steps for two variables, t_1 and t_2 , it requires 64^2 of iterations to be solved.

Another work [22] compares in terms of search efficiency between direct search methods that do not use random decision making to those that do. Non-random search methods include Nelder-Mead, finite difference quasi-Newton method (FDFNLF1) and quasi-Newton method requiring user supplied derivatives (NLF1) while random search method is particle swarm optimization (PSO). The results show that non-randomized search methods required less number of iterations to converge to acceptable pattern performance than randomized search method. However, Nelder-Mead is a local search method and its performance highly depends on the starting point. In order to mitigate convergence difficulties of random search methods, Nelder-Mead method is combined together with PSO [23] and GA [24], forming hybrid optimization algorithms.

Another optimization technique that can be used in pattern synthesis is simulated annealing. This technique represents an analogy to the annealing or tempering of steel, where the initial temperature is high and reduced in a controlled manner to the point where the metal becomes completely rigid and its crystal structure is locked in place. In general, it searches for a minimum in a more general system.

Metropolis [25] proposed the algorithm in order to find the equilibrium configuration of a collection of atoms at a given temperature. Pincus [26] relates this algorithm with mathematical minimization. However, it was Kirkpatrick et al. [27] who propose it in optimization technique for combinatorial (and other) problems.

In [28], simulated annealing was able to synthesise the antenna pattern of circular arc arrays. The method minimises the cost function wherein nulls can be fixed in given directions, while the dynamic range of excitations, beamwidth and other parameters of interest in the design can be controlled. This process avoids the local minima of the cost function and achieves a good approximation to the sum and flat topped beam pattern. Another author by [29] extended the work in [28] for pattern synthesis of cylindrical array using simulated annealing. They also compare its performance with genetic algorithm [30] and found out that genetic algorithm takes longer computational time than simulated annealing for this case.

Genetic Algorithm (GA) is widely used in electromagnetic optimization. Due to its popularity and ease of implementation, it has been chosen for pattern synthesis and will be explained into details in chapter 5. Genetic algorithm (GA) optimizers are robust and stochastic technique based on the Darwinian concepts of natural selection and evolution. They allow a set of populations to develop toward a global optimum solution. The process is based on three important steps; selection, recombination and mutation.

Many authors employ genetic algorithm in pattern synthesis. Rezioui and Azrar [19] implemented a combination of Schelkunoff's method and a genetic algorithm to synthesize equispaced linear and planar arrays. This method applied array factor as a polynomial whose roots are placed in the z plane. A comparison has been made with other methods such as Uniform, Binomial, and Dolph-Chebyshev arrays in term of directivity and side-lobe level. The results show that it has highest directivity compared to its counterparts for linear array.

A simple genetic algorithm also has drawbacks such as poor local searching, premature converging and slow convergence speed [31]. Few other methods have been combined with genetic algorithms to mitigate this problem such as adaptive genetic algorithm (AGAs) using fuzzy logic controller technique [32] or hybrid genetic algorithm using Nelder-Mead method [24]. Adaptive genetic algorithm (AGAs) works by adjusting their control variables according to the variation of the environment in which the GAs are run. In [32], fuzzy logic controller technique is introduced in order to adjust control variables of GA (crossover and mutation probabilities) based on the current performance

measures of GAs (such as maximum, average or minimum fitness and diversity population).

3.4 Conclusions

A few array numerical techniques have been elaborated within this chapter, including numerical methods and closed form analytical array. The well-known full-wave techniques, such as method of moments and finite-difference time domain have been studied. The comparison between both techniques has been summarized. These techniques can calculate mutual coupling but do not allow array optimisation (such as GA or LMS method) easily or quickly because it takes long computation. In certain cases, the simulation might need to be performed more than once whenever the frequency and geometrical of the model change.

Analytical methods have been discussed within this chapter. Most of them are conventional methods such as Binomial, Dolph-Chebyshev and Schelkunoff which are limited to one-dimensional (linear) antenna array. Other analysis as described in 2-D array is based on the array factor (or pattern multiplication method). These techniques are inaccurate since they do not incorporate coupling effect between elements. The AEP do consider mutual coupling but the results need to be extracted from the simulation before running with the optimisation method. Therefore, this thesis focuses on investigating an array analysis using the Induced EMF method. The numerical techniques using the Induced EMF method has been established for a long time. However, it only applies for parallel and 2-D dipole antenna arrays. There is a need to create a 3-D antenna array due to its wide angle steering capability and low side-lobe level.

Resulting from this, a novel 3-D array analysis based on Induced EMF method will be developed. The method employs self and mutual-impedance using the Induced EMF method as it is a good approximation for dipole arrays. The results may not be as accurate as full-wave modelling but the method runs quickly and blends easily with the optimisation technique. The method will be developed using MATLAB [33]. The far-field pattern from this new 3-D array

analysis will be compared with the other full wave techniques as validation to the code.

The array analysis shall be combined with optimization techniques in order to control the beam. From the review, a genetic algorithm has been chosen since it is robust, not easily trapped into local values and easy to implement. By applying a genetic algorithm as described previously, the best characteristics (such as to acquire beam pattern with nulls and maximum at certain angles) might be possible to attain.

References

- [1] Z. Huang, C. A. Balanis, C. R. Birtcher, "Mutual Coupling Compensation in UCAs: Simulation and Experiment," IEEE Transactions on Antennas and Propagation, Vol. 54 (11), pp. 3082, Nov. 2006.
- [2] H. Steyskal, J. S. Herd, "Mutual Coupling Compensation in Small Array Antennas," IEEE Transactions on Antennas and Propagation, vol. 38 (12), pp. 1971, Dec. 1990.
- [3] R. F. Harrington, Field Computation by Moment Methods. Piscataway, NJ: Piscataway. IEEE Press, 1993.
- [4] K. Yee, "Numerical solution of initial boundary value problems involving maxwell's equations in isotropic media," Antennas and Propagation, IEEE Transactions on, vol. 14, pp. 302-307, 1966.
- [5] C. A. Balanis, Antenna Theory: Analysis and Design. Canada: Wiley-Interscience, 2005.
- [6] N. Fourikis, Phased Array-Based Systems and Applications. New York Chichester: Wiley, 1997.
- [7] C. L. Dolph, "A Current Distribution for Broadside Arrays Which Optimizes the Relationship between Beam Width and Side-Lobe Level," Proceedings of the IRE, vol. 34, pp. 335-348, 1946.
- [8] S. A. Schelkunoff, Electromagnetic Waves. Van Nostrand, 1960.
- [9] H. M. James, N. B. Nichols and R. S. Phillips, Theory of Servo-Mechanisms. United States: McGraw-Hill, 1947, pp. 231-261.
- [10] J. Richmond, "Discussion on "A Current Distribution for Broadside Arrays Which Optimizes the Relationship between Beam Width and Side-Lobe Level" (C. L. Dolph)," Proceedings of the IRE, vol. 35, pp. 489-492, 1947.
- [11] D. Barbieri, "A Method for Calculating the Current Distribution of Tschebyscheff Arrays," Proceedings of the IRE, vol. 40, pp. 78-82, 1952.
- [12] C. J. Drane Jr., "Useful approximations for the directivity and beamwidth of large scanning Dolph-Chebyshev arrays," Proceedings of the IEEE, vol. 56, pp. 1779-1787, 1968.
- [13] R. C. Hansen, Phased Array Antennas. New York; Chichester : Wiley, .
- [14] S. A. Schelkunoff, "A mathematical theory of linear arrays," Bell Syst.Tech.J., vol. 22, pp. 80-107, jan, 1943.

- [15] D. F. Kelley and W. L. Stutzman , "Array antenna pattern modeling methods that include mutual coupling effects," *IEEE Transactions on Antennas and Propagation*, vol. 41, pp. 1625-1632, Dec, 1993.
- [16] Q. Wang and Q-Q. He, "An arbitrary conformal array pattern synthesis method that includes mutual coupling and platform effects," *PIER*, vol. 110, pp. 297-311, 2010.
- [17] Z. Xu, H. Li, Q-Z. Liu and J-Y. Li, "Pattern synthesis of conformal antenna array by the hybrid genetic algorithm," *PIER*, vol. 79, pp. 75-90, 2008.
- [18] D. K. Cheng, "Optimization techniques for antenna arrays," pp. 1664-1674, 1971.
- [19] A. Recioui and A. Azrar. Use of genetic algorithms in linear and planar antenna array synthesis based on schelkunoff method. *Microw. Opt. Technol. Lett.* [July 2007]. Vol 49(7), pp. 24 Dec 2010. 2007.
- [20] F. Zhang, F-S. Zhang, C. Lin, G. Zhao and Y-C. Jiao, "Pattern synthesis for planar array based on elements rotation," *Progress in Electromagnetics Research Letters*, vol. 11, pp. 55-64, 2009.
- [21] D. V. Thiel, *Switched Parasitic Antennas for Cellular Communications*. Boston: Boston : Artech House.
- [22] S. J. Blank and M. F. Hutt, "Antenna array synthesis using derivative, non-derivative and random search optimization," *Sarnoff Symposium*, pp. 1-4, 2008.
- [23] P. Koduru, S. Das, and S. M. Welch, "A Particle Swarm Optimization-Nelder Mead Hybrid Algorithm for Balanced Exploration and Exploitation in Multidimensional Search Space", iee.cugb.edu.cn/WorldComp2006/ICA4682.pdf.
- [24] R. Haupt, and Y.C. Chung, "Optimizing backscattering from arrays of perfectly conducting strips," *IEEE Antennas and Propagation Magazine*, Vol. 45, No. 5, October 2003.
- [25] N. Metropolis, "Equation of State Calculations by Fast Computing Machines," *J. Chem. Phys.*, vol. 21, pp. 1087-6, 2004-12-23T16:18:58, 1953.
- [26] M. Pincus, "Letter to the Editor—A Monte Carlo Method for the Approximate Solution of Certain Types of Constrained Optimization Problems," *Operations Research*, vol. 18, pp. 1225-1228, November/December 1970, November/December 1970.

- [27] S. Kirkpatrick, C. D. Gelatt and M. P. Vecchi, "Optimization by Simulated Annealing," *Science*, vol. 220, pp. 671-680, May 13, 1983.
- [28] F. Ares, S. R. Rengarajan, J. A. F. Lence, A. Trastoy and E. Moreno, "Synthesis of antenna patterns of circular arc arrays", *Electronics Letters*, vol. 32, no. 20, 1996.
- [29] J. A. Ferreira and F. Ares, "Pattern synthesis of conformal arrays by the simulated annealing technique", *Electronics Letters*, vol. 33, no. 14, 1997.
- [30] A. Hunter, "Sunderland genetic algorithms package," University of Sunderland, England.
- [31] S. O. Kundukulam and K. S. Beenamole, "Design of a linear array antenna for shaped beam using genetic algorithm," *Int.J.RF Microw.Comput.-Aided Eng.*, vol. 18, pp. 410-416, September, 2008.
- [32] B. Kadri, M. Boussahla and F. T. Bendimerad, "Phase-Only Planar Antenna Array Synthesis with Fuzzy Genetic Algorithms," *CoRR*, vol. abs/1002.1176, 2010.
- [33] C. B. Moler, *Numerical Computing with MATLAB*. Philadelphia: Society for Industrial and Applied Mathematics.

CHAPTER 4:

Computational and Modelling Details of Dipole Antenna Arrays

4.1 Introduction

This chapter describes the method used to analyze radiation pattern of dipole arrays arranged in three-dimensions. The analysis should include mutual coupling since its effect is significant especially for small antenna arrays [1]. Therefore, the Induced EMF method [2, 6] has been chosen since it is simple yet provides a good approximation to consider the mutual impedance effect in dipole antenna arrays. Other higher order methods such as Maxwell's equation [3] provide a more accurate solution by considering the mutual coupling effect in the array environment, and may be solved using the method of moments (MoM) [4] or the finite-difference time-domain method (FDTD) [5]. However, this approach requires large computational resources to solve Maxwell's equations numerically.

The array analysis in this thesis employs the Induced EMF method derived from [6] in order to obtain the current excitation for each element. Then, the pattern is calculated based on the current excitation of each element. Since the pattern for each field is rotated with respect to z-axis, a transformation matrix [7] has been applied for each element. Then, the pattern for each element is summed up to obtain the total radiation pattern. Two models; 2x2 and 12 dipoles arranged at the edge of a cube are chosen as examples for this analysis. The method is suitable for dipole elements arranged in 3-D both in straight and inclined configurations. The results are presented here and compared with other

techniques such as pattern multiplication, method of moments and finite-difference time-domain method.

4.2 Background Theory and Algorithm using Induced EMF Method

4.2.1 2-D Algorithm

The 2-D Algorithm [8] is based on King's technique [9] to obtain the far-field pattern of a half wavelength dipole array arranged side by side, collinearly or parallel in an echelon configuration. Several studies have used mutual impedance to calculate the far-field pattern [10, 11, 12].

The 2-D algorithm [8] has been investigated, modified and extended in this thesis. Figure 4-1 shows four half-wavelength dipoles arranged side by side with spacing of $0.65\lambda_0$ at 2.45 GHz (estimated around 0.08 m apart) as validation to the 3-D Algorithm. The spacing is chosen larger than half-wavelength in order to allow an array of half-wavelength dipole antenna to be arranged at the edge of a cube structure for 3-D analysis. The spacing also should not be greater than a wavelength in order to reduce the effect of grating lobes.

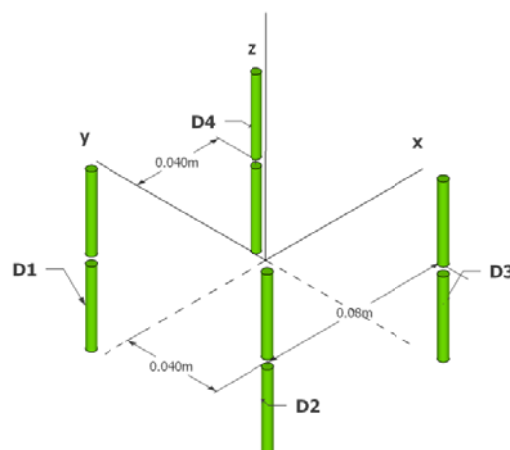


Figure 4-1: Four half-wavelength dipoles with spacing of 0.08 m.

The total far-field pattern is calculated using King's technique [9] for the N ($N=4$) element of vertical half-wavelength dipoles as follows:

$$E_{total}(\theta, \phi) = E_1(\theta, \phi) + E_2(\theta, \phi) + E_3(\theta, \phi) + E_4(\theta, \phi) \quad (4-1)$$

where the electric field for each dipole, E_n , is given from equation (2-1). Therefore, the total electric field, E_{total} , is

$$E_{total}(\theta, \phi) = j\eta \left\{ \frac{\cos\left(\frac{\pi}{2} \cos \theta\right)}{2\pi \sin \theta} \right\} \left\{ \sum_{n=1}^N \frac{I_n e^{-jkR_n}}{R_n} \right\} \quad (4-2)$$

where R_n is the distance from each dipole (x_n, y_n, z_n) to the far-field observation point (r, θ, ϕ) . The equation within the brackets on the left-hand side represents the pattern of a dipole, while the Induced EMF Method (mutual coupling effect) is represented within the right-hand brackets. The far-field observation point is converted from polar coordinates (r, θ, ϕ) to rectangular coordinates (x, y, z) using equations (4-3 to 4-5):

$$x = r \sin \theta \cos \phi \quad (4-3a)$$

$$y = r \sin \theta \sin \phi \quad (4-3b)$$

$$z = r \cos \theta \quad (4-3c)$$

Therefore, the R_n distance is calculated based on equation:

$$R_n = \sqrt{(x - x_n)^2 + (y - y_n)^2 + (z - z_n)^2} \quad n = 1, 2, \dots, N \quad (4-4)$$

Since R_n in the denominator of equation (4-2) is an amplitude variation, it is equal to r (the far field distance).

$$R_n \approx r \quad (4-5)$$

The far-field equation is valid when $R_n \geq \frac{2D^2}{\lambda}$, which is the far-field region.

Therefore, the total far-field as follows:

$$E_{total}(\theta, \phi) = j\eta \frac{\cos\left(\frac{\pi}{2} \cos \theta\right)}{2\pi r \sin \theta} \left\{ \sum_{n=1}^N I_n e^{-jkR_n} \right\} \quad (4-6)$$

A simplified flowchart is given in Figure 4-2 below to explain the overall modified 2-D algorithm.

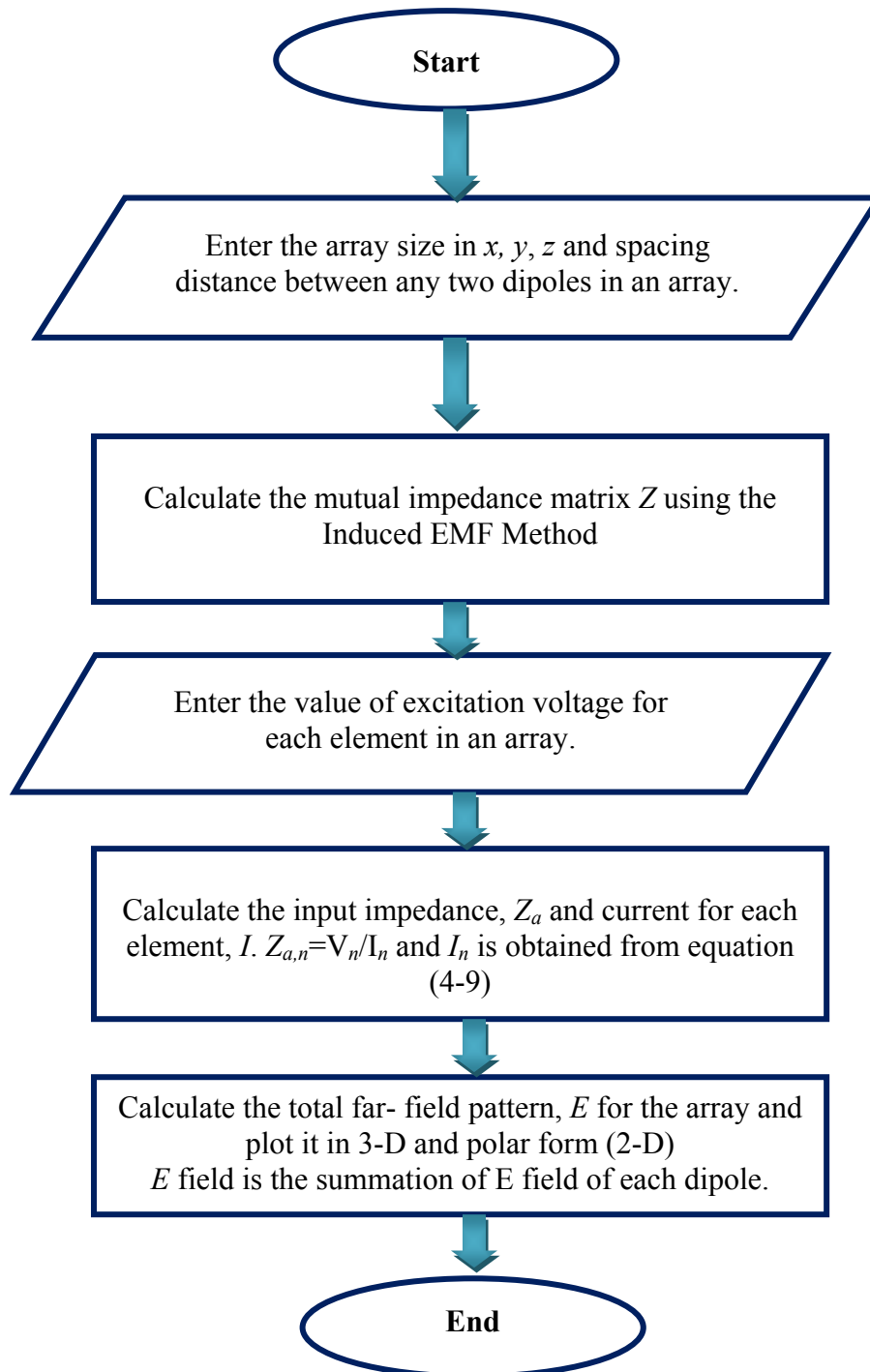


Figure 4-2: Flowchart of the modified 2-D algorithm.

4.2.2 3-D Algorithm

The 3-D algorithm is an extension of the modified 2-D algorithm. The difference between the 2-D and 3-D algorithms is that 2-D can be employed for straight and

parallel dipoles only. 3-D algorithm (as shown in Figure 4-3) is a new technique to calculate the far-field pattern in 3-D dipole arrays incorporates the coupling effect based on the Induced EMF method. It enables the far-field pattern for the dipole arrays to be computed whether the elements are arranged in straight and inclined position and also either in one, two or three-dimensions. Baker and LaGrone [6] found that the mutual impedance could be computed when the dipole is inclined position. 3-D algorithm proves to be useful for an array of dipoles arranged in three dimensions, such as cubic, spherical or icosahedrons. One of the advantages of employing a 3-D algorithm in the array optimisation is the wide scanning ability in three-dimensions by taking into account the coupling effect.

The 3-D algorithm is similar to the modified 2-D algorithm (as shown in Figure 4-2) with several modifications:

1. The mutual impedance matrix is calculated from Baker and LaGrone [6], as it can be applied for straight and inclined elements in an array. As a result, the direction of terminal current vector, \mathbf{I} is along the axis of the dipole antenna.

The root mean square (rms) terminal current vector, \mathbf{I} can be calculated for each dipole, by taking the inverse of the mutual coupling impedance vector, \mathbf{Z} and generator impedance vector, \mathbf{Z}^g and multiplying it with the feed voltage (vector), \mathbf{V}^s [13, 14, 15]. It is obtained from the network analysis as mentioned in Section 2.3.1.1 together with the free excitation model [16].

$$\mathbf{I} = \{\mathbf{Z} + \mathbf{Z}^g\}^{-1}\mathbf{V}^s \quad (4 - 7)$$

The self and mutual impedance matrix, \mathbf{Z} may be computed using the Induced EMF Method using equations (2-46) and (2-47). Therefore, the current in equation (4-7) is calculated in matrices for N dipoles as follows:

$$[\mathbf{I}] = \mathbf{inv}[\mathbf{Z} + \mathbf{Z}^g] * [\mathbf{V}^s] \quad (4 - 8)$$

$$\begin{bmatrix} I_1 \\ I_2 \\ \vdots \\ I_N \end{bmatrix} = \mathbf{inv} \left(\begin{bmatrix} Z_{11} & Z_{12} & \dots & Z_{1N} \\ Z_{21} & Z_{22} & \ddots & Z_{2N} \\ \vdots & \vdots & \ddots & \vdots \\ Z_{N1} & Z_{N2} & \dots & Z_{NN} \end{bmatrix} + \begin{bmatrix} Z_g \\ Z_g \\ \vdots \\ Z_g \end{bmatrix} \right) \times \begin{bmatrix} V_1 \\ V_2 \\ \vdots \\ V_N \end{bmatrix} \quad (4 - 9)$$

2. The transformation matrix [7] has been calculated in order to transform the electric far-field pattern of dipole antenna which the original axis is directed along z-axis (equation 4-6) to any direction the dipole has been inclined. The transformation matrix will be explained in the next section.

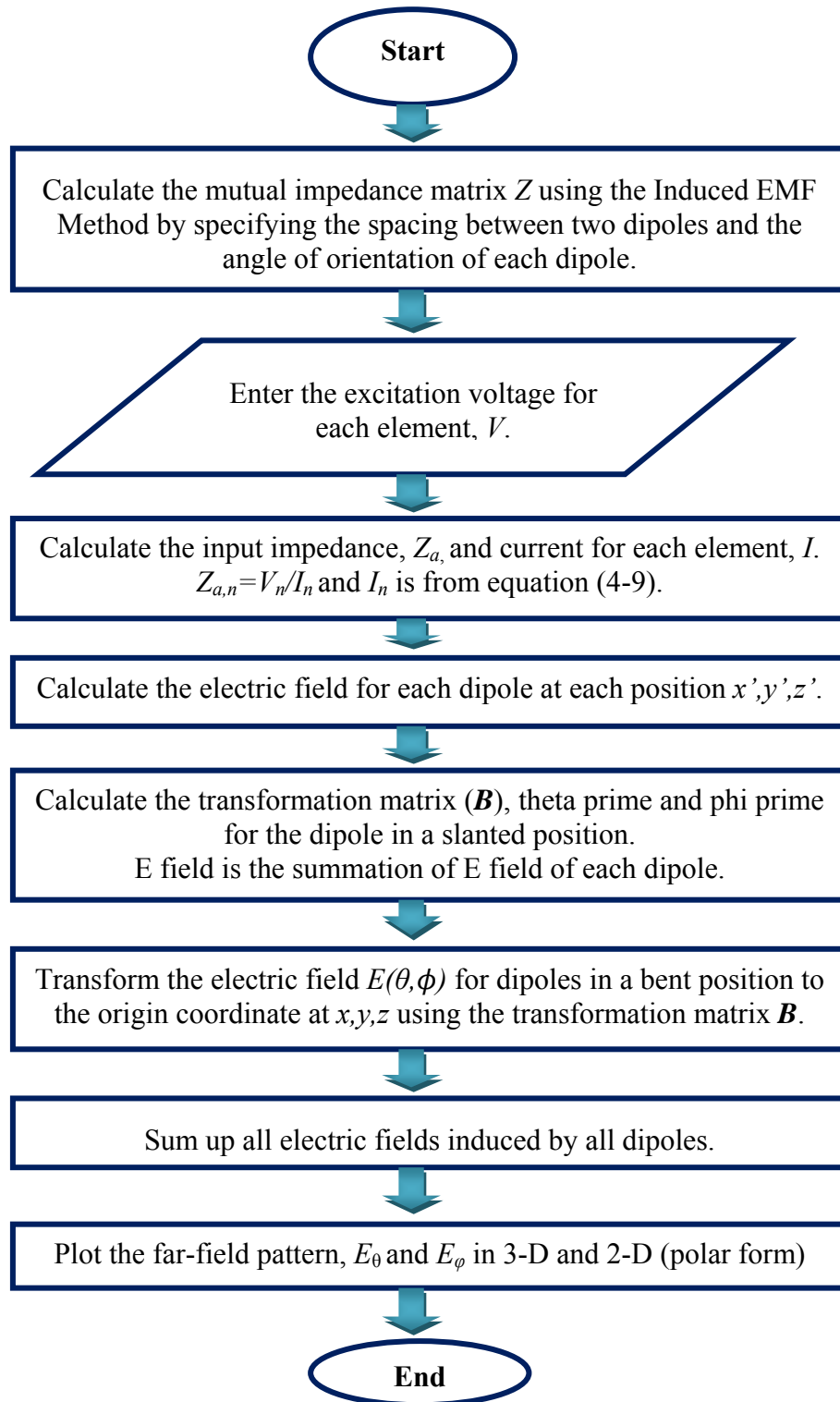


Figure 4-3: Flowchart of the novel 3-D algorithm

4.2.2.1 Euler Angle

The Euler angle has been described as a way of transforming from one given Cartesian coordinate system to another using three successive rotations performed in a specific sequence. Figure 4-4 shows two Cartesian coordinate systems $\{c\}$ and $\{c'\}$. These Cartesian systems can be related via three angle rotations (α , γ , β) known as Euler angles. There are many definitions of these angles in the literature [17-19]. Rahmat-Samii [7] was the first to employ the definition of the Euler angle [20-21] in antenna applications. The choice of rotation angles is arbitrary (xzx , zyz , xyx , xzx , zyz , yxy etc.). There are 12 possible conventions in defining Euler angles. However, the main convention or x convention (classical mechanics) is widely used in celestial mechanics, applied mechanics and in molecular and solid-state physics. Rahmat-Samii [7] derives the use of Euler angles using the x convention.

Figure 4-4 describes angle α as a counter-clockwise rotation about the z -axis which brings the x -axis to the x'' -axis aligned with the line nodes (line of intersection between the xy and $x'y'$ planes); angle β defines a rotation about the line of nodes in a counter-clockwise sense, as indicated, so that it brings the z -axis to the z' -axis; and finally, angle γ is another rotation about the z -axis and aligns the x'' -axis with the x -axis in a counter-clockwise sense, while the y' -axis is on the same plane and perpendicular to the x' -axis and not accounted for in the coordinate transformation. Burger [21] explains a further application of the Euler angle.

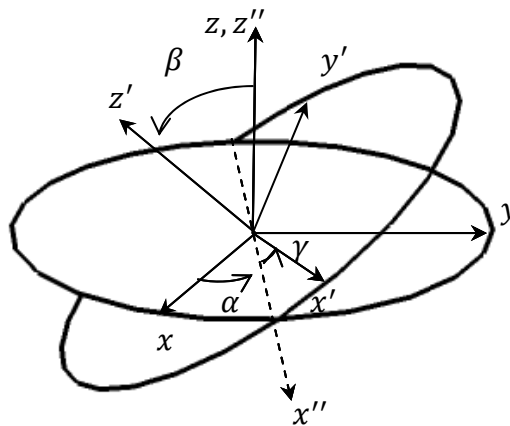


Figure 4-4: Transformation technique and Euler angle.

A set of Euler angles has been applied to an array of 12 dipoles arranged in a cube (Figure 4-5). Cubic dipole array has been chosen considering an efficient way of calculating Euler angle for each dipole that is perpendicular to the z -axis. Moreover, the arrangement of dipoles in 3-D increase capability to steer the beam in 3-D. Cubic arrays have been used in many applications where one of it in MIMO [22]. Several examples are shown in Table 3 to illustrate the relationship of Euler angles to the position of each element in an antenna array.

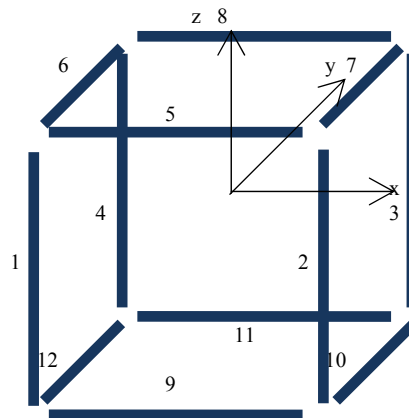


Figure 4-5: An array of 12 dipoles at the edge of cube.

Table 3: The position of dipole elements in rectangular coordinates (x, y, z) and Euler (α, β, γ) .

Index Element	Position (x,y,z)	α	β	γ
1	-0.04,-0.04,0	0	0	0
2	0.04,-0.04,0	0	0	0
3	0.04,0.04,0	0	0	0
4	-0.04,0.04,0	0	0	0
5	0,-0.04,0.04	$-\pi/2$	$-\pi/2$	0
6	-0.04,0,0.04	0	$-\pi/2$	0
7	0.04,0,0.04	0	$-\pi/2$	0
8	0,0.04,0.04	$-\pi/2$	$-\pi/2$	0
9	0,-0.04,-0.04	$-\pi/2$	$-\pi/2$	0
10	0.04,0,-0.04	0	$-\pi/2$	0
11	0,0.04,-0.04	$-\pi/2$	$-\pi/2$	0
12	-0.04,0,-0.04	0	$-\pi/2$	0

4.2.2.2 Transformation Matrix

There are several situations where the feed coordinates or in this case, the far-field pattern coordinates do not coincide with the antenna coordinates [7]. The

transformation matrix has been applied here to present the relationship of the spherical and Cartesian components of one system (i.e. x', y', z') to the spherical and Cartesian components of another system (x, y, z). The fact that the far-field pattern of a dipole is based on a local coordinate where the z' -axis is parallel to the length of the individual dipole should be taken into account. Figure 4-6 illustrates Cartesian and spherical coordinate systems. Two unit vectors have been assigned respectively to Cartesian and spherical coordinates by

$$\{\mathbf{c}\} = \{\mathbf{c}_1, \mathbf{c}_2, \mathbf{c}_3\}^t \quad (4 - 10)$$

$$\{\mathbf{s}\} = \{\mathbf{s}_1, \mathbf{s}_2, \mathbf{s}_3\}^t \quad (4 - 11)$$

Here, t represents the transpose operator (column operator). The two vectors can be assigned as:

$$\mathbf{c}_1 = x, \quad \mathbf{c}_2 = y, \quad \mathbf{c}_3 = z$$

$$\mathbf{s}_1 = r, \quad \mathbf{s}_2 = \theta, \quad \mathbf{s}_3 = \phi$$

where x, y, z and r, θ, ϕ are defined in Figure 4-6.

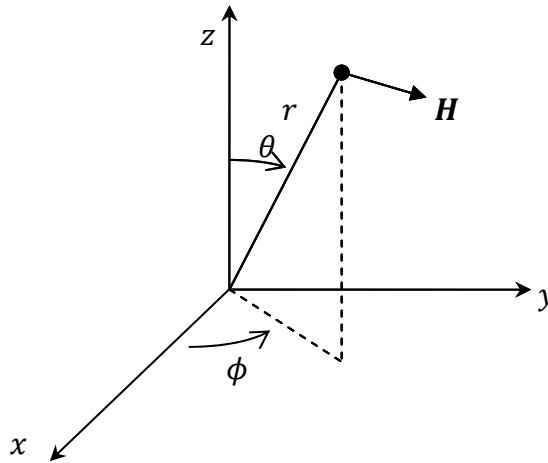


Figure 4-6: The relationship between Cartesian and spherical coordinates.

In this case, the electric field vector, \mathbf{E} has been replaced with vector \mathbf{H} to calculate the far-field pattern. A vector field \mathbf{H} can be expressed in terms of Cartesian or spherical components as follows:

$$\mathbf{H} = \sum_{i=1}^3 H_i^c \mathbf{c}_i \quad (4 - 12)$$

or

$$\mathbf{H} = \sum_{i=1}^3 H_i^s \mathbf{s}_i \quad (4-13)$$

Note that,

$$\mathbf{H} = \{H^s\} = \{H_1^s, H_2^s, H_3^s\}^t = \{H_r, H_\theta, H_\phi\} \quad (4-14)$$

The relationship between spherical and Cartesian components can be defined as follows:

$$({}^s T^c) = \begin{pmatrix} \sin \theta \cos \phi & \sin \theta \sin \phi & \cos \theta \\ \cos \theta \cos \phi & \cos \theta \sin \phi & -\sin \theta \\ -\sin \phi & \cos \phi & 0 \end{pmatrix} \quad (4-15)$$

The superscripts ^s and ^c are used to denote the transformation from Cartesian components to spherical components. Therefore, it is easily proved that

$$\{\mathbf{s}\} = ({}^s T^c)\{\mathbf{c}\} \quad (4-16)$$

$$\{H^s\} = ({}^s T^c)\{H^c\} \quad (4-17)$$

Furthermore, it can be shown that

$${}^c T^s = ({}^s T^c)^{-1} = ({}^s T^c)^t \quad (4-18)$$

In this case, ({}^cT^s) defines a transformation from spherical to Cartesian components.

The relationship between one Cartesian system and another Cartesian system is as follows:

$$\{\mathbf{c}'\} = ({}^{c'} B^c)\{\mathbf{c}\} \quad (4-19)$$

$$\{H^{c'}\} = ({}^{c'} B^c)\{H^c\} \quad (4-20)$$

Here, ({}^{c'}B^c) is the transformation matrix from the Cartesian coordinates {c} and {c'} by using the Euler angle (α, γ, β), defined as:

$$\begin{aligned}
 & ({}^c B^c) \\
 &= \begin{pmatrix} \cos \gamma & \sin \gamma & 0 \\ -\sin \gamma & \cos \gamma & 0 \\ 0 & 0 & 1 \end{pmatrix} \begin{pmatrix} 1 & 0 & 0 \\ 0 & \cos \beta & \sin \beta \\ 0 & -\sin \beta & \cos \beta \end{pmatrix} \begin{pmatrix} \cos \alpha & \sin \alpha & 0 \\ -\sin \alpha & \cos \alpha & 0 \\ 0 & 0 & 1 \end{pmatrix} \\
 &= \begin{pmatrix} B_{11} & B_{12} & B_{13} \\ B_{21} & B_{22} & B_{23} \\ B_{31} & B_{32} & B_{33} \end{pmatrix} \quad (4-21)
 \end{aligned}$$

By expanding the above equation, the transformation matrix, \mathbf{B} can be written as:

$$B_{11} = \cos \gamma \cos \alpha - \sin \gamma \cos \beta \sin \alpha \quad (4-22a)$$

$$B_{12} = \cos \gamma \sin \alpha + \sin \gamma \cos \beta \cos \alpha \quad (4-22b)$$

$$B_{13} = \sin \gamma \sin \beta \quad (4-22c)$$

$$B_{21} = -\sin \gamma \cos \alpha - \cos \gamma \cos \beta \sin \alpha \quad (4-22d)$$

$$B_{22} = -\sin \gamma \sin \alpha + \cos \gamma \cos \beta \cos \alpha \quad (4-22e)$$

$$B_{23} = \cos \gamma \sin \beta \quad (4-22f)$$

$$B_{31} = \sin \beta \sin \alpha \quad (4-22g)$$

$$B_{32} = -\sin \beta \cos \alpha \quad (4-22h)$$

$$B_{33} = \cos \beta \quad (4-22i)$$

In addition, the following relationship can be obtained:

$$({}^c B^c) = ({}^c B^c)^{-1} = ({}^c B^c)^t \quad (4-23)$$

After the transformation matrix, \mathbf{B} , is obtained; the far-field pattern for each element can be calculated. Figure 4-7 shows two systems: an antenna coordinate system $\{\mathbf{c}\}$ and a feed coordinate system $\{\mathbf{c}'\}$. The radiated field of the feed is given as $\{\mathbf{c}'\}$ in spherical components. This technique provides a way of calculating the radiated field in the antenna coordinate system $\{\mathbf{c}\}$. The vector $\{\mathbf{c}\}$ and $\{\mathbf{c}'\}$ are related through a transformation matrix, \mathbf{B} . The feed coordinate system can be replaced with the inclined coordinate antenna system (local coordinate, x', y', z'), which is assumed in this program.

The computation is summarized in two steps:

- Determine the spherical coordinates of a point given on the antenna in terms of the local coordinate system $\{c'\}$.
- Derive the field expression of the radiated field of the feed in the antenna coordinate systems $\{c\}$. Therefore, the relationship of the far-field pattern of the dipole based on local coordinate $\{c'\}$ has been derived with respect to the global coordinate system $\{c\}$.

By referring to Figure 4-7, vectors \mathbf{r} and \mathbf{r}' are classified as the position vectors for point P on the antenna. Vector \mathbf{f} is used to locate the position of the feed in the antenna with respect to the global coordinate system $\{c\}$. Therefore, the relationship between vectors \mathbf{r} and \mathbf{f} is:

$$\mathbf{r}' = \mathbf{r} - \mathbf{f} \quad (4 - 24)$$

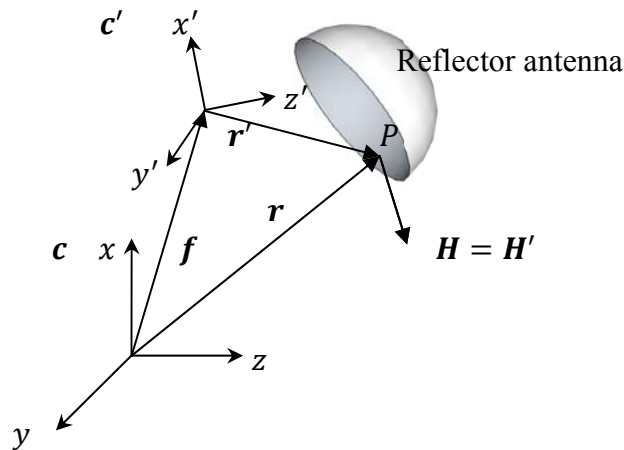


Figure 4-7: Feed and antenna coordinate systems [6].

For the first step, $\{r'^{c'}\}$, the Cartesian components of r' in $\{c\}$ are determined and then the transformation matrix is employed. From equation (4-24), the Cartesian component of r' in $\{c\}$ is written as:

$$r'^c = \{r'^c\} = \{r \sin \theta \cos \phi - f_1, r \sin \theta \sin \phi - f_2, r \cos \theta - f_3\}^t \quad (4 - 25)$$

Here, f_1, f_2 and f_3 are the Cartesian components of \mathbf{f} in $\{c\}$. By using the transformation matrix, A , the Cartesian components of \mathbf{r}' in $\{c'\}$ can be determined, namely

$$\mathbf{r}'^{c'} = \{r'^{c'}\} = ({}^c A^{c'}) \{r'^c\} \quad (4 - 26)$$

Since

$$r'^{c'} = \{r' \sin \theta' \cos \phi', r' \sin \theta' \sin \phi', r' \cos \theta'\}^t \quad (4-27)$$

Therefore, θ' and ϕ' (with respect to the local coordinate) can be easily determined from θ and ϕ (the global coordinate system) using equation (4-26).

For the second step, the spherical components of the radiated field of the feed at this point are calculated in the programme as $\{H^{s'}\}$ in $\{c'\}$. By using $\{H^{s'}\}$, the Cartesian components in $\{c'\}$ can be derived:

$$\{H^{c'}\} = ({}^{c'}T^{s'})\{H^{s'}\} \quad (4-28)$$

Then, the relationship of the Cartesian components of the global coordinate system, $\{H^c\}$, due to the spherical components of the local coordinate system, $\{H^{s'}\}$, are as follows:

$$\{H^c\} = ({}^cA^{c'})\{H^{c'}\} = ({}^cA^{c'})({}^{c'}T^{s'})\{H^{s'}\} \quad (4-29)$$

where $\{H^{c'}\}$ is from equation (4-28).

Using the equation (4-29), the spherical vector of the global coordinate systems, \mathbf{H} , can be derived as:

$$\{H^s\} = ({}^sT^c)\{H^c\} = ({}^sT^c)({}^cA^{c'})({}^{c'}T^{s'})\{H^{s'}\} \quad (4-30)$$

All the previous equations can be summarized as follows:

$$\begin{pmatrix} r' \sin \theta' \cos \phi' \\ r' \sin \theta' \sin \phi' \\ r' \cos \theta' \end{pmatrix} = \begin{pmatrix} A_{11} & A_{12} & A_{13} \\ A_{21} & A_{22} & A_{23} \\ A_{31} & A_{32} & A_{33} \end{pmatrix} \begin{pmatrix} r \sin \theta \cos \phi - f_1 \\ r \sin \theta \sin \phi - f_2 \\ r \cos \theta - f_3 \end{pmatrix} \quad (4-31)$$

From θ and ϕ , the spherical components of \mathbf{H} in $\{\hat{c}\}$ are determined as:

$$\begin{pmatrix} H_r(r, \theta, \phi) \\ H_\theta(r, \theta, \phi) \\ H_\phi(r, \theta, \phi) \end{pmatrix} = \begin{pmatrix} \sin \theta \cos \phi & \sin \theta \sin \phi & \cos \theta \\ \cos \theta \cos \phi & \cos \theta \sin \phi & -\sin \theta \\ -\sin \phi & \cos \phi & 0 \end{pmatrix} \begin{pmatrix} A_{11} & A_{21} & A_{31} \\ A_{12} & A_{22} & A_{32} \\ A_{13} & A_{23} & A_{33} \end{pmatrix} \times \begin{pmatrix} \sin \theta' \cos \phi' & \cos \theta' \cos \phi' & -\sin \phi' \\ \sin \theta' \sin \phi' & \cos \theta' \sin \phi' & \cos \phi' \\ \cos \theta' & -\sin \theta' & 0 \end{pmatrix} \begin{pmatrix} H'_{r'}(r', \theta', \phi') \\ H'_{\theta'}(r', \theta', \phi') \\ H'_{\phi'}(r', \theta', \phi') \end{pmatrix} \quad (4-32)$$

Rahmat-Samii [7] used the above technique on a reflector antenna illuminated by an array of feed horns, where the radiated field of each horn was in its own coordinates and did not coincide with reflector coordinates. However, it may also be applied for the case where the far-field pattern coordinates $(x', y'$,

z') do not coincide with the antenna coordinates (x, y, z) [17, 18]. As a result, the far-field pattern of the dipoles in a global coordinate system can be calculated using the far-field pattern of dipoles due to local coordinate systems. This proves to be useful, especially when the position of the element or dipole in this case, is in inclined configuration such as in a spherical antenna array. The 3-D algorithm code is attached in appendix A and B.

Therefore, the total radiation pattern for N elements is calculated as:

$$\begin{pmatrix} H_r(r, \theta, \phi) \\ H_\theta(r, \theta, \phi) \\ H_\phi(r, \theta, \phi) \end{pmatrix} = \sum_{n=1}^N \left([{}^sT^c] \times [B] \times [{}^cT^{s'}] \times \begin{pmatrix} H'_{r'_n}(r', \theta', \phi') \\ H'_{\theta'_n}(r', \theta', \phi') \\ H'_{\phi'_n}(r', \theta', \phi') \end{pmatrix} \right), \quad (4-33)$$

where

$$({}^sT^c) = \begin{pmatrix} \sin \theta \cos \phi & \sin \theta \sin \phi & \cos \theta \\ \cos \theta \cos \phi & \cos \theta \sin \phi & -\sin \theta \\ -\sin \phi & \cos \phi & 0 \end{pmatrix}, \quad (4-33a)$$

$$B = \begin{pmatrix} B_{11} & B_{12} & B_{13} \\ B_{21} & B_{22} & B_{23} \\ B_{31} & B_{32} & B_{33} \end{pmatrix}, \quad (4-33b)$$

$$({}^cT^{s'}) = \begin{pmatrix} \sin \theta' \cos \phi' & \cos \theta' \cos \phi' & -\sin \phi' \\ \sin \theta' \sin \phi' & \cos \theta' \sin \phi' & \cos \phi' \\ \cos \theta' & -\sin \theta' & 0 \end{pmatrix}, \quad (4-33c)$$

and the far-field radiation pattern for each element assuming the dipole along z -axis,

$$H'_{\theta'_n}(\theta, \phi) \approx \frac{j \eta I_0 e^{-jkr}}{2\pi r} \cdot \frac{\cos(\frac{\pi}{2} \cos \theta)}{\sin \theta}, \quad n = 1, 2, \dots, N \quad (4-34)$$

and $H'_{r'_n}$ is zero in the far-field range and $H'_{\phi'_n}$ is zero due to the dipole position along z -axis.

4.3 Pattern Multiplication Method (without mutual coupling)

A programme of mathematical analysis using the Circular Array Method (Equation 3-36) has been written as a comparison with the 3-D algorithm. Four half-wavelength dipoles arranged in a circular array with radius b , 0.057 m

(approximately 0.08m spacing between two dipoles) as shown in Figure 4-8 is in a similar configuration as the four dipole array in the 3-D algorithm.

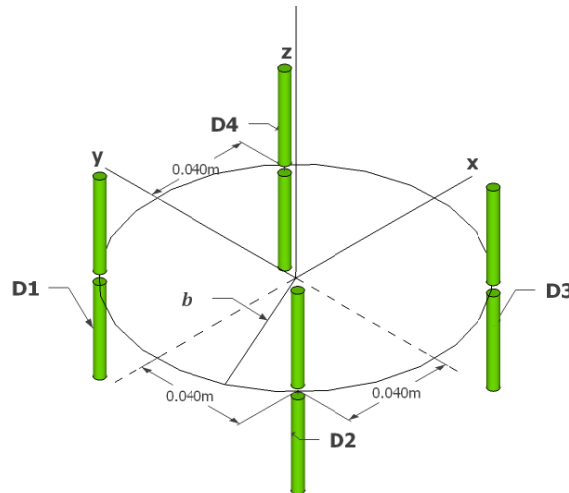


Figure 4-8: 2x2 Dipoles arranged in circular configuration.

4.4 Numerical Modelling using MoM and FDTD

4.4.1 MoM

Two designs have been simulated using method of moments [4]. The 4NEC2++ software [23] is chosen because it is suitable for thin wires. Two examples for an array of four and 12 dipoles are designed at 2.45 GHz. First, four dipoles are arranged as a rectangular array with its axis parallel to the z-axis. The spacing between them is $0.65\lambda_0$, as shown in Figure 4-9(a). The excitation source for each element is a current source. Then, an array of 12 dipoles is designed at the edge of the cube of size $(0.65\lambda_0)^3$ (Figure 4-9(b)).

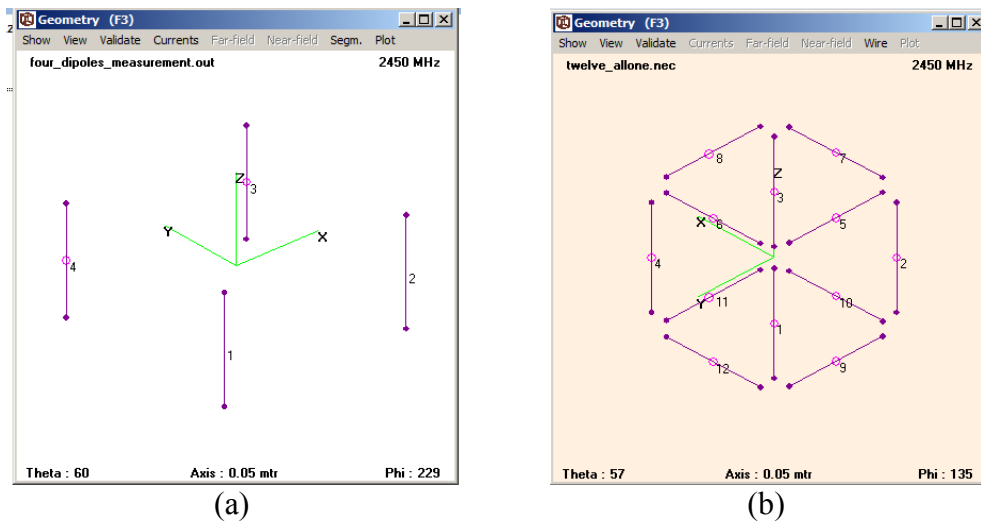


Figure 4-9: Arrays of (a) four and (b) twelve dipoles at 2.45 GHz from 4NEC2++ [22].

4.4.2 FDTD

The previous designs were also simulated using FDTD [5] method via Empire XCcel [24]. Four dipoles are arranged as a rectangular array with its axis parallel to the z-axis (Figure 4-10(a)). The array is fed using four perpendicular lumped ports. Another simulation using 12 dipoles arranged at the edge of a cube has been designed, as shown in Figure 4-10(b). The labelling for dipoles in Figure 4-10 is similar to Figure 4-9.

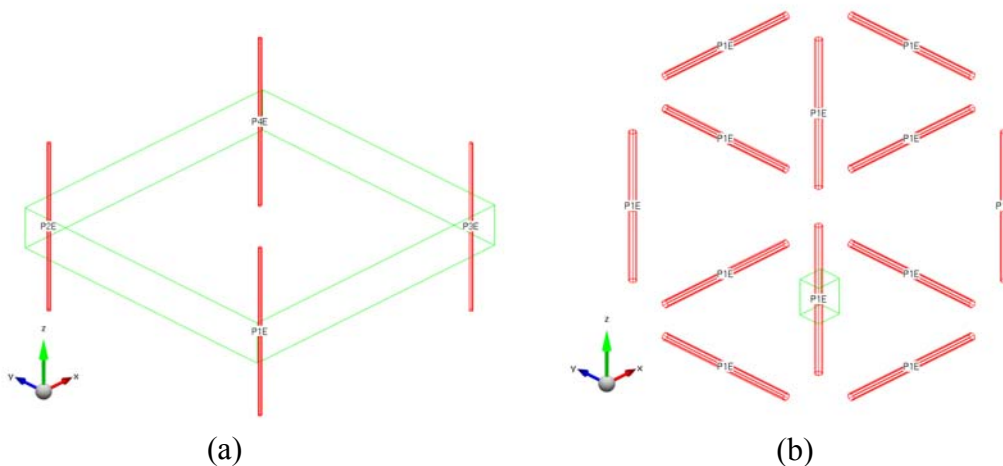


Figure 4-10: Arrays of (a) four and (b) twelve dipoles at 2.45 GHz from Empire XCcel [23].

4.5 Results of the 3-D algorithm.

4.5.1 Mutual impedance

Baker and LaGrone [6] calculated the value of mutual impedance between two dipoles for various configurations using the Induced EMF Method. This thesis has extended [6] in order to include the y -axis for three dimensions for ease of implementation. The results of the real and imaginary mutual impedance between two dipoles for various cases are plotted in Figs. 4-11 to 4-19. The graphs are in similar agreement with [6] and [9]. Baker and LaGrone [6] have made a comparison of their work, [6] with King, [9] and they are in good agreement. The mutual impedance calculated using equation (2-46) and (2-47) is only an extension in y direction so that the mutual impedance between two dipoles can be calculated in three dimensions (x, y, z -axis) instead only in two dimensions (y, z -axis) as in [6]. Equation 2-46 and 2-47 has been used to facilitate the calculation of mutual impedance for cubic dipole in three dimensions. Due to that reason, both methods (equation 2-46 and 2-47) and work in [6] should be in similar agreement and has been proven in Figs. 4-11 to 4-16. However, in Figures 4-17 to 4-19, there are slight discrepancies when theta is varied from 0° to 20° between plots of the imaginary impedance of equation (2-47) and results from Baker. The reason is probably due to the far-field equation which is used to derive the mutual impedance within small range of angle variation and infinitely small spacing, thus resulting inaccuracies to the imaginary impedance. The equations (2-46) and (2-47) are based on Schelkunoff's electric field intensity [25] due to the sinusoidal current distribution in the first antenna.

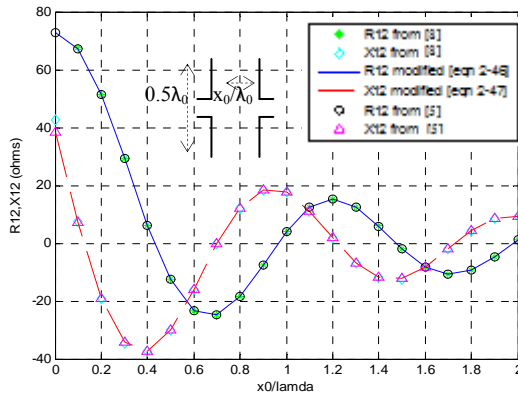


Figure 4-11: Mutual impedance vs spacing (x -axis) for two parallel half-wavelength antennas, non-staggered.

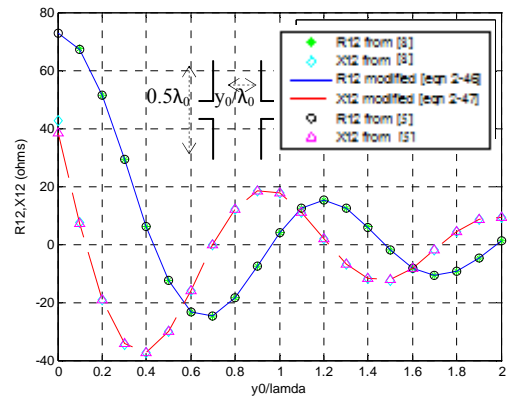


Figure 4-12: Mutual impedance vs spacing (y -axis) for two parallel half-wavelength antennas, non-staggered.

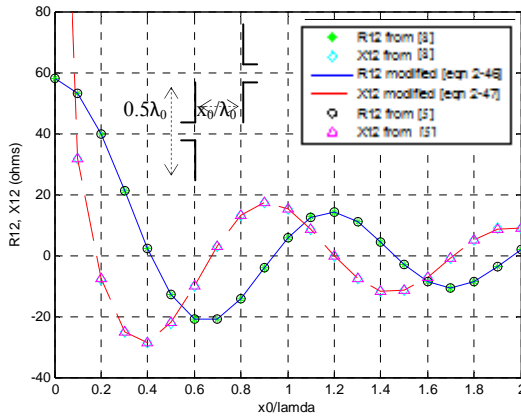


Figure 4-13: Mutual impedance vs spacing (x -axis) for two parallel half-wavelength antennas in echelon, staggered by $0.25\lambda_0$.

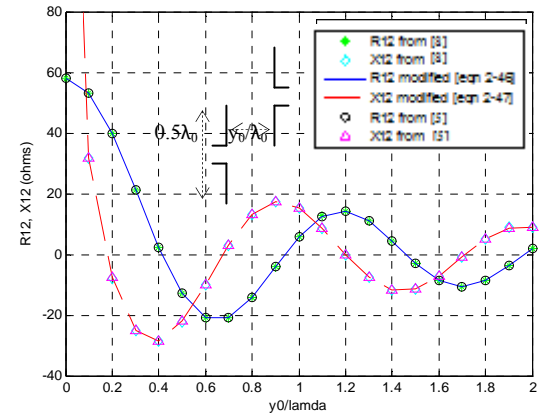


Figure 4-14: Mutual impedance vs spacing (y -axis) for two parallel half-wavelength antennas in echelon, staggered by $0.25\lambda_0$.

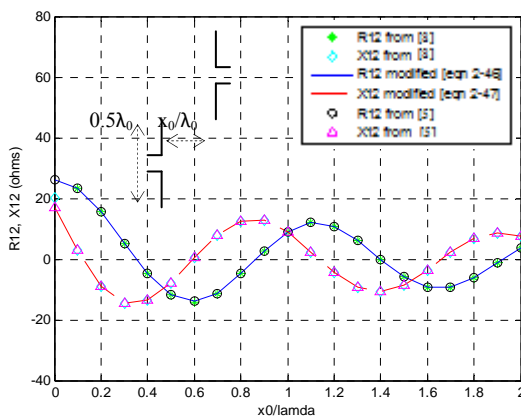


Figure 4-15: Mutual impedance vs spacing (x -axis) for two half-wavelength antennas in echelon, staggered by $0.5\lambda_0$.

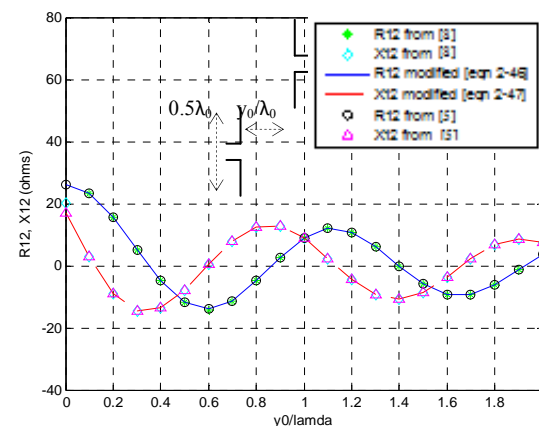


Figure 4-16: Mutual impedance vs spacing (y -axis) for two half-wavelength antennas in echelon, staggered by $0.5\lambda_0$.

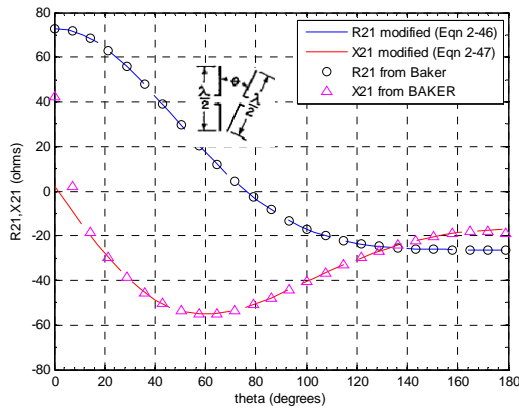


Figure 4-17: Mutual impedance vs interior angle for two half-wavelength antennas in a V configuration (along x -axis)

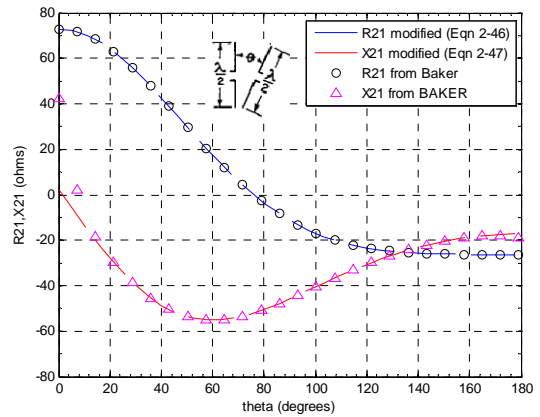


Figure 4-18: Mutual impedance vs interior angle for two half-wavelength antennas in a V configuration along y -axis.

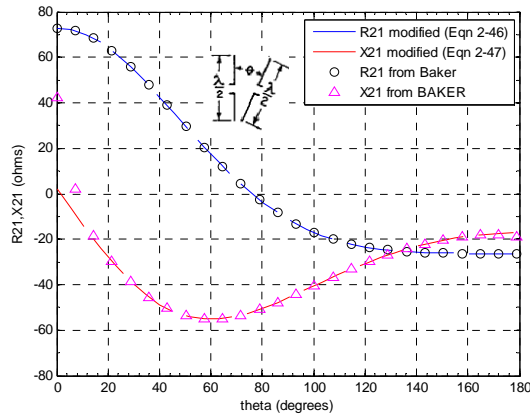


Figure 4-19: Mutual impedance vs interior angle for two half-wavelength antennas in a V configuration (at $\phi = 45^\circ$).

4.5.2 Impedance matrix, Z for four parallel dipoles

The impedance matrix, $[Z]$ has been calculated using equations (2-46) and (2-47) by taking into account mutual coupling effect for an array of four parallel dipoles with a spacing of $0.65\lambda_0$ at 2.45 GHz is shown in Table 4. The self impedance, Z_{mm} of each dipole is $73.1 + 42.5i$ while the mutual impedance between dipoles m and n , Z_{mn} depends on the spacing and angle of orientation between them. The same spacing and parallel configuration of four dipoles resulting similar values of Z_{mn} in the impedance matrix $[Z]$.

Table 4: The impedance matrix, $[Z]$, for four parallel dipoles

Index No	1	2	3	4
1	$73.1 + 42.5i$	$-25.2 - 7.41i$	$-4.62 + 18.93i$	$-25.2 - 7.41i$
2	$-25.2 - 7.41i$	$73.1 + 42.5i$	$-25.2 - 7.41i$	$-4.62 + 18.93i$
3	$-4.62 + 18.93i$	$-25.2 - 7.41i$	$73.1 + 42.5i$	$-25.2 - 7.41i$
4	$-25.2 - 7.41i$	$-4.62 + 18.93i$	$-25.2 - 7.41i$	$73.1 + 42.5i$

4.5.3 Impedance matrix for twelve dipoles in various configurations

The impedance matrix, $[Z]$, has been calculated using equations (2-46) and (2-47) for twelve dipoles (Fig.4-9(b)) is shown in Table 5.

Section 4.5. Results of the 3-D algorithm

Table 5: The impedance matrix, $[Z]$, for 12 dipoles

Index No	1	2	3	4	5	6	7	8	9	10	11	12
1	73.1 + 42.5i	-25.2- 7.41i	-4.62+ 18.93i	-25.2- 7.41i	14.44 + 17.46i	14.44 + 17.46i	1.72- 3.09i	1.72 - 3.09i	-14.44 - 17.46i	-1.72 + 3.09i	-1.72 + 3.09i	-14.44- 17.46i
2	-25.2- 7.41i	73.1+ 42.5i	-25.2- 7.41i	-4.62 + 18.93i	-14.42- 17.55i	1.72 - 3.09i	14.44 + 17.46i	-1.72+ 3.08i	14.43+ 17.55i	-14.44 - 17.46i	1.72 - 3.08i	-1.72 + 3.09i
3	-4.62 + 18.93i	-25.2 - 7.41i	73.1+42.5i	-25.2 - 7.41i	-1.72 + 3.08i	-1.72 + 3.08i	-14.42 - 17.55i	-14.42 - 17.55i	1.72- 3.08i	14.42+ 17.55i	14.42 + 17.55i	1.72 - 3.08i
4	-25.2 - 7.41i	-4.62 + 18.93i	-25.2 - 7.41i	73.1 + 42.5i	1.72 - 3.09i	-14.42 - 17.55i	-1.72+ 3.08i	14.44 + 17.46i	-1.72+ 3.09i	1.72- 3.08i	-14.44- 17.46i	14.43 + 17.55i
5	14.44+ 17.46i	-14.43 - 17.55i	-1.72 + 3.08i	1.72- 3.09i	73.1 + 42.5i	-14.46- 17.55i	14.44 + 17.46i	-25.2- 7.41i	-25.2 - 7.41i	4.18 - 5.51i	-4.62+ 18.93i	-1.72 + 3.09i
6	14.44 + 17.46i	1.72- 3.09i	-1.72+ 3.08i	-14.43- 17.55i	-14.43 - 17.55i	73.1+ 42.5i	-25.2 - 7.41i	14.44 + 17.46i	-4.18 + 5.51i	-4.62 + 18.93i	-4.18 + 5.51i	-25.2 7.41i
7	1.72 - 3.09i	14.44 + 17.46i	-14.43- 17.55i	-1.72 + 3.08i	14.44+ 17.46i	-25.2- 7.41i	73.1 + 42.5i	-14.42 - 17.55i	4.21- 5.5i	-25.2 - 7.41i	4.21 - 5.5i	-4.62+ 18.93i
8	1.72- 3.09i	-1.72 + 3.08i	-14.43 - 17.55i	14.44 + 17.46i	-25.2 - 7.41i	14.44 + 17.46i	-14.43 - 17.55i	73.1 + 42.5i	-4.62 + 18.93i	-4.18 + 5.51i	-25.2 - 7.41i	1.72- 3.08i
9	-14.44- 17.46i	14.43 + 17.55i	1.72 - 3.08i	-1.72+ 3.09i	-25.2 - 7.41i	-4.18 + 5.51i	4.21- 5.5i	-4.62 + 18.93i	73.1+ 42.5i	14.44+ 17.46i	-25.2- 7.41i	-14.43- 17.55i
10	-1.72 + 3.09i	-14.44- 17.46i	14.43 + 17.55i	1.72- 3.08i	4.18 - 5.51i	-4.62 + 18.93i	-25.2 - 7.41i	-4.18 + 5.51i	14.44 + 17.46i	73.1+ 42.5i	-14.43 - 17.55i	-25.2 - 7.41i
11	-1.72 + 3.09i	1.72 - 3.08i	14.43 + 17.55i	-14.44- 17.46i	-4.62 + 18.93i	-4.18+ 5.51i	4.21- 5.5i	-25.2 - 7.41i	-25.2- 7.41i	-14.43- 17.55i	73.1+ 42.5i	14.43+ 17.55i
12	-14.4- 17.46i	-1.72+ 3.09i	1.72 - 3.08i	14.4+ 17.55i	-1.72+ 3.09i	-25.2- 7.41i	-4.62+ 18.93i	1.72 - 3.08i	-14.43- 17.55i	-25.2- 7.41i	14.43+ 17.55i	73.1+ 42.5i

4.5.4 3-D Far-Field Patterns

The 3-D far-field pattern for an array of half-wavelength dipoles is calculated using the 3-D algorithm. Two types of array were tested using this algorithm: 1) four half-wavelength parallel dipoles and 2) twelve half-wavelength dipoles arranged in various configurations. The results are discussed in this section.

4.5.4.1 Four Parallel Dipoles

In this case, an array of four half-wavelength parallel dipoles with a spacing of $0.65\lambda_0$ at 2.45 GHz was chosen and the results are discussed in the next section. The axis of the dipoles is parallel with the z-axis. A diagram of the four dipoles is shown in Figure 4-20. The excitation value (i.e. $1; 0; 0; 0$) can be represented by dipole 1, dipole 2, dipole 3 and dipole 4. A comparison was performed between the Induced EMF Method (3-D algorithm), FDTD, MoM and pattern multiplication method (without coupling) on the far-field pattern. Different excitation was employed to each element of the array to observe the difference between those methods and the behaviour of mutual coupling.

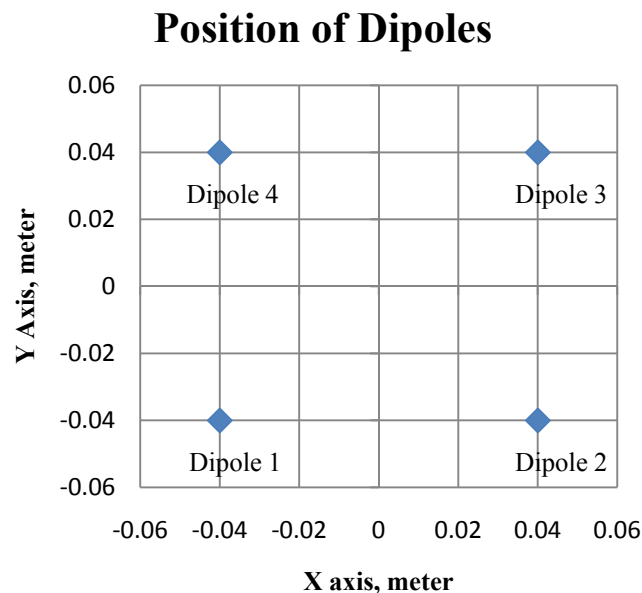


Figure 4-20: Diagram showing the position of each dipole on the xy plane.

4.5.4.1.1 Uniform excitation values

The far-field patterns for four dipoles with an identical excitation amplitude (1V) and 0° phase angle are shown in Figs. 4-21 to 4-25 below. They may be viewed in planar cut (2-D) and 3-D [26].

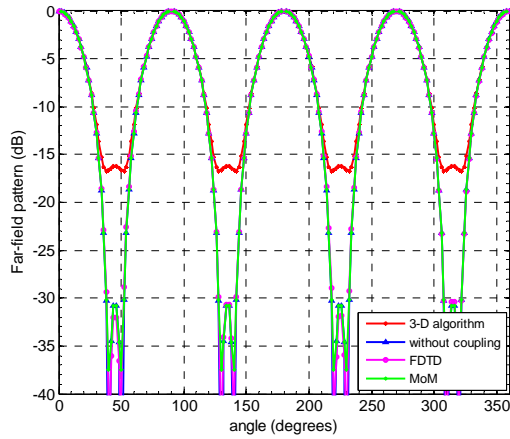


Figure 4-21: 2-D azimuth far-field pattern at $\theta=90^\circ$.

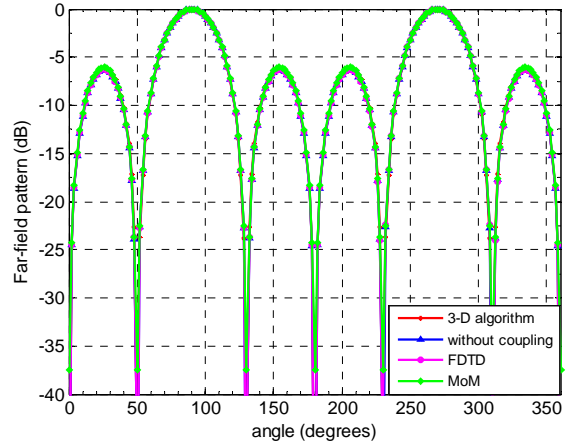


Figure 4-22: 2-D elevation far-field pattern at $\phi=0^\circ$.

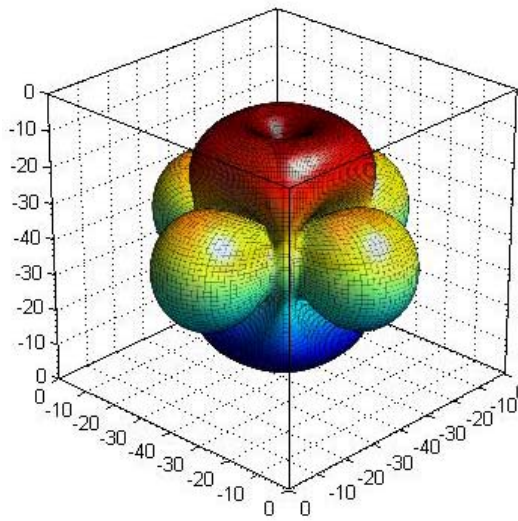


Figure 4-23: 3-D far-field pattern calculated via Induced EMF Method from this thesis (3-D algorithm).

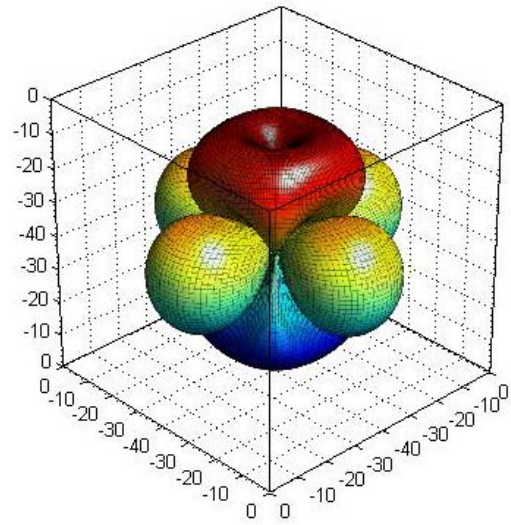


Figure 4-24: 3-D far-field pattern of a circular array calculated using pattern multiplication method.

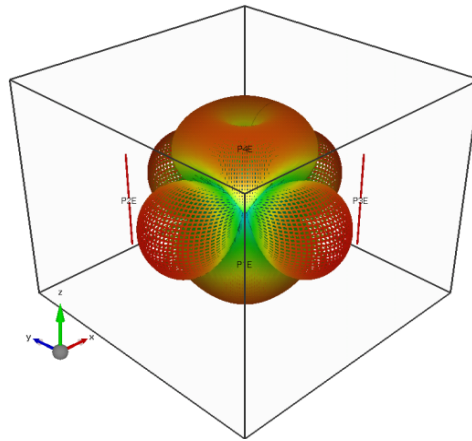


Figure 4-25: The 3-D far-field pattern from Empire XCcel.

It was observed that when all the excitation values are similar, the patterns produced from 3-D algorithm is in similar agreement with other methods except that in Figure 4-21, it generates higher side lobes compared to nulls at azimuth pattern ($\theta=90^\circ$). It is because of the existence of the mutual coupling effect between parallel elements spaced $0.65\lambda_0$ between each other. The effect of coupling between elements increases the side lobe levels in comparison between other methods. Due to this reason, it can be concluded that the coupling effect between elements should not be ignored especially in pattern synthesis and direction finding application because it will resulting inaccuracies to the optimization process. Table 6 summarized the far field pattern comparison in Figures 4-21 and 4-22 between 3-D algorithm, pattern multiplication method, FDTD and MoM.

Table 6: Comparison on the far field pattern.

	$\theta = 90^\circ$ (Azimuth plane)			$\phi = 0^\circ$ (Elevation plane)		
	Pointing beam	Highest side lobe levels, dB	HPBW	Pointing beam	Highest side lobe levels, dB	HPBW
3-D algorithm	$0^\circ, 90^\circ, 180^\circ, 270^\circ$	-16	30°	$90^\circ, -90^\circ$	-6.5	40°
Pattern multiplication	$0^\circ, 90^\circ, 180^\circ, 270^\circ$	-31	30°	$90^\circ, -90^\circ$	-6.5	40°
FDTD	$0^\circ, 90^\circ, 180^\circ, 270^\circ$	-31	30°	$90^\circ, -90^\circ$	-6.5	40°
MoM	$0^\circ, 90^\circ, 180^\circ, 270^\circ$	-31	30°	$90^\circ, -90^\circ$	-6	40°

4.5.4.1.2 Uniform amplitude with different phase.

The far-field patterns for four dipoles with an identical excitation amplitude (0.5V) and different phase shift are shown in Table 7 below. The phase shift is calculated using equation (3-36) to direct the peak of the main beam in the $\theta_0=90^\circ$, $\varphi_0=100^\circ$ direction.

Table 7: Excitation values with uniform amplitude and different phases

Element Index	Amplitude	Phase (degrees)
Dipole 1	0.5	95.4°
Dipole 2	0.5	136.2°
Dipole 3	0.5	-95.4°
Dipole 4	0.5	-136.2°

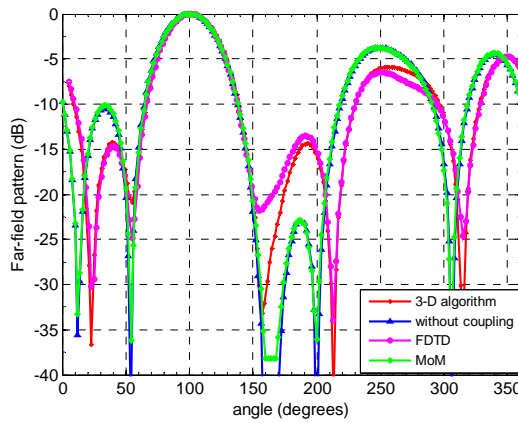


Figure 4-26: Far-field pattern at $\theta=90^\circ$

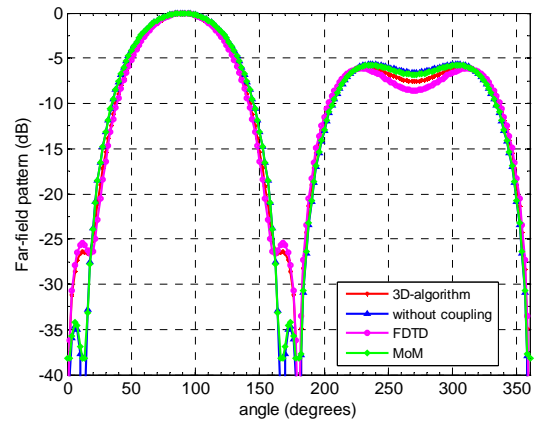


Figure 4-27: Far-field pattern at $\phi=100^\circ$

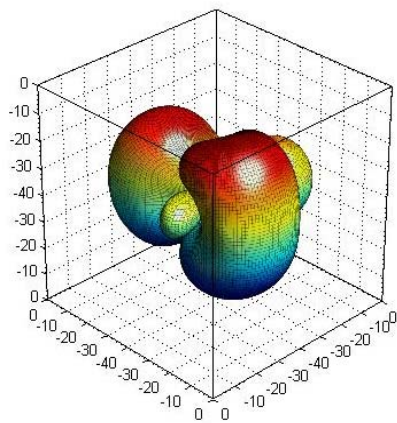


Figure 4-28: 3-D far-field pattern calculated via Induced EMF Method from this thesis (eqn 4-46).

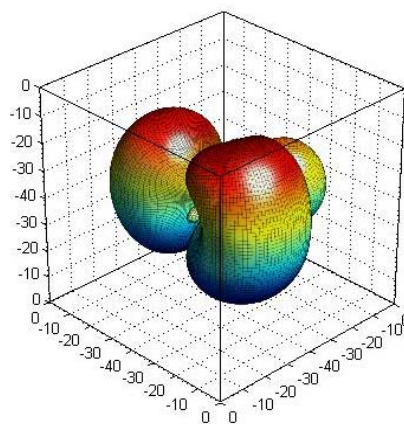


Figure 4-29: 3-D far-field pattern of a circular array calculated using pattern multiplication method (eqn 3-36).

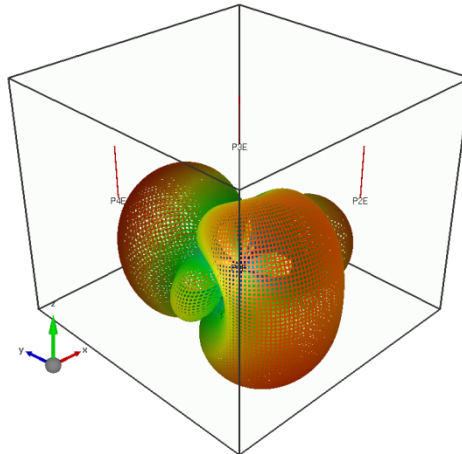


Figure 4-30: The 3-D far-field pattern from simulation (Empire XCcel).

It was observed that the results using the 3-D algorithm are in good agreement, especially with full wave technique; FDTD. By taking into account mutual coupling via the Induced EMF Method, the far-field pattern is better pronounced than conventional pattern multiplication, especially in the side lobes and the null region. Moreover, the side lobes at 190° are better pronounced using the 3-D algorithm and FDTD (Figure 4-26) compared to MoM and the pattern multiplication method. Furthermore, it is noted that the highest side lobe level obtained from MoM and pattern multiplication occurred at 240° while from 3-D algorithm and FDTD occurred at 350° . Therefore, it can be concluded that the coupling effect from the 3-D algorithm affecting the side-lobe levels in the far-field pattern of antenna array. The discrepancies on the far-field pattern between FDTD and MoM are probably because of parameters differences of both methods. Table 8 summarized the far field pattern comparison Figures 4-26 and 4-27 between 3-D algorithm, pattern multiplication method, FDTD and MoM. The results show that they are in close approximations with each other.

Table 8: Comparison on the far field pattern.

	$\theta = 90^\circ$ (Azimuth plane)			$\phi = 100^\circ$ (Elevation plane)		
	Pointing beam	Highest side lobe levels, dB	HPBW	Pointing beam	Highest side lobe levels, dB	HPBW
3-D algorithm	100°	-4.8	45°	90°	-6	60°
Pattern multiplication	100°	-3.5	45°	90°	-5.5	60°
FDTD	100°	-4.8	45°	90°	-6	60°
MoM	100°	-3.5	47°	90°	-5.5	65°

4.5.4.1.3 Different amplitude and phase

The far-field patterns for four dipoles with different excitation (amplitude and phase) are shown in Table 9 below. The phase is chosen so that the main beam is pointed at $\phi=284^\circ$. The difference between red straight line and black dashed line of the Induced EMF method (in Figure 4-31) is that the former using the amplitude given in Table 6 while the latter use a constant amplitude of 0.5 V. Varying the amplitude excitation for each element will change the side-lobe levels of the far-field pattern as shown in Figures 4-31 and 4-32. However, the direction of steering angle remains similar because the phase excitation for each element unchanged either by applying constant amplitude or varying amplitude excitation as in Table 9.

Figure 4-31 shows that the pattern computed from 3-D algorithm agrees with FDTD and MoM. However, it disagrees with pattern multiplication method because of the coupling effect. The position and number of side-lobes and nulls of pattern multiplication differs considerably with other methods. On the other hand, Figure 4-32 shows a small difference between patterns due to the parallel arrangement of the dipoles in x - y plane which increase the coupling considerably in azimuth plane but very small or none at all in elevation plane. Table 10 summarized the far field pattern comparison Figures 4-31 and 4-32 between 3-D algorithm, pattern multiplication method, FDTD and MoM. The result shows that 3-D algorithm, FDTD and MoM are in close approximations with each other except pattern multiplication which differs in azimuth pattern.

Table 9: Excitation values with different amplitude and phases

Element Index	Amplitude rms,	Phase (degrees)
Dipole 1	0.5607	-164.5°
Dipole 2	0.4157	129.2°
Dipole 3	0.0824	45.9°
Dipole 4	0.3294	50.1°

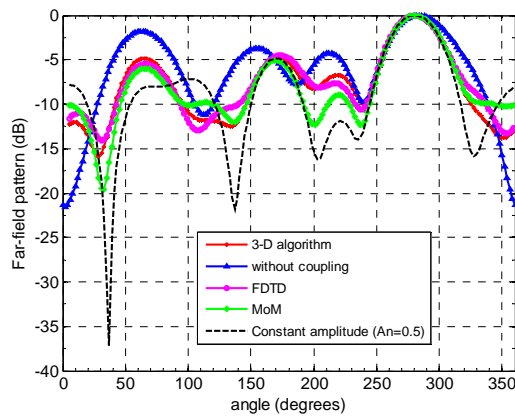


Figure 4-31: Far-field pattern at $\theta=90^\circ$.

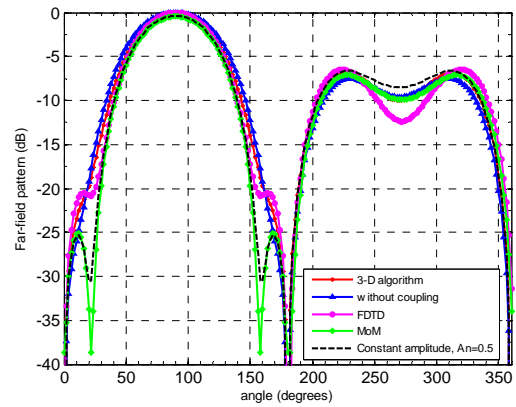


Figure 4-32: Far-field pattern at $\phi=284^\circ$.

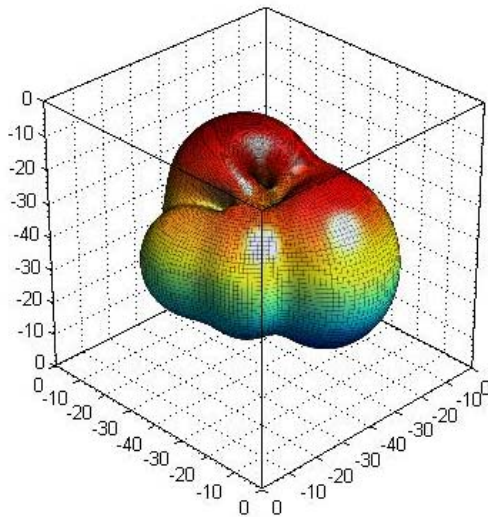


Figure 4-33: 3-D far-field pattern calculated via Induced EMF Method from this thesis (eqn 4-46).

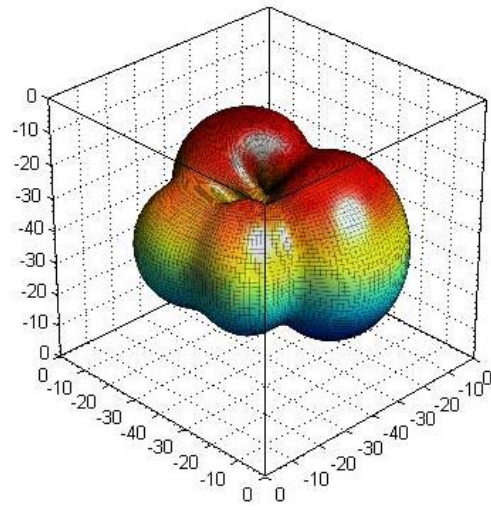


Figure 4-34: 3-D far-field pattern of a circular array calculated using pattern multiplication method (eqn 3-36).

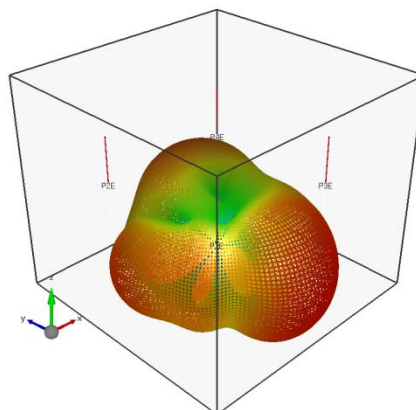


Figure 4-35: 3-D Far-field pattern from Empire XCcel

Table 10: Comparison on the far field pattern.

	$\theta = 90^\circ$ (Azimuth plane)			$\phi = 284^\circ$ (Elevation plane)		
	Pointing beam	Highest side lobe levels, dB	HPBW	Pointing beam	Highest side lobe levels, dB	HPBW
3-D algorithm	280°	-4.5	32.5°	90°	-7.25	62.5°
Pattern multiplication	280°	-2.5	37.5°	90°	-7.5	65°
FDTD	280°	-4.5	32.5°	90°	-7	62.5°
MoM	280°	-4.8	32.5°	90°	-7.25	60°

4.5.4.2 Twelve Dipoles in Various Configurations

The 3-D far-field was computed using the 3-D algorithm for an array of 12 dipoles arranged at the edge of a cube structure (Figure 4-9(b)). The size of the cube is $(0.65\lambda_0 \text{ m})^3$. The excitation value (i.e. 1; 1; 0; 0; 0; 0; 0; 0; 0; 0; 0; 0) can be represented by dipole 1, dipole 2, dipole 3, dipole 4, dipole 5, dipole 6, dipole 7, dipole 8, dipole 9, dipole 10, dipole 11 and dipole 12. The idea is that the 3-D algorithm can be applied to dipoles in any configuration by considering the effect of mutual coupling.

4.5.4.2.1 Uniform Excitation Values

The far-field patterns for 12 dipoles with uniform excitation (1V for amplitudes and zero phases) are shown in Figs. 4-36 to 4-40. By applying uniform excitation for each element, the direction of steering angle is pointing towards $\theta=84^\circ$ and $\phi=6^\circ$.

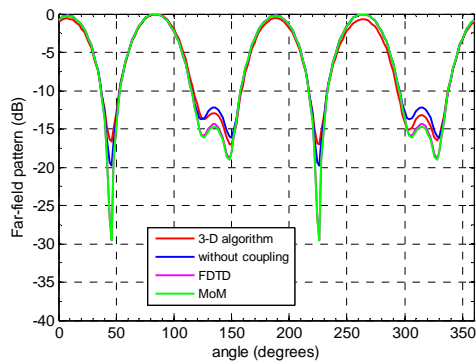


Figure 4-36: Far-field pattern at $\theta=84^\circ$

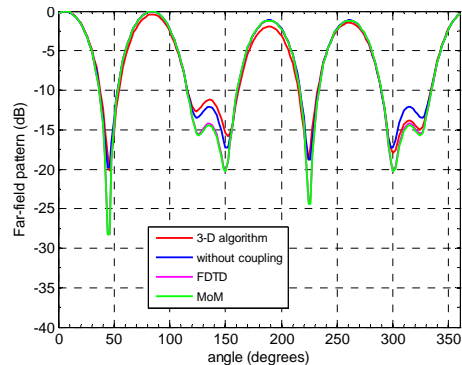


Figure 4-37: Far-field pattern at $\phi=6^\circ$

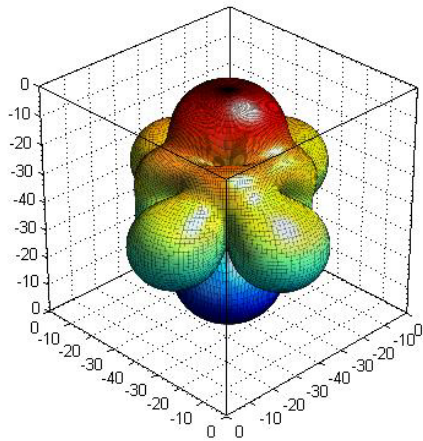


Figure 4-38: 3-D far-field pattern calculated via Induced EMF Method from this thesis (eqn 4-46).

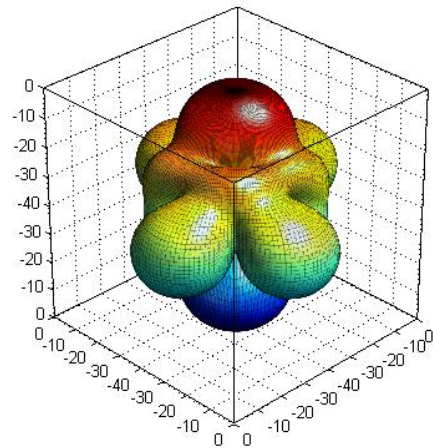


Figure 4-39: 3-D far-field pattern calculated using pattern multiplication method (eqn 3-36).

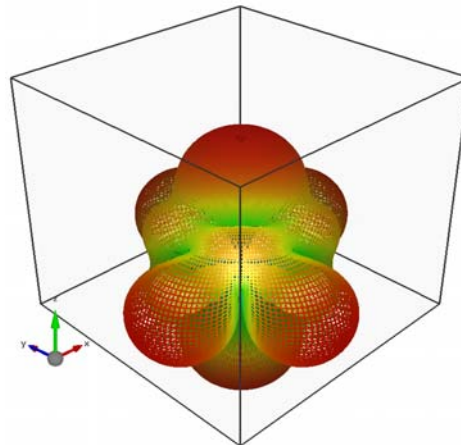


Figure 4-40: 3D far-field pattern from Empire XCcel

It was observed that in this case, the pattern produced from the 3-D algorithm is in similar agreement with other methods. This is maybe due to the uniform spacing and the excitation values for each element, therefore, no significant changes of mutual coupling may be observed in this example. One of changes could be observed from Table 11 with the number of beam steering where the 3-D algorithm only has one maximum beam pointing in the direction of 84° at $\theta=84^\circ$ comparing with other methods that have four steering angles.

Table 11: Comparison on the far field pattern.

	$\theta = 84^\circ$ (Azimuth plane)			$\phi = 6^\circ$ (Elevation plane)		
	Pointing beam	Highest side lobe levels, dB	HPBW	Pointing beam	Highest side lobe levels, dB	HPBW
3-D algorithm	84°	-1	35°	6°, 86°	-2	30°
Pattern multiplication	6°, 84°, 186°, 264°	-12	35°	6°, 86°	-1.5	30°
FDTD	6°, 84°, 186°, 264°	-14.5	35°	6°, 86°	-1.5	30°
MoM	6°, 84°, 186°, 264°	-14.5	35°	6°, 86°	-1.5	30°

4.5.4.2.2 Different amplitude and phases for excited coefficients

The excitation values with the same amplitude and different phases are shown in Table 12, and the far-field patterns are shown in Figs. 4-41 to 4-45. They are similar to those in Section 4.5.4.1.2 but with additional four short-circuited dipoles arranged at the top and bottom of 2x2 dipole array. Therefore, the far-field patterns in Fig. 4-42 are slightly different to the Fig. 4-27 due to the effect of the parasitic elements on top and bottom (vertical plane) of 2x2 dipole array. Figures 4-41 and 4-26 are similar because no additional dipoles or changes existed between them in horizontal plane. However, Figure 4-42 shows the discrepancies existed between the 3-D algorithm, the FDTD, the MoM and pattern multiplication (no coupling) method. The largest difference of 6 dB is occurred especially at side-lobe levels. Overall, a good agreement was achieved between those methods especially in the main beam region.

The discrepancies between the 3-D algorithm and full wave modelling (FDTD and MoM) might be due to the thickness and the feed gap of the dipole in the Induced EMF method. The mutual impedance calculated using the Induced EMF method assumes that the dipole is infinitely thin. It also assumes infinitesimal feed gap between each arm of the dipole. The effect of mutual coupling using Induced EMF Method only bring changes on the terminal current values, not on the element current distribution itself (i.e. the shape of the current). It assumes the current distribution is in sinusoidal form and its phase is

constant. Therefore, it only provides an approximation for mutual coupling between elements. Table 13 summarizes the differences between those methods. Figure 4-41 and 4-42 shows that the far-field pattern from 3-D algorithm is not in good agreement with other methods compared to previous examples. However, the steering angle, the beam width and the highest side lobe level from the 3-D algorithm as mentioned in Table 13 is approximately close with the other methods.

Table 12: Excitation values with the same amplitude but different phases

Element index	Amplitude	Phase (degrees)
1	0.5	95.4°
2	0.5	136.2°
3	0.5	-95.4°
4	0.5	-136.2°
5	0	0
6	0	0
7	0	0
8	0	0
9	0	0
10	0	0
11	0	0
12	0	0

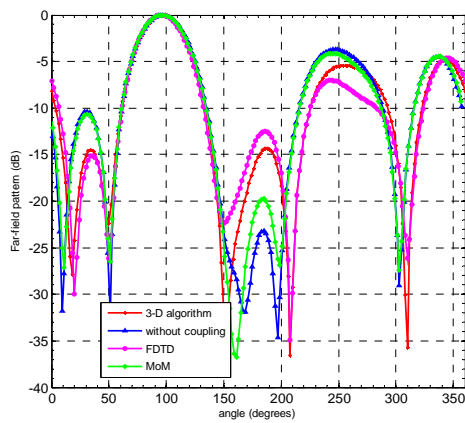


Figure 4-41: Far-field pattern at $\theta=90^\circ$

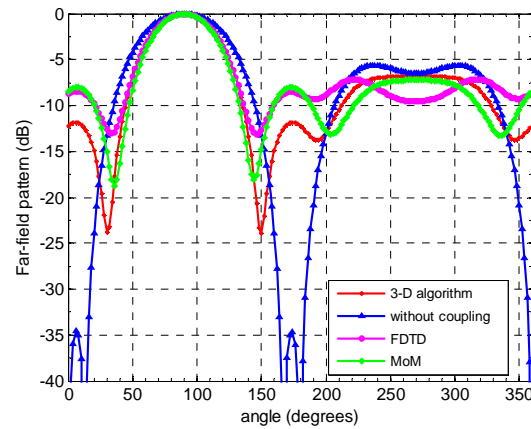


Figure 4-42: Far-field pattern at $\phi=100^\circ$

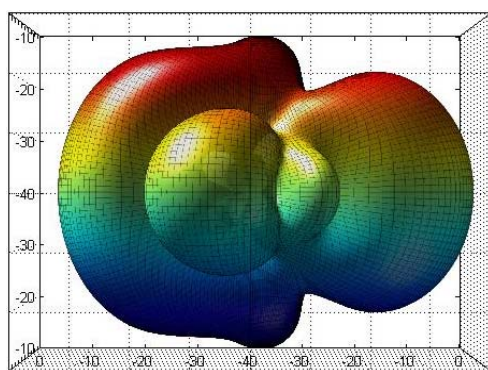


Figure 4-43: 3-D far-field pattern calculated via Induced EMF Method from this thesis (eqn 4-46).

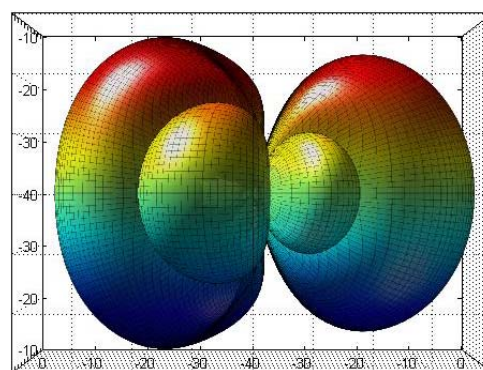


Figure 4-44: 3-D far-field pattern calculated using pattern multiplication method (view from yz axis)

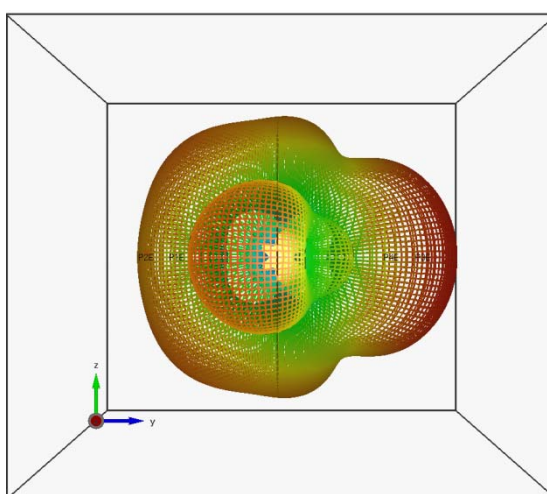


Figure 4-45: 3-D far-field pattern from Empire XCcel

Table 13: Comparison on the far field pattern.

	$\theta = 90^\circ$ (Azimuth plane)			$\phi = 100^\circ$ (Elevation plane)		
	Pointing beam	Highest side lobe levels, dB	HPBW	Pointing beam	Highest side lobe levels, dB	HPBW
3-D algorithm	100°	-4.5	45°	90°	-6.5	60°
Pattern multiplication	100°	-3.5	45°	90°	-5.5	80°
FDTD	100°	-4.5	45°	90°	-7	60°
MoM	100°	-3.5	45°	90°	-6.5	60°

4.5.4.2.3 Different amplitude and phase

The excitation values with different amplitudes and phases are shown in Table 14 and the far-field patterns are shown in Figs. 4-46 to 4-50. Figure 4-46 shows that the far-field pattern computed from 3-D algorithm is in close agreement with

the pattern computed using FDTD. On the other hand, the pattern computed from MoM agrees with pattern multiplication method. Figure 4-47 shows small discrepancies in the far-field pattern of those methods. However, it shows that the steering angle, number of side lobes and nulls from 3-D algorithm, FDTD and MoM are similar. The far-field pattern obtained from 3-D algorithm encompasses the coupling effect and agrees well with FDTD and MoM. Table 15 shows the comparison of the steering angle, the highest side-lobe level, and the beam-width obtained from the pattern in Figures 4-46 and 4-47.

Table 14 : Excitation values with the different amplitude but phases

Element Index	Amplitude	Phase (degrees)
1	0.5607	-164.5°
2	0.4157	129.2°
3	0.0824	45.9°
4	0.3294	50.1°
5	0	0
6	0	0
7	0	0
8	0	0
9	0	0
10	0	0
11	0	0
12	0	0

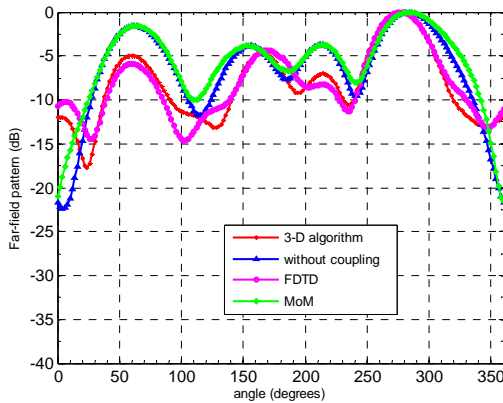


Figure 4-46: E far-field pattern at theta=90°

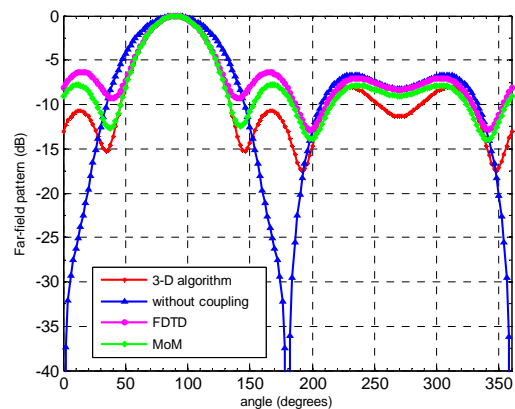


Figure 4-47: E far-field pattern at phi=280°

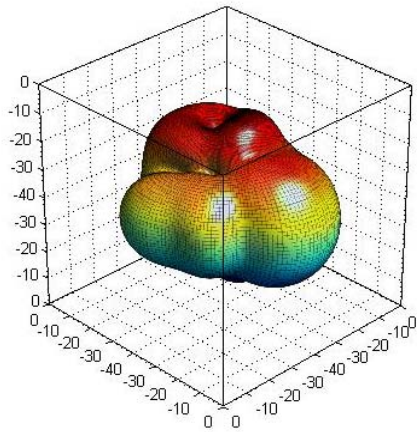


Figure 4-48: 3-D far-field pattern calculated via Induced EMF Method from this thesis (eqn 4-46).

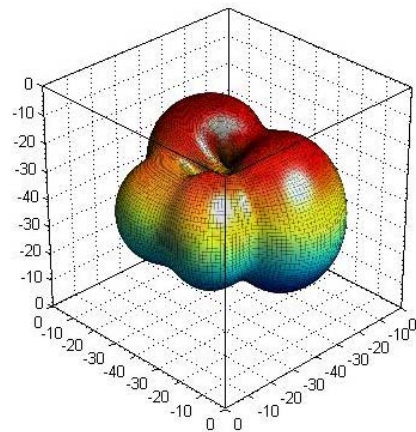


Figure 4-49: 3-D far-field pattern calculated using pattern multiplication method.

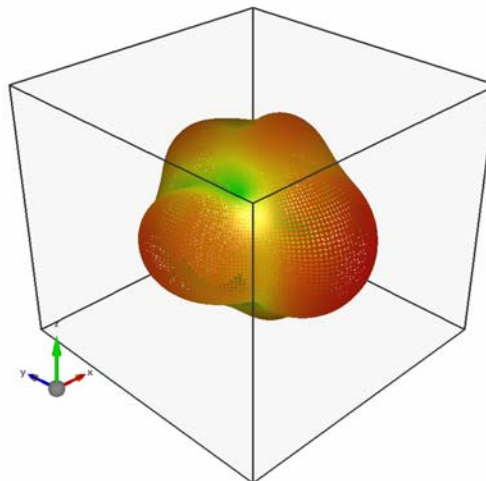


Figure 4-50: 3-D Far Field pattern from Empire XCcel.

Table 15: Comparison on the far field pattern.

	$\theta = 90^\circ$ (Azimuth plane)			$\phi = 280^\circ$ (Elevation plane)		
	Pointing beam	Highest side lobe levels, dB	HPBW	Pointing beam	Highest side lobe levels, dB	HPBW
3-D algorithm	280°	-4	40°	90°	-8	60°
Pattern multiplication	280°	-2	50°	90°	-7	80°
FDTD	280°	-4	40°	90°	-6.5	60°
MoM	280°	-2	55°	90°	-7.5	60°

4.6 Conclusions

This chapter explained the use of 2-D algorithm to calculate the far-field patterns for an array of dipole antennas in free space using the Induced EMF Method. The method incorporates the coupling effect but only applicable to parallel dipole antenna arrays. Then, a new 3-D algorithm is developed to calculate the far-field pattern for 3-D dipole arrays based on the Induced EMF method. It is an extension work of the 2-D algorithm. Two set of examples were tested: a) four parallel dipoles; and b) 12 dipoles arranged at the edge of a cube in free space. The advantage of using the 3-D algorithm is that it includes the mutual coupling effect between elements and applicable for dipoles arranged in straight and inclined position. Thus, the pattern computation is more accurate than the conventional array theory. The algorithm is built from scratch, thus allowing a degree of flexibility in optimising any critical variables such as the number and the spacing between elements. It is quick, efficient and compatible to work with array optimization techniques (such as genetic algorithm). All those criteria are essential in order to obtain fast and fairly accurate results. Moreover, the degree of flexibility allows it to be cost-effective, since the feed network in a phased array (i.e. phase shifter, attenuator) are complex and costly as the number of elements increase. On the other hand, other method such as the active element pattern depends on the modelling software and thus places a restriction on the fixed structure. The results from the 3-D algorithm are compared with conventional array analysis and full wave modelling such as FDTD (Empire XCcel) and MoM (4NEC2++). The results are in good agreement especially for 2x2 dipole arrays. In conclusion, the comparisons show that the 3-D algorithm based on the Induced EMF is sufficient to compute the far-field pattern considering the mutual coupling effect for an array of dipoles either in 1-D, 2-D or 3-D. Later on, the 2x2 dipole array is chosen for pattern control using genetic algorithm (will be explained in chapter 5) and measurement (chapter 7) since it consists small number of elements thus requiring simpler feeding network.

References

- [1] H. Steyskal, J. S. Herd, "Mutual Coupling Compensation in Small Array Antennas," IEEE Transactions on Antennas and Propagation, vol. 38 (12), pp. 1971, Dec. 1990.
- [2] P. S. Carter, "Circuit Relations in Radiating Systems and Applications to Antenna Problems," Proceedings of the Institute of Radio Engineers, vol. 20, pp. 1004, June, 1932.
- [3] J. C. Maxwell, "XXV. On physical lines of force," Philosophical Magazine Series 4, vol. 21 & 23, pp. 161-175, 1861.
- [4] R. F. Harrington, Field Computation by Moment Methods. Piscataway, NJ: Piscataway, NJ: IEEE Press, 1993.
- [5] K. Yee, "Numerical solution of initial boundary value problems involving maxwell's equations in isotropic media," Antennas and Propagation, IEEE Transactions on, vol. 14, pp. 302-307, 1966.
- [6] H. Baker and A. LaGrone, "Digital computation of the mutual impedance between thin dipoles. " Antennas and Propagation, IRE Transactions on, Vol. 10, pp. 172-178, 1962.
- [7] Y. Rahmat-Samii, "Useful coordinate transformations for antenna applications," Antennas and Propagation, IEEE Transactions on, Vol. 27, pp. 571-574, 1979.
- [8] G. Abdalla, "Switched Pattern Control," MSc theses, Loughborough University, United Kingdom, 2006.
- [9] H. E. King, "Mutual impedance of unequal length antennas in echelon." Antennas and Propagation, IRE Transactions on, Vol. 5, pp. 306-313, July 1957.
- [10] P. Ioannides and C. A. Balanis. "Mutual coupling in adaptive circular arrays." Antennas and Propagation Society International Symposium, 2004, IEEE, pp. 403-406, 2004.
- [11] H. Ebersbach, D. V. Thiel, and M. Leckenby, "Modelling Yagi-Uda antennas using point source approximation," Electronic Letters, Vol. 40, Sept. 2004.
- [12] D. V. Thiel and V. Moyle, "Using mutual coupling to calculate the radiation pattern for parasitic patch antennas." In Antennas and Propagation Society International Symposium, 2003, IEEE, 2003, Vol 1, pp. 597-600.

- [13] K. Takamizawa. "Analysis of highly coupled wideband antenna arrays using scattering parameter network models." PhD thesis, Virginia Polytechnic Institute and State University, United States, 2002.
- [14] D. F. Kelley and W. L. Stutzman, "Array antenna pattern modeling methods that include mutual coupling effects," *IEEE Transactions on Antennas and Propagation*, Vol. 41, pp. 1625-1632, Dec 1993.
- [15] K. M. Lee and R. Chu, "Analysis of mutual coupling between a finite phased array of dipoles and its feed network." *IEEE Transactions on Antennas and Propagation*, Vol. 36, pp. 1681-1699, Dec 1988.
- [16] A. A. Oliner and R. G. Malech, "Mutual coupling in infinite scanning arrays." In *Microwave Scanning Antennas*, R. C. Hansen (Ed.). New York: Academic, 1966, p. 195.
- [17] T. Milligan, "More applications of Euler rotation angles." *Antennas and Propagation Magazine*, IEEE, Vol. 41, pp. 78-83, 1999.
- [18] E. Khoomwong and C. Phongcharoenpanich, "Analysis of an arbitrarily rotated slot on a conducting spherical cavity." In *Microwave Conference, 2007. APMC 2007. Asia-Pacific, 2007*, pp. 1-4.
- [19] C. Phongcharoenpanich, D. Boonrod and M. Krairiksh, "Radiation characteristics of inclined slot antenna on conducting spherical cavity." In *Communications, 2003. APCC 2003. The 9th Asia-Pacific Conference on, 2003*, pp. 964-968, Vol. 3.
- [20] H. Goldstein, *Classical Mechanics*. San Francisco: Addison Wesley, 2001.
- [21] H. A. Burger, "Use of Euler-rotation angles for generating antenna patterns." *IEEE Antennas Propagation Magazine*, Vol. 37, pp. 56-63, April 1995.
- [22] B. N. Getu and J. B. Andersen, "The MIMO cube - a compact MIMO antenna," *Wireless Communications, IEEE Transactions on*, vol. 4, pp. 1136, may, 2005.
- [23] T. Mashall, "Numerical electromagnetics code (method of moments)". Internet: <http://www.nec2.org/>, [May 28, 2011].
- [24] "Empire XCell". Internet: <http://www.empire.de/>, [May 28, 2011].
- [25] S. A. Schelkunoff, *Electromagnetic Waves*. Van Nostrand, 1960.

[26] J. C. Bregains, F. Ares and E. Moreno, "Visualizing the 3-D polar power patterns and excitations of planar arrays with Matlab." *Antennas and Propagation Magazine, IEEE*, Vol. 46, pp. 108, April 2004.

CHAPTER 5:

Pattern control of a Four Dipole Antenna Array using a Genetic Algorithm

5.1 Introduction

In the previous chapter, a 3-D array analysis with mutual coupling has been extensively investigated and developed. Two examples were given such as 2x2 dipoles (2-D array) and cubic dipoles arrays (3-D array). This chapter describes ways to control the pattern of an array using a Genetic Algorithm. A Genetic Algorithm was chosen, because it is robust, not easily trapped in local maxima (or minima) and is suitable for complex problems (with a large number of variables), especially those involving mutual coupling [1]. Moreover, GAs have large applications in electromagnetic problems such as a thinning array [2], low side-lobe levels [3], antenna array element failure [4] and pattern null steering [5].

In this case, a pattern synthesis is performed using a combination of the 3-D Algorithm and a Genetic Algorithm. From Chapter Four, a 2-D array (consisted of four dipoles) has been chosen due to its ease of computation and also it requires less complexity of feeding network compared to 3-D array (cubic dipole). The excitation voltages (amplitude and phase) of four dipoles are varied in order to meet the requirement of a cosine-shaped main beam [6], which may be steered to any direction. Then, the optimized pattern obtained from Genetic

Algorithm is compared with a pattern multiplication method for best performance.

5.2 Introduction to Genetic Algorithms

Genetic Algorithms are search algorithms based on the mechanics of natural selection and natural genetics. They were originally developed by John Holland, with his colleagues and students at the University of Michigan. A feature of this algorithm is its robustness in many different environments [7]. Many papers and dissertations have written about GAs in function optimization and control applications.

The genetic algorithm (GA) allows a set of populations to develop toward a globally optimal solution. The process is based on three important steps: selection, recombination and mutation. Johnson and Rahmat-Samii [8] elaborate some of the basic GA terminology in Table 16.

Table 16: Genetic Algorithm terminology

GA Terminology	Definition
Gene	Coded optimisation parameter. The basic building block in GA (variable).
Chromosome	A trial solution vector (string) consisting of genes. A combination set of genes/parameters.
Generation	Successively created populations (an iterations)
Population	Set of trial solutions
Parent	Member of the current generation
Child	Member of the next generation
Fitness	A number assigned to an individual representing a measure of goodness.

Many papers discuss the process of genetic algorithms [9, 10]. A simple genetic algorithm has been chosen as the optimisation technique for pattern synthesis. The algorithms begin with a population of strings (chromosomes) selected at random. GA then generates the next generation via the principle of natural selection, in which good populations (better results or fitness values) are encouraged to survive and bad populations (worse results) are eliminated. The

natural selection procedures are reproduction, crossover and mutation. This whole process is repeated, yielding a global optimum solution because the selection is based on the principle of the survival of the fittest.

Johnson and Rahmat-Samii [8, 11] list several advantages of genetic algorithms (global optimisation technique):

- Stochastic search processes which are substantially independent of starting points.
- Applicable to situations that have non-differentiable and discontinuous objective functions.
- Able to search within the global solution space and find global maxima or minima.
- Well suited to a discrete search space.
- Well suited for a broadband problem and new problems in which the solution spaces are not known.
- Fast convergence rate even though the search space is significantly large.
- An easy to implement and uncomplicated program.

A simple genetic algorithm (SGA) was chosen for the beam pattern synthesis combined with the 3-D Algorithm. Figure 5-1 illustrates a block diagram of SGA. It can be divided into three stages: coding and initialisation; reproduction; generation replacement.

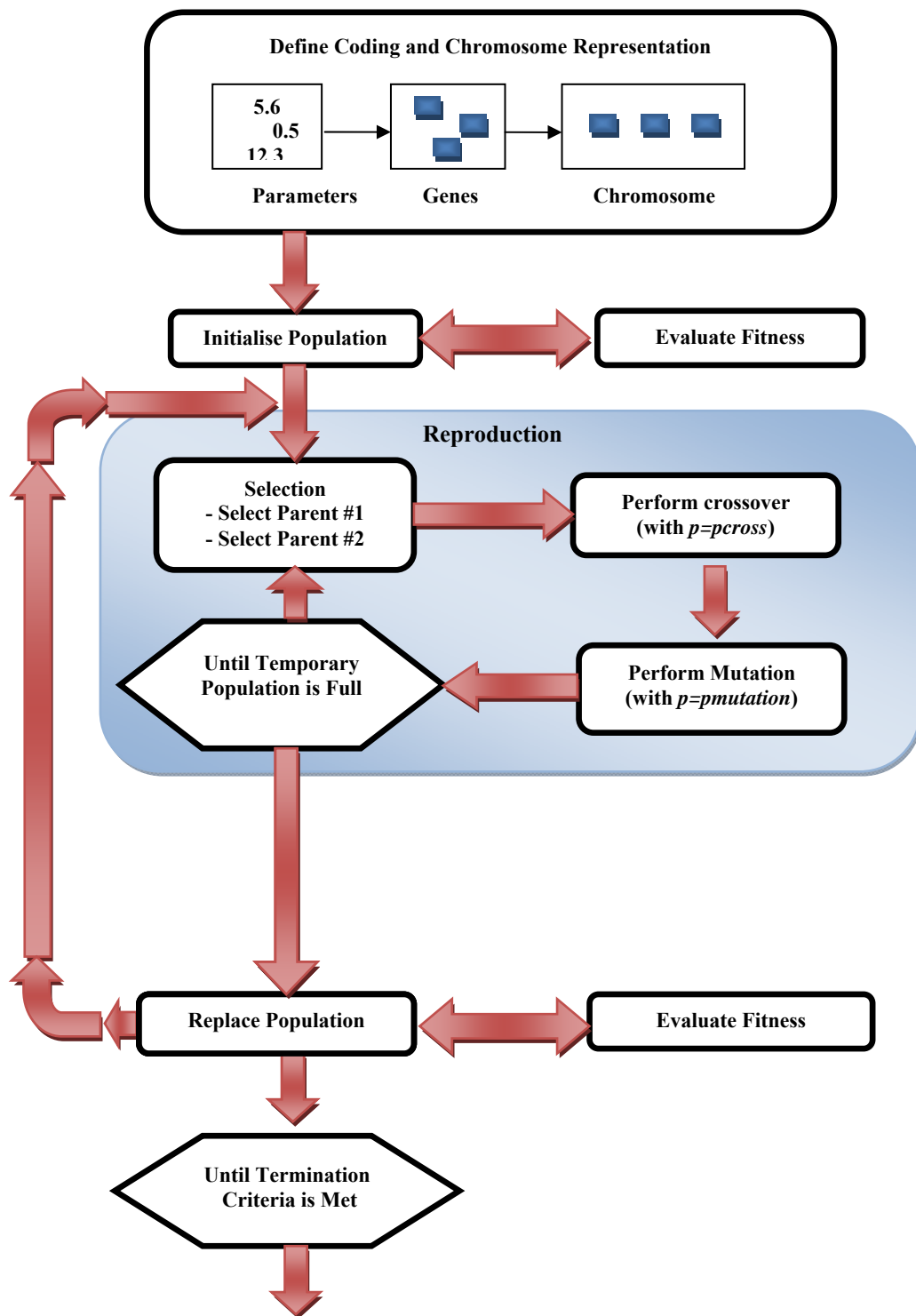


Figure 5-1: Block diagram of a simple genetic algorithm optimiser [8].

5.2.1 Initialisation and Coding

At this stage, a solution set is randomly generated and encoded as a gene for each parameter. This process allows the genetic algorithm to operate on a coding of the parameter instead of the parameter itself [8]. A string of genes can be represented as one chromosome. Each of these chromosomes is called an individual. The set of individuals is referred to as a current generation. A fitness value is assigned to every individual in the set by evaluating its fitness function.

A coding process provides a transition from the parameter space (usually consisting of real numbers) to the chromosome space (a finite length of string). There are at least three types of chromosome representation (or coding technique): binary, Gray and real-value coding. Weile and Michielssen [12] present a summary regarding chromosome representation. Typically, a binary coding technique (a combination of zeros and ones) is used for the coding process, as suggested by Holland [13]. Holland states that binary coding provides GA with the largest space to search for and facilitate the similarities between successful chromosomes. Many researchers have used Gray coding to eliminate ‘Hamming cliffs’ issue caused by binary coding (transforming the search space with Gray coding). The ‘Hamming distance’ between two strings of equal length refers to the number of positions in which two strings are different. Hamming cliffs are the gaps between the codings of adjacent integers separated by a Hamming distance greater than one. Hamming cliffs will yield an assumption that binary coding can convert an initially simple, unimodal function of real numbers into a deceptive binary function. The advantage of the Gray code is that it is constructed so that coding of adjacent integers differs in only one bit position.

However, Mathias and Whitley [14] point out that there is no reason to believe that Gray codes are helpful for arbitrary problems. Even though Gray codes improve performance on certain test functions such as the De Jong’s test suite function, its performance on arbitrary functions corresponds to binary code. If a function is difficult to optimise in standard binary space, the same will occur with Gray codes. Thus, it has lost popularity and been replaced with real-coded GA.

Wright [15] claims that the use of real-valued genes in GAs offers advantages in numerical function optimisation over binary encoding. The strengths include:

- The efficiency of the GA is increased, as there is no need to convert chromosomes to phenotypes before each function evaluation.
- Less memory is required, as efficient floating-point internal computer representations can be used directly.
- No loss in precision due to the discretisation of binary or other values, since only real-number representation is used.
- Greater freedom to use different genetic operators such as mutation and crossover techniques based on real-number representation.

The disadvantage of the real-coded is that the crossover and mutation process are more complicated than binary and Gray coding.

5.2.2 Reproduction

The reproduction stage consists of three sub-processes: selection, crossover and mutation. It generates a new generation from the current generation. First, a pair of individuals is selected from the population to act as parents. The parents go through crossover and mutation, to produce a pair of children. These children become the new generation. The selection, crossover and mutation processes are repeated until all individuals have been placed in a new generation. The new generation will replace the current generation. The selection, crossover and mutation process is explained further in the following sections.

5.2.2.1 Selection Strategies

Selection employs the fitness function in the genetic algorithm optimisation process. A fitness function is a measure of the ‘goodness’ of an individual in that generation. However, selection cannot solely choose the best individual because it might not lead to the optimal solution. Some of the chromosomes that have worse results can be selected according to the procedure of the selection techniques. This ensures that certain traits carried by them do not entirely

disappear from the population. Some selection strategies are discussed, such as population decimation, proportionate selection (or roulette wheel selection), tournament selection and stochastic universal sampling. Some of the methods are described here to provide an understanding of the process.

Population Decimation is the simplest strategy based on the survival of the fittest chromosomes with the removal of the least fit. Individuals are ranked based on their fitness value from the largest to the smallest. A random minimum fitness is then chosen as the cut-off point. Any individual fitness which is less than that value is removed from the population. The remaining individuals are then randomly assigned in pairs to generate a new generation. The process is repeated until the new generation is filled.

The advantage of population decimation is its simplicity. However, the disadvantage is that any unique characteristic that the removed individual possesses is totally lost from the population. It is common that the loss happens before the genetic algorithm acknowledges the beneficial effect of a unique characteristic in that individual. The good characteristic is difficult to retrieve once it has been lost in the process. Therefore, it is better to keep good genes whenever possible.

Proportionate Selection, sometimes called Roulette Wheel Selection (or ‘RWS’), is the most well known strategy used [16]. The selection of individuals is based on a probability of selection as in equation (5-1).

$$p_{selection} = \frac{f(parent_i)}{\sum_i f(parent_i)} \quad (5 - 1)$$

where $f(parent_i)$ is the fitness of the i -th parent. The probability of selecting an individual from the population relates to the fitness of the individual. Individuals with better fitness will be involved in the creation of the next generation more frequently than less fit individuals. The distinction between population decimation and proportionate selection is that there is still a finite possibility that highly unfit individuals will participate in the creation of the next generation (at least some of the mating) thus preserving their genetic information.

Tournament Selection is attributed to the unpublished work by Wetzel and studied in Brindle’s dissertation [17]. It is a strategy where a random

selection of a sub-population of N individuals is made from the population. The individual with the highest fitness in the selected sub-population wins the tournament and becomes the selected individual. The remaining sub-population members are returned to general population and the process is repeated.

Stochastic Universal Sampling ('SUS') [18] is a variation from roulette wheel selection. The individuals are mapped to neighbouring segments of a line and each individual's size segment is proportional to its fitness. Equally spaced pointers are then placed over the line. The number of pointers, $NPointer$, depends on the number of individuals to be selected. Therefore, the step size between the pointers is $1/NPointer$ and the position of the first pointer is randomly generated within the range $[0, 1/NPointer]$.

Figure 5-2 illustrates the process. For six individuals to be selected, the step size between the pointers is $1/6=0.167$. The position of the first pointer is within the range of $[0, 0.167]$ and is randomly generated. In this case, the position of the first pointer is at 0.1. The position of pointer 2 is obtained by adding fixed step size to pointer 1, and the process goes on. As a result, each pointer selects an individual of 1, 2, 3, 4, 6 and 8 to participate in the new generation.

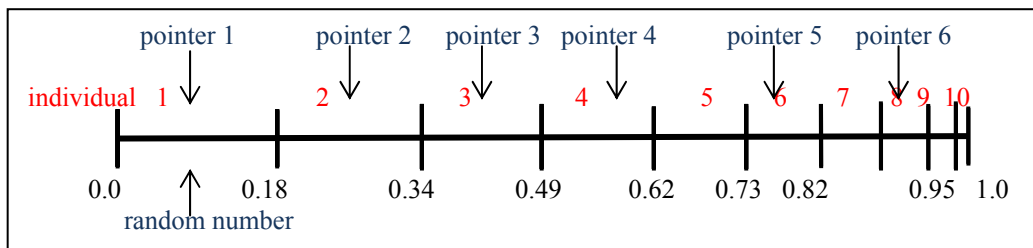


Figure 5-2: Stochastic universal sampling

5.2.2.2 Crossover

After the selection process, a pair of individuals will create a pair of children using the basic genetic algorithm operators, crossover and mutation. Crossover and mutation are applied with probability p_{cross} and $p_{mutation}$ respectively.

The crossover operator works on a pair of parents and generates a pair of children. If $p > p_{cross}$, a random location in the chromosomes is selected. The portion of the chromosome preceding the selected point is copied from parent 1

to child 1 and from parent 2 to child 2 (Figure 5-3). Meanwhile, the portion of the chromosome of parent 1 following the randomly selected point is positioned in the corresponding placement in child 2 and vice versa for the remaining portion of parent 2's chromosome. On the other hand, if $p < p_{cross}$, the entire chromosome of parent 1 is copied into child 1 and the same goes for parent 2 and child 2. The purpose of crossover is to rearrange the genes with the object of producing a better combination of genes. As a result, more fit individuals are developed.

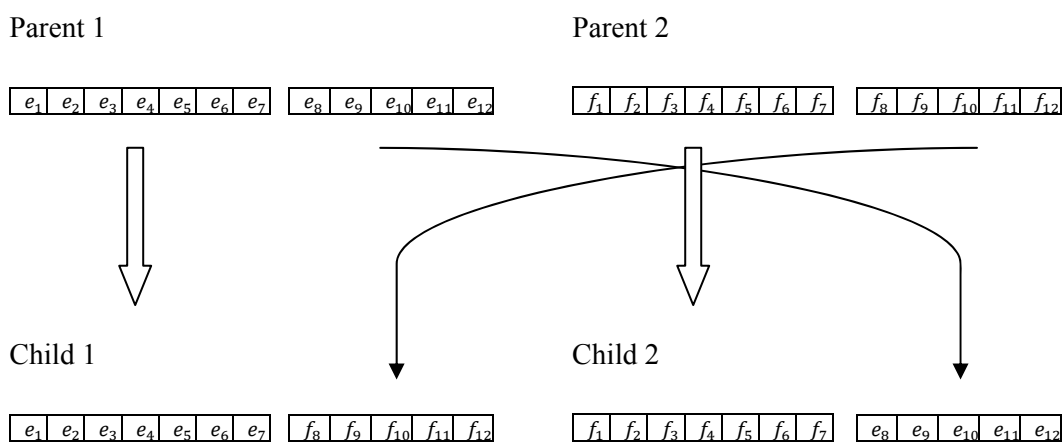


Figure 5-3: Crossover operation.

5.2.2.3 Mutation

The aim of mutation is to provide a means of searching parts of the solution surface that are not represented in the genetic makeup of the current population. If $p > p_{mutation}$, an element in the chromosome string is randomly selected and altered. For binary encoding, the alteration involves selecting a bit from the chromosome string and inverting it. This means that 1 becomes 0 and vice versa. If other coding is used (such as real-coding), a more complicated form of mutation is required.

5.2.3 Generation Replacement

In the generation replacement process, the new generation replaces the current generation together with the fitness values that are assigned to each individual. The termination criterion is then evaluated and if it has not been met, the reproduction process is repeated.

5.2.4 Termination Criteria

The process is repeated until a termination condition has been achieved. Generally, the terminating conditions may be one of the following:

- Set number of iterations.
- Set time reached.
- A cost that is lower than an acceptable minimum.
- Set number of cost function evaluations.
- A best solution has not changed after a set number of iterations.
- Operator termination.

Usually a number of generations (or iterations) are chosen because of their simplicity. The other conditions are more difficult to be realized. If the optimised results obtained from this process are not satisfactory, the parameters need to be altered and the process needs to be run again. Linden [19] gives suggestion on how to monitor the process of the genetic algorithm and what actions should be taken if the process is slow or the results converge slowly. De Jong [16], Schaffer *et al.* [20] and Grefenstette [21] proposed the control parameter values (number of individuals, crossover and mutation rate) in order to obtain the best performance of GA.

The last generation will produce a set of chromosomes that is different from the initial generation. It is common that the fitness values increase throughout the process, since only the best fitted chromosomes from the previous generation are selected to go through to the next level.

5.3 Radiation Pattern Control using a Combination of the 3-D (based on the Induced EMF Method) and a Genetic Algorithms

5.3.1 Computation of the Far-Field Radiation Pattern

The basic geometry of a three-dimensional antenna array is shown in Figure 5-4. The position of each element and orientation is varied and not limited to any direction. The far-field radiation pattern for N elements of dipole antenna array

was calculated using the 3-D algorithm (equation 4-46 in Chapter 4) and shown as follows:

$$\begin{Bmatrix} H_r(r, \theta, \phi) \\ H_\theta(r, \theta, \phi) \\ H_\phi(r, \theta, \phi) \end{Bmatrix} = \sum_{n=1}^N \left([{}^s T^c] \times [B] \times [{}^c T^s'] \times \begin{Bmatrix} H'_{r'_n}(r', \theta', \phi') \\ H'_{\theta'_n}(r', \theta', \phi') \\ H'_{\phi'_n}(r', \theta', \phi') \end{Bmatrix} \right), \quad (5-2)$$

where the electric field for theta component,

$$H'_{\theta'}(\theta, \varphi) \approx \frac{j \eta I_0 e^{-jkr}}{2\pi r} \cdot \frac{\cos(\frac{\pi}{2} \cos \theta)}{\sin \theta} \quad (5-3)$$

and I_0 is the vector of complex excitation weights

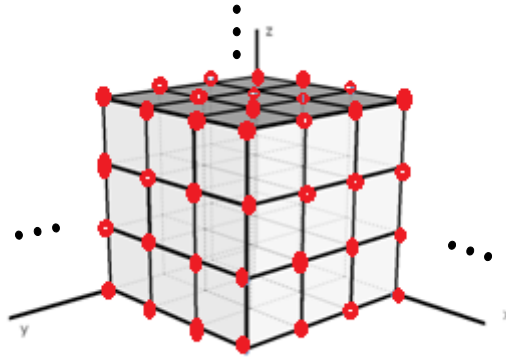


Figure 5-4: Antenna elements (represented by red dots) are placed in 3-D coordinates with same spacing.

For the work described in this thesis, the method is applied to four vertical dipoles with $0.9\lambda_0$ spacing at 2.45GHz. The reason for selecting this spacing is for practical reasons which will be explained later and will become apparent in Chapter 7. The complex excitation weights are optimised in order to obtain the desired radiation pattern.

5.3.2 GA Specifications

The 3-D algorithm is run together with the genetic algorithm toolbox [10] (shown in Figure 5-5) in order to obtain the excitation value for each element in an array. It is modified for pattern synthesis purposes and is attached in Appendix C. There are at least five factors affecting the GA performance:

Section 5.3. Radiation Pattern Control using a Combination of the 3-D (based on the Induced EMF Method) and a Genetic Algorithms

- the method of representing solutions (how it is encoded as chromosomes)
- initial population of solutions (the group of chromosomes created at the beginning of the evolution process)
- fitness function
- genetic operators (e.g. three basic operators, selection, crossover and mutation)
- control parameters (e.g. the size of the population of chromosomes and probabilities of crossover and mutation).

Pham and Karaboga [22] state that the control parameters tend to be less problem dependent in comparison with the former four factors. Therefore, the study of the control parameters to improve the GA performance might be useful for array optimization. Previous works on control parameters (shown in table 17) to obtain good performance have been done by De Jong [16], Schaffer *et al.* [20], and Grefenstette [21].

Table 17: GA control parameters using different methods.

Control parameters	De Jong [16]	Schaffer [20]	Grefenstette [21]
Population size	50-100 (50)	20-30 (20 was chosen)	30
Probability of crossover	0.60	0.75-0.95 (0.75 was chosen)	0.95
Probability of mutation	0.001	0.005-0.01 (0.005 was chosen)	0.01

The optimization is run with all the above three methods. Table 18 shows other specifications for the work described in this thesis.

Table 18: Parameters for the genetic and the 3-D algorithms.

Genetic Algorithm Parameters	Specification
Number of Generations	700
Number of Variables (or Genes)	8 (4 for amplitude and 4 for phase of each dipole)
Range of Variables	Amplitude [0, 1]; Phase $[-\pi, \pi]$
Coding Representation	Binary
Selection Strategy	Stochastic Universal Sampling 'sus'

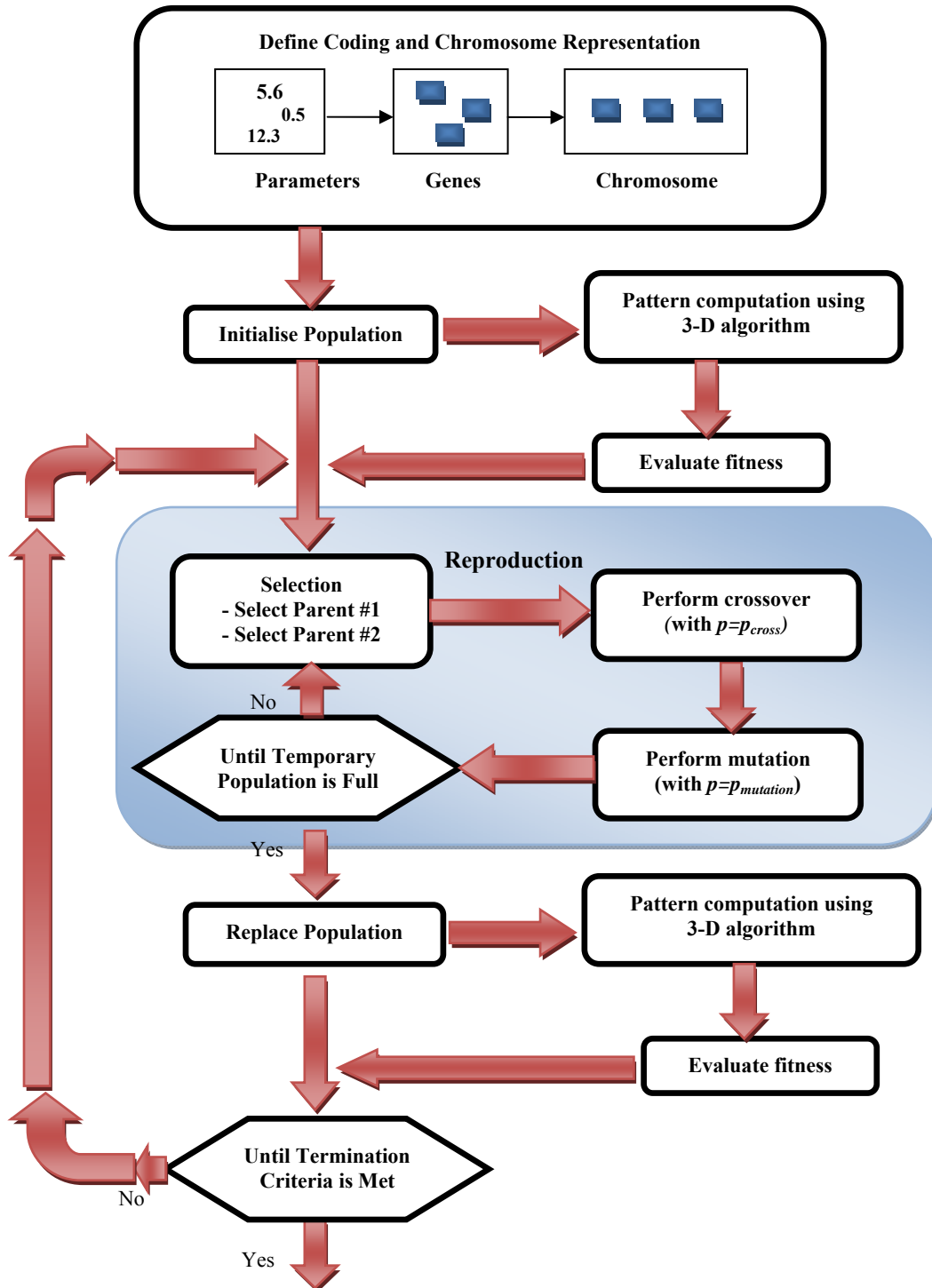


Figure 5-5: Flowchart of the genetic algorithm and the 3-D Algorithm.

5.3.3 Desired Pattern

A cosine-shaped main beam pattern [6, 18] was chosen due to its simplicity. The restriction is added by assuming its HPBW is 30° and side-lobe level of -10 dB

imposed on the desired pattern. Figure 5-6 shows a cosine-shaped main beam pattern directed towards 120° with 30° beamwidth. A balance between the side-lobe level of -10dB and maximum beam is required so that the aim of steering the main beam can be achieved.

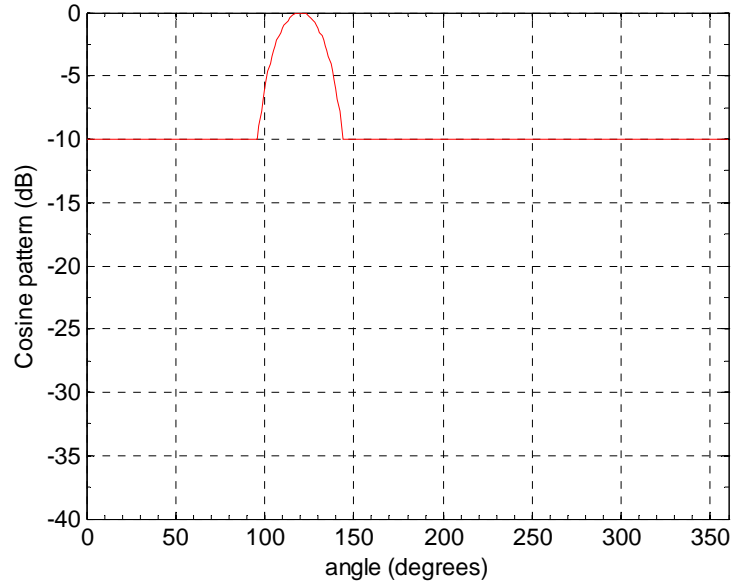


Figure 5-6: A cosine shaped main beam pattern directed towards 120° with side-lobe levels of -10dB.

5.3.4 Fitness Function

The fitness function, sometimes known as the objective function, aims to assign a fitness value to each individual. It is a measure of how fit or good each individual is in the population. The fitness function is the only connection between the physical problem being optimised and the genetic algorithm. There are several fitness functions in pattern synthesis such as the least mean square function [23, 24], absolute error [25, 26] and so on.

In this case, the absolute error [25, 26] has been chosen as an objective function to evaluate the best fitness values of each individual. Each pattern is calculated as depicted in Figure 5-5 and compared with the desired radiation pattern to obtain the fitness values of each individual. The fitness function, $f(x)$, is defined as [26]:

$$fitness, f(x) = \frac{1}{1 + \sum_{i=1}^Q P_0 |S_{a_i} - S_{c_i}|} \quad (5 - 4)$$

where Q is a number of sampling points in the far-field pattern, P_0 is a penalty constant which ranges from [0-1], S_d is desired radiation pattern and S_c is the far-field pattern calculated using the 3-D algorithm. The penalty constant, p_0 is chosen as 0.05 using trial and error so that the values of fitness function within [0, 1].

5.4 Results of Pattern Control Using Genetic Algorithm

The 2-D pattern synthesis for a parallel dipole array is performed at a single plane of $\theta_0=90^\circ$. For 3-D arrays, the analysis and synthesis of a 3-D far-field pattern becomes more complex and difficult. Zhang [27] suggests that the 3-D pattern synthesis problem should be transformed into a multi-2D pattern synthesis problem. The method sampled the data of the 3-D far-field pattern on several cutting planes. However, the technique requires more data than 2D array, thus slowing the performance of the genetic algorithm.

5.4.1 Steerable Main Beam at 100°

The aim of this work is to steer the main beam for whole region of xy -plane by varying the amplitude and phase of array elements. However, since the dipoles are arranged symmetrically, only 45° range is covered. Other steering directions can be obtained by applying the same excitation values (obtained from synthesizing process) to the different element numbers. Meanwhile, the steering angles of 0° , 90° , 180° and 270° can be obtained by exciting all elements with 1. As a result, the steering angles from 100° to 140° are selected with a 10° step. Because of wide beam of HPBW, a step angle of 10° is sufficient to cover beam steering for whole xy -plane.

Figure 5-7 shows the performance of the genetic algorithm based on control parameters suggested by De Jong [16], Schaffer [20] and Grefenstette [21]. The highest fitness function is obtained by using parameters suggested by Grefenstette, which is followed by De Jong and Schaffer. Figure 5-8 shows the patterns obtained from the genetic algorithm in comparison with the desired main beam cosine pattern steering to 100° . It is observed that the pattern due to the parameters proposed by Grefenstette is the closest agreement in terms of the

main beam and side lobe levels to the desired pattern. It is due to the highest fitness function obtained by Grefenstette compared to De Jong and Schaffer. Moreover, patterns optimised by all those parameters are in close agreement. It is because the largest difference of the fitness values are insignificant, roughly 0.03 difference. Meanwhile, Figure 5-9 shows a comparison made between the GA optimised pattern and the pattern derived from the technique to direct the peak of the main beam in the (θ_0, ϕ_0) direction in a circular array. Four dipoles arranged in square are similar to four dipoles arranged in circular (as in Sections 3.2.2.2.2 and 4.3). However, circular array only used constant amplitude with uniform phase excitation. In optimization technique, amplitude and phase excitation for each element has been optimized to satisfy desired pattern. Therefore, the optimized patterns proposed by three authors are in closer agreement compared to the method using circular array. All patterns are plotted in 2° step which clearly defined the position of nulls and side-lobes that are missing from Figure 5-8. In a circular array, the amplitude excitation is constant while the phase excitation (α_n) for each element can be selected as:

$$\alpha_n = -kb \sin \theta_0 \cos(\phi_0 - \phi_n) \quad (5 - 5)$$

where k is the wave number, b is the radius of the circular array and (θ_0, ϕ_0) is the direction of the main beam and ϕ_n is the phi angle. The aim is to determine whether the GA produces the optimised results compared with other method, and the results show that they are in agreement with each other.

Figures 5-10 and 5-11 show the amplitude and phase excitation for the GA optimised and the circular array patterns respectively.

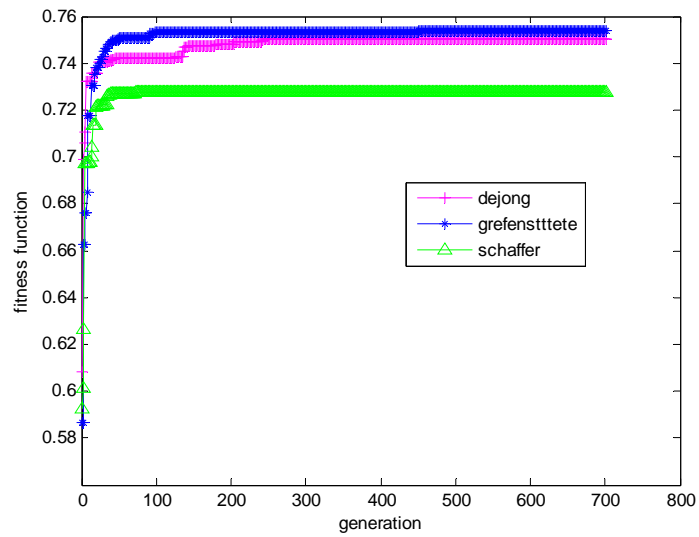


Figure 5-7: Performance of GA when steering at 100°.

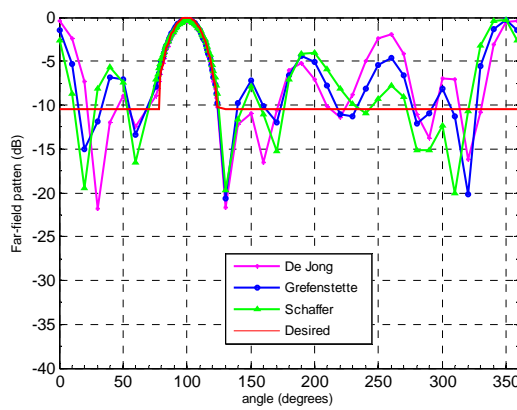


Figure 5-8: Comparison between the GA optimised and desired pattern.

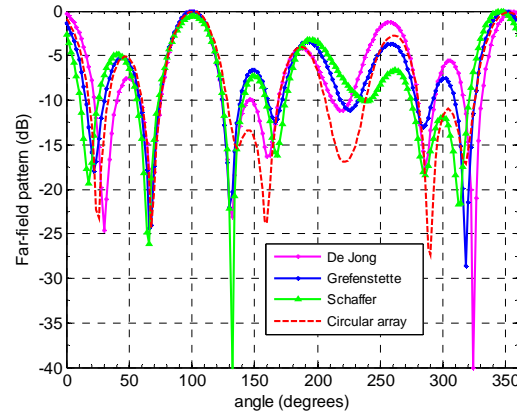


Figure 5-9: Comparison between the GA optimised and circular array pattern in 2° step.

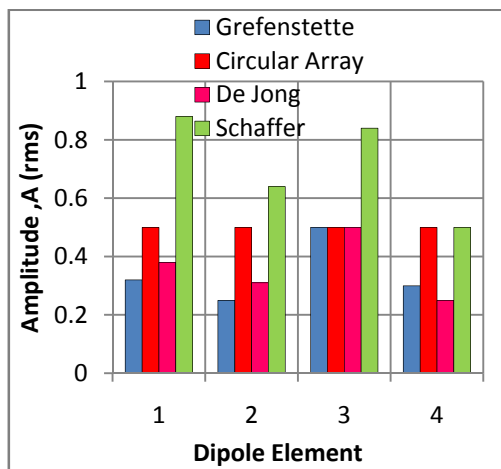


Figure 5-10: Amplitude excitation versus number of elements of dipole antennas.

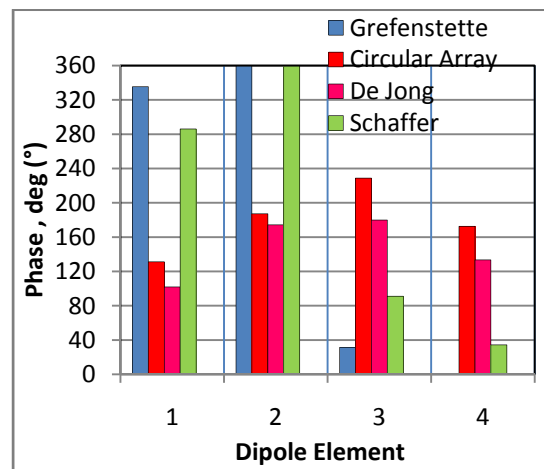


Figure 5-11: Phase excitation versus number of elements of dipole antennas.

5.4.2 Steerable Main Beam at 110°

Figure 5-12 to 5-16 show the synthesis results of the genetic algorithm when the main beam cosine pattern steers at 110° . Figure 5-12 shows that the fitness functions from three sets of control parameters (i.e. De Jong, Schaffer and Grefenstette) converge close to each other. The fitness function for all plots converges significantly estimated from 0.66 to almost 0.8 for 700 generations. At 700th generations, all the plots converge at the same fitness value. As a result, it was observable that the GA optimised patterns from those three authors as shown in Figure 5-13 are in similar agreement with each other. Figure 5-14 shows the sampling of optimised pattern for every 2° . It is observed that there is a deeper null at angle 140° formed in Figure 5-14 as compared to Figure 5-13. This is due to the small step of 2° which brings clarity to the pattern. The small step cannot be used in optimised pattern because of the priority to meet the main beam of the desired pattern.

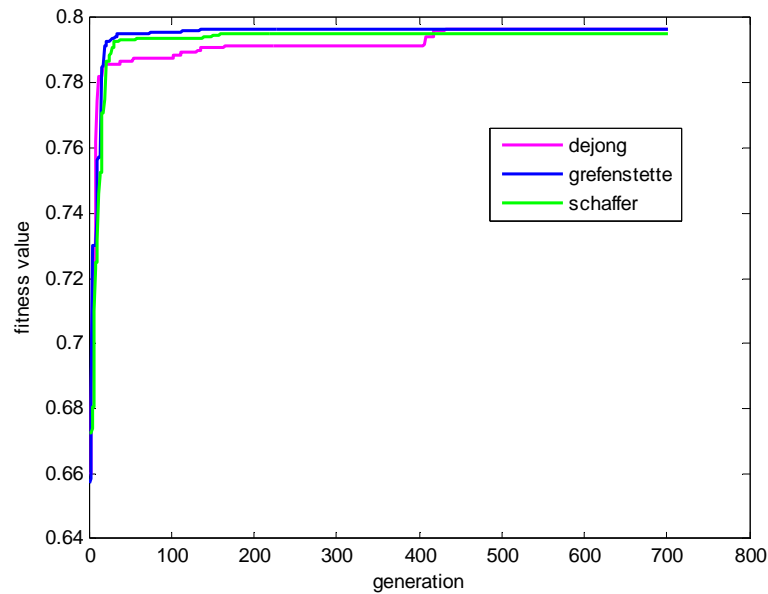


Figure 5-12: Performance of GA when steering at 110° .

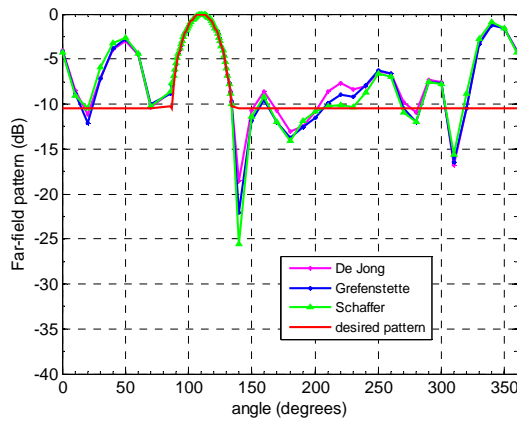


Figure 5-13: Comparison between the GA optimised and desired pattern

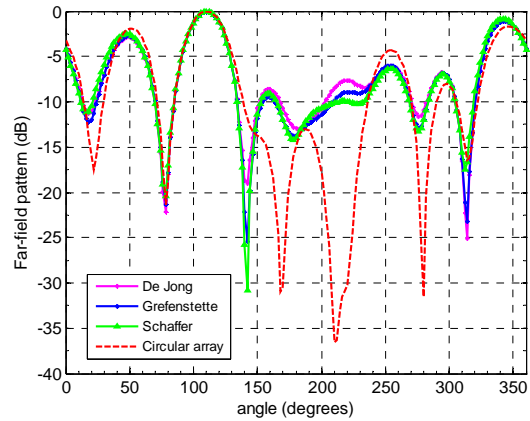


Figure 5-14: Comparison between the GA optimised and circular array pattern in 2° step.

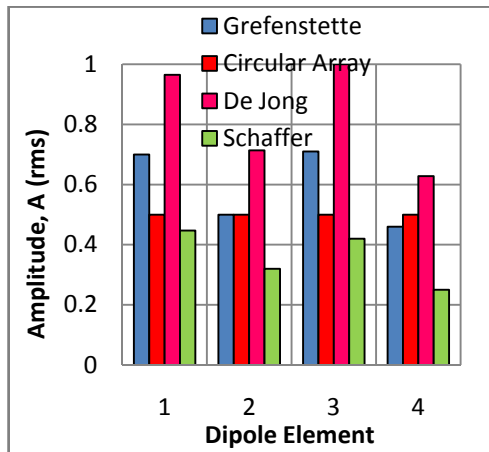


Figure 5-15: Amplitude excitation versus number of elements of dipole antennas.

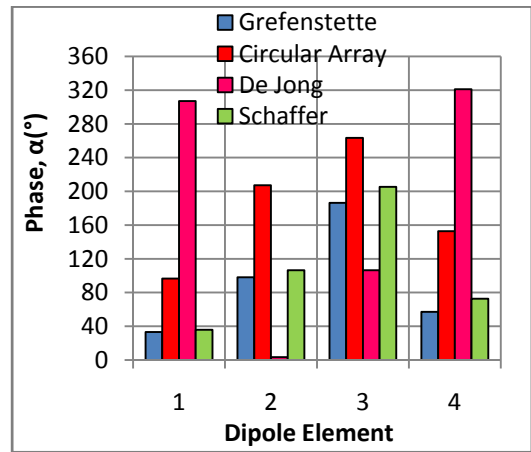


Figure 5-16: Phase excitation versus number of elements of dipole antennas.

5.4.3 Steerable Main Beam at 120°

Figures 5-17 to 5-21 show the synthesis results of the genetic algorithm when the main beam cosine pattern steers at 120°. Figure 5-18 shows that the plot obtained by Schaffer has the highest fitness value in comparison with other plots. Therefore, Figure 5-19 shows that the optimised pattern by Schaffer is the closest agreement to the desired pattern in terms of main beam and side lobe levels. Figure 5-20 and 5-21 show the amplitude and phase excitation of the optimised pattern for each plots.

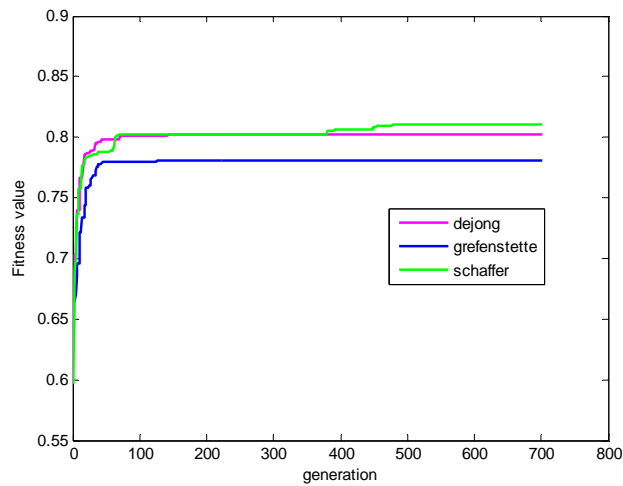


Figure 5-17: Performance of GA when steering at 120°.

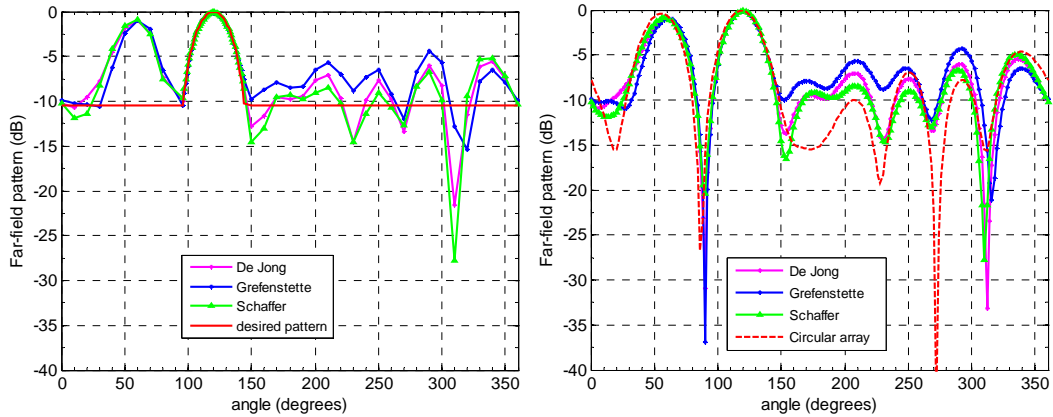


Figure 5-18: Comparison between the GA optimised and desired pattern

Figure 5-19: Comparison between the GA optimised and circular array pattern in 2° step.

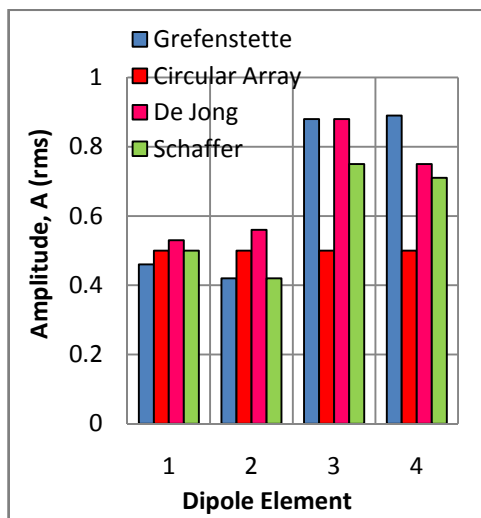


Figure 5-20: Amplitude excitation versus number of elements of dipole antennas.

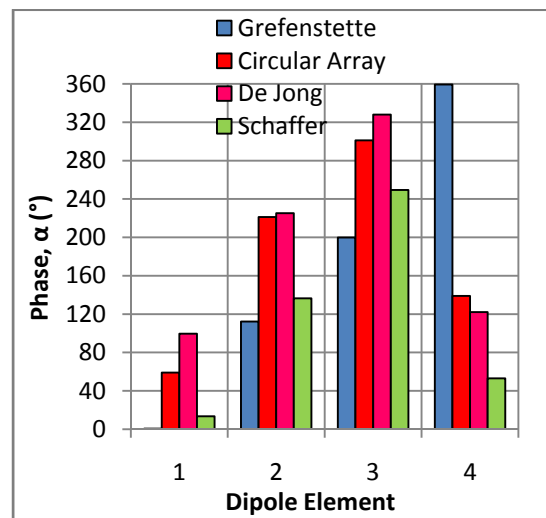


Figure 5-21: Phase excitation versus number of elements of dipole antennas.

5.4.4 Steerable Main Beam at 130°

Figure 5-22 to 5-26 show the synthesis results of the genetic algorithm when the main beam cosine pattern steers at 130°.

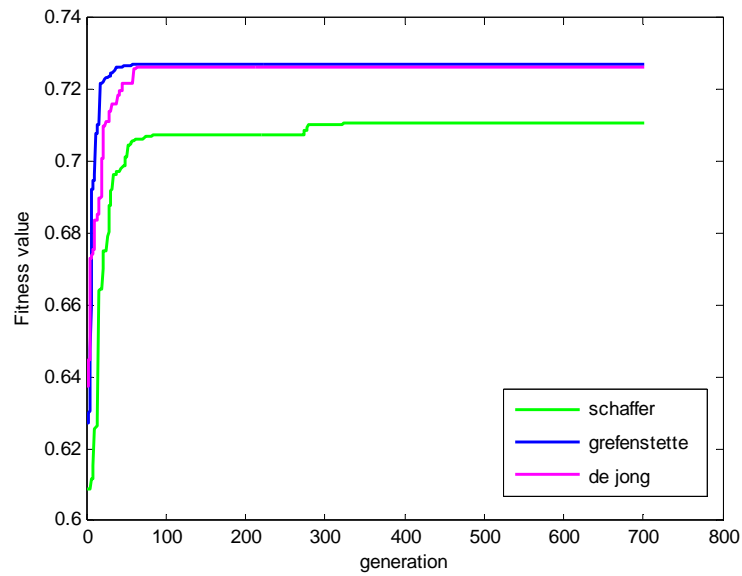


Figure 5-22: Performance of GA when steering at 130°.

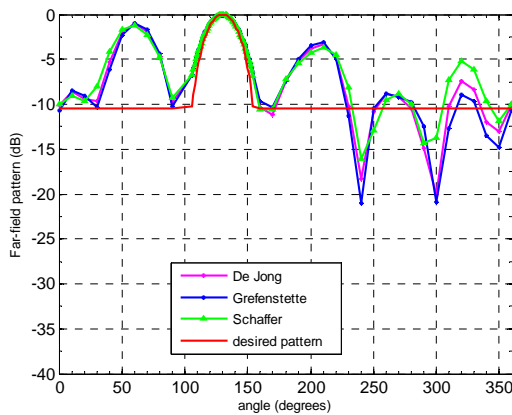


Figure 5-23: Comparison between the GA optimised and desired pattern.

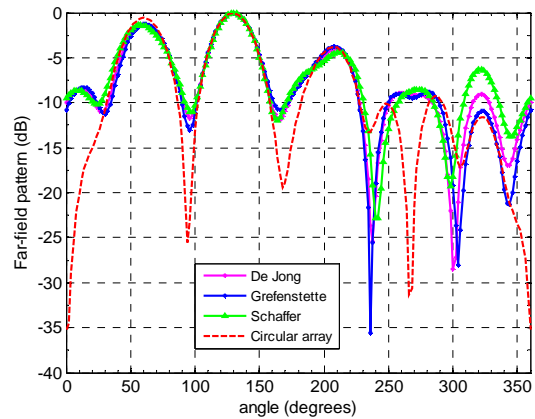


Figure 5-24: Comparison between the GA optimised and circular array patterns in 2° step.

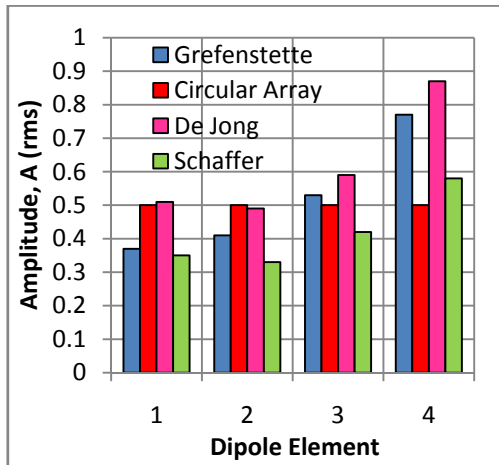


Figure 5-25: Amplitude excitation from GA for each dipole element.

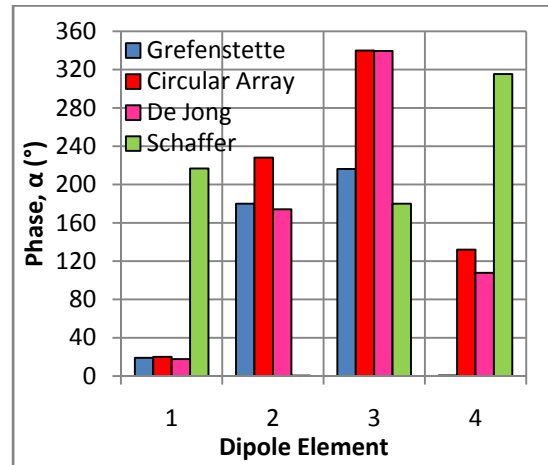


Figure 5-26: Phase excitation from GA for each dipole element.

5.4.5 Steerable Main Beam at 140°

Figures 5-27 to 5-31 show the synthesis results of the genetic algorithm when the main beam cosine pattern steers at 140°.

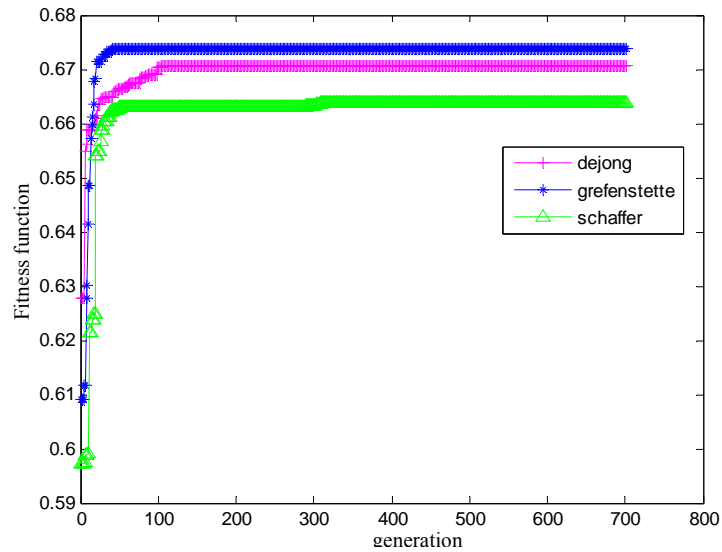


Figure 5-27: Performance of GA when steering at 140°.

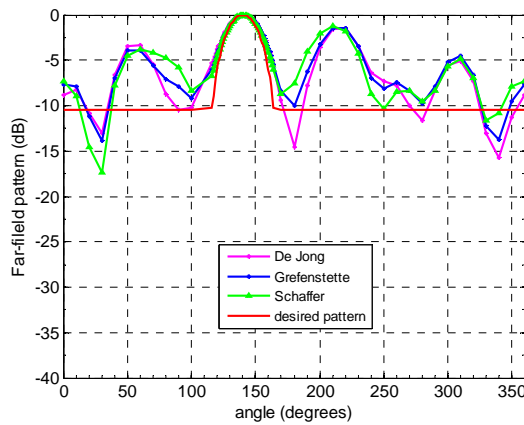


Figure 5-28: Comparison between the GA optimised and desired pattern.

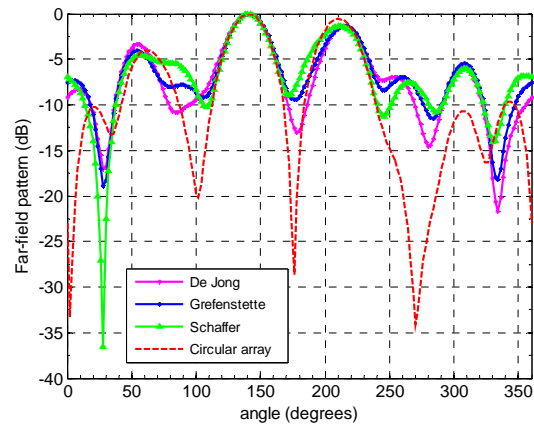


Figure 5-29: Comparison between the GA optimised and circular array pattern in 2° step.

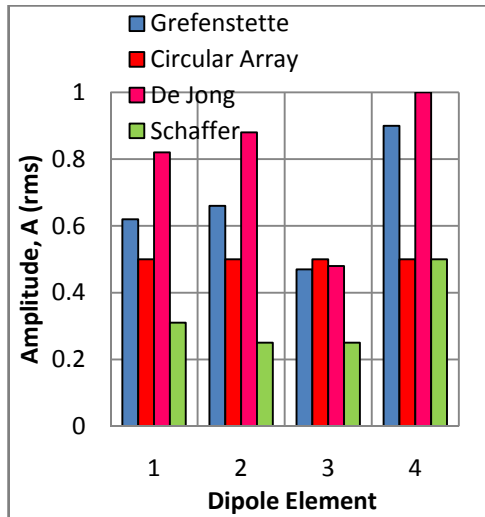


Figure 5-30: Amplitude excitation versus number of elements of dipole antennas.

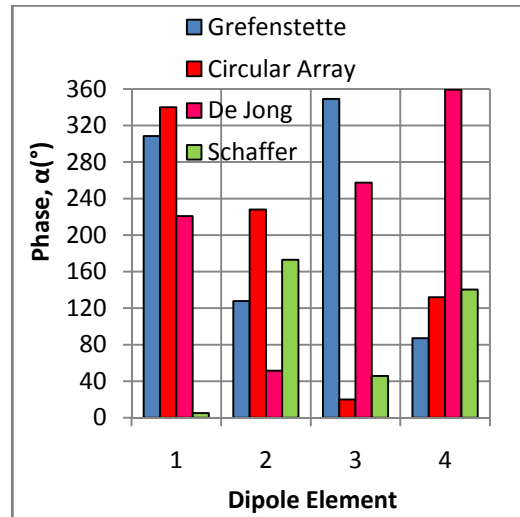


Figure 5-31: Phase excitation versus number of elements of dipole antennas.

5.5 Computational Run Time of 3-D Algorithm and Other Numerical Techniques.

The advantage of the 3-D algorithm is that it requires short computation time to find the far-field pattern which makes it computationally efficient when working with optimization algorithms. Plus, it includes the coupling effect between elements which affect the pattern especially in small antenna arrays. The runtime for 3-D algorithm has been computed using CPUTIME [28] commands using

MATLAB. CPUTIME command returns the CPU time in seconds that has been used by the MATLAB process since MATLAB started. Figure 5-32 shows the script of this code to calculate the computational run time of 3-D algorithm.

```
%at start of timing store current cputime
t0=cputime;

%main work.....

t1=cputime;
%print the total operation time
sprintf('Total time for calculation was %g \n ', t1-t0)
```

Figure 5-32: Script code (MATLAB) to calculate the run time for 3-D algorithm

Table 19 summarizes the computational run time of 3-D algorithm and other commercial software which runs on the same computer based on 2x2 dipole antenna array models. It is observed that the run-time computation for 3-D algorithm is 3.54 seconds which is shorter in comparison with Empire XCcel (FDTD) but slightly longer than NEC (MoM). This is because Empire XCcel is a full wave modelling software and provides very accurate results based on well-defined geometries. On the other hand, 3-D algorithm is based on a closed form approximations and computationally efficient. Even though the run time it takes is slightly longer than the NEC, it works efficiently with the optimization techniques such as genetic algorithm since there are existing genetic algorithm toolboxes available in MATLAB. To the author's knowledge, there is no existing NEC software that offers the optimization techniques together to optimise the pattern of an antenna array. Many studies used the active element pattern (Section 3.2.3.1) as in [29] in order to optimize the far-field pattern obtained from commercial software and combine it with optimization techniques. Therefore, it places a restriction where the active element pattern can be used only on a fixed structural geometry of antenna. The active element pattern need to be extracted (or simulated) again from the software if there is a change in the position of the antenna elements or its frequency.

Table 19: Run time comparison for 2x2 dipole antenna arrays.

	3-D algorithm	FDTD (Empire XcCel)	MoM (NEC)
Average computation run time	3.54 sec	7 minutes	1.95 sec

5.6 Discussion

The results in Figure 5-5 to 5-31 indicates the capability of 2-D dipole array to steer the main beam over an angular range $[100^\circ, 145^\circ]$ with a step size of 10° . Due to the symmetry of dipoles position in square array, the beam can be steered over whole range (360°) of the xy -plane. The beam width of the steered main beam nearly remains constant over the entire steer angle. The optimum performance for all the cases is occurred when the main beam is scanned towards an angle of 120° with the highest fitness value more than 0.8.

The GA was run for beam steering of $[100^\circ, 140^\circ]$ using the control parameters proposed by three authors: De Jong, Schaffer and Grefenstette to obtain the good performance. The results show that different sets of control parameters generate almost similar shape of GA optimised patterns especially for the main beam. The differences between the GA optimised patterns occur at the side-lobe levels.

It was observable that the GA performance converges quickly for all the above cases. Moreover, the cosine main beam pattern with HPBW of 30° is steered successfully to the desired angle. However, the target of a side-lobe level of -10dB is difficult to achieve for whole region aside from the main beam. On the other hand, it is observed that there is large variation for amplitude and phase excitations optimised using the control parameters proposed by three authors in Figures 5-10, 5-11, 5-15, 5-16, 5-20, 5-21, 5-25, 5-26, 5-30 and 5-31. One of the reasons is that the genetic algorithm produced different combination of excitation for each element. However, if each method has almost similar values of fitness function such as in Figure 5-12, the optimised pattern is similar to each other (Figure 5-13) even though the excitation values for each element are different (Figures 5-15 and 5-16).

The discrepancies between desired pattern and optimised patterns may be due to the following reasons:

- The small number of elements. Increasing the number of elements allows flexibility in the pattern control of the antenna array. However, the disadvantage of increasing number of elements is that it complicates the feeding network of the antenna array. Moreover, higher number of elements will increase number of variables that need to be optimised in genetic algorithm thus slowing the optimisation process. Therefore, a 2-D array of four dipoles antenna has been chosen for optimization process.
- The arrangement of four dipoles along a square geometry makes the pattern difficult to add to in a constructive and deconstructive manner, thus making it difficult to obtain a low side-lobe level. Thus large spacing between elements ($0.9\lambda_0$) influences the antenna array to generate grating lobes (more than 1 main beam) in the far-field pattern. The spacing has been chosen as it is the smallest spacing that could be obtained in the measurement set-up (in Chapter 7). The arrangement of balun in diagonal position connected with the coaxial cable complicates the dipole elements to be spaced less than $0.9\lambda_0$ apart. It is desirable to obtain small spacing in order to demonstrate the coupling effect and also to reduce the grating lobe effect on the pattern.
- The number of sampling points in the desired pattern plays an important role in achieving the desired pattern [26]. There has to be a compromised between the main beam region and the side-lobe region since the main objective is to steer the main beam while achieving as the lowest side-lobe level possible. Therefore, a 1° step has been used for the main beam region and a 10° step for the side-lobe region.
- The constant value of the control parameters (crossover and mutation probability) are used within GA. The control parameters can be adjusted for example based on individual fitness and the population diversity measurements using a fuzzy controller (FLC). Kadri, Boussahla and Bendimerad [30] show that using a fuzzy controller results in a better

agreement between the desired and calculated radiation patterns compared with those obtained using simple GA.

- The number of populations and generations in GA. Increasing the number of populations and generations will increase the searching space of the genetic algorithm. Linden [19] gives suggestions on how to monitor the performance of GA. However, increasing those parameters means more time consumption as there are more loops to run. Moreover, the 3-D algorithm has many repeated *'for'* loops resulting processing bottlenecks which slows the code significantly. The problem could be mitigated by re-coding the processor intensive functions in C and using the new C files to generate *'mex'* files. The *'mex'* files can be treated as normal MATLAB function, with a large increased in processing speed [31, 32]. For example, the time taken for one case to synthesize using MATLAB takes one to five hours depending on the processor. Therefore, a compromise should be considered when running GA using MATLAB.

5.7 Conclusions

This chapter demonstrates a technique to steer the main beam pattern and low side-lobe levels using a simple genetic algorithm. For four parallel dipoles spaced $0.9\lambda_0$ apart at 2.45 GHz, the cosine shaped main beam has been steered within the range $[100^\circ, 145^\circ]$ with a step of 10° . Due to the symmetry arrangement, the steering angle can be extended to the whole entire range of xy-plane. The optimum performance for the above cases is occurred when the steering angle is at 120° with the highest fitness more than 0.8. The GA was run with the control parameters proposed by three authors: De Jong, Schaffer and Grefenstette to obtain the good performance. The results show that even though different sets of control parameters have been used, the shape of GA optimised pattern is similar especially in the main beam region. The radiation pattern calculated using 3-D algorithm includes mutual coupling effect between elements. The run time to simulate 2x2 parallel dipoles between those three software; 3-D algorithm, Empire XCcel and NEC has been discussed. 3-D algorithm requires approximately 1.59 sec longer than NEC but less than 7 minutes than Empire XCcel for each simulation. Therefore, its combination with GA runs quickly and took between 45 minutes to 5 hours for each optimization process. Even though the run time for 3-D algorithm is slightly longer than NEC, it works efficiently with the optimization techniques and can be optimized for non fixed geometry and change in frequency unlike other software such as NEC and Empire XCcel.

References

- [1] K. K. Yan, Y. Lu, "Sidelobe reduction in array-pattern synthesis using Genetic Algorithm," IEEE Transactions on Antennas and Propagation, vol. 45, pp. 1117, July, 1997.
- [2] R. L. Haupt, "Thinned arrays using genetic algorithms," IEEE Transactions on Antennas and Propagation, vol. 42, pp. 993, July, 1994.
- [3] Y. C. Chung and R. Haupt, "Low-sidelobe pattern synthesis of spherical arrays using a genetic algorithm," Microwave Opt Technol Lett, vol. 32, pp. 412-414, 2002.
- [4] S. A. Mitilineos and C. N. Capsalis, "On array failure mitigation using genetic algorithms and a priori joint optimization," Antennas and Propagation Magazine, IEEE, vol. 47, pp. 227, Oct., 2005.
- [5] P. Sattari and N. Hejazi, "Array pattern null steering using genetic algorithm by element position perturbations," in Electrical and Computer Engineering, 2008. CCECE 2008. Canadian Conference on, 2008, pp. 000423.
- [6] D. H. Werner and A. J. Ferraro. "Cosine pattern synthesis for single and multiple main beam uniformly spaced linear arrays." IEEE Transactions on Antennas and Propagation 37(11), pp. 1480. 1989.
- [7] D. E. Goldberg, Genetic Algorithms in Search, Optimization, and Machine Learning. USA: Addison-Wesley Publishing Company. Inc., 1989.
- [8] J. M. Johnson and Y. Rahmat-Samii, "An introduction to genetic algorithms," in Electromagnetic Optimization by Genetic Algorithms, 1st ed., Y. Rahmat-Samii and E. Michielssen, Eds. New York: John Wiley & Sons, Inc, 1999, pp. 1.
- [9] A. J. Chipperfield, P. J. Fleming and C. M. Fonseca. "Genetic algorithm tools for control systems engineering." Presented at Adaptive Computing in Engineering Design and Control. 1994.
- [10] A. J. Chipperfield and P. J. Fleming. "The MATLAB genetic algorithm toolbox." Internet: <http://www.sheffield.ac.uk/acse/research/ecrg/gat.html>. [2011]
- [11] J. M. Johnson and Y. Rahmat-Samii, "Genetic algorithm optimization for aerospace electromagnetic design and analysis," in Aerospace Applications Conference, 1996. Proceedings, 1996, pp. 87.

- [12] D. Weile and E. Michielssen, "Genetic algorithms: Theory and advanced techniques," in *Electromagnetic Optimization by Genetic Algorithms*, 1st ed., Y. Rahmat-Samii and E. Michielssen, Eds. New York: John Wiley & Sons, Inc, 1999.
- [13] J. H. Holland, *Adaptation in Natural and Artificial Systems*. Cambridge, MA, USA: MIT Press, 1992.
- [14] K. E. Mathias and L. D. Whitley, "Transforming the Search Space with Gray Coding," in *Proceedings of the First IEEE Conference on Evolutionary Computation, IEEE World Congress on Computational Intelligence*, vol. 1, 1994, pp 513-518.
- [15] A. H. Wright, "Genetic algorithms for real parameter optimization," in *Foundations of Genetic Algorithms*, 1991, pp. 205-218.
- [16] K. A. De Jong, "An analysis of the behaviour of a class of genetic adaptive systems." PhD thesis, University of Michigan, United States, 1975.
- [17] A. Brindle, "Genetic algorithms for function optimization." PhD Thesis, University of Alberta, Canada, 1981.
- [18] J. E. Baker, "Reducing bias and inefficiency in the selection algorithm," in *Proceedings of the Second International Conference on Genetic Algorithms on Genetic Algorithms and their Application*, Cambridge, Massachusetts, United States, 1987, pp. 14-21.
- [19] D. Linden, " Rules of thumb for GA parameters, GA monitoring, GA parameter optimization, and enhancement of GA efficiency " in *Electromagnetic Optimization by Genetic Algorithms*, 1st ed., Y. Rahmat-Samii and E. Michielssen, Eds. New York: John Wiley & Sons, Inc, 1999, pp. 30.
- [20] J. D. Schaffer, R. A. Caruana, L. J. Eshelman and R. Das. "A study of control parameters affecting on-line performance of genetic algorithms for function optimisation," in *Proceedings of Third International Conference on Genetic Algorithms and Their Applications*, George Mason University, Fairfax, Virginia, 1989, pp. 51-61.
- [21] J. J. Grefenstette, "Optimization of control parameters for genetic algorithm," *IEEE Trans. On Systems, Man and Cybernetics*, 1986, pp. 122-128.
- [22] D. T. Pham and D. Karaboga." Genetic algorithms with variable mutation rates: Application to fuzzy logic controller design," in *Proceedings of the*

Institution of Mechanical Engineers, Part 1: Journal of Systems and Control Engineering, Vol. 211, no. 2, pp 157-167, 1997.

[23] R. J. Allard, D. H. Werner and P. L. Werner, "Radiation pattern synthesis for arrays of conformal antennas mounted on arbitrarily-shaped three-dimensional platforms using genetic algorithms," IEEE Transactions on Antennas and Propagation, vol. 51, pp. 1054, May, 2003.

[24] Z. Xu, H. Li, Q. -Z. Liu, J. -Y. Li, "Pattern synthesis of conformal antenna array by the hybrid genetic algorithm," Progress In Electromagnetics Research, PIER 79, 75-90, 2008.

[25] A. A. Abdelaziz and H. A. Kamal, "Sector Synthesis of Antenna Array Using Genetic Algorithm," Journal of Theoretical and Applied Information Technology, vol. 4, pp. 160, 2008.

[26] S. O. Kundukulam and K. S. Beenamol, "Design of a linear array antenna for shaped beam using genetic algorithm," Int.J.RF Microw.Comput.-Aided Eng., vol. 18, pp. 410-416, September, 2008.

[27] F. Zhang, F. - Zhang, C. Lin, G. Zhao and Y. -. Jiao, "Pattern synthesis for planar array based on elements rotation," Progress in Electromagnetics Research Letters, vol. 11, pp. 55-64, 2009.

[28] A. J. O'Connor, "Introduction to MATLAB," Griffith University, Brisbane, Australia.

[29] Q. Wang, Q. -Q. He, " An arbitrary conformal array pattern synthesis method that includes mutual coupling and platform effects," Progress in Electromagnetics Research, vol. 110, pp. 297-311, 2010.

[30] B. Kadri, M. Boussahla and F. T. Bendimerad, "Phase-Only Planar Antenna Array Synthesis with Fuzzy Genetic Algorithms," CoRR, vol. abs/1002.1176, 2010.

[31] D.W. Ansell, "Antenna Performance Optimisation using Evolutionary Algorithms." PhD thesis, University of Cranfield, UK, 2004.

[32] "MEX-files Guide." Internet: <http://www.mathworks.co.uk/support/tech-notes/1600/1605.html>, 2012 [March 11, 2012].

CHAPTER 6:

Measurement

6.1 Introduction

In this chapter, the actual design and experimental validation are outlined in detail. The phased array system consists of 2x2 dipole antennas, power divider, phase shifter and attenuation circuit and voltage supply are designed and constructed. The characteristics such as return loss and transmission coefficient for each element are simulated and measured. The frequency of operation is chosen at 2.45 GHz since the anechoic chamber is working below 3 GHz. Then, all the elements are set-up before the pattern measurement takes place. The elements are held together using a Rohacell substrate mounted on the platform. Several trials are made to the prototype in order to find the optimum results. The measured pattern is then compared with the simulation using the 3-D algorithm to confirm the validity of the method.

6.2 The Description of the Array Hardware

A block diagram of phased-array dipole antenna system is presented in Figure 6-1. It may be divided into five basic units: power supply, vector network analyzer, Wilkinson divider, attenuator and phase shifter circuit and dipole array. Vector Network Analyzer generates RF signal and splits it into four output signals with equal amplitude and phase using Wilkinson Divider. The four RF signals then flow into the Attenuator and Phase Shifter Circuit. The attenuator and phase shifter circuit is used to control the amplitude and phase of the input signal to each element of antenna array. The amplitude and phase of the signal is controlled by the 30 V power supply and later on it was changed to batteries. All will be explained in detail in the next section. The dipole antennas here act as transmitters in the far-field measurement in an anechoic chamber.

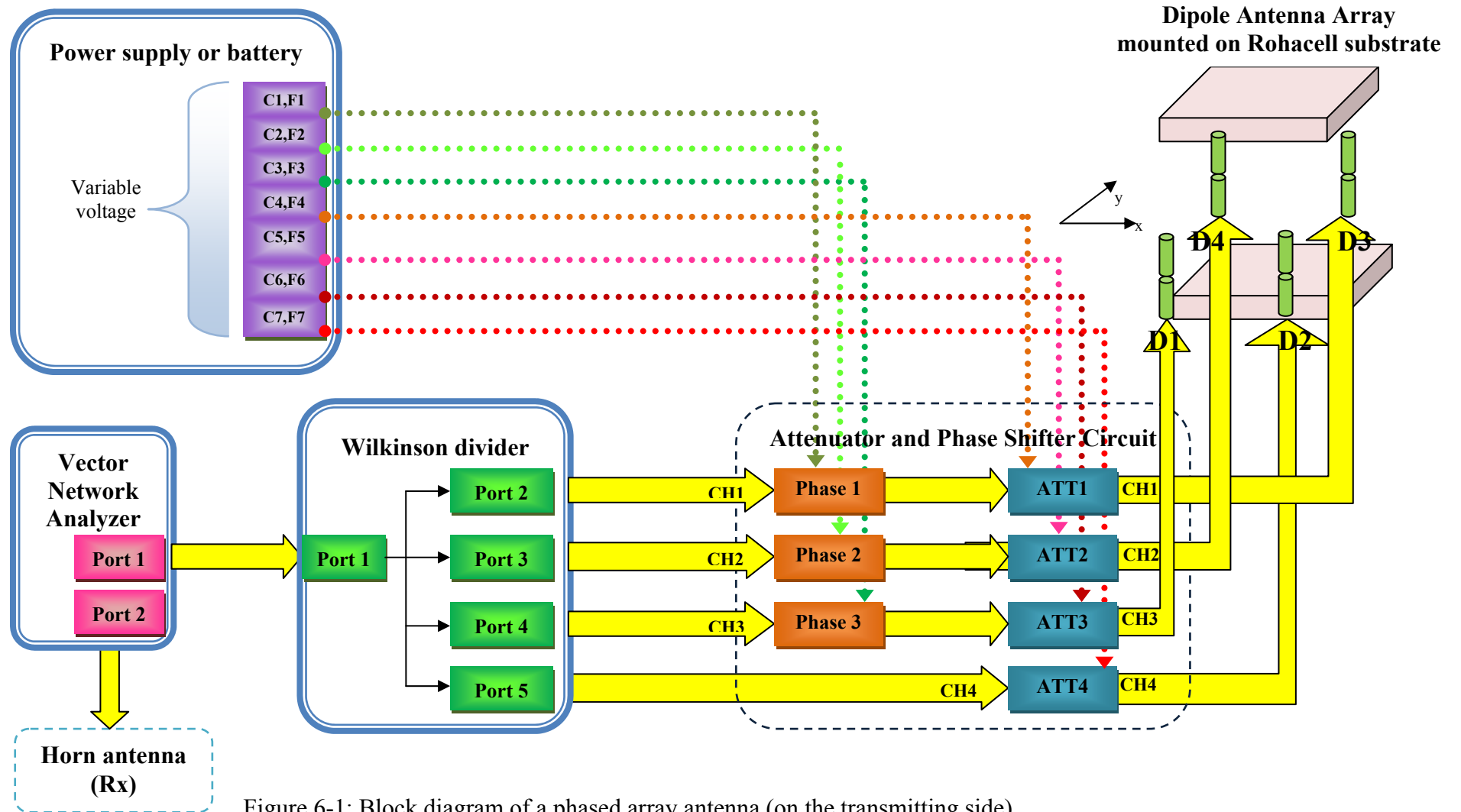


Figure 6-1: Block diagram of a phased array antenna (on the transmitting side).

6.2.1 Dipole Antenna

A conventional centre-fed dipole antenna may be made from a single wire. It consists of two metal conductors of rod or wire, oriented parallel and collinear with each other (in line with each other), with a small space between them. A balun (balanced to unbalanced converter) was designed together with each dipole to cancel the net current flow to the ground on the outside part of the outer conductor of the coaxial cable. This is because the inner and outer sides of the conductors of the coaxial cable are not coupled to the antenna in the same way, thus creating an unbalanced system [1]. Figure 6-2(a) shows the connection between coaxial cable and dipole antenna without a balun. The unbalanced system will create a net current flow, I_3 , on the outer surface of the coaxial cable. Figure 6-2(b) shows that by incorporating a balun between coaxial cable and dipole will make the impedance, Z_c , very large, thus choking the outside current, I_3 , in the unbalanced system, resulting in a balanced system.

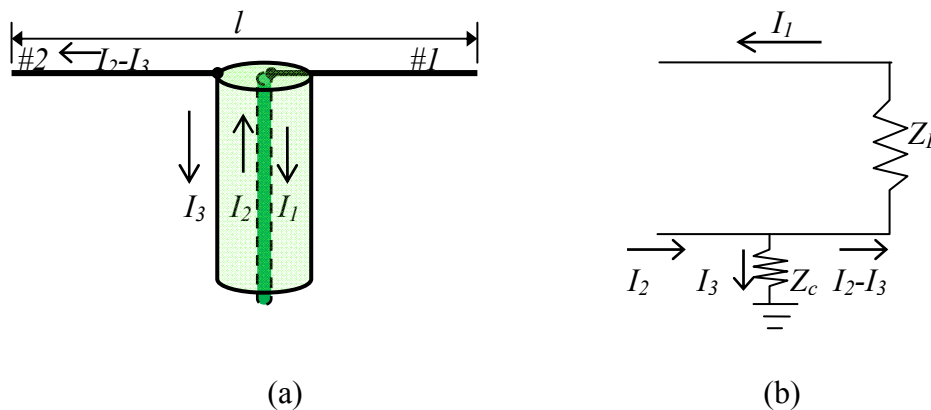


Figure 6-2: (a) The unbalanced coaxial line without a balun, (b) The circuit of balanced system with a balun.

For this case, a balun design from [2] was chosen due to its ease of manufacture together with the dipole element. Moreover, the design provides a wide band frequency range to match with the resonance frequency of the dipole antenna. Figure 6-3 shows the balun consists of two lengths of coaxial transmission lines, d and e , connected to each other (Figure 6-3). The symbols Z_d , Z_e and Z_{de} represent the characteristic impedance of lines d , e and the coupled lines de .

In Figure 6-3, terminal H represents the connection for the external unbalanced source (or load), while terminals F and G are the points of connection for the balanced load (or source). The centre conductors of lines d and e are connected at D , while the outer conductors of both lines are connected at C . The end point of the centre conductor of line e is at E . The length from point E to point FG is $\lambda_0/4$ at resonant frequency.

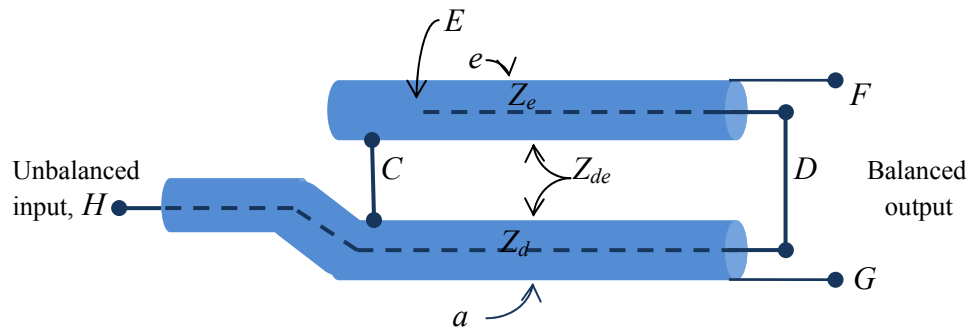


Figure 6-3: The schematic of a wide band balun.

6.2.2 Wilkinson Power Divider

A Wilkinson divider [3] is used to divide the amplitude equally and in phase of the radio frequency signal from one input source into several output sources. In addition, it provides high isolation between output ports and approximately matched impedance around 20 per cent of the frequency band. The divider can be made in microstrip or stripline form.

Kowalczyk [4] based on Pozar [5] designed two-way Wilkinson divider at 2.45 GHz. The design is similar to those shown in Figure 6-4(a) and (b). The design employs two quarter-wavelength lines ($\frac{\lambda_g}{4}$), impedance characteristic of $\sqrt{2}Z_0$ and a lumped isolation resistor of $2Z_0$. Z_0 is the characteristic impedance of the stripline, which is usually 50Ω . Theoretically, the output signal resulting from this divider is $-1/2$ or $-3dB$ at each port, with the isolation between the output ports being zero.

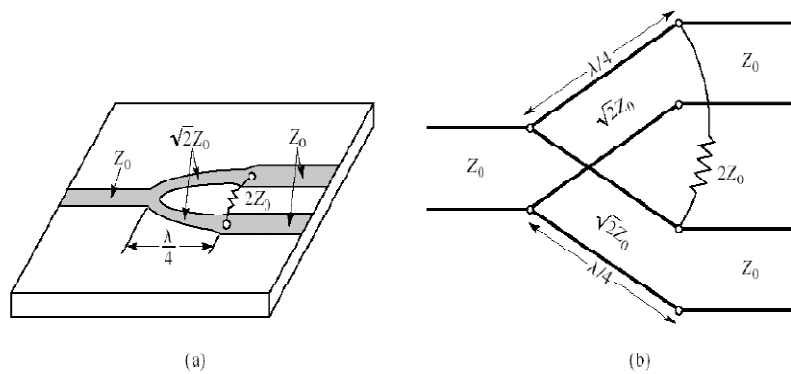


Figure 6-4: a) Two-way Wilkinson divider in microstrip form. b) Equivalent transmission line circuit [5].

For the work described in this thesis, a four-way Wilkinson divider was designed to obtain four output signals with the same amplitude and phase. This may be made using two cascades of two-way Wilkinson dividers, as shown in the following section. Therefore, the output signal for each port is further divided by two, which is equivalent to $1/(4)$ of the input signal.

6.2.3 Phase Shifter and Attenuation Circuit

A control circuit consists of phase shifters and attenuators are soldered onto a *FR4* substrate (Figure 6-5). The aim is to control the amplitude and phase of each signal to the antenna array. The 50Ω surface-mounted voltage variable attenuators EVA-3000+ [6] and phase shifters JSPHS-2484+ [7] were obtained from Mini Circuits. The maximum control voltage for attenuators is 9 V, and for phase shifters is 15 V. The phase range for the phase shifter is 0–180°. The operating frequency for both EVA-3000+ and JSPHS-2484+ are from 0.05 to 3 GHz and 2.15 to 2.484 GHz respectively. The copper track has been etched on *FR4* with a thickness of 2.54 mm. The attenuators and phase shifters are then soldered onto the copper track. The width of the copper track has been set to 3.8 mm at 2.45 GHz, similar to the width track on Wilkinson Divider. However, the width track has been narrowed down to smaller width due to the small size of the leg of the phase shifter chips which cannot be avoided. Moreover, the phase shifter and attenuator circuit is difficult to simulate in electromagnetic softwares, thus complicates the design of the circuit. The DC (direct current) voltage, which acts as the supply and control voltage to both chips, is fed from the DC power supply of 30 V using 5 m of thin cables. The long cables ensure that the feed

network can be rotated together with the antenna array during the far-field pattern measurement.

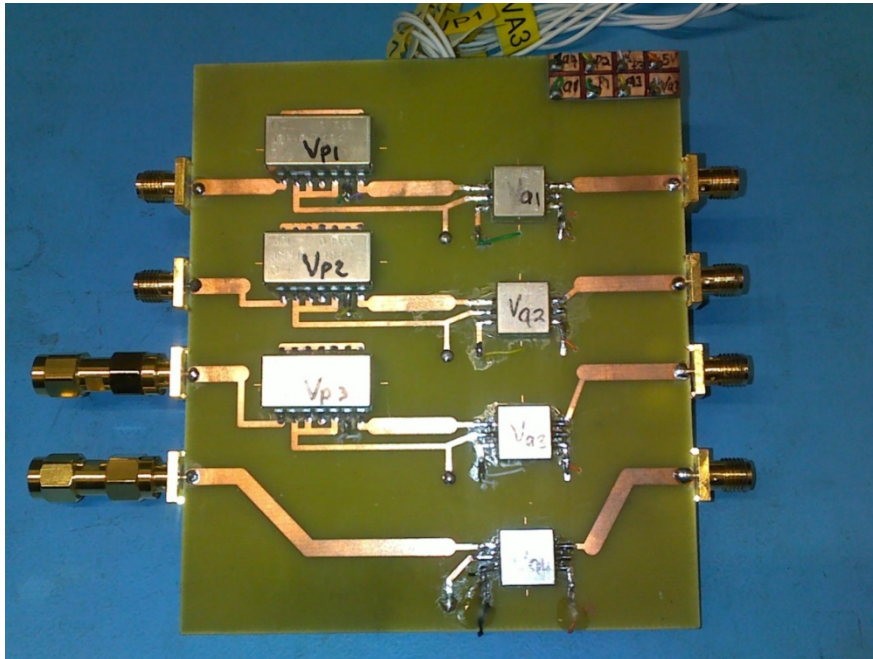


Figure 6-5: Wilkinson divider, phase shifter and attenuation circuit at 2.45 GHz.

6.2.4 Vector Network Analyser

In this case, a vector network analyser (VNA 37397D) from Anritsu was used for reflection (S_{11}) and transmission (S_{12}) coefficient measurement. The measured value is always a combination of the actual value and the systematic measurement errors. Systematic errors are repeatable errors due to imperfections in the components, connectors and fixtures. The VNA needs to be calibrated first in order to remove systematic errors and take into account the presence of any accessories (i.e. adaptors) that may have been added to enable specific measurements to be made. The calibration can be performed in many ways; such as using SOLT (Short, Open, Load and Thru line) or AUTOCAL Calibration [8].

6.2.5 Voltage Supply

Seven +30 V DC voltage supplies were used as voltage controls for JHPHS 2484+ and EVA 3000+ and another +5 V was used as the voltage supply for JHPHS 2484+ (Figure 6-6). The DC voltages are varied according to the desired amplitude and phase of the signals. However, the ratio between the maximum

Section 6.2. The Description of the Array Hardware

and minimum amplitude and phase of the input signals should not be too large to ensure that they are physically realizable. At a later stage, another voltage supply circuit with batteries (+18 V or 2 x 9 V and -4.5 V or 3 x 1.5 V) and voltage regulator circuits have been designed to replace voltage generator and shown in Figure 6-7.

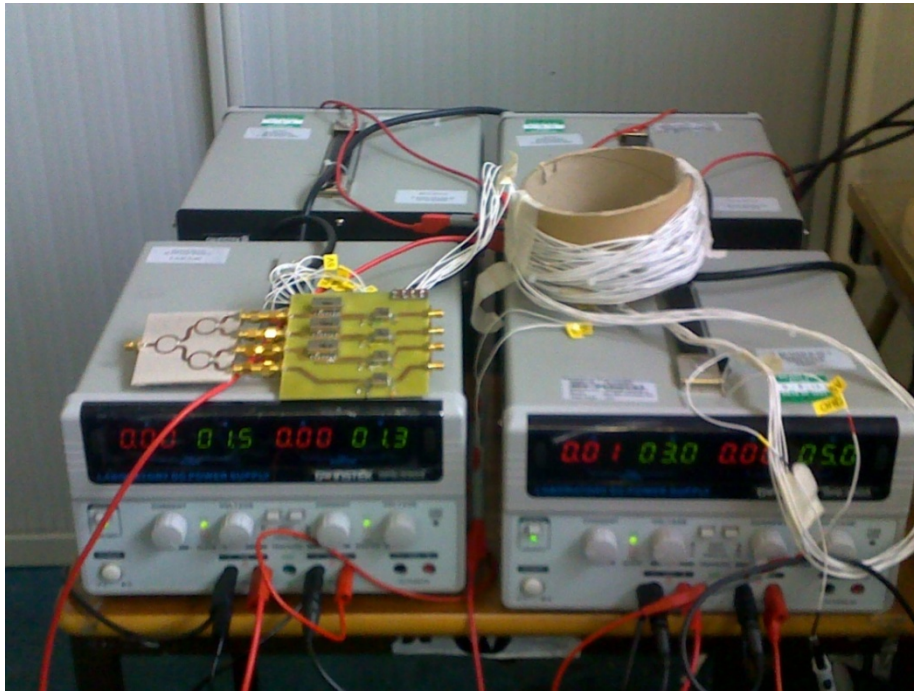


Figure 6-6: DC voltage supplies for JHPHS 2484+ and EVA 3000+.

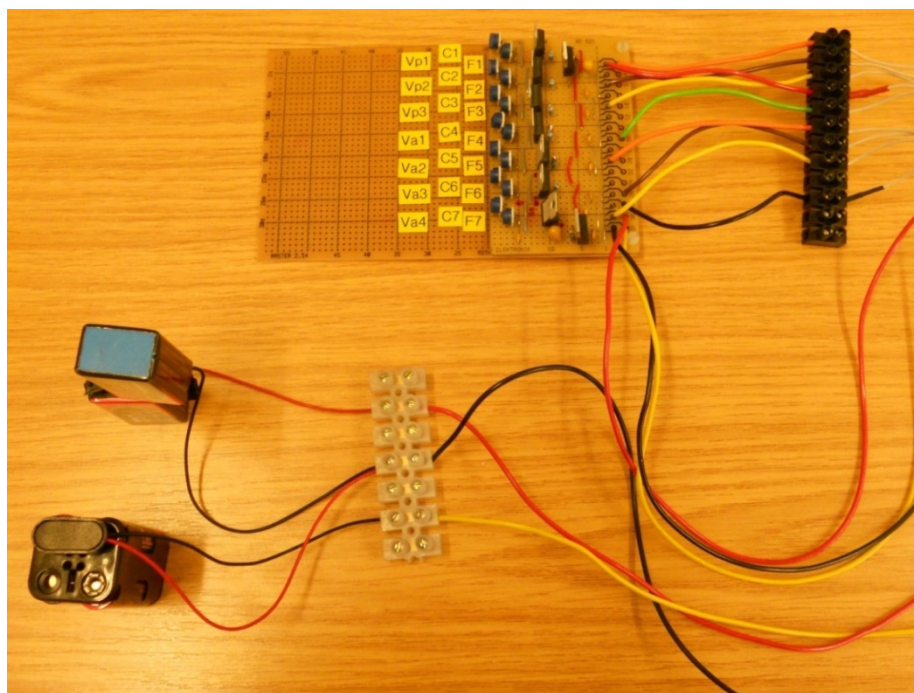


Figure 6-7: Battery supplies and voltage regulator circuit.

6.3 Simulation, Fabrication and Measurement Results

6.3.1 Dipole Antennas

The simulation for each dipole antenna was performed using Empire XCcel (Figure 6-8). Each dipole was fed using a perpendicular lumped port as an excitation source. The length and diameter of each dipole is shown in Table 19 to match with the fabrication. Four centre-fed half-wavelength dipole antennas at 2.45 GHz were then fabricated using RG-58/U coaxial cable and soldered to male SMA connectors (Figure 6-9). The simulation and measurement return loss for each dipole is shown in Figures 6-10 to 6-13.

The return loss for each dipole was measured using Anritsu VNA [8]. It is observed that the resonant frequency for measured plots is shifted compared to the simulated plots in Figure 6-10 to 6-13. However, all the measured return loss falls at desired frequency of 2.45 GHz. It is due to the cut-and-try approach during S_{11} measurement. The different traits between simulated and measured plots are due to several reasons:

- The measured plot for all dipoles has got more resonances and ripples as compared to the simulated plot. Ripples occurred at the earliest frequencies in dipole 4 is probably because of the improper calibration that been performed in the first place. Extra ripples and resonances from the measured plot especially in dipole 1 could be due to the losses (copper and conductor) experienced when designing the dipole.
- The simulation model as shown in Figure 6-8 depicted the design of a dipole with a perfect perpendicular lumped port and not considering balun and connector used as in fabrication. Future work on designing a dipole with a balun will bring the simulation results closer to the measurement.
- Additionally, the fabricated antenna has experienced some tolerance error when assembling the antenna, balun and connector. The diameter of dipole antenna is thin (2.06 mm) make it susceptible to break during measurement.

Figures 6-10 to 6-13 shows that dipole#2 has better return loss in comparison to other three dipoles.

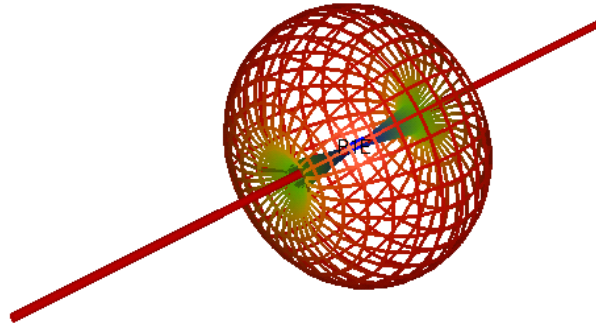


Figure 6-8: A model of a dipole antenna and its far field pattern using Empire XCcel.

Table 20: The length and diameter of four dipole antennas

Index No.	Length (mm) with 2 mm feed gap	Diameter (mm)
1	52.73	2.06
2	53.12	2.06
3	53.55	2.06
4	53.12	2.06

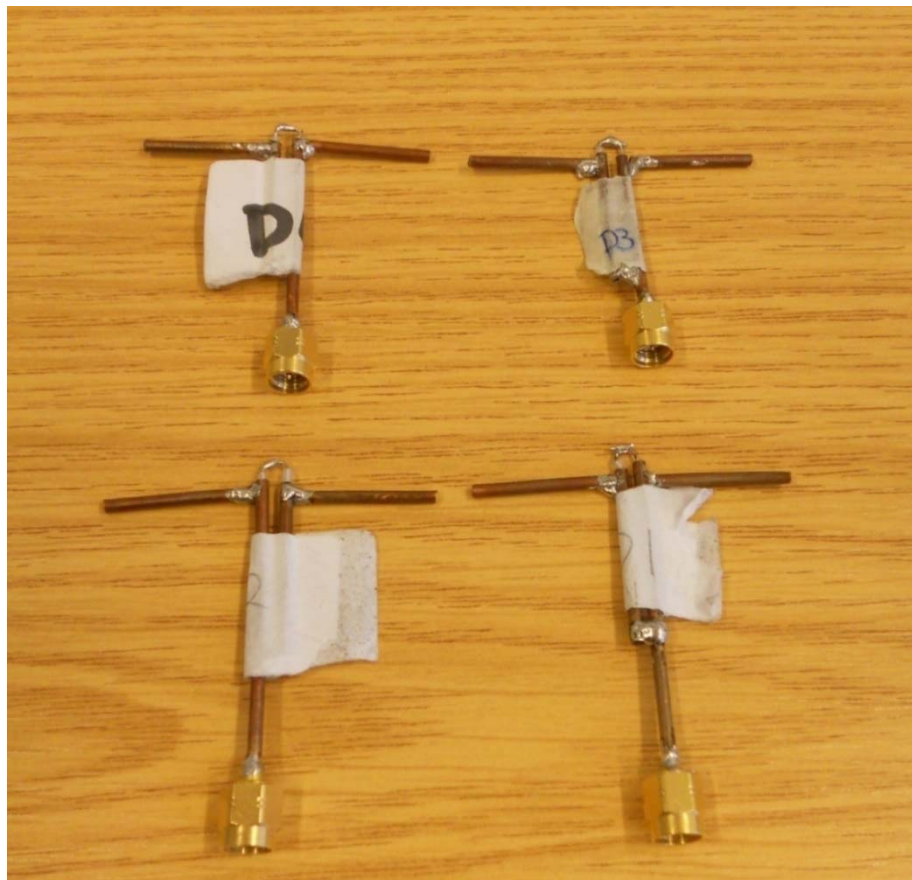


Figure 6-9: Four fabricated dipole antennas with balun.

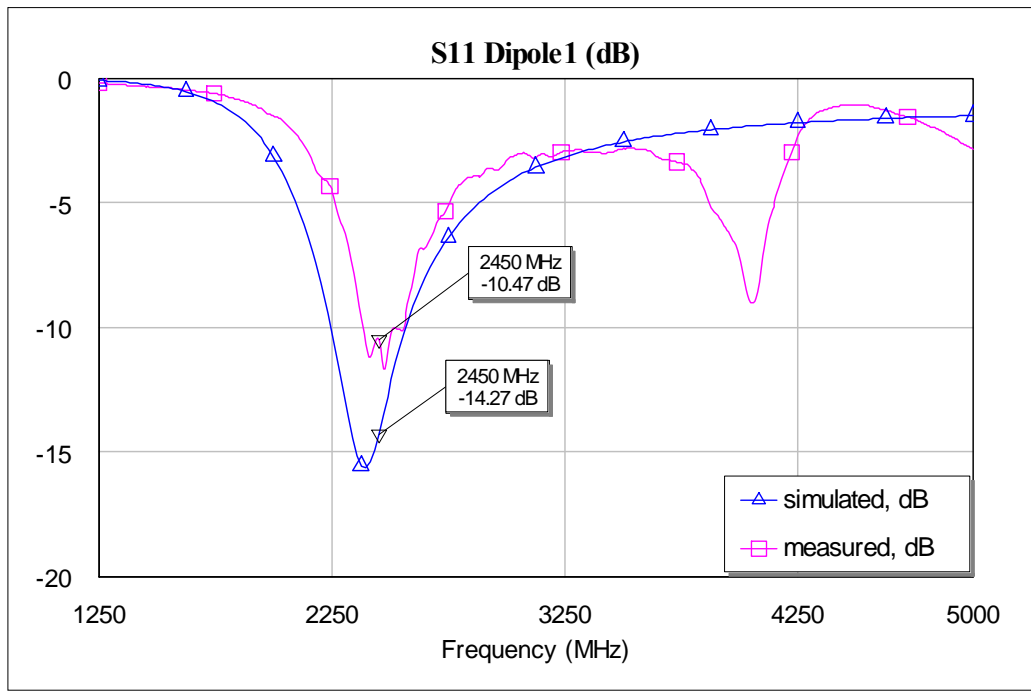


Figure 6-10: Simulated and measured return loss for dipole 1.

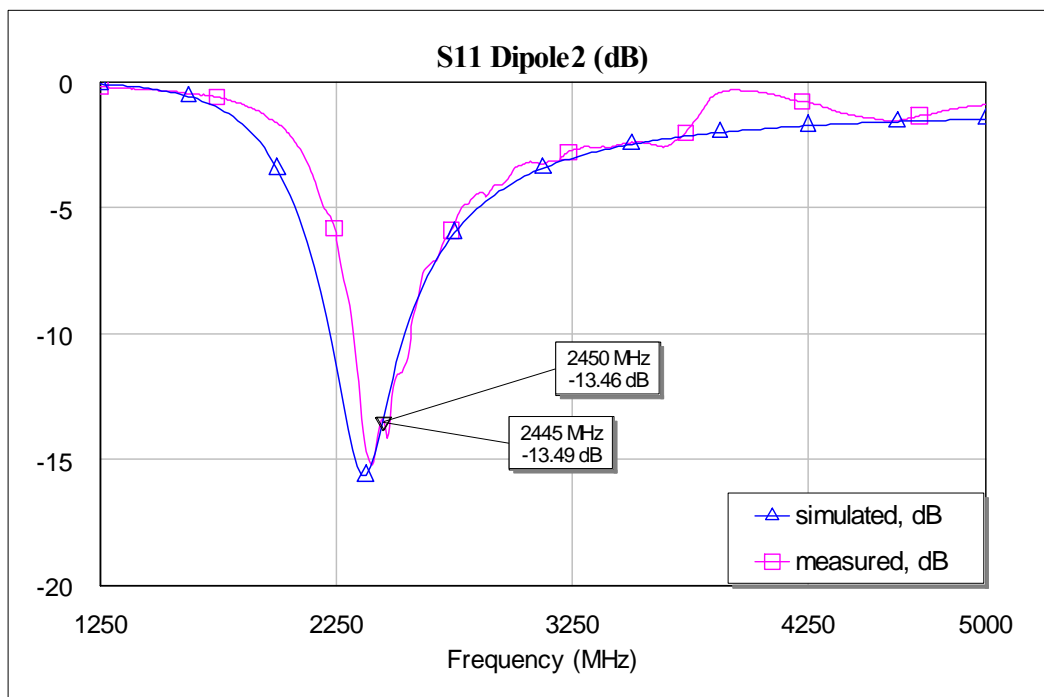


Figure 6-11: Simulated and measured return loss for dipole 2.

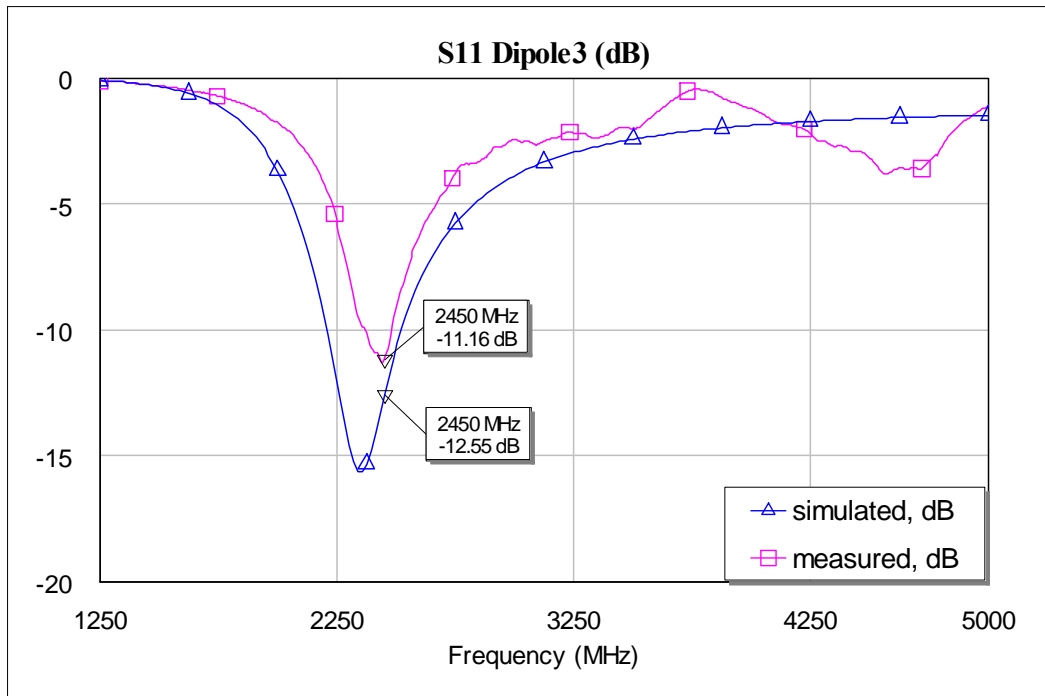


Figure 6-12: Simulated and measured return loss for dipole 3.

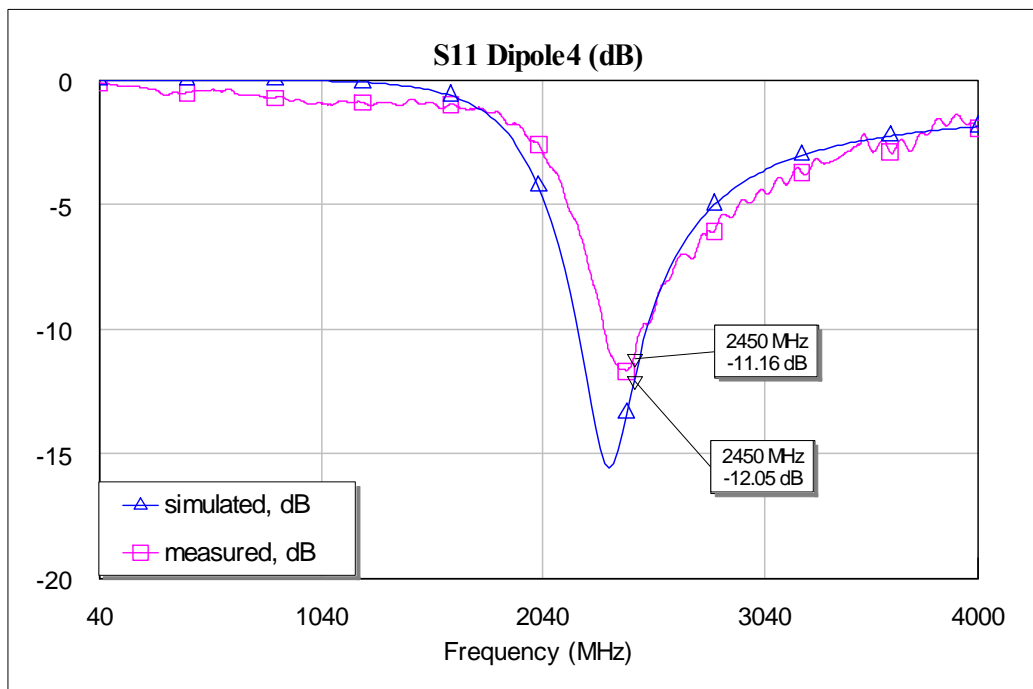


Figure 6-13: Simulated and measured return loss for dipole 4.

6.3.2 Four-way Wilkinson Divider

A Four-way Wilkinson divider was designed using Empire XCcel to split into four output signals with equi-amplitude and phase. The desired frequency of 2.45

GHz and Z_0 of 50Ω requires the isolation resistors (R_1 , R_2 and R_3) to be $2Z_0=100\Omega$. The size of the resistor chosen for this design was SMD1210 (inch). The impedance for the quarter-wavelength lines was $\sqrt{2}Z_0=70.7\Omega$. The dielectric substrate used is *Rogers-RT/Duroid6002* ($\epsilon_R=2.94$) with a thickness of 1.524 mm. The conductor thickness is 0.1 mm. The microstrip line ports are used to excite and terminate the signal at ports 1 to 5. The dimension for the design is shown in (Figure 6-14).

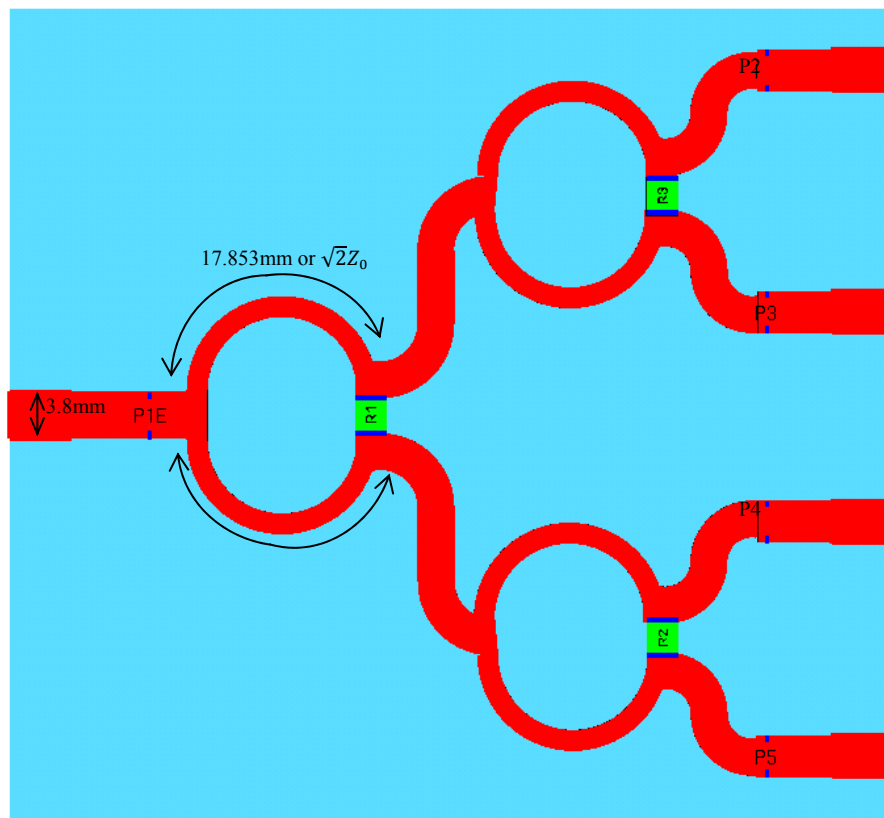


Figure 6-14: The design of a 4:1 Wilkinson Divider using Empire XCcel.

After it was simulated (the results are shown in Figure 6-15 to Figure 6-21), the modelling files were then converted into Gerber files for etching purposes. The 4:1 Wilkinson divider was etched onto a Rogers-RT/Duroid6002 [9] with a thickness of 1.524 mm with copper traces on top of it and ground at the bottom (Figure 6-15). An isolation high frequency chip resistor of 100Ω with a case size of 1206 (obtained from Vishay Thin Film [10]) was then soldered onto every divider. The connectors were also soldered at the end of each track using SMA end launch jack 1.57 PCB, obtained from RS Components, UK [11].

Figure 6-16 shows how to measure S_{11} of Wilkinson divider and Figure 6-17 shows the simulation result for S_{11} is -18.7 dB, while the measurement result is -15.35 dB at 2.45 GHz. The measured plot follows the similar pattern as in the simulated plot with slightly different magnitudes. This could be due to the losses (copper and conductor) in the feeding network. Additionally, the difference of the thickness of the copper lines between quarter wavelength lines (approximately 2 mm) and feeding lines (3.8 mm) resulting losses in the feeding network.

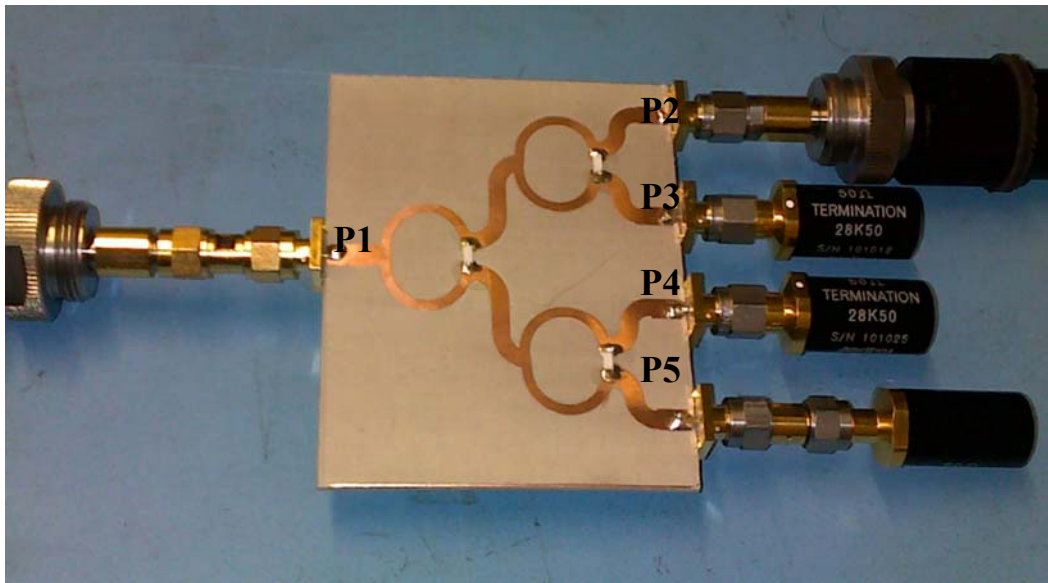


Figure 6-15: Fabrication of the 4:1 Wilkinson divider and its S_{12} measurement.

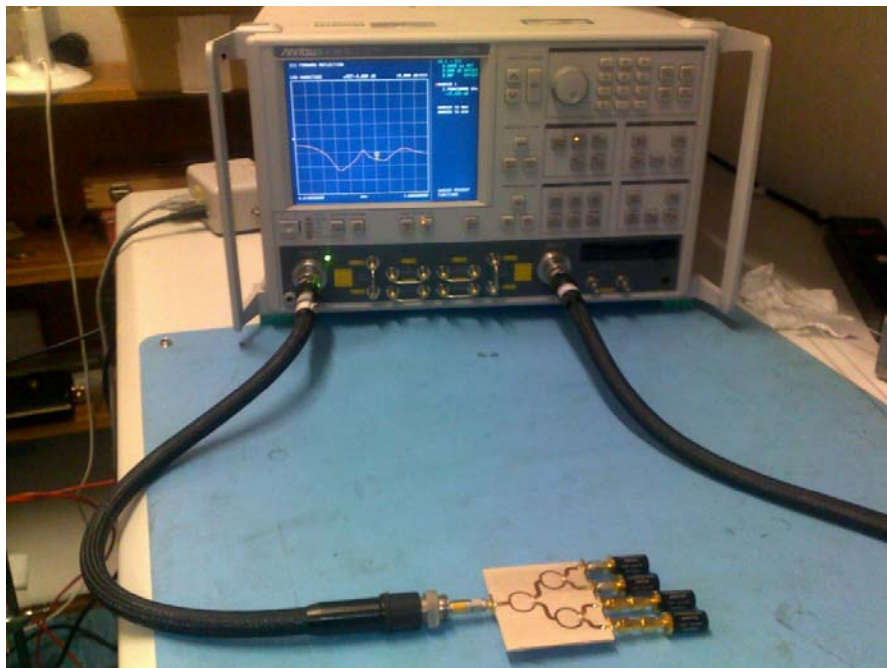


Figure 6-16: Measurement of the S_{11} parameter using VNA.

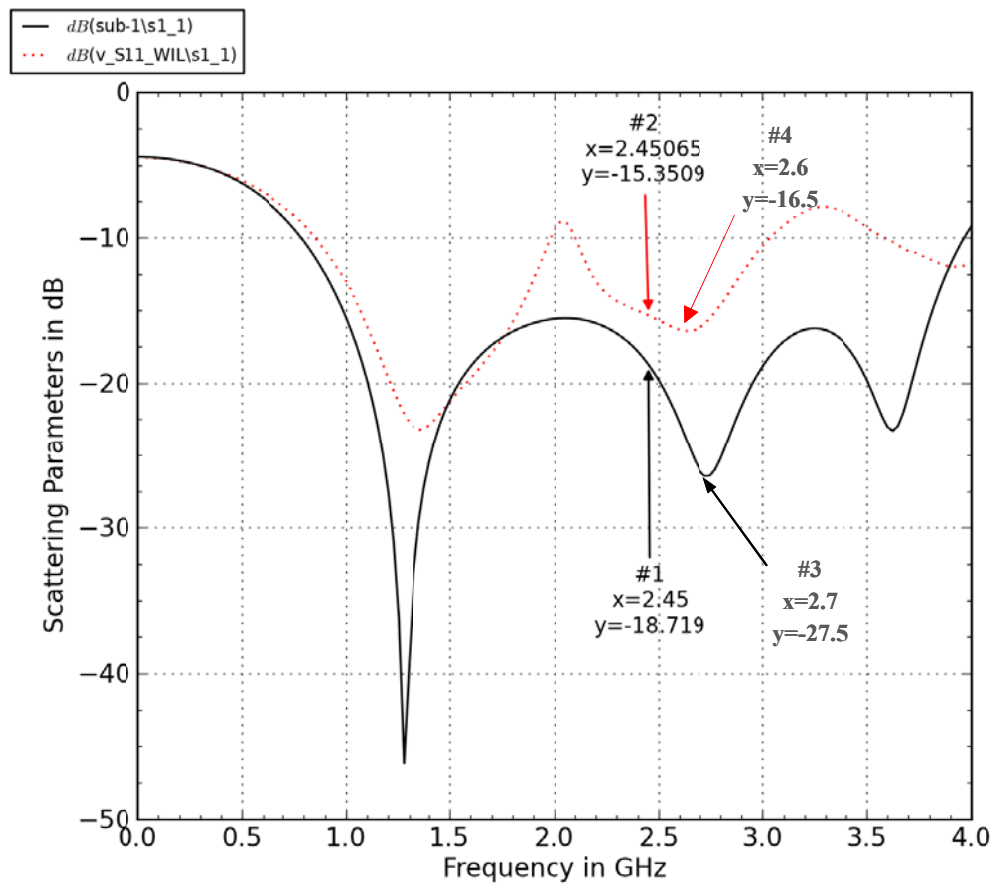


Figure 6-17: Simulation (black line) and measured results (red-dotted) of S_{11} .

The transmission coefficients between the input (port 1) and output ports (ports 2, 3, 4 and 5) may be obtained by connecting one input and output cable of the network analyser to the input (port 1) and output port (i.e. port 2) to obtain S_{21} . The remaining ports are terminated with 50Ω load impedances (Figure 6-15). A similar technique was then repeated by interchanging the output cable to ports 3, 4 and 5 in order to obtain insertion losses for S_{31} , S_{41} and S_{51} . Figures 6-18 to 6-21 show the simulation and measurement results magnitude and phase of S_{21} , S_{31} , S_{41} and S_{51} respectively. They show that the magnitude of simulation and measurement results are in good agreement with each other around -6 dB at desired frequency, as expected. It means that the signal transmitted from port 1 will be reduced by 6 dB when it reached at port 2, 3, 4 and 5. However, it should be noted that S_{21} reduced substantially at 2.05 GHz about -11 dB. The same phenomenon occurred to S_{31} at 1.75 GHz, S_{41} at 1.52 GHz and S_{51} at 1.8 GHz. It is possibly due to the fabrication process, the effect of the connectors which are not included in simulation and measurement errors. However the

abovementioned frequency is less than 2.1 GHz and is not being used in the upcoming measurement.

The phase of simulated and measured results at 2.45GHz differ approximately 110° for all cases. It is possibly due to the extra length of copper added on top of FR4 for the soldering process of internal resistor which is not included in simulation. However, the simulated and measured phase between all ports are almost similar (around 20° and -90° respectively) that ensures the output signals of each port are in phase with each other. The current distribution for the 4:1 Wilkinson Divider at 2.45 GHz is shown in Figure 6-22.

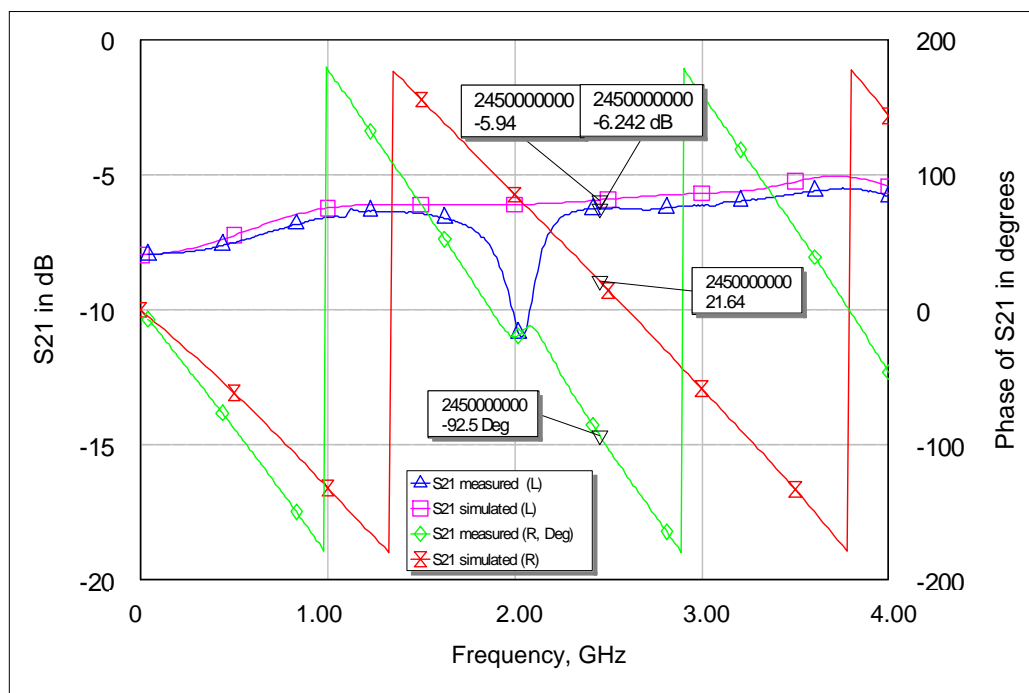


Figure 6-18: Simulated (magenta line) and measured (blue line) magnitude of S_{21} are on the left axis (L) while the simulated (red line) and measured (green line) angle of S_{21} are on the right axis of the graph.

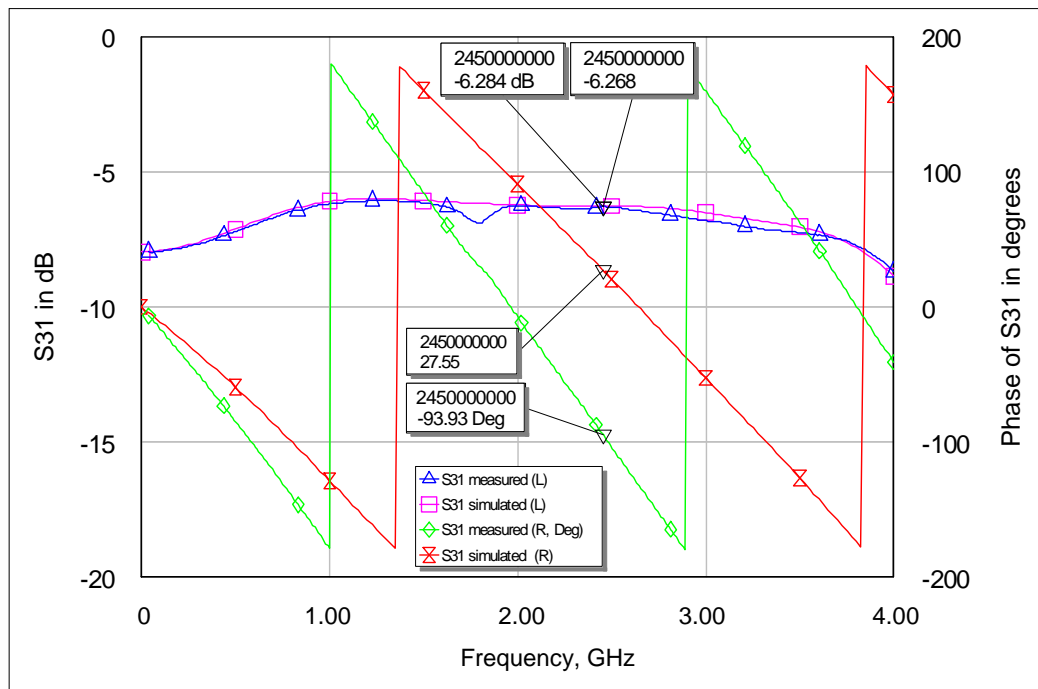


Figure 6-19: Simulated (magenta line) and measured (blue line) magnitude of S_{31} are on the left axis (L) while the simulated (red line) and measured (green line) angle of S_{31} are on the right axis of the graph.

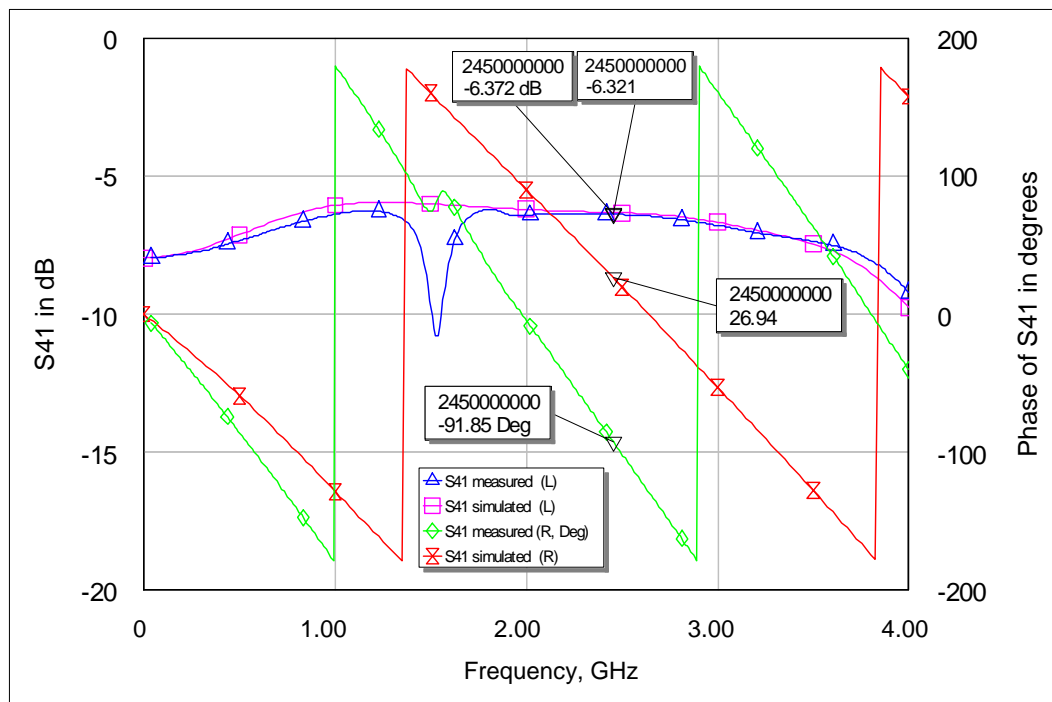


Figure 6-20: Simulated (magenta line) and measured (blue line) magnitude of S_{41} are on the left axis (L) while the simulated (red line) and measured (green line) angle of S_{41} are on the right axis of the graph.

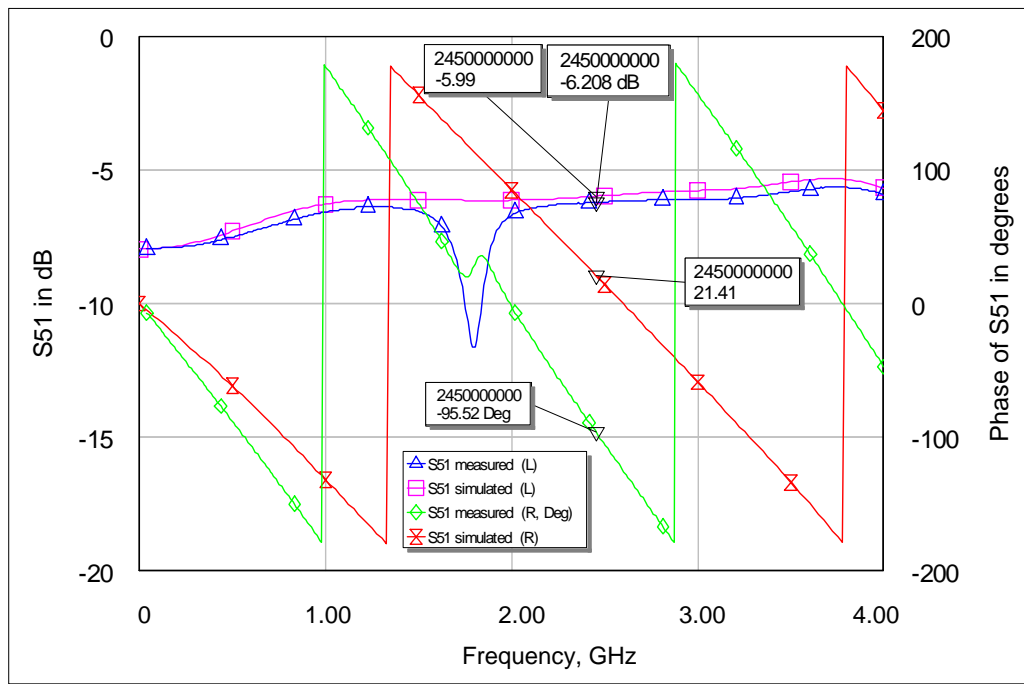


Figure 6-21: Simulated (magenta line) and measured (blue line) magnitude of S_{51} are on the left axis (L) while the simulated (red line) and measured (green line) angle of S_{51} are on the right axis of the graph.

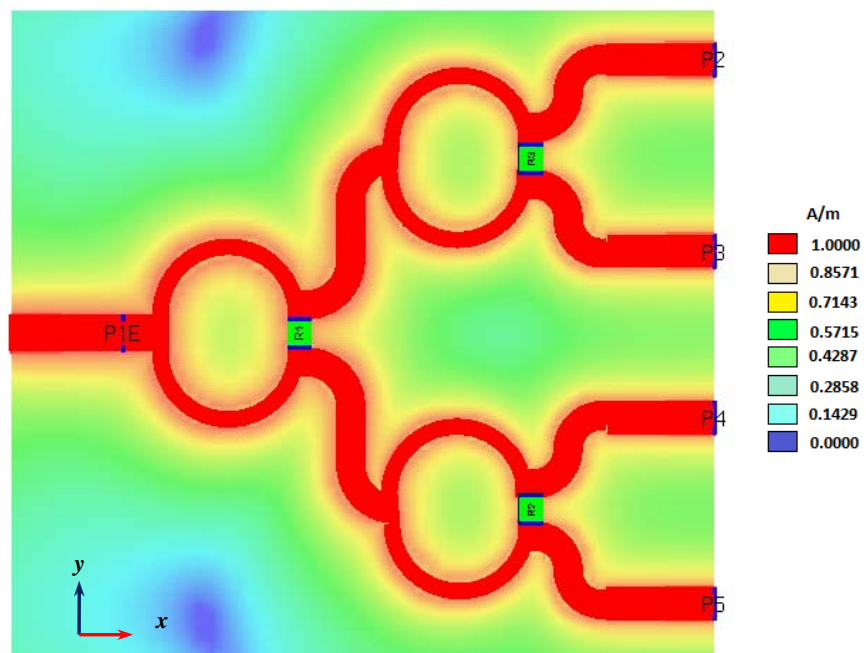


Figure 6-22: The current distribution of the 4:1 Wilkinson divider at 2.45 GHz using Empire XCcel.

6.3.3 Phase Shifter and Attenuator Circuit

One of the main concerns regarding phased-array systems is their calibration. Figure 6-23 elaborates some points where the phase and amplitude errors may be introduced in a phased-array antenna. Points 1 to 3 introduce errors in the RF phase and amplitude control sections, while the remaining points (points 4 to 7) introduce the errors that exist in the physical antenna configuration. There are several reasons for these errors, including [12]:

- Improper control voltages being applied to the phase shifter and attenuator (1).
- Unwanted amplitude variations (insertion loss) across the control range of the phase shifter (2).
- Unwanted phase variations across the amplitude range of the attenuator (3).
- Discontinuities at the interfaces between lines and connectors (4).
- Differences in the length of transmission lines (5).
- The air interface discontinuity (6).
- Mutual coupling between antennas (7).

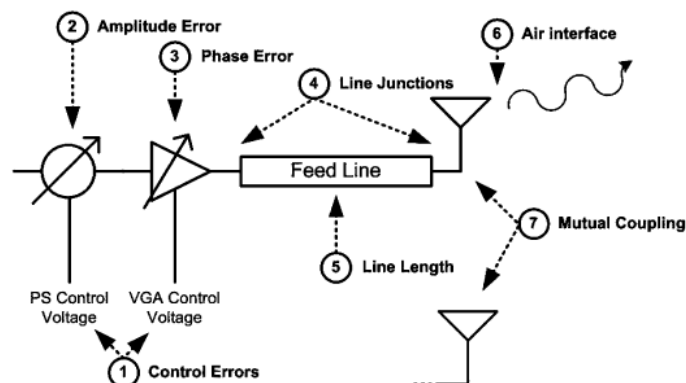


Figure 6-23: Points where phase and amplitude errors may be introduced in each branch of a phased array antenna [12].

The value of the attenuation (EVA-3000+) and phase shift (JSPHS-2484+) for each dipole are controlled by DC voltage from the power supply and

later on battery (Figures 6-6 and 6-7). The characteristics of the feed network consisted of a Wilkinson divider and a control circuit were measured using VNA Anritsu at 2.45 GHz (Figures 6-24 and 6-25). First, the phase shift and insertion loss for the feed network were measured when V_p was varied and V_{att} was kept constant. V_p and V_{att} represent the voltage control for the phase shifter (JSPHS-2484+) and attenuator (EVA-3000+) respectively. Later, the same measurements were performed with V_{att} was varied while V_p was kept constant. It is difficult to control the attenuation and phase shift between each channel simultaneously because there are seven voltage controls in the network; thus varying one voltage will influence the attenuation and phase shift of the remaining channels.



Figure 6-24: Feed network characteristics measurement.

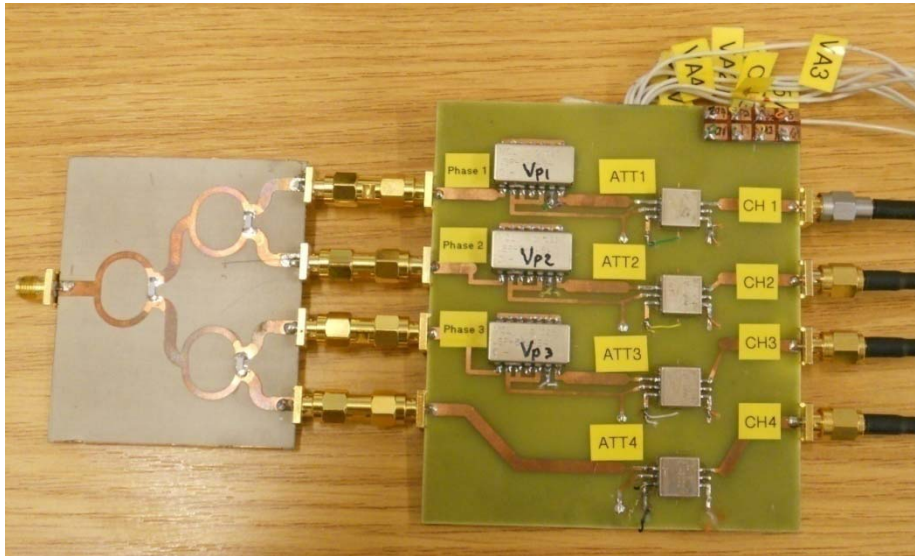


Figure 6-25: Four-way Wilkinson divider, phase shifter and attenuator circuit.

Figure 6-26 shows the characteristics of the phase shift of the feed network versus V_p , while V_{att} is kept constant. The value of V_{att} has been kept to that value as in Figure 6-26 and 6-27 in order to keep the attenuation for each channel as close as possible with each other. The results show that the phase shift is in linear relationship with the control voltage, V_p for CH1, CH2, and CH3 (labelled in Figure 6-26). Figure 6-27 shows the insertion loss of S_{12} for the output ports when V_{att} is kept constant throughout the phase shift measurement for each port. The measured plots show that CH3 nearly has constant attenuation, while CH1 has a maximum of 3 dB attenuation and CH2 has a maximum of 7 dB attenuation as V_p is varied. The reason of CH2 has large attenuation is possibly due to the reflection caused by different transmission line thickness in CH2. The study of the phase shifter and attenuator circuit may be included in the future work of this thesis.

Figure 6-28 shows the characteristics of the phase shift of the feed network versus V_{att} , while V_p is kept constant. The value of V_p has been kept to that value as in Figures 6-28 and 6-29 in order to maintain constant phase between each channel. It is observed that the largest phase shift for four channels occurred when V_{att} is at low voltages. There is no phase shift occurred when V_{att} at 5V for all channels and remain constant until 8V. Figure 6-29 shows the insertion loss for all channels when V_p is kept constant while V_{att} is varied. The

measured plots show that the insertion loss decreased as V_{att} increased from 0-8V.

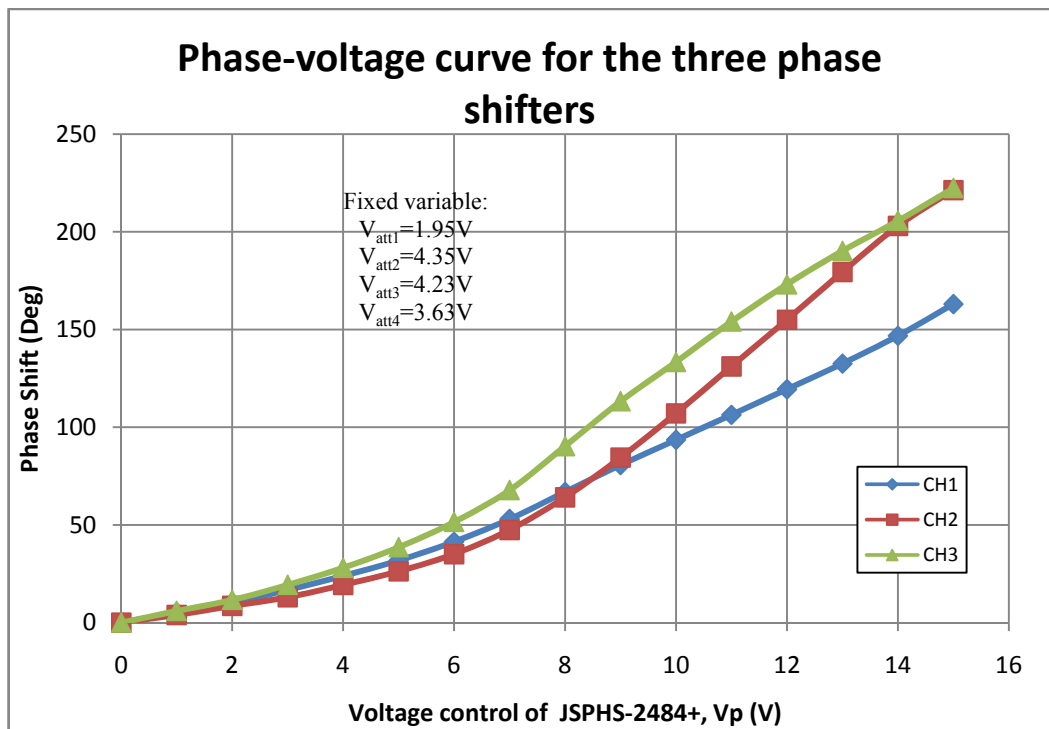


Figure 6-26: Phase shift characteristics for each port versus voltage control of the phase shifter, V_p .

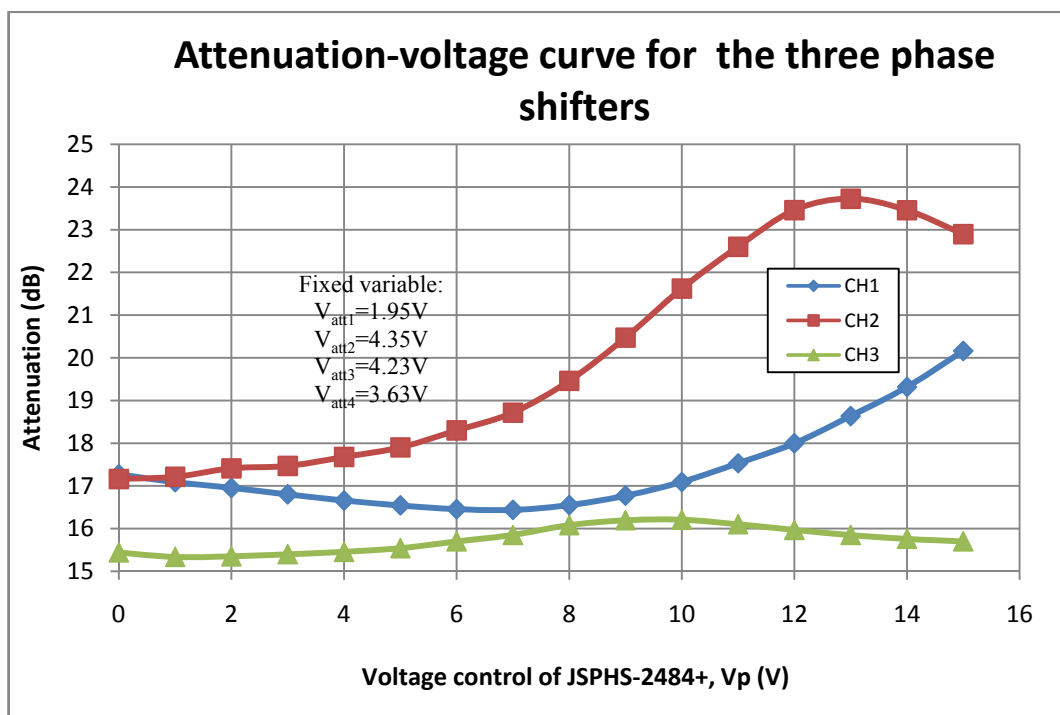


Figure 6-27: Insertion loss for each port versus voltage control of the phase shifter, V_p .

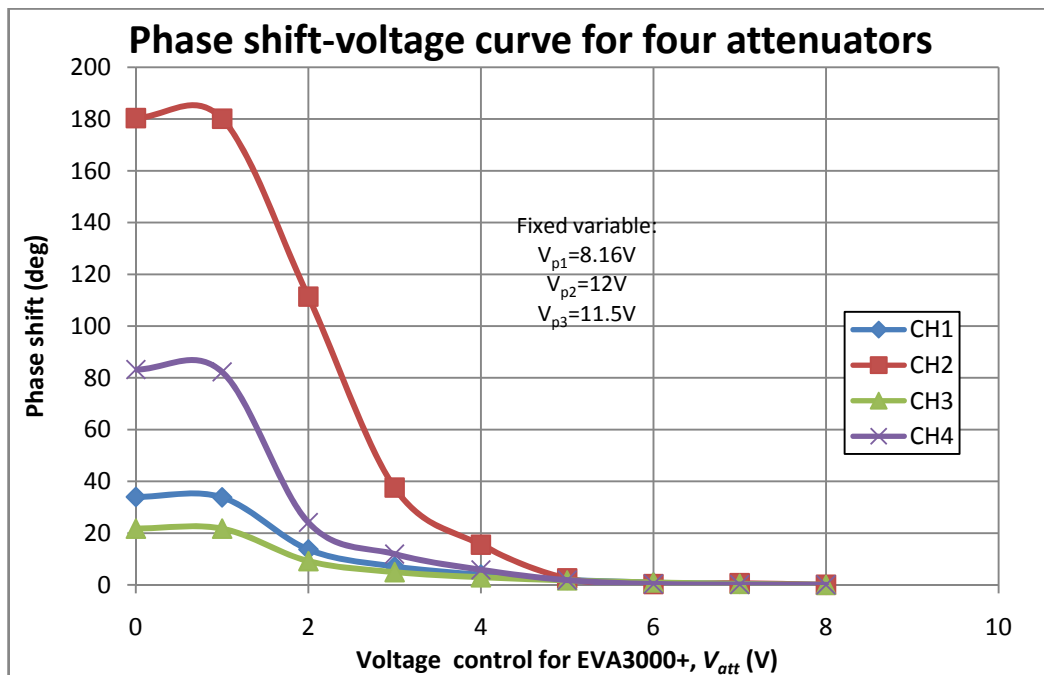


Figure 6-28: Phase shift characteristics for each port versus the control voltage of the attenuator, V_{att} .

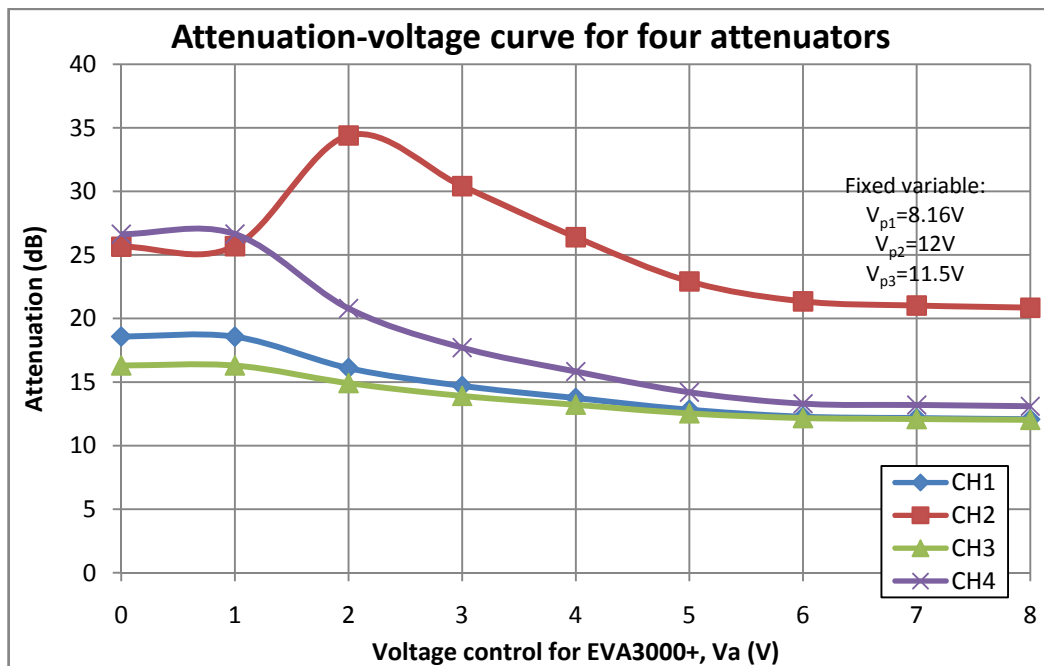


Figure 6-29: Insertion loss for each port versus the control voltage of the attenuator, V_{att} .

From the simulated and measured results in this section, it can be concluded that each device meets the work requirement of this thesis. All those devices will be connected altogether before the array pattern is measured.

6.4 Measurement Set-up

6.4.1 Anechoic Chamber

The measurement set-up was built in an anechoic chamber at the Electrical and Electronic Department at Loughborough University. The anechoic chamber is designed with absorbing material which covers the walls, ceiling and floor to prevent any unwanted reflections during the measurement procedure. It is a controlled measurement environment. The purpose is to create free-space conditions for the design test, because it diminishes reflection and allows direct measurement of the azimuth pattern. It is not influenced by dynamic environment factors that might occurring in the far-field test range such as reflections from buildings, vegetation, seasonal changes, snow or ice. It ensures very accurate measurement results and allows repeatability of the results at any time.

The chamber properties are designed to ensure that an accurate antenna measurement within a certain tolerance can be achieved. The characteristics of the chamber include:

- It acts as a closed metal box that eliminates radio wave energy from outside the chamber, which might severely attenuate the signal propagation inside the chamber.
- The absorber lining inside of the chamber is made of foam impregnated with a carbon-like substance, enabling it to absorb radio frequency energy.
- The pyramidal shape of the absorber assists in breaking up any standing waves present inside the chamber.

The wiring diagram of the anechoic chamber at Loughborough University is shown in Figure 6-30.

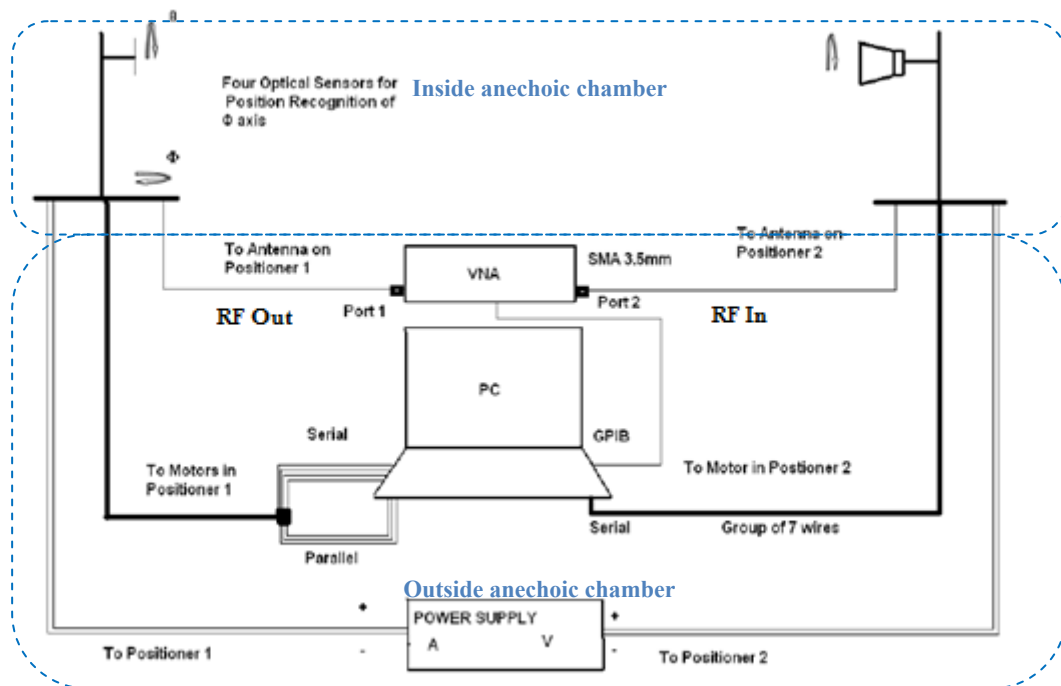


Figure 6-30: Wiring diagram of Loughborough University's anechoic chamber [13]

6.4.2 Transmitter and Receiver Set-up

The Loughborough University anechoic chamber has dimensions of 7 x 3 x 3 m. The two antenna positioners are so made that the distance between antennas becomes approximately 3.9 m. The largest dimension of the dipole antenna array is 110 mm. Therefore, by exploiting the far-field distance equation ($2D^2/\lambda_0$), the critical point of the far-field distance for the dipole antenna array at 2.45 GHz is 197 mm, which shows that the measurement can be performed in the anechoic chamber. The dipole array is known as the device under test (DUT) in this measurement.

The receiving end positioner is fixed and can only rotate the antenna in elevation (θ) plane while the transmitting end positioner can be rotated in both directions: azimuth (ϕ) and elevation (θ) planes. The transmitter is connected to port 1 and the receiver is connected to port 2 of the VNA. This set-up is also explained in Figure 6-30.

For the far-field measurement pattern, a clamp was built to hold the feed network together with the device under test when it is rotating either in the θ or ϕ direction. The DUT consists of 2x2-dipole antenna array which is connected at

the transmitting side of the VNA (Figure 6-31). The power supplies for the attenuators and phase shifters were replaced by +18V and -4.5V battery supplies (Figure 6-32). On the other side, a broadband horn antenna (1-18 GHz) was used to act as a receiver (Figure 6-33). The VNA range is up to 6 GHz and the frequency of the device under test is within the frequency range of the chamber. The rotation of the tower (or positioner) can be controlled with the aid of control software. The measured data (S_{12}) is recorded for every step of 2° for accuracy.

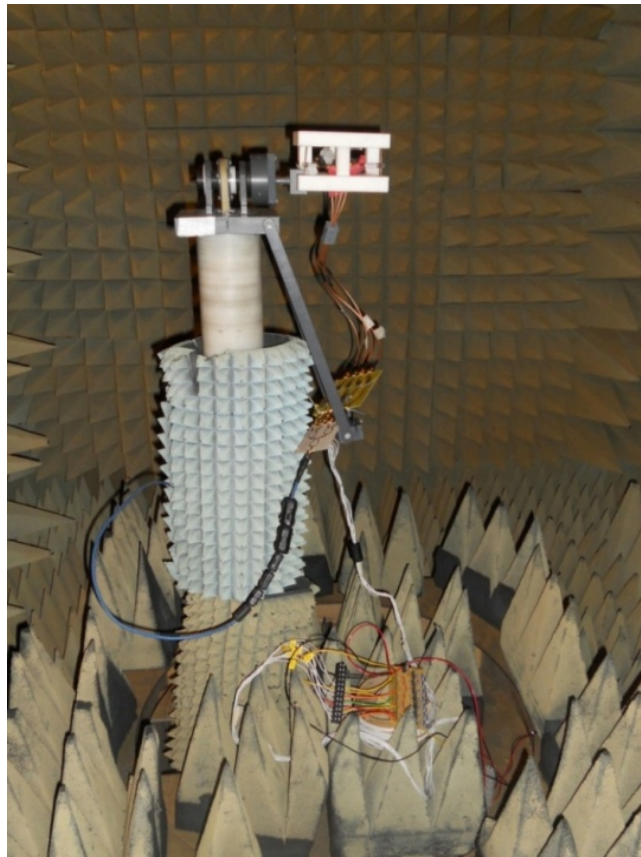


Figure 6-31: Measurement set-up in an anechoic chamber for dipole antenna arrays (transmitter) with the feed network.

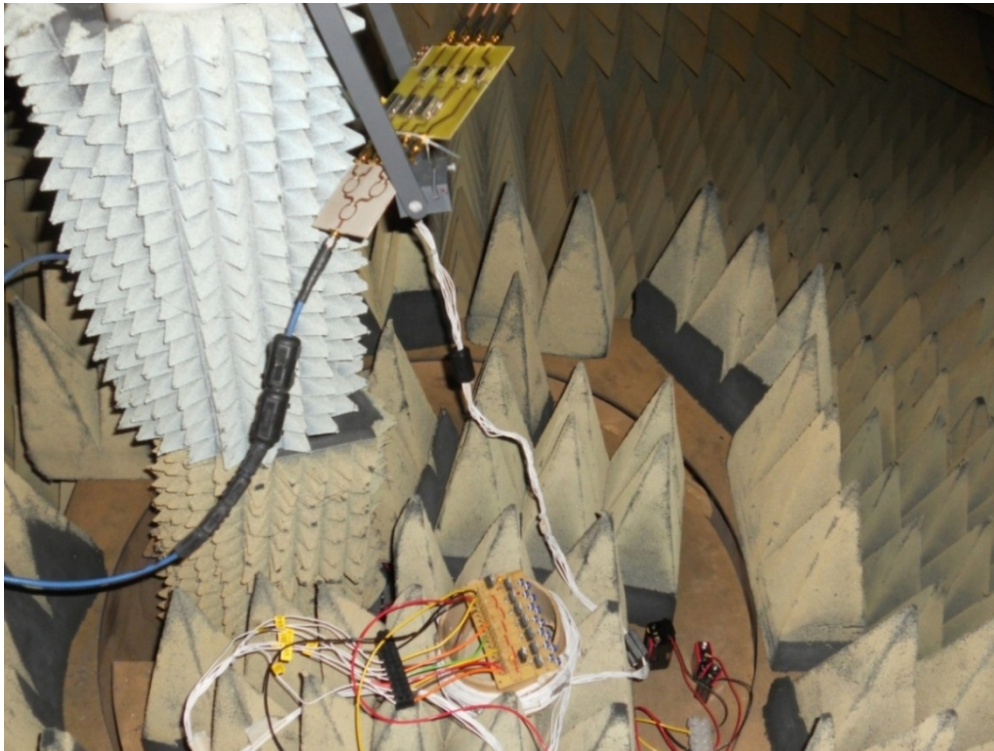


Figure 6-32: The feed network is connected to the batteries, which act as control voltages for the surface mounted attenuator and phase shifter.

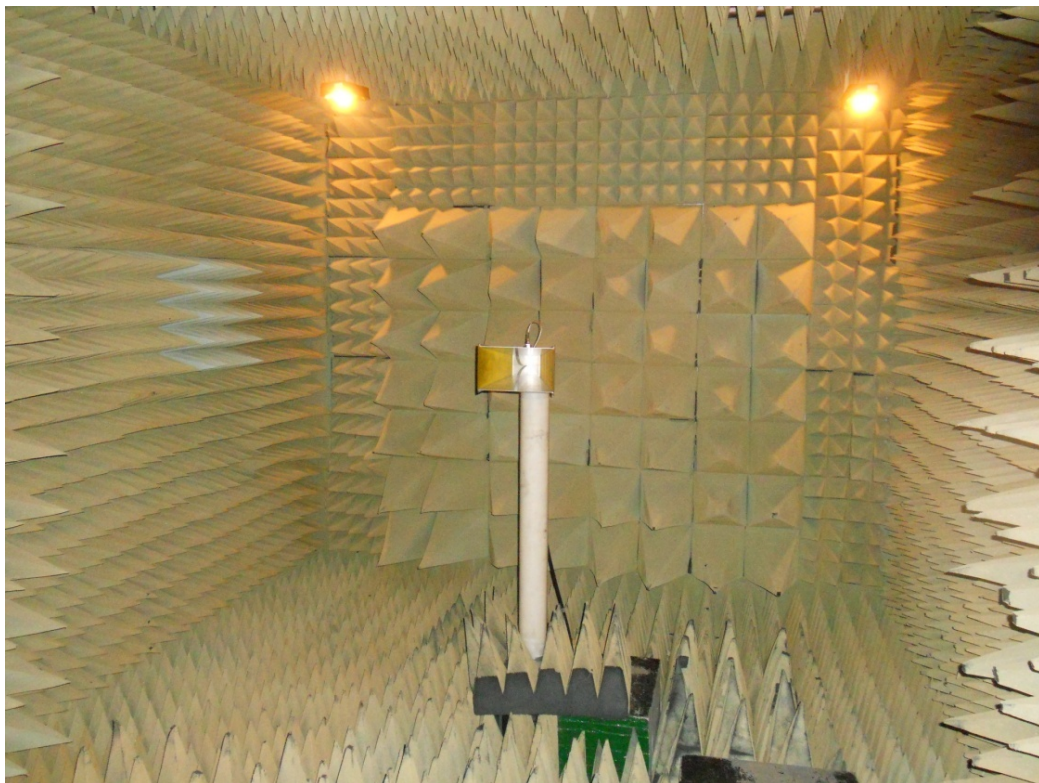


Figure 6-33: Measurement set-up of a horn antenna (1-18 GHz) at the receiving side in an anechoic chamber.

6.4.3 Device under Test: 2x2-Dipole Array with a Feed Network

The aim of this measurement was to measure the far-field pattern for 2x2-dipole arrays with different amplitude and phase excitation of each element. The dipole arrays are held together with spacing 110mm using Rohacell substrates [14] and mounted onto the platform. The spacing is chosen as small as possible in order to demonstrate the effect of mutual coupling. However, due to the arrangement of 2x2 dipoles (2-D array) in diagonal position, the length of balun, connector and cables enabling the smallest spacing that can be obtained is 110mm. Additionally, the spacing is chosen in order to allow the connector and cables through the hole of antenna array as in Figure 6-34. The feed for each dipole is connected to the feed network using four coaxial cables (Figure 6-34). Since the 3-D dipoles array is more complex than 2-D array and requires more feeding network than 2x2 dipole array, the 2-D array has been chosen for pattern measurement. The dipoles are arranged as in Figure 6-34 so that the pattern measurement can be performed for 2-D array and thus validate the 3-D algorithm.

The antenna structure is complex, since it involves not only an antenna array but also the feed network, batteries and voltage regulator circuit, coaxial and thin cables. Therefore, three trials were done with the dipole array in order to validate the 3-D algorithm

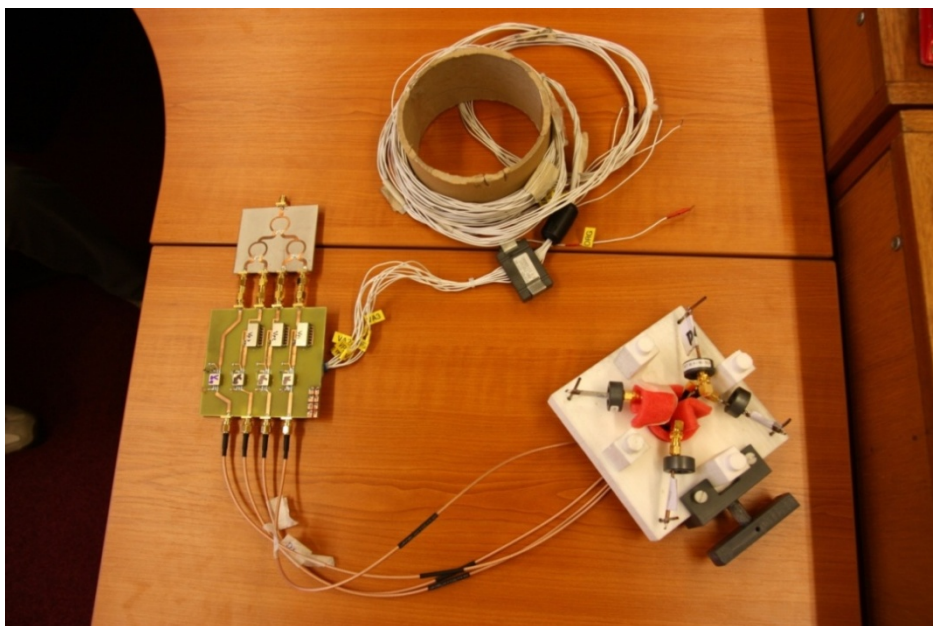


Figure 6-34: Four dipole antennas with the feed network.

6.4.3.1 Trial 1

The first trial is shown in Figure 6-35. Four dipole antennas were connected to the four-port feed network via right angle SMA (F) connectors and SMA (M) straight connectors at the other end. Ferrite rings were placed as close as possible to the feed point of the antenna in order to choke out any unwanted induced current flowing on the outer surface of the coaxial cable shield [15].

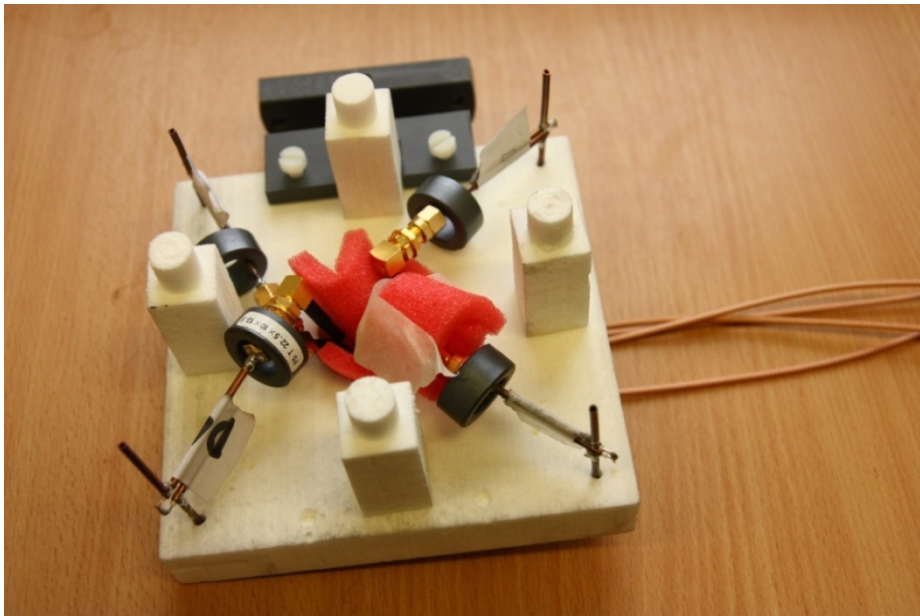


Figure 6-35: Trial 1 of a 2x2-dipole antenna array.

6.4.3.2 Trial 2

The 3-D algorithm only takes into account the mutual coupling effects between antenna elements. Therefore, the possibility of any other effects or coupling with other objects should be removed or kept as far away as possible from the dipole array. The first trial has significant metal right angle SMA connectors, which influence the far-field pattern of the dipole antenna array. Therefore, they were replaced with straight SMA connectors (Figure 6-36) in order to reduce the metal interaction with the dipole array. Moreover, four additional slots were cut (Figure 6-37) to allow connection between the straight SMA semi-flexible coaxial cables, worms and dipole antennas.

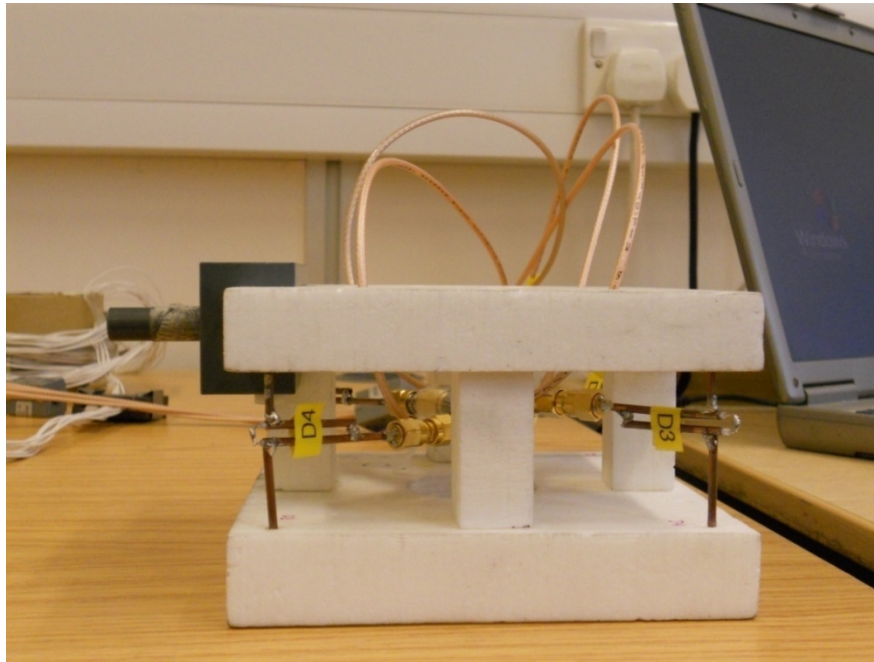


Figure 6-36: The set-up of the dipole antenna array with SMA (M-M) straight coaxial cable, worms and tape to hold the four dipoles together.

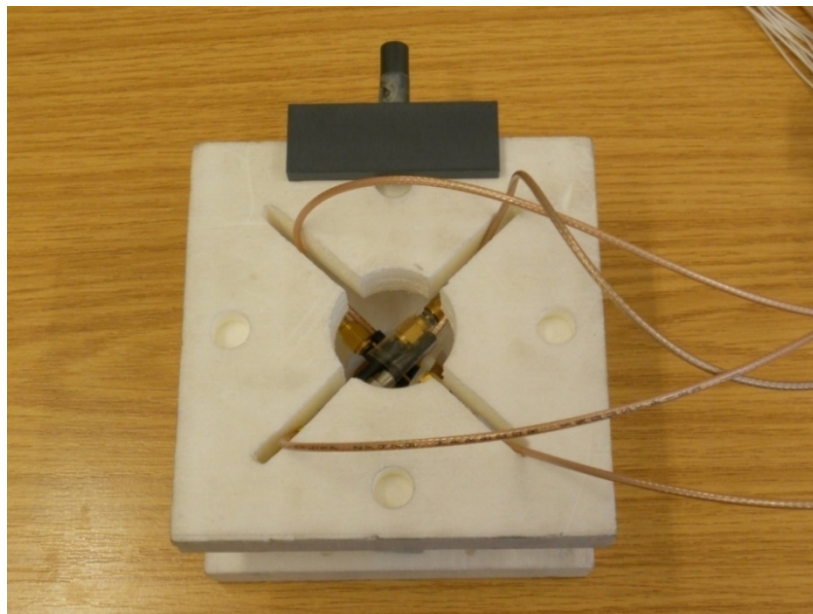


Figure 6-37: Four slots were added to Trial 1 to allow the set-up of straight SMA connectors, worms and semi-flexible coaxial cables.

6.4.3.3 Trial 3

In Trial 3, ferrite rings were added to the structure of Trial 2 in order to suppress the interference from the induced current flowing out of the shield of the coaxial cable. Tie cables were used to hold all the dipoles and the ferrite rings together

so that the structure remained robust and fixed during the pattern measurement (Figures 6-38 and 6-39).

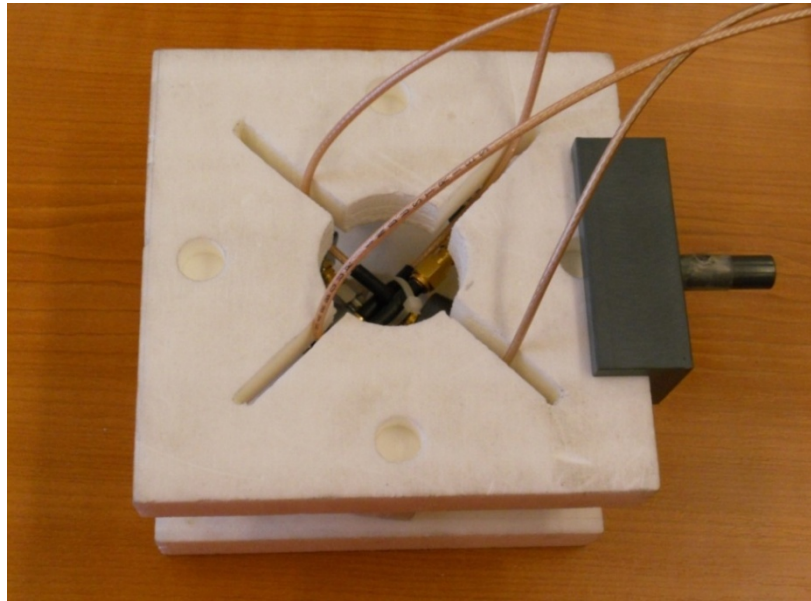


Figure 6-38: Top view of the dipole array with ferrite rings.

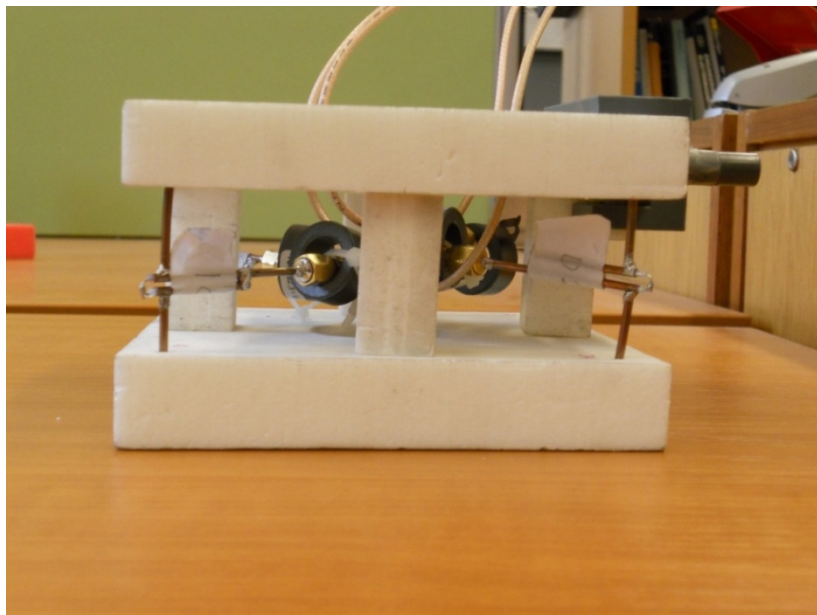


Figure 6-39: Side view of the dipole array with ferrite rings.

6.4.4 Simulation and Measurement Results

To set up the measurement, the dipole array was connected to the transmitting side together with its feed network clamped onto the tower. A broadband horn antenna (1-18 GHz) was connected onto the receiving side. The position of the

device under test should be in the line of sight of the horn antenna to achieve maximum signal strength. After the measurement set-up was completed, the calibration for 12 full terms was performed. The S parameters and far-field pattern were then measured. The results are given in the next section.

6.4.4.1 Trial 1 (Sample #1)

Figure 6-40 shows the measured return loss of the dipole antenna array with a feed network. It is observed that the resonance occurred at 2.56 GHz instead of 2.45 GHz. It is also noted that the measured plot contains ripples and extra resonance. The reason is probably due to the effect of power divider and phase shifter and attenuator circuit that slightly shift the operating frequency and creates extra ripples and resonance to the measured plot. Unfortunately, the measured plot could not be compared with simulated plot since it is difficult to simulate the feed network containing phase shifter and attenuator chips. The control voltage applied to the phase shifter, V_p , and attenuator, V_{att} , is shown in Table 20 (which is known as sample #1).

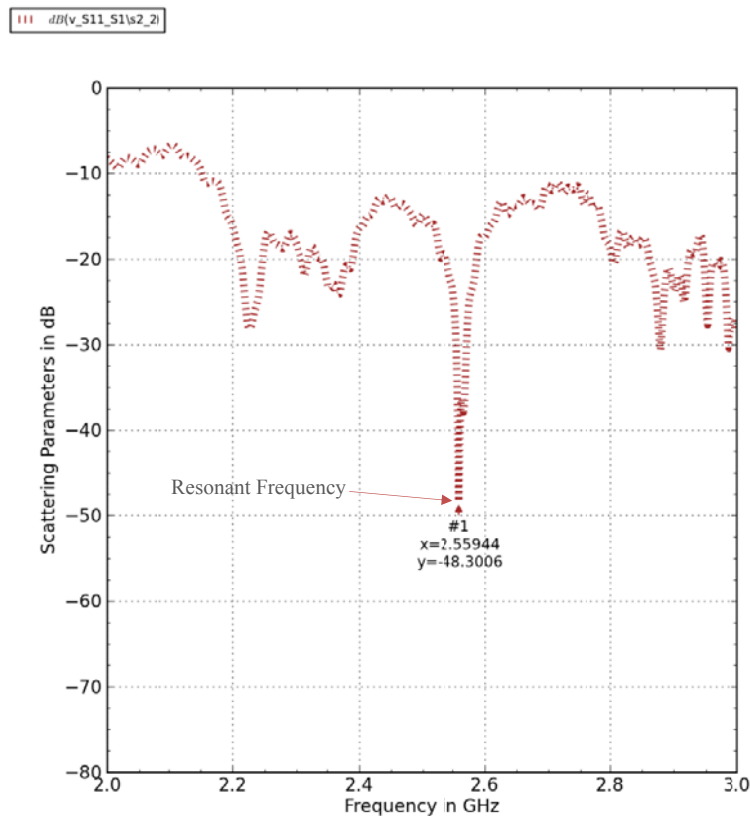


Figure 6-40: Measured S_{11} of Trial 1. The x - and y -label refers to the Frequency (GHz) and S parameters (dB) according to the x - and y -axis respectively.

Table 21: Voltage control of sample#1 applied to attenuator and phase shifter.

Channel no.	V_{att} (V)	V_p (V)
CH1	1.40	8.12
CH2	3.90	10.70
CH3	1.91	8.60
CH4	2.60	

The S_{21} , S_{31} , S_{41} and S_{51} (magnitude and phase) of the feed network (in Figures 6-41 and 6-42 respectively) were measured at specific frequencies so that it could be used to obtain the simulated pattern. The amplitude (in dB) for each port was then converted into the antilog (Table 22) and both amplitude and phase were employed in the 3-D algorithms. The port number, as shown in Figure 6-14, is connected to the dipole antenna arranged as described in the previous chapter. The far-field pattern was then measured in the anechoic chamber at several frequencies for every step of 2° . Both simulated and measured far-field patterns were compared and shown in the next section.

6.4.4.1.1 Results at f=2.45 GHz

Figures 6-41 to 6-42 show the magnitude (in dB) and phase (in degrees) of the input of the dipole array. A frequency of 2.45 GHz was selected because it is the intended or desired resonant frequency of this research. Table 21 shows the excitation values used in the 3-D algorithm. Figures 6-43 and 6-44 show the comparison between the simulated and measured patterns for co-polar and cross-polar antenna array. It is noted that the measured plot in Figure 6-43 is in close agreement with the simulated plot within the range of 0° - 140° . However, the measured plot from 140° - 360° do not agree well with the simulated plot. The measured plot slightly shifted from the simulated plot. One of the reasons is due to the position of the tower which disrupting the measured pattern within the range of 140° - 360° . In addition, it is observed that from Figure 6-40 that the measured pattern is not at the resonant frequency. Meanwhile, the difference of the cross-polar patterns between simulated and measured plots is large. The measured cross polar pattern for all angles from Figure 6-44 is less than -14dB. The cross-polarization could be improved by positioning the dipoles in straight arrangement. However, it should be noted that it was impossible to get the

arrangement of dipoles perfectly straight. Thus, the imperfection (or skewed dipole) increased the cross-polarization of the pattern.

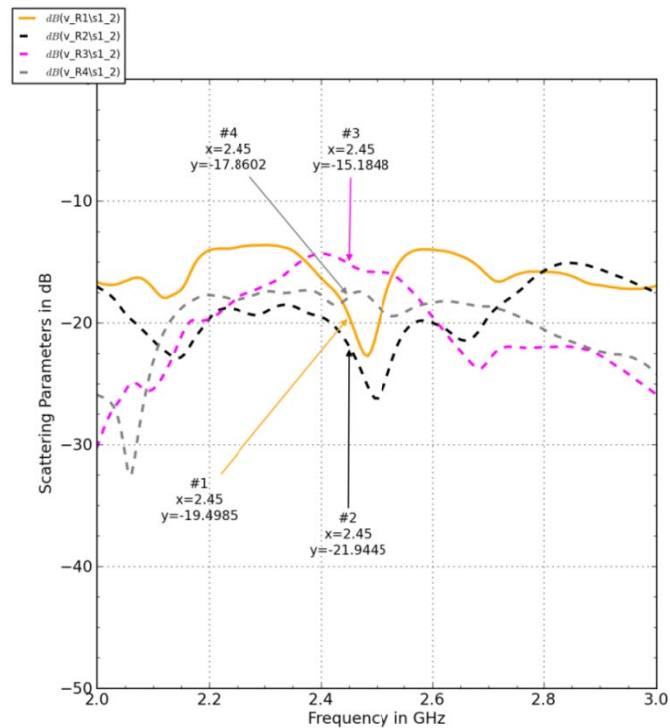


Figure 6-41: Magnitude of S_{21} , S_{31} , S_{41} and S_{51} (in dB) at 2.45 GHz of the feed network. The x - and y -label refers to the Frequency (GHz) and S parameters (dB) according to the x - and y -axis respectively.

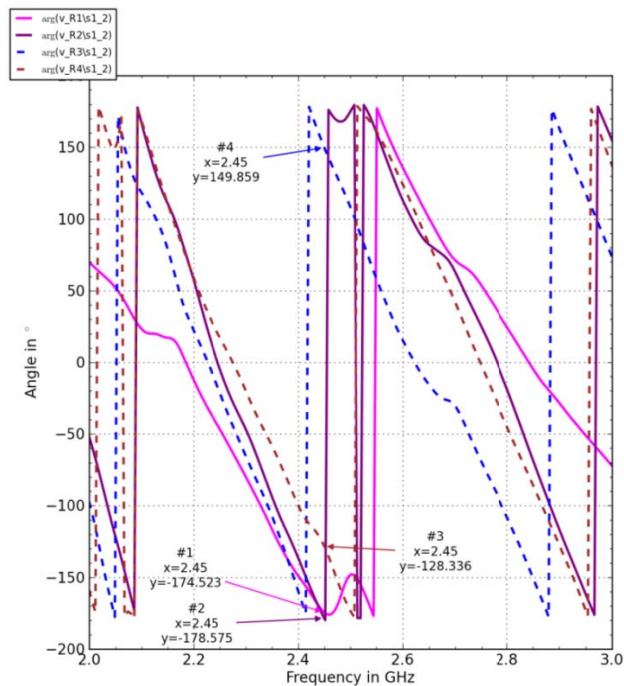


Figure 6-42: Phase of S_{21} , S_{31} , S_{41} and S_{51} (in degrees) at 2.45 GHz of the feed network. The x - and y -label refers to the Frequency (GHz) and phase ($^{\circ}$) according to the x - and y -axis respectively.

Table 22: The magnitude and phase applied at each dipole antenna in 3D algorithm.

S parameter	Dipole Antenna	Marker	File name	Amplitude (dB) (Figure 6-41)	Normalized Amplitude (V)	Phase (degrees) (Figure 6-42)
S_{21}	3	#4	R3	-17.8602	0.1279	149.86
S_{31}	4	#2	R2	-21.9445	0.07994	-178.58
S_{41}	1	#3	R4	-15.1848	0.1741	-128.34
S_{51}	2	#1	R1	-19.4985	0.1059	-174.52

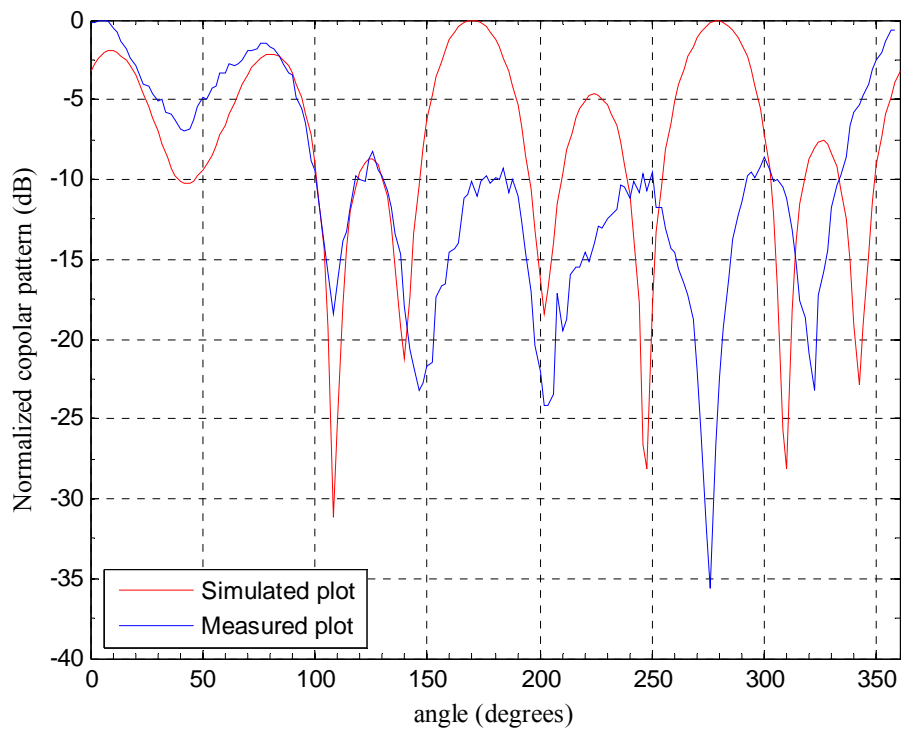


Figure 6-43: The 3-D algorithm simulated (red) and measured (blue) plots for the co-polar pattern at 2.45 GHz.

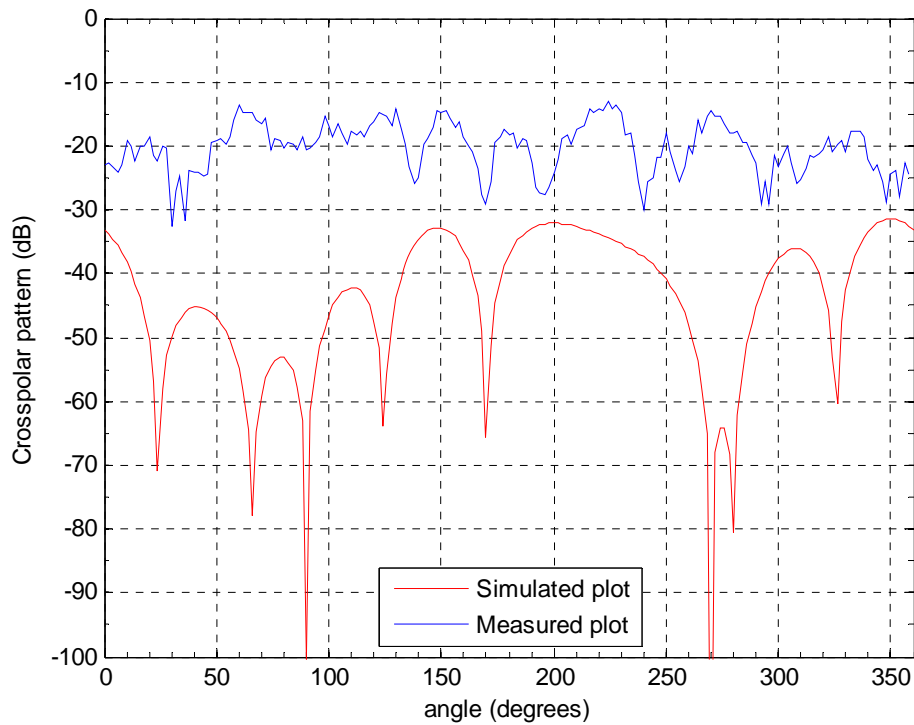


Figure 6-44: The 3-D algorithm simulated (red) and measured (blue) plots for the cross-polar pattern at 2.45 GHz.

6.4.4.1.2 Results at $f=2.56$ GHz

Referring to the return loss parameter in Figure 6-40, it is observed that the resonant frequency has been shifted from its desired frequency at 2.45 GHz to 2.56 GHz. The frequency shift is probably due to the assembling of the antenna array with all other elements; i.e. the divider, control circuit, cables, battery and voltage regulator circuit. The same voltage control as in Table 20 was applied to the attenuator (EVA-3000+) and phase shifter (JPHPS-2484+). However, as the attenuation and phase shift change with frequency, the magnitude and phase of S_{12} for each port is measured (as shown in Figure 6-45 and 6-46) and converted at 2.56 GHz (Table 22). Figure 6-47 shows the co-polar patterns from the 3-D algorithm and the measurement. The measured pattern does not agree well with the simulated pattern. However, it is observed that a deep null occurred in the measured pattern (denoted in blue line) around 260° , which shows its agreement with the 3-D algorithm (denoted in red line). In addition, the number of lobes and nulls between the simulated and measured plots are similar. Therefore, a slight modification has been performed on Trial 1 to obtain a good agreement between 3-D algorithm simulated pattern and measured pattern.

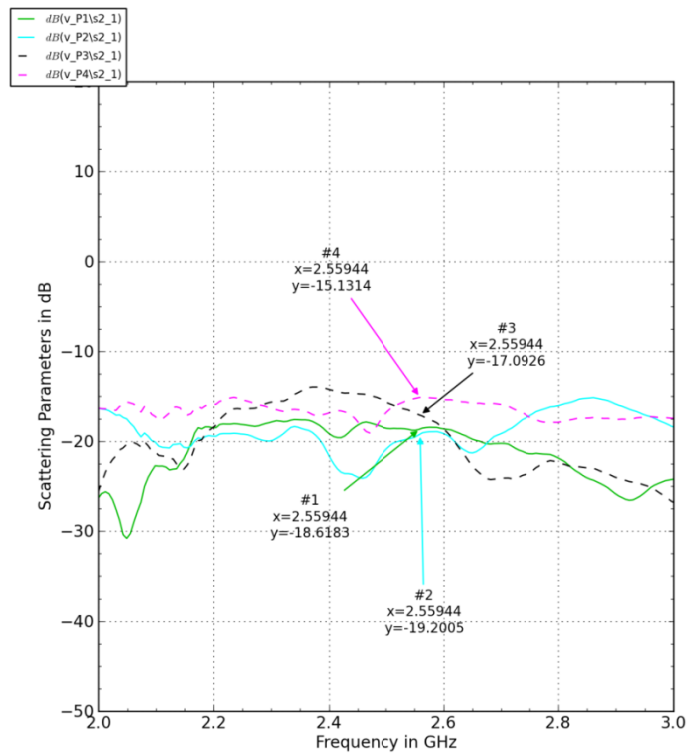


Figure 6-45: Amplitude of S_{21} , S_{31} , S_{41} , S_{51} , (in dB) at 2.56 GHz of the feed network. The x - and y -label refers to the Frequency (GHz) and S parameters (dB) according to the x - and y -axis respectively.

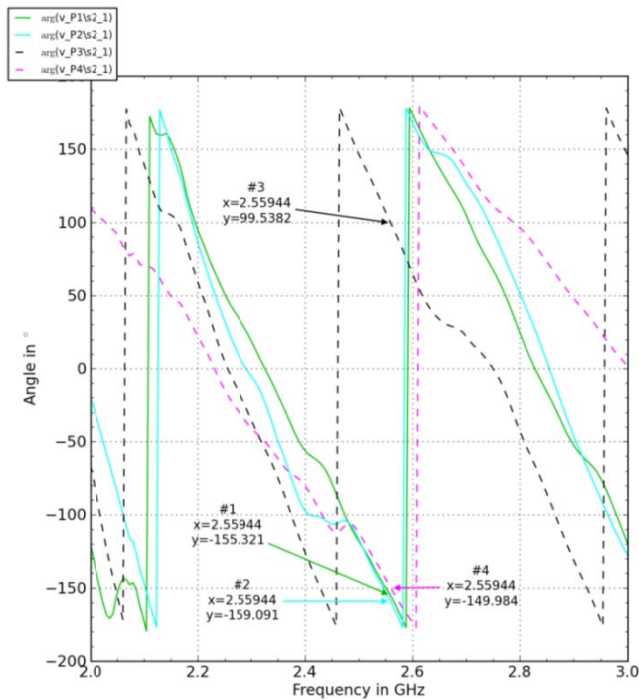


Figure 6-46: Phase of S_{21} , S_{31} , S_{41} , S_{51} , (in degrees) at 2.56 GHz of the feed network. The x - and y -label refers to the Frequency (GHz) and phase ($^{\circ}$) according to the x - and y -axis respectively.

Table 23: The magnitude and phase applied at each dipole antenna (at 2.56 GHz) in the 3-D algorithm.

S parameters	Dipole Antenna	Marker	File name	Amplitude (dB) (Figure 6-45)	Normalized Amplitude (V)	Phase (deg) (Figure 6-46)
S_{21}	3	#3	P1	-18.618	0.117	-155.32
S_{31}	4	#4	P2	-19.201	0.110	-159.09
S_{41}	1	#1	P3	-17.093	0.140	99.54
S_{51}	2	#2	P4	-15.131	0.175	-149.98

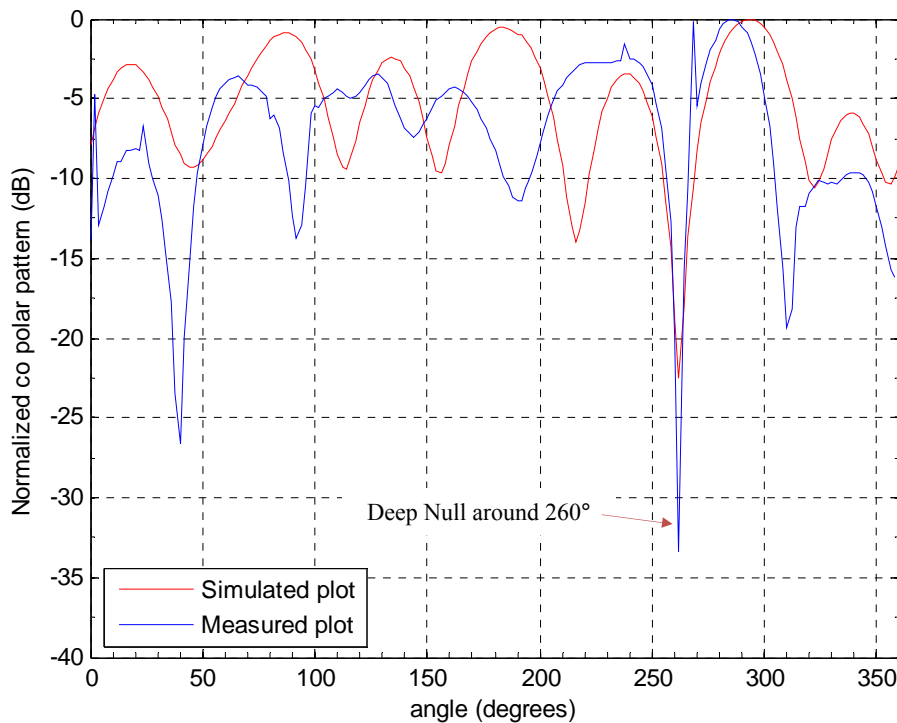


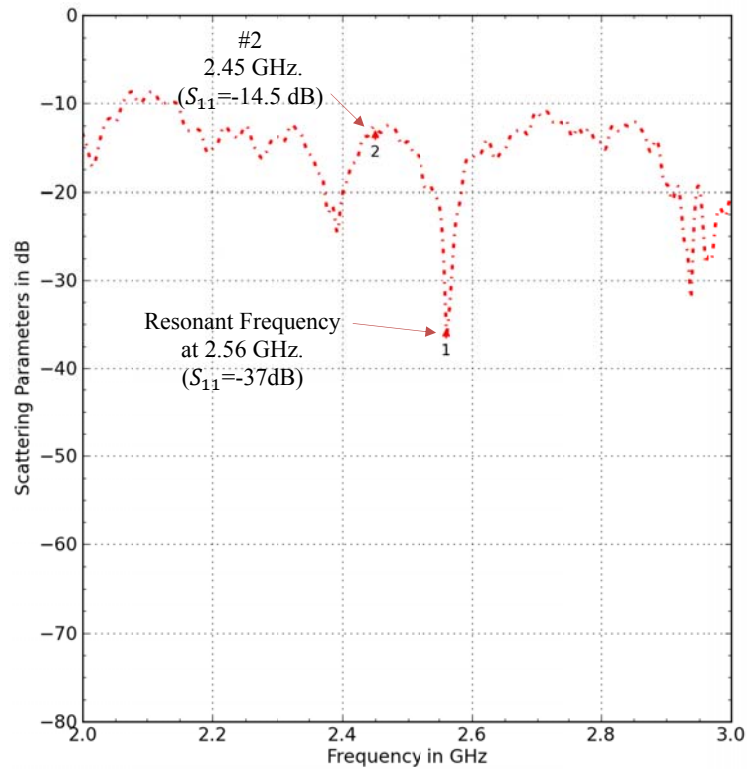
Figure 6-47: The 3-D algorithm simulated (red) and measured (blue) plots for co-polar pattern at 2.56 GHz.

6.4.4.2 Trial 1 with different voltage (Sample #2)

A different sample of voltage control applied to four attenuators and three phase shifters (known as sample #2), shown in Table 23. The aim was to observe that by changing the voltage control, the measured pattern of the dipole array also changed. Thus, the steerable beam with amplitude and phase control is realizable. Figure 6-48 shows the S_{11} for Trial 1 with sample #2 voltage controls. It is observed that there is a small change to the return loss for sample #2 in comparison with sample #1. Moreover, it is observed that the resonant frequency is at 2.56 GHz which is similar to the resonant frequency obtained in Figure 6.40.

Table 24: Voltage control of sample#2 applied to attenuator and phase shifter.

Channel no.	V_{att} (V)	V_p (V)
CH1	4.00	9.12
CH2	3.00	14.85
CH3	0.50	3.06
CH4	7	

Figure 6-48: Measured S_{11} for Trial 1 with sample #2.

6.4.4.2.1 Results at $f=2.45$ GHz

The magnitude and phase of S_{21} , S_{31} , S_{41} and S_{51} was measured at 2.45 GHz, shown in Figure 6-49 and 6-50. Table 24 shows the excitation values for each dipole at 2.45 GHz. Figures 6-51 and 6-52 show the co-polar and cross-polar simulation of the 3D algorithm and measurement at 2.45 GHz with sample #2. Figure 6-51 shows that the co-polar pattern is in good agreement from 45° to 180° but not in good agreement in the other range. The agreement for the range of angle is almost similar to Section 6.4.4.1.1. Even though, overall, the co-polar pattern of the 3-D algorithm is not in good agreement with the measured pattern, the pattern is different in comparison with the pattern obtained from sample #1 (Figure 6-43). It shows that by changing the amplitude and phase of the antenna array, the shape and magnitude of the pattern also changed. On the other hand, it

is noted that from Figure 6-52 that the measured cross-polar pattern for all angles is less than -10dB which is slightly higher than the measured cross polar pattern in Figure 6-44. The reason is probably because of the inconsistent position of the dipole structure during the measurement.

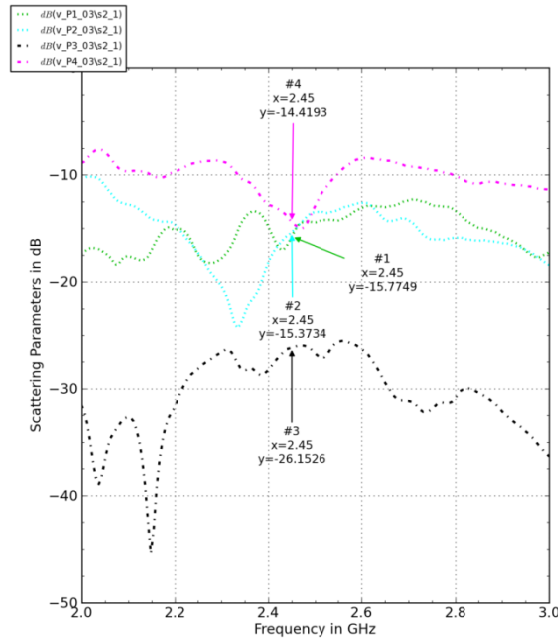


Figure 6-49: Sample #2's magnitude of S_{21} , S_{31} , S_{41} , S_{51} , (in dB) at 2.45 GHz. The x - and y -label refers to the frequency (GHz) and S parameters (dB) according to the x - and y -axis respectively.

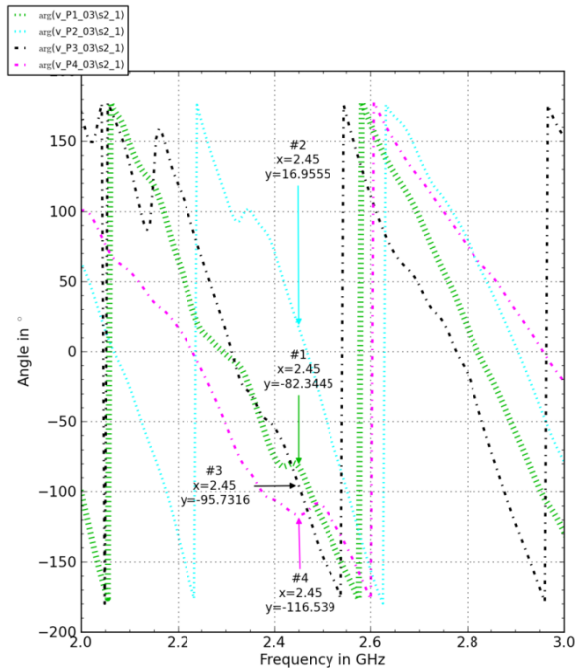


Figure 6-50: Sample #2's phase of S_{21} , S_{31} , S_{41} and S_{51} (in degrees) at 2.45 GHz. The x - and y -label refers to the frequency (GHz) and phase ($^{\circ}$) according to the x - and y -axis respectively.

Section 6.4. Measurement Set-up

Table 25: The magnitude and phase applied at each dipole antenna in the 3-D algorithm.

S parameters	Dipole Antenna	Amplitude (dB) (Figure 6-49)	Normalized Amplitude (V)	Phase (deg) (Figure 6-50)
S_{21}	3	-15.775	0.1626	-82.34
S_{31}	4	-15.388	0.1700	16.77
S_{41}	1	-26.153	0.0492	-95.73
S_{51}	2	-14.419	0.1901	-116.15

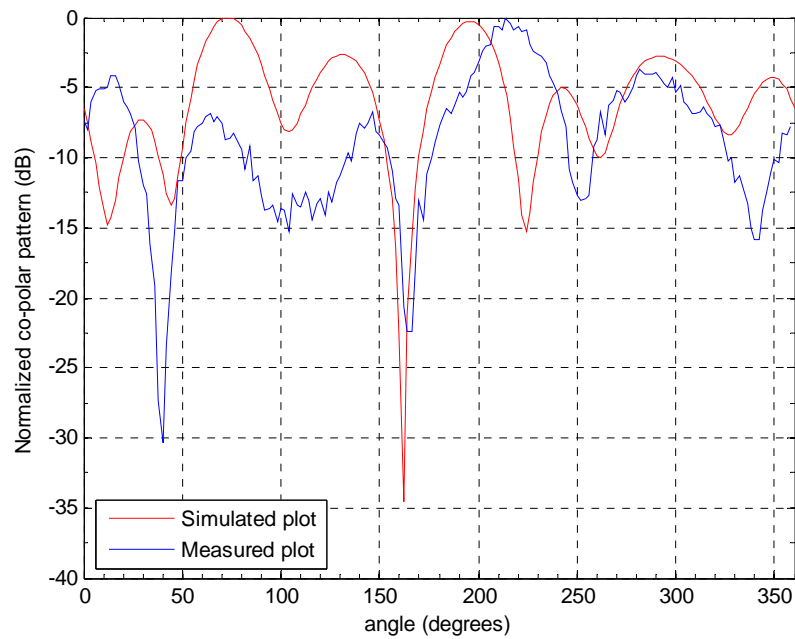


Figure 6-51: Sample #2's co-polar 3-D algorithm simulated (red) and measured (blue) plots at 2.45 GHz.

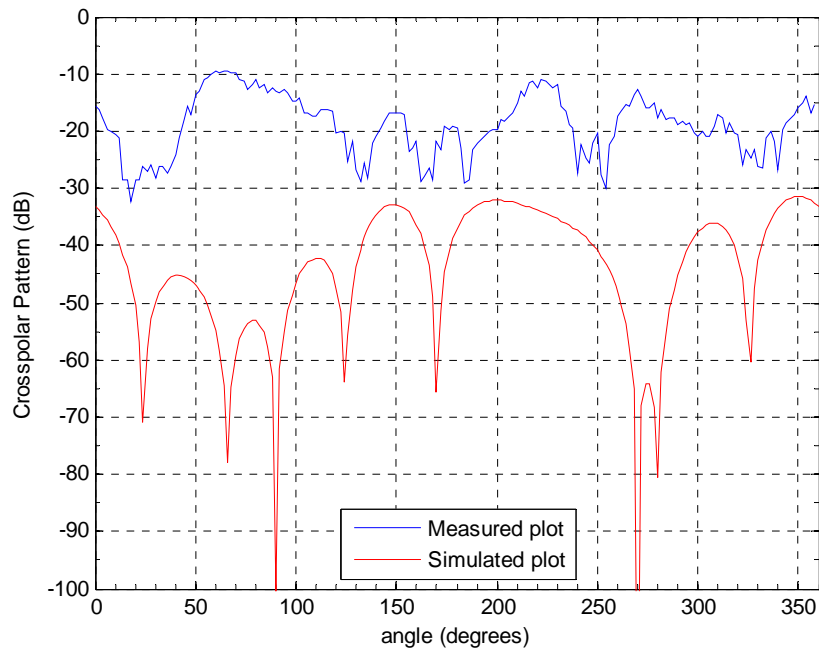


Figure 6-52: Sample #2's cross-polar 3-D algorithm simulated (red) and measured (blue) plots at 2.45 GHz..

6.4.4.2.2 Results at $f=2.56$ GHz

From S_{11} graphs (Figure 6-48), it is observed that the resonant frequency for sample #2 occurred at 2.56 GHz. However, since the operating frequency of the phase shifter is limited to 2.484 GHz, the measured pattern is not performed at 2.56 GHz. Moreover, even though the measured pattern is performed at 2.56 GHz, the results are expected not in good agreement with the 3-D algorithm due to the results obtained in Figure 6-47. Therefore, several modifications are made to Trial 1 in order to achieve good agreement between the 3-D algorithm and the measurement pattern.

6.4.4.3 Trial 2

It is observed that the measured patterns in Trial 1 are not in good agreement with the 3-D algorithm (simulation results). Therefore, few modifications have been made to Trial 1, as mentioned in Section 6.4.3.2. Figure 6-53 shows the measured return loss of the dipole antenna array of Trial 2 with the feed network. The control voltage applied to the phase shifter, V_p , and attenuator, V_{att} , of Trial 2 is shown in Table 25. The far-field pattern of Trial 2 is taken at several frequencies (at 2.54 and 2.56 GHz), and is shown in the next section.

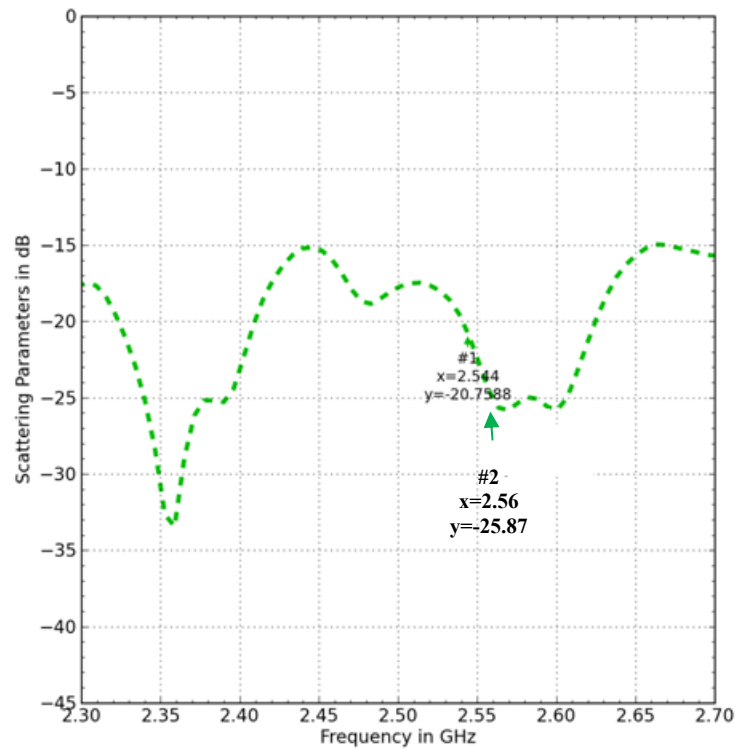


Figure 6-53: Measured S_{11} of Trial 2. The x - and y -label refers to the frequency (GHz) and S parameters (dB) according to the x - and y -axis respectively.

Table 26: Voltage control of sample#1 applied to attenuator and phase shifter.

Channel no.	V_{att} (V)	V_p (V)
CH1	1.40	8.12
CH2	3.90	10.70
CH3	1.91	8.60
CH4	2.60	

6.4.4.3.1 Results at $f=2.54$ GHz

The magnitude and phase of S_{21} , S_{31} , S_{41} and S_{51} was measured at 2.54 GHz, shown in Figure 6-54 and 6-55. Table 26 shows the final input feed for each dipole at 2.54 GHz. Figure 6-56 shows that the measured co-polar pattern is in good agreement with 3-D algorithms pattern, especially within the region of 265° to 130° .

The differences arise between both measured and the 3-D algorithm patterns especially within the region from 130° to 265° are probably due to several reasons:

- The losses from the copper and dielectric are not taken into account in the 3-D algorithm. Such an examples is the dielectric constant for Rohacell substrate ($\epsilon=1.06$ at $f=2.5\text{GHz}$) which is not taken into account in the 3-D algorithm.
- There are other elements such as the feed network, coaxial cable, battery and voltage regulator circuits that might affect the pattern, even though they are placed as far as possible from the dipole array.
- The 3-D algorithm, which employs the Induced EMF method, assumes an infinitely thin dipole antenna element and infinitesimal feed gap.
- Inaccurate values of voltage control applied to the attenuator and phase shifter.

On the other hand, the measured co-polar pattern is not in good agreement from 130° to 265° due to the shading from the tower (or positioner) at angle 180° (Figure 6-57). However, the number of side lobes and nulls within this range is matched with the 3-D algorithm.

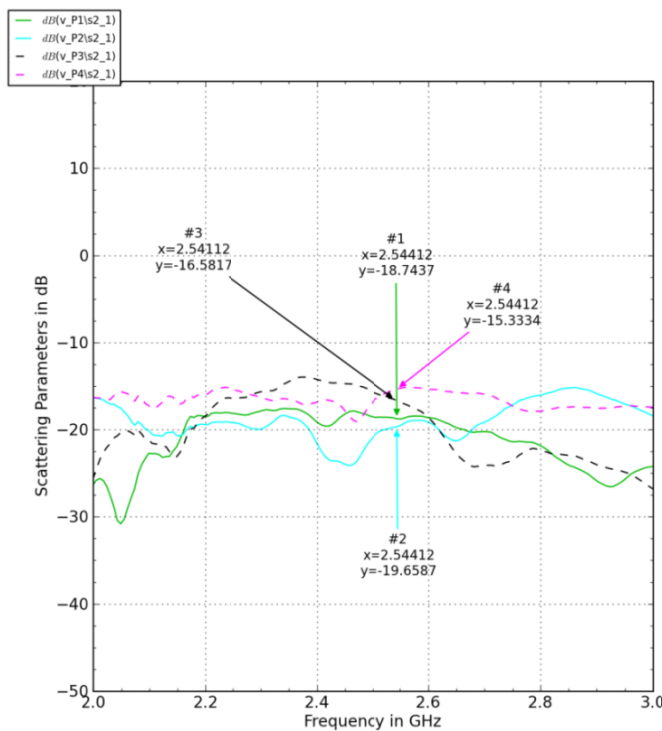


Figure 6-54: Magnitude of S_{21} , S_{31} , S_{41} and S_{51} (in dB) at 2.54 GHz of the feed network. The x - and y -label refers to the frequency (GHz) and S parameters (dB) according to the x - and y -axis respectively.

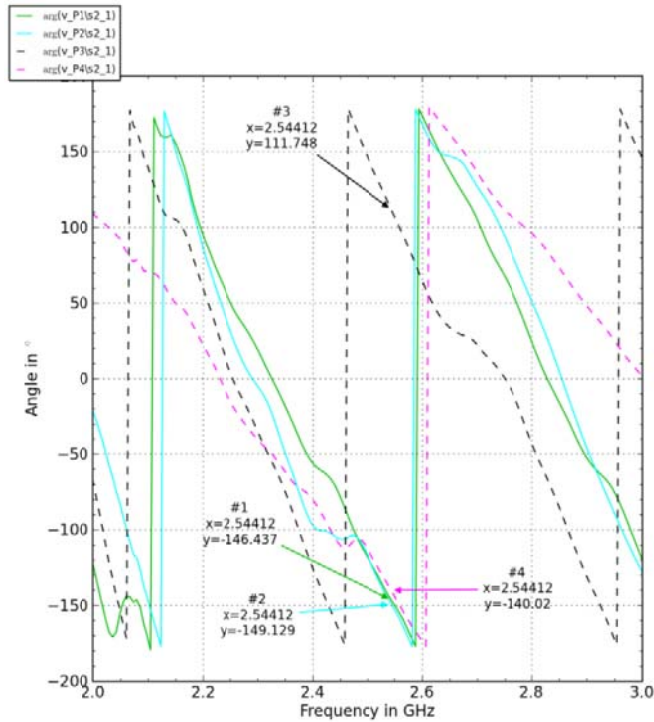


Figure 6-55: Phase of S_{21} , S_{31} , S_{41} and S_{51} (in degrees) at 2.54 GHz of the feed network. The x - and y -label refers to the frequency (GHz) and phase ($^{\circ}$) according to the x - and y -axis respectively.

Table 27: The magnitude and phase applied at each dipole antenna (at 2.54 GHz) in the 3D algorithm.

S parameters	Dipole Antenna	Marker	File name	Amplitude (dB) (Figure 6-54)	Normalized Amplitude (V)	Phase (deg) (Figure 6-55)
S_{21}	3	#3	P1	-18.744	0.116	-146.44
S_{31}	4	#4	P2	-19.658	0.104	-149.13
S_{41}	1	#1	P3	-16.582	0.148	111.75
S_{51}	2	#2	P4	-15.333	0.171	-140.02

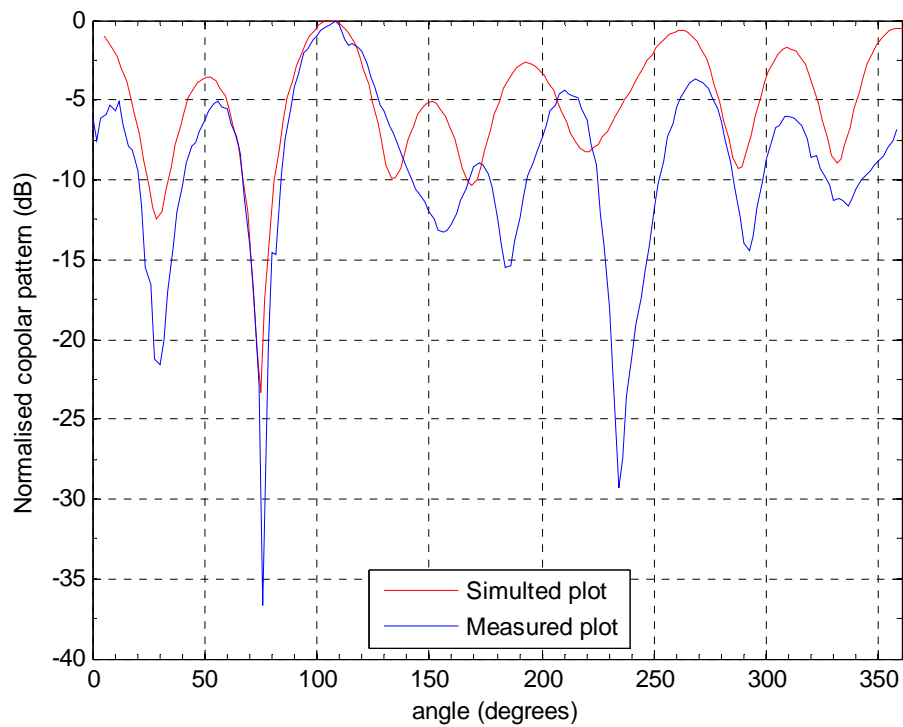


Figure 6-56: The 3-D algorithm simulated (red) and measured (blue) plots for the co-polar pattern at 2.54 GHz

6.4.4.3.2 Results at $f=2.56$ GHz

Another measurement was taken at 2.56 GHz. The magnitude and phase of S_{12} was measured, and the results are shown in Figure 6-57 and 6-58. Table 27 shows the final input feed for each dipole at 2.56 GHz. Figure 6-59 shows the co-polar patterns for both the 3-D algorithm and the measurement at 2.56 GHz. It is observed that both are in good agreement in terms of location, number and size of the lobe in the region of 0° to 130° and 270° to 360° . On the other hand, the measured pattern is not in good agreement from 130° to 270° due to the existence of the tower (or positioner) at 180° which affects the line of sight of the measurement. The measured pattern behaves almost similarly with the pattern in Figure 6-56. However, Figure 6-56 shows a better agreement in terms of the number of nulls and side lobes compared to Figure 6-59. On the other hand, Figure 6-59 shows that the agreement between simulated and measured main beam at 110° is better than the main beam in Figure 6-56.

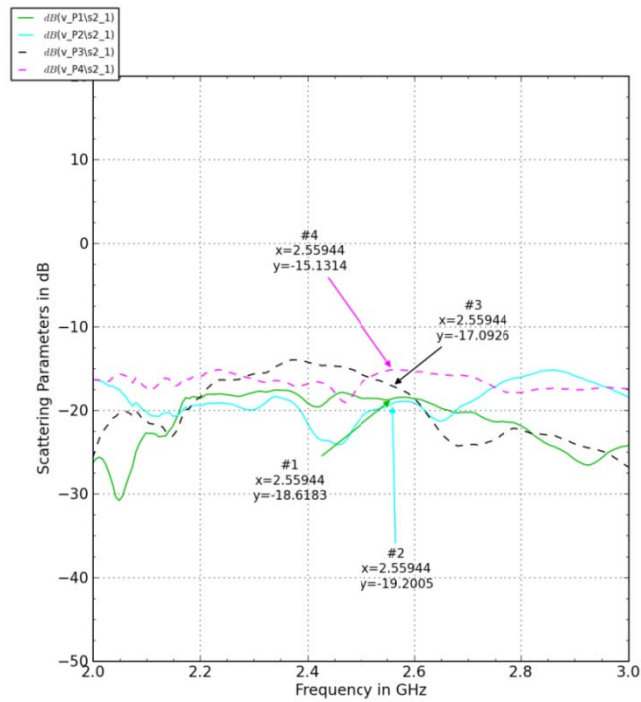


Figure 6-57: Magnitude of S_{21} , S_{31} , S_{41} and S_{51} (in dB) at 2.56 GHz of the feed network. The x - and y -label refers to the frequency (GHz) and S parameters (dB) according to the x - and y -axis respectively.

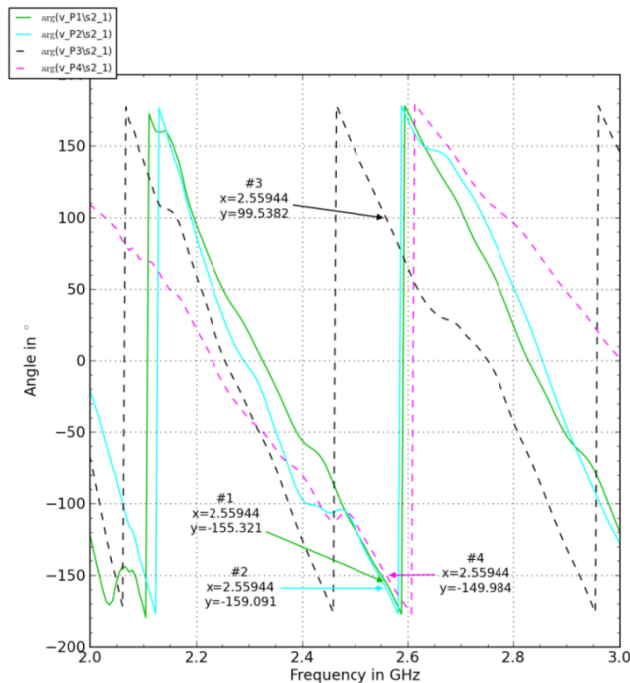


Figure 6-58: Phase of S_{21} , S_{31} , S_{41} and S_{51} (in degrees) at 2.56 GHz of the feed network. The x - and y -label refers to the frequency (GHz) and phase ($^{\circ}$) according to the x - and y -axis respectively.

Table 28: The magnitude and phase applied at each dipole antenna (at 2.56 GHz) in the 3-D algorithm.

S parameters	Dipole Antenna	Marker	File name	Amplitude (dB) (Figure 6-57)	Normalized Amplitude (V)	Phase (deg) (Figure 6-58)
S_{21}	3	#3	P1	-18.618	0.117	-155.32
S_{31}	4	#4	P2	-19.201	0.110	-159.09
S_{41}	1	#1	P3	-17.093	0.140	99.54
S_{51}	2	#2	P4	-15.131	0.175	-149.98

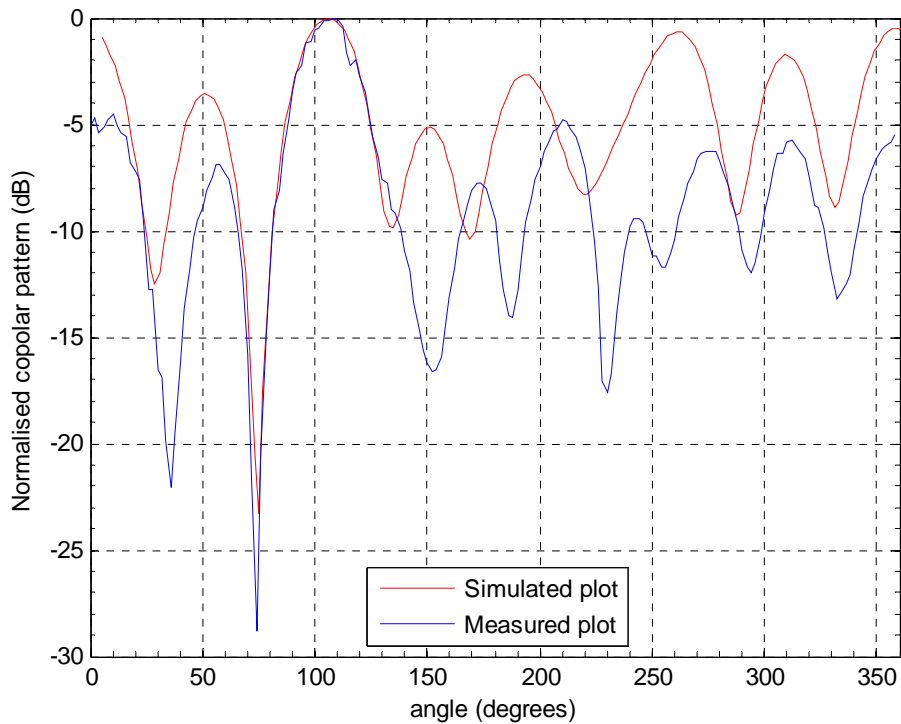


Figure 6-59: The 3-D algorithm simulated (red) and measured (blue) plots for the cross-polar pattern at 2.56 GHz.

6.4.4.4 Trial 3

In Trial 3, the ferrite cores were added to the Trial 2 set-up in order to increase the accuracy of the measured pattern. The ferrite cores were held together in a fixed position using a tie cable. However, the measured far-field pattern obtained was not in good agreement, which is probably due to the imperfectly parallel dipole structure that caused by ferrite rings, as shown in Figure 6-39. Therefore, the results are not included in this thesis.

6.5 Conclusions

This chapter discusses the fabrication and measurement set-up used to validate the 3-D algorithm based on the 2x2 dipole antenna arrays. The 2x2 dipoles are chosen because of the less feeding network required compared to cubic (or twelve) dipole arrays. The spacing has been chosen as small as possible to demonstrate the mutual coupling effect. However, the arrangement of balun and cables for 2x2 dipoles for pattern measurement only allows that the minimum spacing that can be obtained is 110 mm. The fabrication consists of 4 dipole antennas mounted on Rohacell substrate, 4 way power divider, phase shifter and attenuator circuit and supply source. The measurement such as S_{11} , S_{21} , S_{31} , S_{41} and S_{51} for each device is performed to ensure good performance. The measured plots of S_{11} for four dipoles are slightly higher than the simulated plots. One of the reasons is because the simulated model used perfectly perpendicular lumped port as to feed the dipole instead of the existence of balun in practical. However, the simulated and measured plots of S_{11} fall within the same region and covered the desired frequency. On the other hand, the measured plot of S_{11} for Wilkinson divider follows the similar pattern as in the simulated plot with slightly different magnitudes. This could be due to the losses (copper and conductor) and the difference of the thickness in the feeding network. On the other hand, the good agreement of the magnitude and phase of the transmission coefficients of S_{21} , S_{31} , S_{41} and S_{51} ensures that the output signals of each port are divided with the same amplitude and in phase with each other. Next, the characteristics of the phase shifters and attenuators have been measured because of the unwanted amplitude and phase variations (insertion loss) introduced from the phase shifters and attenuators respectively. The results show that the phase shift is in linear relationship with the control voltage for four channels, CH1, CH2, CH3 and CH4. Then, three trials are performed to measure the normalised far-field pattern of dipole antenna array. All devices such as the feed network, dipoles antenna, cables, battery and voltage regulator circuit are assembled for pattern measurement. The cables that connected the feed network, voltage regulator circuit and batteries should be long in order to mitigate their coupling effect on the dipole array. The measurement results are compared with the 3-D algorithm.

The results show that the Trial Two's measured patterns at the resonant frequency of 2.54 and 2.56 GHz are in good agreement with the 3-D algorithm. The disagreement between the simulated and measured plots has been justified. that disturbs the line of sight between the transmitter and receiver. The tower effect could be reduced by using a thinner tower. It is also observed that there is a small shift in the resonant frequency at 2.45 GHz (desired frequency) to 2.54 and 2.56 GHz which is highly due to the effect of the feed network. However, those frequency shifts have already been considered in the 3-D algorithm. In conclusion, this chapter provides a verification that the 3-D algorithm based on the Induced EMF method is useful for the three-dimension array analysis considering the mutual coupling of dipole antenna arrays.

References

- [1] C. A. Balanis, *Antenna Theory: Analysis and Design*. Canada: Wiley-Interscience, 2005.
- [2] W. K. Roberts, "A new wide balun". Proceedings of the IRE, Vol. 45 (12), pp. 1628-1631, Dec. 1957.
- [3] E. J. Wilkinson, "An n-way hybrid power divider. *Microwave Theory and Techniques, IRE Transactions on*, Vol. 8 (1), pp. 116-118, 1960.
- [4] E. K. Kowalczyk, C. J. Panagamuwa, R. D. Seager, J. Y. C. Varadoglou, "Characterising the Linearity of an Optically Controlled Photoconductive Microwave Switch". Proceedings of the Antennas and Propagation Conference (LAPC) 2010, pp. 597-600, Nov 2010.
- [5] D. M. Pozar, *Microwave Engineering*. Reading, Mass.; Wokingham: Addison-Wesley, 1990.
- [6] Mini-Circuits, "Surface Mount Voltage Variable Attenuator, EVA-3000+" datasheet.
- [7] Mini-Circuits, "Surface Mount Phase Shifter, JPHPS-2484+" datasheet.
- [8] Anritsu, *Series 37XXXD Vector Network Analyzer Operation Manual* [Online]. Available at: <http://www.anritsu.com/en-US/Downloads/Manuals/Operations-Manual/DWL1982.aspx>. [Accessed Feb 2012].
- [9] Rogers Corporation, "RT/Duroid® 6002 High Frequency Laminates", 1.6002 datasheet, 2010. [Revised Apr. 2011].
- [10] Vishay Dale Thin Film, "High Frequency (up to 20 GHz) Resistor, Thin Film Surface Mount Chip", 60093 datasheet. [Revised Dec. 2011].
- [11] RS Components Ltd, "SMA End Launch JK 1.57PCB" [Online]. Available at: <http://uk.rs-online.com/web/>. [Accessed Feb. 19, 2012].
- [12] C. T. Charles, "A calibrated phase and amplitude control system for phased-array transmitters". PhD Thesis, University of Washington, US, 2006.
- [13] M. I. Khattak, "Microwave Measurement Techniques for Wearable Antennas". PhD Thesis, Loughborough University, UK, 2010.
- [14] Evonik Industries AG, "Rohacell®" [Online]. Available at: <http://www.rohacell.com/product/rohacell/en/Pages/default.aspx>. [Accessed Apr. 1, 2012].

[15] S. Saario, D. V. Thiel, J. Lu and S. G. O'Keefe, "An assessment of cable radiation effects on mobile communications antenna measurements". In *IEEE Antennas and Propagation Society International Symposium*, 1997, pp. 24-24.

CHAPTER 7:

Final Conclusions

This chapter presented a summary of the work that has been carried throughout this thesis plus a list of contributions to the field of antenna array analysis. Other possible alternatives to enhance or improvise the work discussed in this thesis will be highlighted in the future work section.

7.1 Summary of Research

A novel array analysis using the Induced EMF method (or known as the 3-D algorithm) considering the mutual coupling effect in antenna arrays has been presented in this thesis. It may be applied in any dimensions (one, two or three dimensions) and configurations (straight or slanted dipole position). The pattern comparison was performed with full wave techniques, such as FDTD and MoM, and conventional pattern multiplication method. A pattern synthesis was then performed using the 3-D Algorithm with the aid of a genetic algorithm in order to steer the beam pattern to any direction. A prototype using dipole antennas at 2.45 GHz was built and the pattern measurement was performed on 2x2 dipole antennas in order to verify the 3-D algorithm.

Chapter One presented an introduction of the phased array antenna and its capability to shape or electronically steer the main beam pattern to the desired direction. Electronic beam steering is preferable than mechanical beam steering due to the fast and flexibility of electronic equipment such as phase shifter applied on each element. The performance of electronic beam steering depends on the accurate and fast calculations of the antenna radiation pattern. As a result, the technique becomes computationally efficient when working with optimisation methods to generate antenna arrays. However, the radiation pattern of antenna array is easily affected by mutual coupling effect between antenna elements. Numerical techniques such as FDTD and MoM are very accurate since

they consider this effect but require long computation and large memory. On the other hand, the calculation of the far-field pattern without the mutual coupling effect (such as pattern multiplication) resulting inaccurate decisions by the optimisation method. So it was concluded to develop a 3-D array analysis which is not only accurate (considering the mutual coupling effect) but computationally efficient when working with optimization techniques.

Due to the main objective to develop an array analysis for 3-D arrays, Chapter Two presented mathematical background related to the characteristics of the dipole elements and arrays of antennas. A conventional pattern multiplication for antenna arrays and the mutual coupling effect between elements were explained in detail. Other methods such as the active input impedance and the active element pattern considering the mutual coupling effect in antenna arrays were briefly introduced. The active input impedance using the Induced EMF method has been developed long time ago but only applicable for parallel dipoles (2-D). Therefore, this thesis further developed this method so that it may be applied to 3-D arrays where the elements can be arranged in any orientation and dimensions.

A number of electromagnetic modelling techniques to analyse the far-field pattern have been highlighted in Chapter Three. It was necessary to review the work of others in order to determine the efficiency and accuracy of each technique. Numerical techniques such as MoM and FDTD are accurate, versatile, able to treat complex geometries and coupling between elements. MoM is based on frequency domain method while FDTD is based on time domain method. The differences between both methods have been summarized. On the other hand, array analysis techniques are computationally efficient when working on with optimization techniques. Several techniques of array analysis have been explained by investigating 1-D (linear), 2-D (planar or circular) and 3-D (spherical, cube) arrays. At the end of the chapter, a number of optimization techniques, i.e. sequential uniform sampling, gradient search, Nelder-Mead simplex, simulated annealing and the genetic algorithm, which are used for pattern synthesis, were summarised.

Chapter Four provided the development of the pattern analysis of antenna arrays using the Induced EMF method. The method or known as 3-D algorithm

takes into account the mutual coupling effect between elements. The algorithm was tested for 2-D and 3-D arrays and was applicable for elements arranged in any configuration. For 2-D array, an example was performed using a 2x2-dipole arranged in a rectangular grid, while another example using twelve dipoles arranged at the edge of a cube structure was performed for 3-D analysis. The pattern was compared with numerical techniques, such as FDTD, MoM and a conventional pattern multiplication method. The pattern comparison for the azimuth and elevation plane of each technique has been summarized in each table. The comparison includes beam characteristics such as the direction of the maximum beam, highest side lobe level and beam width. The results from 3-D algorithm consider the mutual coupling effect unlike pattern multiplication technique. The pattern discrepancy between the 3-D Algorithm and full wave techniques is because the mutual impedance calculated using the Induced EMF method assumes that the dipole is infinitely thin with no feed gap. Therefore it assumes that sinusoidal current distribution with the same phase occurred for entire length of each dipole. However, the analysis is sufficient for dipole antenna arrays. On the other hand, the discrepancies occurred between MoM and FDTD are probably because of parameters differences of both methods. FDTD is suitable for complex antenna geometries where MoM isn't because the computational time and storage for MoM rise significantly when number of segments increases.

Chapter Five has discussed one of the applications of developing a novel, accurate and computationally efficient of the 3-D algorithm. The pattern calculated from 3-D algorithm needs to be electronically steered into any desired direction while removing any interference in other directions. This already been achieved using a genetic algorithm by varying the amplitude and phase excitation of each element. It was demonstrated using a 2x2-dipole array arranged in rectangular coordinates with a spacing of $0.9\lambda_0$ between the elements. The results indicate that the genetic algorithm tends to converge quickly and the optimized pattern meets the designer's specification. Then, the runtime between the 3-D algorithm and other numerical techniques have been compared. It was observed that based on those runtime, the 3-D algorithm is computationally efficient when

working with genetic algorithm. The obstacles and limitations of this technique were discussed at the end of this chapter.

In Chapter Six, the pattern simulated from 3-D algorithm was verified with the pattern measurement from the fabrication of 2x2-dipole antenna arrays. The justification on using 2x2 dipole antennas with spacing of 110 mm has been presented. Then, a feed network was designed to feed the four-dipole antenna array with different amplitudes and phases. The feed network consists of a Wilkinson divider and a circuit consist of surface-mounted voltage control phase shifters and attenuators. The S_{11} , simulated and measured plots for each dipole is performed and they fall within the same region and covered the desired frequency. Then, the measured plot of S_{11} for Wilkinson divider is in good agreement with the simulated plot except that the measured magnitude of S_{11} is slightly higher than the simulated plot. The justifications on the disagreement between simulated and measured plots have been discussed in detail. Meanwhile, a good agreement has been achieved of the magnitude and phase of the transmission coefficients of S_{21} , S_{31} , S_{41} and S_{51} between simulated and measured plots for each port of Wilkinson Divider. Thus, the results confirmed that the output signal coming through each port is divided with similar amplitude and phase of each other. The irregularities and differences occurred between those plots are also been highlighted. Then, the unwanted amplitude and phase variations (insertion loss) occurred in phase shifters and attenuators initiated a study on phase and attenuation characteristics between four channels, CH1, CH2, CH3 and CH4. The observation confirmed that the phase shift for each channel is in linear relationship with the control voltages. The circuit was controlled using battery during measurement. The dipole array was mounted using Rohacell to make it robust. The entire device was mounted on the platform in the anechoic chamber for pattern measurement. Three trials are made in order to find a good agreement between the 3-D algorithm and the measurement pattern. The measurement results are compared with the 3-D algorithm. The results show that the Trial Two's measured patterns at the resonant frequency of 2.54 and 2.56 GHz are in good agreement with the 3-D algorithm. The disagreement between the simulated and measured plots has been justified. Results presented here provide a verification that the simulated plots based on 3-D algorithm

considering mutual coupling between elements matches well with the measured plots on the normalised far-field pattern.

Finally, this work has achieved the following contributions:

- *The study and development of three-dimension array analysis for dipole antenna arrays considering the mutual coupling effect which is fairly accurate, fast and efficient. This leads to a significant improvement in the computational efficiency compared with a full-wave analysis.*
- *The optimization to find the 'best fit' to the desired pattern using a combination of the 3-D algorithm and a genetic algorithm.*
- *The validation of the 3-D algorithm with experimental work using a 2x2 dipole antenna array and a feed network consists of phase shifter and attenuator.*

7.2 Future Study

The research presented in this dissertation may be extended in several ways. The 3-D algorithm may include the radius and the length of the dipole antenna. The work presented here assumes the dipole radius is infinitely thin and applicable only to half-wavelength dipole antenna. The half-wavelength restriction is due to the simplified electric field characteristics of E_θ and E_ϕ that were used in this algorithm. However, the mutual impedance provided by Baker is applicable for any length of dipole antenna array. The algorithm may also be extended to the near-field pattern with additional complexity, since the 3-D algorithm assumed that the radial electric field component, E_r , is zero for all cases.

In addition, the algorithm may be extended to other types of antenna such as microstrip or printed dipoles. The algorithm also has to take into account other effects such as those from the feed network and the mismatch that occurs between the feed network and the array elements. It affects the accuracy of the pattern of the antenna array, since in practice; the feed network contributes significant changes to the antenna arrays.

The optimization technique may be developed by performing pattern synthesis for 3-D patterns. There are few papers optimize the pattern in 3-D,

since it is more complex compared to 2-D. However, the 3-D optimization will be time-consuming since the 3-D pattern contains lots of data to be optimized. Moreover, the 3-D pattern synthesis may be extended to azimuth and elevation direction finding applications. The optimization technique may also consider other things to be optimized, such as the spacing and number of elements, so that the design of the feeding network will be less complicated and more cost-effective. Nowadays, the aim of the phased array system is getting an accurate performance rather than its cost. As a result, the number of antenna elements is large and the feeding network designed with it is complicated. However, it is desirable to obtain a small and cost-effective phased array antenna without degrading its performance.

Last but not least, the study of phase shifter and attenuator circuit should be explored in details. The attenuation and phase shift values are dependable of each other making the measurement process complicated. It is also difficult to obtain the attenuation and phase shift of each signals to the desired values because tune in one DC voltage of one channel resulting a change of phase and attenuation in three other channels. The study in this area will ensure that the phased array system is working sequentially and efficiently.

Appendix A: 3D Algorithm for 2x2 Dipole Arrays

```
%main program
lamda=3/(24.5); % change with frequency
radius=4.7*lamda;
theta=(0.01:2:360.01)*pi/180;
phi=(0.01:2:360.01)*pi/180;
[a,b]=size(theta);
[c,d]=size(phi);
theta=theta';

%transform the (r,theta,phi) to (x,y,z) coordinates

r1=radius*sin(theta)*cos(phi);      %x
r2=radius*sin(theta)*sin(phi);      %y
r3=radius*cos(theta);                %z

%-----
%position of each centre fed dipole in x,y,z axis
x1=-0.055;
y1=-0.055;
z1=0.001;
d1=[x1 y1 z1];

x2=0.055;
y2=-0.055;
z2=0;
d2=[x2 y2 z2];

x3=0.055;
y3=0.055;
z3=0;
d3=[x3 y3 z3];

x4=-0.055;
y4=0.055;
z4=0;
d4=[x4 y4 z4];

%plot the position of each dipole in x,y,z axis
dd=[d1;d2;d3;d4];
figure
scatter3(dd(:,1),dd(:,2),dd(:,3),'c','filled');
```

Appendix A: 3-D Algorithm for 2x2 Dipole Arrays

```

%spacing between two centre fed dipoles in (x,y,z) axis
s12=[abs(x2-x1)*24.5/3 abs(y2-y1)*24.5/3 abs(z2-z1)*24.5/3];
s13=[abs(x3-x1)*24.5/3 abs(y3-y1)*24.5/3 abs(z3-z1)*24.5/3];
s14=[abs(x4-x1)*24.5/3 abs(y4-y1)*24.5/3 abs(z4-z1)*24.5/3];
s21=[abs(x2-x1)*24.5/3 abs(y2-y1)*24.5/3 abs(z2-z1)*24.5/3];
s23=[abs(x3-x2)*24.5/3 abs(y3-y2)*24.5/3 abs(z3-z2)*24.5/3];
s24=[abs(x4-x2)*24.5/3 abs(y4-y2)*24.5/3 abs(z4-z2)*24.5/3];
s32=[abs(x3-x2)*24.5/3 abs(y3-y2)*24.5/3 abs(z3-z2)*24.5/3];
s31=[abs(x3-x1)*24.5/3 abs(y3-y1)*24.5/3 abs(z3-z1)*24.5/3];
s34=[abs(x4-x3)*24.5/3 abs(y4-y3)*24.5/3 abs(z4-z3)*24.5/3];
s41=[abs(x4-x1)*24.5/3 abs(y4-y1)*24.5/3 abs(z4-z1)*24.5/3];
s42=[abs(x4-x2)*24.5/3 abs(y4-y2)*24.5/3 abs(z4-z2)*24.5/3];
s43=[abs(x4-x3)*24.5/3 abs(y4-y3)*24.5/3 abs(z4-z3)*24.5/3];

array=4;

Z11=73.1+42.5i; %self impedance
%calculate the mutual impedance between two dipoles
for r=1:array
    for s=1:array
        if s==r
            Z(r,s)=Z11;
        elseif (s==3&&r==2) || (s==2&&r==3)
            Z(r,s)=impedance(0.5,0.5,s23(1,1),s23(1,2),s23(1,3),2*pi/180,0);
        elseif (s==4&&r==1) || (s==1&&r==4)
            Z(r,s)=impedance(0.5,0.5,s14(1,1),s14(1,2),s14(1,3),4*pi/180,0);
        elseif (s==3&&r==4) || (s==4&&r==3)
            Z(r,s)=impedance(0.5,0.5,s34(1,1),s34(1,2),s34(1,3),4*pi/180,0);
        elseif (s==2&&r==1) || (s==1&&r==2)
            Z(r,s)=impedance(0.5,0.5,s12(1,1),s12(1,2),s12(1,3),2*pi/180,0);
        elseif (s==3&&r==1) || (s==1&&r==3)
            Z(r,s)=impedance(0.5,0.5,s13(1,1),s13(1,2),s13(1,3),0,0);
        elseif (s==2&&r==4) || (s==4&&r==2)
            Z(r,s)=impedance(0.5,0.5,s24(1,1),s24(1,2),s24(1,3),6*pi/180,0);
        end
    end
end

Chrom=[0.1727 148.25*pi/180 0.1033 -175.14*pi/180 0.1304 -
129.64*pi/180 0.07825 -179.94*pi/180];

V=[Chrom(1,1)*exp(1*j*Chrom(1,2)); Chrom(1,3)*exp(1*j*Chrom(1,4));
Chrom(1,5)*exp(1*j*Chrom(1,6)); Chrom(1,7)*exp(1*j*Chrom(1,8))];

source=[50 50 50 50];%perfect match
Zs=diag(source);
Ifeed=inv(Z+Zs)*V;
Vfeed=Z*Ifeed;

r=1;

%-----

```

Appendix A: 3-D Algorithm for 2x2 Dipole Arrays

```
%dipole1

A=calculateA(0,0,0); %(alpha,beta,gamma for dipole 2)
[theta_prime
phi_prime]=findThetaPhiPrime(x1,y1,z1,A,theta,phi,radius);
[Etheta1 Ephi1]=calculateEfield(d1,Ifeed(1,r),r1,r2,r3,theta_prime);
[Et1
Ep1]=transformE(Etheta1,Ephi1,theta,phi,theta_prime,phi_prime,A);

%-----
-

%dipole2

A=calculateA(0,2*pi/180,0); %(alpha,beta,gamma for dipole 2)
[theta_prime
phi_prime]=findThetaPhiPrime(x2,y2,z2,A,theta,phi,radius);
[Etheta2 Ephi2]=calculateEfield(d2,Ifeed(2,r),r1,r2,r3,theta_prime);
[Et2
Ep2]=transformE(Etheta2,Ephi2,theta,phi,theta_prime,phi_prime,A);

%-----
--

%dipole3

A=calculateA(0,0,0); %(alpha,beta,gamma for dipole 2)
[theta_prime
phi_prime]=findThetaPhiPrime(x3,y3,z3,A,theta,phi,radius);
[Etheta3 Ephi3]=calculateEfield(d3,Ifeed(3,r),r1,r2,r3,theta_prime);
[Et3
Ep3]=transformE(Etheta3,Ephi3,theta,phi,theta_prime,phi_prime,A);

%-----
---

%dipole4

A=calculateA(0,4*pi/180,0); %(alpha,beta,gamma for dipole 2)
[theta_prime
phi_prime]=findThetaPhiPrime(x4,y4,z4,A,theta,phi,radius);
[Etheta4 Ephi4]=calculateEfield(d4,Ifeed(4,r),r1,r2,r3,theta_prime);
[Et4
Ep4]=transformE(Etheta4,Ephi4,theta,phi,theta_prime,phi_prime,A);

%-----
-----

%summation of both E fields

E_theta=Et1+Et2+Et3+Et4;
E_phi=Ep1+Ep2+Ep3+Ep4;

Efield=sqrt((abs(E_theta)).^2+(abs(E_phi)).^2);

maxi=max(max(Efield));
```

Appendix A: 3-D Algorithm for 2x2 Dipole Arrays

```
Efield2=Efield/maxi; %normalized the Electric Field

row=46;      %theta=90 deg,
column=46;   %phi=90 deg

max_phi=phi(column)*180/pi
max_theta=theta(row)*180/pi

Sh_p=(Efield2(row,:));      %E field at theta=90deg
Sv_p=(Efield2(:,column));   %E field at phi=90deg

figure
polar_dB(phi*180/pi,20*log10(Sh_p),-30,0,20,'*-b');

figure
polar_dB(theta*180/pi,20*log10(Sv_p),-30,0,20,'*-r');

%plot far-field pattern in 3D
threeDplot(Efield2,theta,phi);
```

Appendix A: 3-D Algorithm for 2x2 Dipole Arrays

```

%impedance function
function Z21=impedance(L1,L2,xx0,y0,z0,the,ph)
%L1=length of dipole 1
%L2=length of dipole 2
%xx0=spacing between dipole 1 and 2 along x axis
%y0=spacing between dipole 1 and 2 along y axis
%z0=spacing between dipole 1 and 2 along z axis
%the=bent angle of dipole 2 along xz plane
%ph=bent angle of dipole 2 along xy plane

a=-L2/2;
b=L2/2;
n=51; %choose n as odd number so s not equal to 0
hh=(b-a)/n;

s(1,1)=a;
s(1,n+1)=b;

for k=1:1:floor(n/2) %even number
    x=2*k;
    s(1,x)=a+x*hh;
end

for k=2:1:floor(n/2+1) %odd number
    x=2*k-1;
    s(1,x)=a+x*hh;
end

sz=s*cos(the);
sy=s*sin(the)*sin(ph);
sx=s*sin(the)*cos(ph);
rho=sqrt((sx+xx0).^2+(y0+sy).^2);
r=sqrt(rho.^2+(z0+sz).^2);
r1=sqrt(rho.^2+(z0+sz+L1/2).^2);
r2=sqrt(rho.^2+(z0+sz-L1/2).^2);

factor_a=((1./rho.^2).*((sin(2*pi*r1).*(sz+z0+L1/2)./r1)+(sin(2*pi*r2).*(sz+z0-L1/2)./r2)-
(2*cos(pi*L1)*sin(2*pi*r).*(sz+z0)./r)).*(sx.^2+xx0*sx+y0*sy+sy.^2));
;
factor_b=(2*sin(2*pi*r)*cos(pi*L1)./r-sin(2*pi*r1)./r1-
sin(2*pi*r2)./r2).*sz;
current_max=(sin(2*pi*(L2/2-abs(s))))./s;
factor1=(factor_a+factor_b).*current_max;

fact_a=((1./rho.^2).*((cos(2*pi.*r1).*(sz+z0+L1/2)./r1)+(cos(2*pi.*r2).*(sz+z0-L1/2)./r2)-
2*cos(pi*L1)*cos(2*pi.*r).*(sz+z0)./r).*(sx.^2+xx0*sx+y0*sy+sy.^2));
fact_b=(2*cos(2*pi.*r)*cos(pi*L1)./r-cos(2*pi.*r1)./r1-
cos(2*pi.*r2)./r2).*sz;
factor2=(fact_a+fact_b).*current_max;

total_a=0;
for k=1:floor(n/2)
    x=2*k;
    total_a=total_a+(factor1(1,x));
end

```

Appendix A: 3-D Algorithm for 2x2 Dipole Arrays

```

total_b=0;
for k=2:floor(n/2+1)
    x=2*k-1;
    total_b=total_b+(factor1(1,x));
end

total_2a=0;
for k=1:floor(n/2)
    x=2*k;
    total_2a=total_2a+(factor2(1,x));
end

total_2b=0;
for k=2:floor(n/2+1)
    x=2*k-1;
    total_2b=total_2b+(factor2(1,x));
end

R21=-30*Integrand(factor1,total_a,total_b,a,b,n);
X21=-30*Integrand(factor2,total_2a,total_2b,a,b,n);
Z21=R21+X21*1i;

%Integration function according to Simpson's rule
function Int=Integrand(factor1,tot_a,tot_b,a,b,n)

hh=(b-a)/n;
Int=hh/3*(factor1(1,1)+2*tot_a+4*tot_b+factor1(1,n+1));

end

%calculateA function to calculate [A] for transformation matrix
function A=calculateA(alpha,beta,gamma)

A11=cos(gamma)*cos(alpha)-sin(gamma)*cos(beta)*sin(alpha);
A12=cos(gamma)*sin(alpha)+sin(gamma)*cos(beta)*cos(alpha);
A13=sin(gamma)*sin(beta);
A21=-sin(gamma)*cos(alpha)-cos(gamma)*cos(beta)*sin(alpha);
A22=-sin(gamma)*sin(alpha)+cos(gamma)*cos(beta)*cos(alpha);
A23=cos(gamma)*sin(beta);
A31=sin(beta)*sin(alpha);
A32=-sin(beta)*cos(alpha);
A33=cos(beta);

A=[(A11) (A12) (A13);(A21) (A22) (A23);(A31) (A32) (A33)];

end

%findThetaPhiPrime to calculate theta' and phi' for transformation
matrix
function [theta_prime
phi_prime]=findThetaPhiPrime(x1,y1,z1,A,theta,phi,radius)

b=181;
d=181;

```

Appendix A: 3-D Algorithm for 2x2 Dipole Arrays

```

r1=radius*sin(theta)*cos(phi);      %x
r2=radius*sin(theta)*sin(phi);      %y
r3=radius*cos(theta);                %z

for a=1:b
    for c=1:d
        result=A*[(r1(a,c));(r2(a,c));(r3(a))];
        angheta=result(3)/radius;
        ThetaQuarter=theta_fun(a,angheta);           %call
    theta_fun
        theta_prime(a,c)=ThetaQuarter;
        angphi=result(2)/(radius*sin(theta_prime(a,c)));
        angr=result(1)/(radius*sin(theta_prime(a,c)));
        PhiQuarter=phi_fun(angphi, angr);           %call phi_fun
        phi_prime(a,c)=PhiQuarter;
    end
end

end

%theta_fun function
function ThetaQuarter=theta_fun(a,angheta)
%angheta is cosine argument

ThetaQuarter=acos(angheta);

end

%phi_fun function
function PhiQuarter=phi_fun(angphi, angr)

%angphi is sine argument
%angr is cosine argument

if (angphi>=0)&(angr>=0)
    PhiQuarter=asin(angphi);
elseif (angphi>=0)&(angr<0)
    angle=asin(abs(angphi));
    PhiQuarter=pi-angle;
elseif (angphi<0)&(angr<0)
    angle=asin(abs(angphi));
    PhiQuarter=pi+angle;
elseif (angphi<0)&(angr>=0)
    angle=asin(abs(angphi));
    PhiQuarter=2*pi-angle;
end

end

%calculateEfield function based on terminal current
function [Ethetas Ephis]=calculateEfield(d1,I,r1,r2,r3,theta)

b=181;%73%normal simulation points
d=181;
lamda=3/(24.5);

```


Appendix A: 3-D Algorithm for 2x2 Dipole Arrays

```

radius=4.7*lamda;%7.2*lamda;

for c=1:d
    for a=1:b
        R=sqrt((r1(a,c)-d1(1,1))^2+(r2(a,c)-d1(1,2))^2+(r3(a)-
d1(1,3))^2);
        Ethetas(a,c)=(1i*60/(radius))*I*exp(-
1i*2*pi*R/lamda)*cos(0.5*pi*cos(theta(a,c)))/sin(theta(a,c));
    end
end

Ephis(b,d)=0;

end

%transform the Efield from (x',y',z') coordinates to
(x,y,z)coordinates
function [Et
Ep]=transformE(Ethetal,Ephil,theta,phi,theta_prime,phi_prime,A)

b=181;
d=181;

for a=1:b
    for c=1:d
        [prime
unprimed]=calculate(theta(a),phi(c),theta_prime(a,c),phi_prime(a,c))
;
        vectorE=[0;Ethetal(a,c);Ephil(a,c)];
        E=unprimed*A'*prime*vectorE;
        Et(a,c)=E(2);
        Ep(a,c)=E(3);
    end
end

end

%threeDplot to plot far-field pattern in 3D
function threeDplot(rho,theta,phi)

%rho is the normalized Efield
[s_t,a]=size(theta);
[b,s_p]=size(phi);
level_db=40;

for m=1:s_t
    for n=1:s_p
        if (rho(m,n)<10^(-level_db/20))
            rho(m,n)=0;
        else rho(m,n)=20*log10(rho(m,n))+level_db;
        end
    end
end

end

XX=sin(theta)*cos(phi).*rho;
YY=sin(theta)*sin(phi).*rho;
ZZ=cos(theta)*ones(1,s_p).*rho;

```

Appendix A: 3-D Algorithm for 2x2 Dipole Arrays

```
fig_power=figure('Name','3D Polar Power Pattern in
dBs','NumberTitle','off');
ps=surf(XX,YY,ZZ, 'Edgecolor','black','EdgeAlpha', 0.20,
'Linewidth', 1.00);

for k=1:s_t
    rho3(:,:,k)=rho(:,:,k);
end

alpha(0.6);

tick_pos=(-level_db:10:level_db);
ticks=abs(tick_pos)-level_db;

set(gca,'XTick',tick_pos,'XTickLabel',ticks);

set(gca,'YTick',tick_pos,'YTickLabel',ticks);

set(gca,'ZTick',tick_pos,'ZTickLabel',ticks);

set(gca, 'Xcolor', 'black', 'Ycolor','black', 'Zcolor' , 'black' ) ;

xlabel('x-axis, dB');
ylabel('y-axis, dB');
zlabel('z-axis, dB');

axis equal; axis auto; box on;camlight; lightangle(0,45); lighting
gouraud; camproj ('perspective');

function hpol = polar_dB(theta,rho,rmin,rmax,rticks,line_style)
% Input Parameters Description
% -----
% - theta (in degrees) must be a row vector from 0 to 360 degrees
% - rho (in dB) must be a row vector
% - rmin (in dB) sets the minimum limit of the plot (e.g., -60 dB)
% - rmax (in dB) sets the maximum limit of the plot (e.g., 0 dB)
% - rticks is the # of radial ticks (or circles) desired. (e.g., 4)
% - linestyle is solid (e.g., '-') or dashed (e.g., '--')
%
% Tabulate your data accordingly, and call polar_dB to provide the
% 2-D polar plot
%
% Credits:
%     S. Bellofiore
%     S. Georgakopoulos
%     A. C. Polycarpou
%     C. Wangsvick
%     C. Bishop
%
% Tabulate your data accordingly, and call polar_dB to provide the
% 2-D polar plot
%
% Note: This function is different from the polar.m (provided by
% MATLAB) because RHO is given in dB, and it can be negative
%-----
---
```

```

% Convert degrees into radians
theta = theta * pi/180;

% Font size, font style and line width parameters
font_size = 16;%16
font_name = 'Times';
line_width = 1.5;

if nargin < 5
    error('Requires 5 or 6 input arguments.')
elseif nargin == 5
    if isstr(rho)
        line_style = rho;
        rho = theta;
        [mr,nr] = size(rho);
        if mr == 1
            theta = 1:nr;
        else
            th = (1:mr)';
            theta = th(:,ones(1,nr));
        end
    else
        line_style = 'auto';
    end
elseif nargin == 1
    line_style = 'auto';
    rho = theta;
    [mr,nr] = size(rho);
    if mr == 1
        theta = 1:nr;
    else
        th = (1:mr)';
        theta = th(:,ones(1,nr));
    end
end
if isstr(theta) | isstr(rho)
    error('Input arguments must be numeric.');
```

```

end
if any(size(theta) ~= size(rho))
    error('THETA and RHO must be the same size.');
```

```

end

% get hold state
cax = newplot;
next = lower(get(cax, 'NextPlot'));
hold_state = ishold;

% get x-axis text color so grid is in same color
tc = get(cax, 'xcolor');
```

```

% Hold on to current Text defaults, reset them to the
% Axes' font attributes so tick marks use them.

fAngle = get(cax, 'DefaultTextFontAngle');
fName = get(cax, 'DefaultTextFontName');
fSize = get(cax, 'DefaultTextFontSize');
fWeight = get(cax, 'DefaultTextFontWeight');
```

Appendix A: 3-D Algorithm for 2x2 Dipole Arrays

```

set(cax, 'DefaultTextFontAngle', get(cax, 'FontAngle'), ...
'DefaultTextFontName', font_name, ...
'DefaultTextFontSize', font_size, ...
'DefaultTextFontWeight', get(cax, 'FontWeight') )

% only do grids if hold is off

if ~hold_state
    % make a radial grid
    hold on;
    % v returns the axis limits
    % changed the following line to let the y limits become negative
    hhh=plot([0 max(theta(:))],[min(rho(:)) max(rho(:))]);
    v = [get(cax,'xlim') get(cax,'ylim')];
    ticks = length(get(cax,'ytick'));
    delete(hhh);
    % check radial limits (rticks)
    if rticks > 5 % see if we can reduce the number
        if rem(rticks,2) == 0
            rticks = rticks/2;
        elseif rem(rticks,3) == 0
            rticks = rticks/3;
        end
    end
    % define a circle
    th = 0:pi/50:2*pi;
    xunit = cos(th);
    yunit = sin(th);
    % now really force points on x/y axes to lie on them exactly
    inds = [1:(length(th)-1)/4:length(th)];
    xunits(inds(2:2:4)) = zeros(2,1);
    yunits(inds(1:2:5)) = zeros(3,1);
    rinc = (rmax-rmin)/rticks;
    % label r
    % change the following line so that the unit circle is not
multiplied
    % by a negative number. Ditto for the text locations.

    for i=(rmin):rinc:rmax %for i=(rmin+rinc):rinc:rmax
        is = i - rmin;

        plot(xunit*is,yunit*is,'-','color',tc,'linewidth',0.5);
        text(0,is-1.7,[' '
num2str(i)], 'verticalalignment', 'bottom', 'fontsize', 14 );
        %text(0,is+rinc/20,[' ' num2str(i)], 'verticalalignment', 'bottom'
);
    end
    %text(-5,36,'Phi','fontsize',14);
    % plot spokes
    th = (1:6)*2*pi/12;
    cst = cos(th); snt = sin(th);
    cs = [-cst; cst];
    sn = [-snt; snt];
    plot((rmax-rmin)*cs,(rmax-rmin)*sn,'-
','color',tc,'linewidth',0.5);
    % plot the ticks
    george=(rmax-rmin)/30; % Length of the ticks
    th2 = (0:36)*2*pi/72;
    cst2 = cos(th2); snt2 = sin(th2);

```

Appendix A: 3-D Algorithm for 2x2 Dipole Arrays

```

cs2 = [(rmax-rmin-george)*cst2; (rmax-rmin)*cst2];
sn2 = [(rmax-rmin-george)*snt2; (rmax-rmin)*snt2];
plot(cs2,sn2,'-','color',tc,'linewidth',0.15); % 0.5
plot(-cs2,-sn2,'-','color',tc,'linewidth',0.15); % 0.5
% annotate spokes in degrees
% Changed the next line to make the spokes long enough
rt = 1.1*(rmax-rmin);
for i = 1:max(size(th))
    text(rt*cst(i),rt*snt(i),int2str(abs(i*30-
90)), 'horizontalalignment', 'center' );
    if i == max(size(th))
        loc = int2str(90);
    elseif i*30+90<=180
        loc = int2str(i*30+90);
    else
        loc = int2str(180-(i*30+90-180));
    end
    text(-rt*cst(i),-
rt*snt(i),loc, 'horizontalalignment', 'center' );
end
% set view to 2-D
view(0,90);
% set axis limits
% Changed the next line to scale things properly
axis((rmax-rmin)*[-1 1 -1.1 1.1]);
end

% Reset defaults.
set(cax, 'DefaultTextFontAngle', fAngle , ...
'DefaultTextFontName', font_name, ...
'DefaultTextFontSize', fSize, ...
'DefaultTextFontWeight', fWeight );

% transform data to Cartesian coordinates.
% changed the next line so negative rho are not plotted on the other
side

for i = 1:length(rho)
    if (rho(i) > rmin)
        if theta(i)*180/pi >=0 & theta(i)*180/pi <=90
            xx(i) = (rho(i)-rmin)*cos(pi/2-theta(i));
            yy(i) = (rho(i)-rmin)*sin(pi/2-theta(i));
        elseif theta(i)*180/pi >=90
            xx(i) = (rho(i)-rmin)*cos(-theta(i)+pi/2);
            yy(i) = (rho(i)-rmin)*sin(-theta(i)+pi/2);
        elseif theta(i)*180/pi < 0
            xx(i) = (rho(i)-rmin)*cos(abs(theta(i))+pi/2);
            yy(i) = (rho(i)-rmin)*sin(abs(theta(i))+pi/2);
        end
    else
        xx(i) = 0;
        yy(i) = 0;
    end
end
end

% plot data on top of grid

if strcmp(line_style, 'auto')
    q = plot(xx,yy);

```

```
else
    q = plot(xx,yy,line_style);
end

if nargin > 0
    hpol = q;
end

if ~hold_state
    axis('equal');axis('off');
end

% reset hold state
if ~hold_state, set(cax,'NextPlot',next);
end
```

Appendix B: 3D Algorithm for 12 Dipole Arrays arranged at the edge of Cube

```

%main program
lamda=3/(24.5);
radius=4.7*lamda;
theta=(0.01:2:360.01)*pi/180;
phi=(0.01:2:360.01)*pi/180;
[a,b]=size(theta);
[c,d]=size(phi);
theta=theta';

r1=radius*sin(theta)*cos(phi);      %x
r2=radius*sin(theta)*sin(phi);     %y
r3=radius*cos(theta);

%-----
-----

Z11=73.1+42.5i;

array=12;

%calculate the mutual impedance between two dipoles
for r=1:array
    for s=1:array
        if s==r
            Z(r,s)=Z11;
        elseif
(s==2&&r==1)|| (s==3&&r==2)|| (s==3&&r==4)|| (s==4&&r==1)|| (s==1&&r==2)
|| (s==2&&r==3)|| (s==4&&r==3)|| (s==1&&r==4)
            Z(r,s)=impedance(0.5,0.5,0,0.65333,0,0,0);
        elseif
(s==3&&r==1)|| (s==1&&r==3)|| (s==2&&r==4)|| (s==4&&r==2)
            Z(r,s)=impedance(0.5,0.5,0,0.92395,0,0,0);
        %dipole 5
        elseif (s==5&&r==1)|| (s==1&&r==5)
            Z(r,s)=impedance(0.5,0.5,0.32666,0,0.32666,pi/2,0);
        elseif (s==5&&r==2)|| (s==2&&r==5)
            Z(r,s)=impedance(0.5,0.5,-0.32666,0,0.32666,pi/2,0);
    end
end

```

Appendix B: 3-D Algorithm for 12 Dipole Arrays arranged at the edge of cube.

```

elseif (s==5&&r==3) || (s==3&&r==5)
Z(r,s)=impedance(0.5,0.5,-0.32666,-0.65333,0.32666,pi/2,0);
elseif (s==5&&r==4) || (s==4&&r==5)
Z(r,s)=impedance(0.5,0.5,0.32666,-0.65333,0.32666,pi/2,0);
    %dipole 6
elseif (s==1&&r==6) || (s==6&&r==1)
Z(r,s)=impedance(0.5,0.5,0,0.32666,0.32666,pi/2,pi/2);
elseif (s==2&&r==6) || (s==6&&r==2)
Z(r,s)=impedance(0.5,0.5,-
0.65333,0.32666,0.32666,pi/2,pi/2);          elseif
(s==3&&r==6) || (s==6&&r==3)
Z(r,s)=impedance(0.5,0.5,-0.65333,-
0.32666,0.32666,pi/2,pi/2);
elseif (s==4&&r==6) || (s==6&&r==4)
Z(r,s)=impedance(0.5,0.5,0,-0.32666,0.32666,pi/2,pi/2);
elseif (s==5&&r==6) || (s==6&&r==5)
Z(r,s)=impedance(0.5,0.5,0,-0.32666,0.32666,pi/2,pi/2);
    %dipole 7
elseif (s==1&&r==7) || (s==7&&r==1)
Z(r,s)=impedance(0.5,0.5,0.65333,0.32666,0.32666,pi/2,pi/2);
elseif (s==2&&r==7) || (s==7&&r==2)
Z(r,s)=impedance(0.5,0.5,0,0.32666,0.32666,pi/2,pi/2);
elseif (s==3&&r==7) || (s==7&&r==3)
Z(r,s)=impedance(0.5,0.5,0,-0.32666,0.32666,pi/2,pi/2);
elseif (s==4&&r==7) || (s==7&&r==4)
Z(r,s)=impedance(0.5,0.5,0.65333,-
0.32666,0.32666,pi/2,pi/2);
elseif (s==5&&r==7) || (s==7&&r==5)
Z(r,s)=impedance(0.5,0.5,0,0.32666,0.32666,pi/2,pi/2);
elseif (s==6&&r==7) || (s==7&&r==6)
Z(r,s)=impedance(0.5,0.5,0,0.65333,0,0,0);
    %dipole 8
elseif (s==1&&r==8) || (s==8&&r==1)
Z(r,s)=impedance(0.5,0.5,0.32666,0.65333,0.32666,pi/2,0);
elseif (s==2&&r==8) || (s==8&&r==2)
Z(r,s)=impedance(0.5,0.5,-0.32666,0.65333,0.32666,pi/2,0);
elseif (s==3&&r==8) || (s==8&&r==3)
Z(r,s)=impedance(0.5,0.5,-0.32666,0,0.32666,pi/2,0);
elseif (s==4&&r==8) || (s==8&&r==4)
Z(r,s)=impedance(0.5,0.5,0.32666,0,0.32666,pi/2,0);
elseif (s==5&&r==8) || (s==8&&r==5)
Z(r,s)=impedance(0.5,0.5,0,0.65333,0,0,0);
elseif (s==6&&r==8) || (s==8&&r==6)
Z(r,s)=impedance(0.5,0.5,0,0.32666,0.32666,pi/2,pi/2);
elseif (s==7&&r==8) || (s==8&&r==7)
Z(r,s)=impedance(0.5,0.5,0,-0.32666,0.32666,pi/2,pi/2);
    %dipole 9
elseif (s==1&&r==9) || (s==9&&r==1)
Z(r,s)=impedance(0.5,0.5,0.32666,0,-0.32666,pi/2,0);
elseif (s==2&&r==9) || (s==9&&r==2)
Z(r,s)=impedance(0.5,0.5,-0.32666,0,-0.32666,pi/2,0);
elseif (s==3&&r==9) || (s==9&&r==3)
Z(r,s)=impedance(0.5,0.5,-0.32666,-0.65333,-0.32666,pi/2,0);
elseif (s==4&&r==9) || (s==9&&r==4)
Z(r,s)=impedance(0.5,0.5,0.32666,-0.65333,-0.32666,pi/2,0);
elseif (s==5&&r==9) || (s==9&&r==5)
Z(r,s)=impedance(0.5,0.5,0,0.65333,0,0,0);
elseif (s==6&&r==9) || (s==9&&r==6)
Z(r,s)=impedance(0.5,0.5,0.65333,-0.32666,-0.32666,pi/2,0);
elseif (s==7&&r==9) || (s==9&&r==7)

```


Appendix B: 3-D Algorithm for 12 Dipole Arrays arranged at the edge of cube.

```

Z(r,s)=impedance(0.5,0.5,-0.65333,-0.32666,-0.32666,pi/2,0);
elseif (s==8&&r==9) || (s==9&&r==8)
Z(r,s)=impedance(0.5,0.5,0,0.92395,0,0,0);
%dipole 10
elseif (s==1&&r==10) || (s==10&&r==1)
Z(r,s)=impedance(0.5,0.5,0.65333,0.32666,-
0.32666,pi/2,pi/2);
elseif (s==2&&r==10) || (s==10&&r==2)
Z(r,s)=impedance(0.5,0.5,0,0.32666,-0.32666,pi/2,pi/2);
elseif (s==3&&r==10) || (s==10&&r==3)
Z(r,s)=impedance(0.5,0.5,0,-0.32666,-0.32666,pi/2,pi/2);
elseif (s==4&&r==10) || (s==10&&r==4)
Z(r,s)=impedance(0.5,0.5,0.65333,-0.32666,-
0.32666,pi/2,pi/2);
elseif (s==5&&r==10) || (s==10&&r==5)
Z(r,s)=impedance(0.5,0.5,0.65333,-0.32666,0.32666,pi/2,0);
elseif (s==6&&r==10) || (s==10&&r==6)
Z(r,s)=impedance(0.5,0.5,0,0.92395,0,0,0);
elseif (s==7&&r==10) || (s==10&&r==7)
Z(r,s)=impedance(0.5,0.5,0,0.65333,0,0,0);
elseif (s==8&&r==10) || (s==10&&r==8)
Z(r,s)=impedance(0.5,0.5,0.65333,-0.32666,-0.32666,pi/2,0);
elseif (s==9&&r==10) || (s==10&&r==9)
Z(r,s)=impedance(0.5,0.5,0,0.32666,0.32666,pi/2,pi/2);
%dipole 11
elseif (s==1&&r==11) || (s==11&&r==1)
Z(r,s)=impedance(0.5,0.5,0.32666,0.65333,-0.32666,pi/2,0);
elseif (s==2&&r==11) || (s==11&&r==2)
Z(r,s)=impedance(0.5,0.5,-0.32666,0.65333,-0.32666,pi/2,0);
elseif (s==3&&r==11) || (s==11&&r==3)
Z(r,s)=impedance(0.5,0.5,-0.32666,0,-0.32666,pi/2,0);
elseif (s==4&&r==11) || (s==11&&r==4)
Z(r,s)=impedance(0.5,0.5,0.32666,0,-0.32666,pi/2,0);
elseif (s==5&&r==11) || (s==11&&r==5)
Z(r,s)=impedance(0.5,0.5,0,0.92395,0,0,0);
elseif (s==6&&r==11) || (s==11&&r==6)
Z(r,s)=impedance(0.5,0.5,0.65333,0.32666,-0.32666,pi/2,0);
elseif (s==7&&r==11) || (s==11&&r==7)
Z(r,s)=impedance(0.5,0.5,-0.65333,0.32666,-0.32666,pi/2,0);
elseif
(s==8&&r==11) || (s==11&&r==8) || (s==9&&r==11) || (s==11&&r==9)
Z(r,s)=impedance(0.5,0.5,0,0.65333,0,0,0);
elseif (s==10&&r==11) || (s==11&&r==10)
Z(r,s)=impedance(0.5,0.5,0,-0.32666,0.32666,pi/2,pi/2);
%dipole 12
elseif (s==1&&r==12) || (s==12&&r==1)
Z(r,s)=impedance(0.5,0.5,0,0.32666,-0.32666,pi/2,pi/2);
elseif (s==2&&r==12) || (s==12&&r==2)
Z(r,s)=impedance(0.5,0.5,-0.65333,0.32666,-
0.32666,pi/2,pi/2);
elseif (s==3&&r==12) || (s==12&&r==3)
Z(r,s)=impedance(0.5,0.5,-0.65333,-0.32666,-
0.32666,pi/2,pi/2);
elseif (s==4&&r==12) || (s==12&&r==4)
Z(r,s)=impedance(0.5,0.5,0,-0.32666,-0.32666,pi/2,pi/2);
elseif (s==5&&r==12) || (s==12&&r==5)
Z(r,s)=impedance(0.5,0.5,-0.65333,0.32666,-
0.32666,pi/2,pi/2);
elseif (s==6&&r==12) || (s==12&&r==6)
Z(r,s)=impedance(0.5,0.5,0,0.65333,0,0,0);

```

Appendix B: 3-D Algorithm for 12 Dipole Arrays arranged at the edge of cube.

```

elseif (s==7&&r==12) || (s==12&&r==7)
Z(r,s)=impedance(0.5,0.5,0,0.92395,0,0,0);
elseif (s==8&&r==12) || (s==12&&r==8)
Z(r,s)=impedance(0.5,0.5,-0.65333,-0.32666,-
0.32666,pi/2,pi/2);
elseif (s==9&&r==12) || (s==12&&r==9)
Z(r,s)=impedance(0.5,0.5,0,-0.32666,0.32666,pi/2,pi/2);
elseif (s==10&&r==12) || (s==12&&r==10)
Z(r,s)=impedance(0.5,0.5,0,0.65333,0,0,0);
elseif (s==11&&r==12) || (s==12&&r==11)
Z(r,s)=impedance(0.5,0.5,0,-0.32666,-0.32666,pi/2,pi/2);
end
end
end

V=[0.560784314*exp(-1j*2.870553287);
0.415686275*exp(1j*2.254554728);
0.082352941*exp(1j*0.8008);0.329411765*exp(1j*0.874717955); 0; 0; 0;
0; 0; 0; 0; 0];

%mutual coupling effect
source=[50 50 50 50 50 50 50 50 50 50 50 50];
Zs=diag(source);
Ifeed=inv(Z+Zs)*V;

r=1;

%-----
%dipole1
x1=-0.3267*lamda; %(x=-0.04,y=-0.04,0)
y1=-0.3267*lamda;
z1=0;
d1=[x1 y1 z1];

A=calculateA(0,0,0); %(alpha,beta,gamma for dipole 2)
[theta_prime
phi_prime]=findThetaPhiPrime2deg(x1,y1,z1,A,theta,phi,radius);
[Etheta1
Ephi1]=calculateEfield2deg(d1,Ifeed(1,r),r1,r2,r3,theta_prime);
[Et1
Ep1]=transformE2deg(Etheta1,Ephi1,theta,phi,theta_prime,phi_prime,A)
;

%-----
-
%dipole2
x2=0.3267*lamda;%(x=0.04,-0.04,0)
y2=-0.3267*lamda;
z2=0;
d2=[x2 y2 z2];

A=calculateA(0,0,0); %(alpha,beta,gamma for dipole 2)
[theta_prime
phi_prime]=findThetaPhiPrime2deg(x2,y2,z2,A,theta,phi,radius);
[Etheta2
Ephi2]=calculateEfield2deg(d2,Ifeed(2,r),r1,r2,r3,theta_prime);
[Et2
Ep2]=transformE2deg(Etheta2,Ephi2,theta,phi,theta_prime,phi_prime,A)
;

```

Appendix B: 3-D Algorithm for 12 Dipole Arrays arranged at the edge of cube.

```

%-----
--
%dipole3
x3=0.3267*lamda;%(0.04,0.04,0)
y3=0.3267*lamda;
z3=0;
d3=[x3 y3 z3];

A=calculateA(0,0,0); %(alpha,beta,gamma for dipole 2)
[theta_prime
phi_prime]=findThetaPhiPrime2deg(x3,y3,z3,A,theta,phi,radius);
[Etheta3
Ephi3]=calculateEfield2deg(d3,Ifeed(3,r),r1,r2,r3,theta_prime);
[Et3
Ep3]=transformE2deg(Etheta3,Ephi3,theta,phi,theta_prime,phi_prime,A)
;

%-----
---
%dipole4
x4=-0.3267*lamda;%(-0.04,0.04,0)
y4=0.3267*lamda;
z4=0;
d4=[x4 y4 z4];

A=calculateA(0,0,0); %(alpha,beta,gamma for dipole 2)
[theta_prime
phi_prime]=findThetaPhiPrime2deg(x4,y4,z4,A,theta,phi,radius);
[Etheta4
Ephi4]=calculateEfield2deg(d4,Ifeed(4,r),r1,r2,r3,theta_prime);
[Et4
Ep4]=transformE2deg(Etheta4,Ephi4,theta,phi,theta_prime,phi_prime,A)
;

%-----
-----
%dipole5
x5=0;
y5=-0.04;
z5=0.04;
d5=[x5 y5 z5];

A=calculateA(-pi/2,-pi/2,0); %(alpha,beta,gamma for dipole 2)
[theta_prime
phi_prime]=findThetaPhiPrime2deg(x5,y5,z5,A,theta,phi,radius);
[Etheta5
Ephi5]=calculateEfield2deg(d5,Ifeed(5,r),r1,r2,r3,theta_prime);
[Et5
Ep5]=transformE2deg(Etheta5,Ephi5,theta,phi,theta_prime,phi_prime,A)
;

%-----
-----
%dipole6
x6=-0.04; %(-0.04,0,0.04)
y6=0;
z6=0.04;
d6=[x6 y6 z6];

```

Appendix B: 3-D Algorithm for 12 Dipole Arrays arranged at the edge of cube.

```

A=calculateA(0,-pi/2,0); %(alpha,beta,gamma for dipole 2)
[theta_prime
phi_prime]=findThetaPhiPrime2deg(x6,y6,z6,A,theta,phi,radius);
[Etheta6
Ephi6]=calculateEfield2deg(d6,Ifeed(6,r),r1,r2,r3,theta_prime);
[Et6
Ep6]=transformE2deg(Etheta6,Ephi6,theta,phi,theta_prime,phi_prime,A)
;

%-----
-----
%dipole7
x7=0.04;
y7=0*lamda;
z7=0.04;%*lamda;
d7=[x7 y7 z7];

A=calculateA(0,-pi/2,0); %(alpha,beta,gamma for dipole 2)
[theta_prime
phi_prime]=findThetaPhiPrime2deg(x7,y7,z7,A,theta,phi,radius);
[Etheta7
Ephi7]=calculateEfield2deg(d7,Ifeed(7,r),r1,r2,r3,theta_prime);
[Et7
Ep7]=transformE2deg(Etheta7,Ephi7,theta,phi,theta_prime,phi_prime,A)
;

%-----
-----
%dipole8
x8=0;%32666*lamda; (0,0.04,0.04)
y8=0.04;%65333*lamda;
z8=0.04;%32666*lamda;
d8=[x8 y8 z8];

A=calculateA(-pi/2,-pi/2,0); %(alpha,beta,gamma for dipole 2)
[theta_prime
phi_prime]=findThetaPhiPrime2deg(x8,y8,z8,A,theta,phi,radius);
[Etheta8
Ephi8]=calculateEfield2deg(d8,Ifeed(8,r),r1,r2,r3,theta_prime);
[Et8
Ep8]=transformE2deg(Etheta8,Ephi8,theta,phi,theta_prime,phi_prime,A)
;

%-----
-----
%dipole9
x9=0;%32666*lamda;(0,-0.04,-0.04)
y9=-0.04;
z9=-0.04;%32666*lamda;
d9=[x9 y9 z9];

A=calculateA(-pi/2,-pi/2,0); %(alpha,beta,gamma for dipole 2)
[theta_prime
phi_prime]=findThetaPhiPrime2deg(x9,y9,z9,A,theta,phi,radius);
[Etheta9
Ephi9]=calculateEfield2deg(d9,Ifeed(9,r),r1,r2,r3,theta_prime);

```

Appendix B: 3-D Algorithm for 12 Dipole Arrays arranged at the edge of cube.

```

[Et9
Ep9]=transformE2deg(Etheta9,Ephi9,theta,phi,theta_prime,phi_prime,A)
;

%-----
-----
%dipole10
x10=0.04;%65333*lamda;(0.04,0,-0.04)
y10=0;%.32666*lamda;
z10=-0.04;%32666*lamda;
d10=[x10 y10 z10];

A=calculateA(0,-pi/2,0); %(alpha,beta,gamma for dipole 2)
[theta_prime
phi_prime]=findThetaPhiPrime2deg(x10,y10,z10,A,theta,phi,radius);
[Etheta10
Ephi10]=calculateEfield2deg(d10,Ifeed(10,r),r1,r2,r3,theta_prime);
[Et10
Ep10]=transformE2deg(Etheta10,Ephi10,theta,phi,theta_prime,phi_prime
,A);

%-----
-----
%dipole11
x11=0;%.32666*lamda;(0,0.04,-0.04)
y11=0.04;%65333*lamda;
z11=-0.04;%32666*lamda;
d11=[x11 y11 z11];

A=calculateA(-pi/2,-pi/2,0); %(alpha,beta,gamma for dipole 2)
[theta_prime
phi_prime]=findThetaPhiPrime2deg(x11,y11,z11,A,theta,phi,radius);
[Etheta11
Ephi11]=calculateEfield2deg(d11,Ifeed(11,r),r1,r2,r3,theta_prime);
[Et11
Ep11]=transformE2deg(Etheta11,Ephi11,theta,phi,theta_prime,phi_prime
,A);

%-----
-----
%dipole12
x12=-0.04;% (-0.04,0,-0.04)
y12=0;%.32666*lamda;
z12=-0.04;%32666*lamda;
d12=[x12 y12 z12];

A=calculateA(0,-pi/2,0); %(alpha,beta,gamma for dipole 2)
[theta_prime
phi_prime]=findThetaPhiPrime2deg(x12,y12,z12,A,theta,phi,radius);
[Etheta12
Ephi12]=calculateEfield2deg(d12,Ifeed(12,r),r1,r2,r3,theta_prime);
[Et12
Ep12]=transformE2deg(Etheta12,Ephi12,theta,phi,theta_prime,phi_prime
,A);

%-----
-----
%summation of both E dipoles

```

Appendix B: 3-D Algorithm for 12 Dipole Arrays arranged at the edge of cube.

```
E_theta=Et1+Et2+Et3+Et4+Et5+Et6+Et7+Et8+Et9+Et10+Et11+Et12;
E_phi=Ep1+Ep2+Ep3+Ep4+Ep5+Ep6+Ep7+Ep8+Ep9+Ep10+Ep11+Ep12;

Efield=sqrt((abs(E_theta)).^2+(abs(E_phi)).^2);

maxi=max(max(Efield));

Efield2=Efield/maxi;

val1=46;val2=51;
t=theta(val1)*180/pi
p=phi(val2)*180/pi

Sh_p=Efield(val1,:)/maxi;      %normalized far-field pattern
Sv_p=Efield(:,val2)/maxi;     %normalized far-field pattern
threeDplot(Efield2,theta,phi); %plot 3D far-field pattern
```

Appendix C: 3D Algorithm (2x2 dipole arrays) with Genetic Algorithm

```
%main program
% sga.m
%
% This script implements the Simple Genetic Algorithm described
% in the examples section of the GA Toolbox manual.
%
% Author:      Andrew Chipperfield
% History:     23-Mar-94      file created
%
% tested under MATLAB v6 by Alex Shenfield (22-Jan-03)

NIND = 40;           % Number of individuals per subpopulations
MAXGEN = 700;       %%usually 700 maximum Number of generations
GGAP = .9;          % Generation gap, how many new individuals are
                    % created
NVAR = 4;           % Number of variables, four dipoles
PRECI = 8;          % Precision of binary representation

% Build field descriptor
FieldD = [rep([PRECI PRECI],[1, NVAR]); rep([0 -pi;1 pi],[1,
NVAR]);...
          rep([0 0; 0 0; 1 1;1 1], [1,
NVAR])];%len,lb,ub,code,scale,,lbinc,ubinc

% Initialise population
Chrom = crtbp(NIND, 2*NVAR*PRECI);%row=ind,col=nvar*preci

% Reset counters
Best = NaN*ones(MAXGEN,1);      % best in current population
gen = 0;                        % generational counter

% Evaluate initial population
ObjV = objfun1(bs2rv(Chrom,FieldD)); % call objfun1
```

Appendix C: 3D Algorithm (2x2 dipole arrays) with Genetic Algorithm

```
% Track best individual and display convergence
Best(gen+1) = min(ObjV);%min
plot(abs(Best),'ro');xlabel('generation'); ylabel('(f(x))');
text(0.5,0.95,['Best = ',
num2str(abs(Best(gen+1)))], 'Units', 'normalized');
drawnow;
phen1=bs2rv(Chrom,FieldD);

% Generational loop
while gen < MAXGEN,
    % Assign fitness-value to entire population
    FitnV = ranking(ObjV);

    % Select individuals for breeding
    %select choice a)sus=stochastic universal sampling,
b) rws=rhoullete
    %wheel selection,
    SelCh = select('sus', Chrom, FitnV, GGAP);

    % Recombine selected individuals (crossover)
    SelCh = recomb('xovsp',SelCh,0.7);

    % Perform mutation on offspring
    SelCh = mut(SelCh);

    % Evaluate offspring, call objective function
    ObjVSel = objfun1(bs2rv(SelCh,FieldD));

    % Reinsert offspring into current population
    [Chrom ObjV]=reins(Chrom,SelCh,1,1,ObjV,ObjVSel);

    % Increment generational counter
    gen = gen+1;

    % Update display and record current best individual
    Best(gen+1) = min(ObjV);%min
    plot(abs(Best),'ro'); xlabel('generation');
ylabel('(f(x))');
    text(0.5,0.95,['Best = ',
num2str(abs(Best(gen+1)))], 'Units', 'normalized');
    drawnow;
end

phen=bs2rv(Chrom,FieldD);
```


Appendix C: 3D Algorithm (2x2 dipole arrays) with Genetic Algorithm

```
% OBJFUN1.M      (OBJective function for De Jong's FUNction 1)
%
% This function implements the De Jong function 1.
%
% Syntax:  ObjVal = objfun1(Chrom,rtn_type)
%
% Input parameters:
%   Chrom    - Matrix containing the chromosomes of the current
%              population. Each row corresponds to one
individual's
%              string representation.
%              if Chrom == [], then special values will be
returned
%   rtn_type - if Chrom == [] and
%              rtn_type == 1 (or []) return boundaries
%              rtn_type == 2 return title
%              rtn_type == 3 return value of global minimum
%
% Output parameters:
%   ObjVal   - Column vector containing the objective values of
the
%              individuals in the current population.
%              if called with Chrom == [], then ObjVal contains
%              rtn_type == 1, matrix with the boundaries of the
function
%              rtn_type == 2, text for the title of the graphic
output
%              rtn_type == 3, value of global minimum
%
%
% Author:      Hartmut Pohlheim
% History:    26.11.93    file created
%             27.11.93    text of title and rtn_type added
%             30.11.93    show Dim in figure title
%             16.12.93    rtn_type == 3, return value of global
minimum
%             01.03.94    name changed in obj*
%             21.01.03    updated for MATLAB v6 by Alex
Shenfield

function [ObjVal] = objfun1(Chrom,rtn_type)
% Dimension of objective function
    Dim = 8;%8 for 4 vertical dipole array 4 for 2 dipoles
    Nind= 40;
% Compute population parameters
    [Nind,Nvar] = size(Chrom);

    %x=decode(Chrom);
% Check size of Chrom and do the appropriate thing
% if Chrom is [], then define size of boundary-matrix and
values
    if Nind == 0
        % return text of title for graphic output
        if rtn_type == 2
            ObjVal = ['DE JONG function 1-' int2str(Dim)];
        % return value of global minimum
        elseif rtn_type == 3
            ObjVal = 0;
        % define size of boundary-matrix and values
```

```

else
    % lower and upper bound, identical for all n variables
    ObjVal = [0 -pi;1 pi];
    ObjVal = ObjVal(1:2,ones(Dim,1));
end
% if Dim variables, compute values of function
elseif Nvar == Dim
    % function 1, sum of xi^2 for i = 1:Dim (Dim=30)
    % n = Dim, -5.12 <= xi <= 5.12
    % global minimum at (xi)=(0) ; fmin=0
    %ObjVal = -(0.7*abs(sin(pi*(Chrom-3)))./abs(pi*(Chrom-3)));%
sum((Chrom .* Chrom)')';
    % ObjVal = diag(Chrom * Chrom'); % both lines produce the
same
    % otherwise error, wrong format of Chrom
    for id=1:Nind
        C=Chrom(id,:);
        [Sw]=compute3(C); %call compute3(C) function;
        ObjVal(id)=fitness(Sw); %call fitness(Sw);
    end

    ObjVal=ObjVal';
else
    error('size of matrix Chrom is not correct for function
evaluation');
end

% End of function

```

Appendix C: 3D Algorithm (2x2 dipole arrays) with Genetic Algorithm

```

%compute3 function
function [Sw]=compute3(Chrom)

L=0.5;
global dist Z;
ang1=(0.01:10:110)*pi/180;    %max_rad-30=lowbound
ang2=(116:1:164)*pi/180;    %lowbound+6:upperbound-6
ang3=(170:10:359)*pi/180;    %upperbound
ang=[ang1 ang2 ang3];

theta=ang;
phi=ang;
[m,n]=size(theta);
[s,t]=size(phi);
r=4.3;
arraySize=4;

dist=[-0.4492 -0.4492 0;0.4492 -0.4492 0;0.4492 0.4492 0;-0.4492
0.4492 0];

x1(t,n)=0;
y1(t,n)=0;
z1=0;
A(t,n)=0;

V=[Chrom(1,1)*exp(1*j*Chrom(1,2)) Chrom(1,3)*exp(1*j*Chrom(1,4))
Chrom(1,5)*exp(1*j*Chrom(1,6)) Chrom(1,7)*exp(1*j*Chrom(1,8))];

%impedance
a=73.1+1i*42.5;
b=-7.68 + 18.44*1i;
c=13.86 - 4.38*1i;
Z=[a b c b;b a b c;c b a b;b c b a];

v_t=V.';
Zimp=[50 50 50 50];
Zs= diag(Zimp);
Ifeed=(Z+Zs)\v_t;
l=3/24.5;    %calculates lamda at f=2.44 GHz

r=1;
%-----
%dipole1

A=calculateA(0,0,0); %(alpha,beta,gamma for dipole 2)
[theta_prime
phi_prime]=findThetaPhiPrime(x1,y1,z1,A,theta,phi,radius);
[Etheta1
Ephi1]=calculateEfield(d1,Ifeed(1,r),r1,r2,r3,theta_prime);
[Et1
Epl]=transformE(Etheta1,Ephi1,theta,phi,theta_prime,phi_prime,A);

%-----
----
%dipole2

A=calculateA(0,0,0); %(alpha,beta,gamma for dipole 2)

```

Appendix C: 3D Algorithm (2x2 dipole arrays) with Genetic Algorithm

```

[theta_prime
phi_prime]=findThetaPhiPrime(x2,y2,z2,A,theta,phi,radius);
[Etheta2
Ephi2]=calculateEfield(d2,Ifeed(2,r),r1,r2,r3,theta_prime);
[Et2
Ep2]=transformE(Etheta2,Ephi2,theta,phi,theta_prime,phi_prime,A);

%-----
%-----
%dipole3

A=calculateA(0,0,0); %(alpha,beta,gamma for dipole 2)
[theta_prime
phi_prime]=findThetaPhiPrime(x3,y3,z3,A,theta,phi,radius);
[Etheta3
Ephi3]=calculateEfield(d3,Ifeed(3,r),r1,r2,r3,theta_prime);
[Et3
Ep3]=transformE(Etheta3,Ephi3,theta,phi,theta_prime,phi_prime,A);

%-----
%-----
%dipole4

A=calculateA(0,0,0); %(alpha,beta,gamma for dipole 2)
[theta_prime
phi_prime]=findThetaPhiPrime(x4,y4,z4,A,theta,phi,radius);
[Etheta4
Ephi4]=calculateEfield(d4,Ifeed(4,r),r1,r2,r3,theta_prime);
[Et4
Ep4]=transformE(Etheta4,Ephi4,theta,phi,theta_prime,phi_prime,A);

%-----
%-----
%summation of both E fields

E_theta=Et1+Et2+Et3+Et4;
E_phi=Ep1+Ep2+Ep3+Ep4;

Efield=sqrt((abs(E_theta)).^2+(abs(E_phi)).^2);

maxi=max(max(Efield));

row=13;
%theta cut at theta=90 deg
Sw=(Efield(row,:)/maxi);%Sw(theta=90,:)row vector[x x x x ....]

```

Appendix C: 3D Algorithm (2x2 dipole arrays) with Genetic Algorithm

```
%fitness function calculated
function z=fitness(Sw)

max_rad=7*pi/9;           %steer the beam to the desired
direction
[Sd ang]=desiredcosine(max_rad); %call desiredcosine function

[Q c]=size(ang);
P02=0.05;

total=0;
for i=1:c
total=total+abs(Sd(1,i)-Sw(1,i));%compare the GA pattern with
desired cosine pattern
end

z=-1/(1+P02*total);      %calculate the cost function for each
individual

%desiredcosine is the desired pattern
function [Sd ang]=desiredcosine(max_rad)

delta=30*pi/180;

ang1=(0.01:10:110)*pi/180;%max_rad-30=lowbound
ang2=(116:1:164)*pi/180;%lowbound+6:upperbound-6
ang3=(170:10:359)*pi/180;%upperbound
ang=[ang1 ang2 ang3];
[r c]=size(ang);
low_bound=max_rad-delta;
upper_bound=max_rad+delta;

for i=1:c
    if ang(i)>low_bound&&ang(i)<upper_bound
        Sd(i)=cos(pi/2*((ang(i)-max_rad)/delta));
    else
        Sd(i)=0.3;
    end
end
end
```

Appendix D: Effects of Element Spacing and Orientation on the Far-field Pattern of Four Dipole Antenna Arrays

D.1 Parameters Variation

This appendix provides parameters variation using the 3-D algorithm in order to observe its changes to the pattern of 2x2 dipole antenna array. The simulations are used to study the range of accuracy of four dipole arrays in measurement set-up. For example, if the far-field pattern alters tremendously even though the spacing of the four dipoles array is changed by small amount, then the measurement process will be pointless. It is because the dipole antennas are handmade, thus they are not in perfect arrangement and prone to errors. Therefore, it presents an obstacle to the measurement set-up to ensure that the position and angle of the dipole elements are as close as possible to the ones being used in simulation. Several parameters are varied in these simulations: spacing in parallel, spacing in echelon, and slanted angle of dipole antennas.

The simulation may be divided into few sections:

- 1) Design of the sample (for example 4 dipoles array) used in the measurement study.
- 2) Spacing in parallel variation.
- 3) Spacing in echelon variation.
- 4) Spacing with dipole elements are tilted in certain angles.

D.2 Design Sample used in Measurement Study

The positions of a 4-element parallel dipole antenna array are illustrated in Figure D-1 with a spacing of $0.9\lambda_0$ (110 mm) at 2.45 GHz. Table 28 shows the excitation amplitude and phase for each dipole. The excitation values are chosen in order to steer the beam to 100° while maintaining lowest side-lobe level possible.

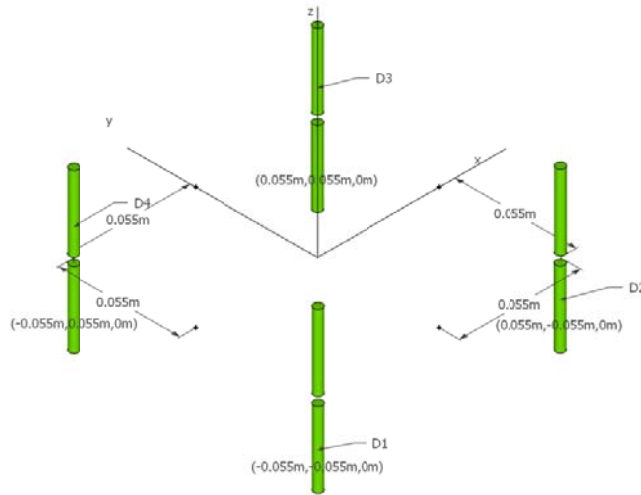


Figure D-1: The position of ideal straight dipole antennas.

Table 29: The excitation amplitude (V) and phase (degrees) applied to each dipole.

Dipole	Amplitude, V	Phase, degrees
1	0.3454	148.25
2	0.2066	-175.14
3	0.2608	-129.64
4	0.1565	-179.94

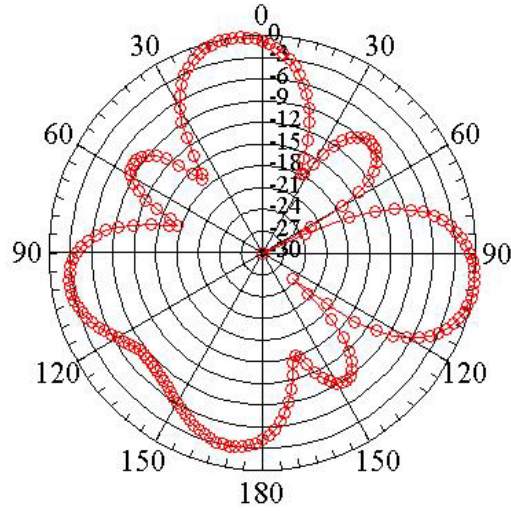


Figure D-2: The normalised azimuth far-field radiation pattern for a parallel dipole array computed using a 3-D algorithm.

D.3 Calculation of the Array Factor of Four Dipoles

The array factor demonstrating the far-field pattern in Figure D-2 can be calculated using the 3-D algorithm. It is observed that two main beams, a deep null approximately at angle 62° and the second null is approximately at 125° are formed in Figure D-2.

The main beams and nulls could be derived from the array factor of four dipoles:

$$AF(\theta, \phi) = \sum_{n=1}^4 A_n e^{j[ka \sin \theta_0 \cos(\phi_0 - \phi_n) + \alpha_n]} \quad (d-1)$$

$$AF(\theta, \phi) = AF_1(\theta, \phi) + AF_2(\theta, \phi) + AF_3(\theta, \phi) + AF_4(\theta, \phi) \quad (d-2)$$

where

$$\left. \begin{aligned} AF_1(\theta, \phi) &= 0.3454e^{j\left[\frac{2\pi}{\lambda} \times 0.6352\lambda \times \sin \theta \cos\left(\phi - \frac{5\pi}{4}\right) + \frac{148.25\pi}{180}\right]} \\ AF_2(\theta, \phi) &= 0.2066e^{j\left[\frac{2\pi}{\lambda} \times 0.6352\lambda \times \sin \theta \cos\left(\phi - \frac{7\pi}{4}\right) - \frac{175.14\pi}{180}\right]} \\ AF_3(\theta, \phi) &= 0.2608e^{j\left[\frac{2\pi}{\lambda} \times 0.6352\lambda \times \sin \theta \cos\left(\phi - \frac{\pi}{4}\right) - \frac{129.64\pi}{180}\right]} \\ AF_4(\theta, \phi) &= 0.1565e^{j\left[\frac{2\pi}{\lambda} \times 0.6352\lambda \times \sin \theta \cos\left(\phi - \frac{3\pi}{4}\right) - \frac{179.94\pi}{180}\right]} \end{aligned} \right\} (d-2a)$$

Appendix D: Effects of the Element Spacing and Orientation on the Far-field Pattern of Four Dipole Antenna Arrays

Equation (d-2) is obtained by applying the amplitude and phase excitation from Table 28. The total AF for maximum beam of (θ_0, ϕ_0) at $(90^\circ, 100^\circ)$ and $(90^\circ, 355^\circ)$ is:

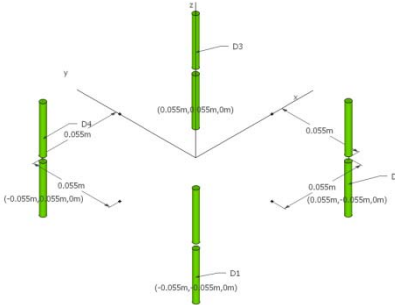
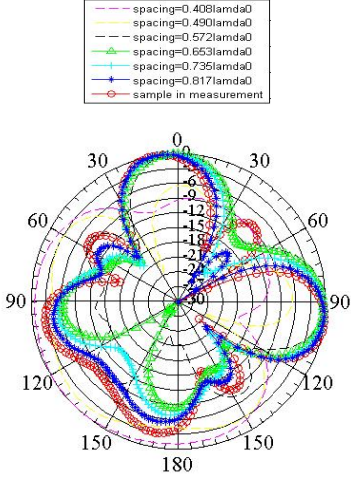
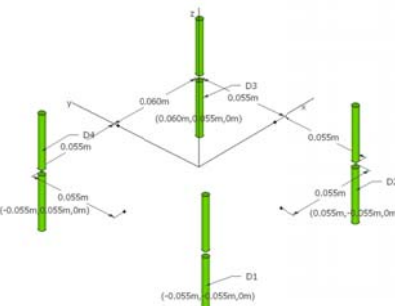
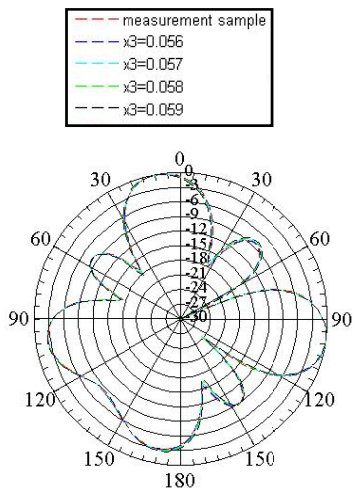
$$AF(\theta, \phi) \approx 1 \quad (\text{d} - 3)$$

The nulls could be obtained by applying the position of the null (for example approximately at $(90^\circ, 62^\circ)$) in equation (d-2) to obtain:

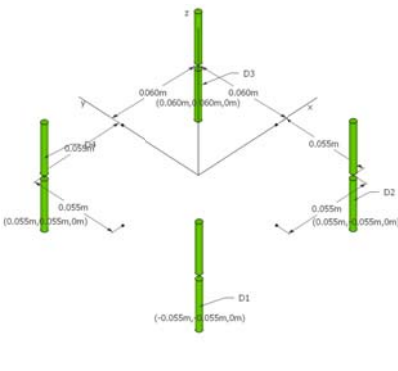
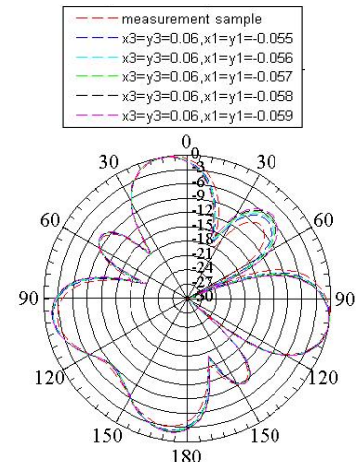
$$\begin{aligned} AF(90^\circ, 62^\circ) &= 0.3454e^{j(-70.43^\circ)} + 0.2066e^{j(-242^\circ)} + 0.2608e^{j(89^\circ)} + 0.1565e^{j(-113^\circ)} \\ &= 0.11568 - j0.32544 - 0.1 + j0.182 + 0.005 + j0.2608 - 0.0611 - j0.144 \\ &= -0.0409 - j0.02664 \end{aligned} \quad (\text{d} - 4)$$

$$AF_{dB}(90^\circ, 62^\circ) = -26 \text{ dB}$$

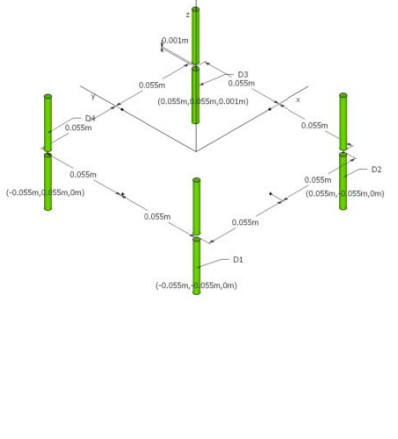
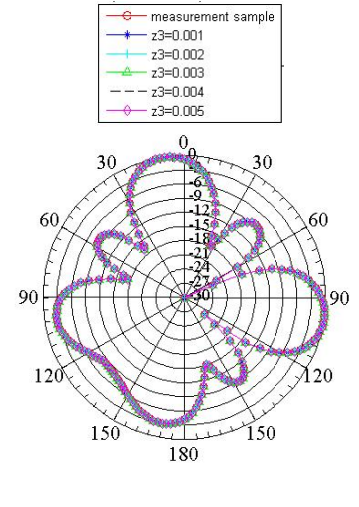
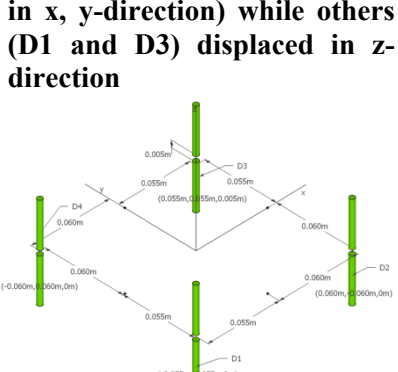
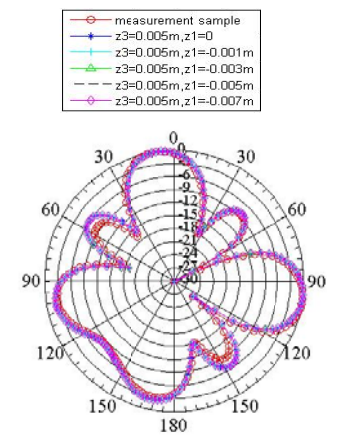
D.4 Effect of varying spacing in parallel on the pattern

No.	Simulation Model	Variation	Effect to the normalised pattern at theta=90	Observation on the far-field pattern
1	<p>Parallel Dipole with Uniform Spacing</p> 	<p>Spacing variation from $0.408\lambda_0$ to $0.898\lambda_0$ (0.050 m to 0.110 m with 0.010 m step) in x and y-direction.</p>		<ul style="list-style-type: none"> • Grating lobes (multiple main beams) are formed when the spacing is greater than $0.49\lambda_0$ (0.060 m). • The spacing between antenna elements plays a crucial role in antenna arrays. • Large spacing creates high grating lobes. • Small spacing increases the coupling effect and influence the performance of antenna arrays.
2	<p>Parallel dipole with Dipole#3 (D3) displaced along x-axis.</p> 	<p>Spacing is varied for dipole 3 (D#3) along the x-axis, x_3 from [0.055 m: 0.059 m] by 1 mm.</p>		<ul style="list-style-type: none"> • The azimuth far-field pattern is similar in all cases even if the position of dipole 3 is shifted by 1 mm from $x_3=0.055$ m (measurement sample shown by the red-dashed line) to $x_3=0.059$ m (black-dashed line).

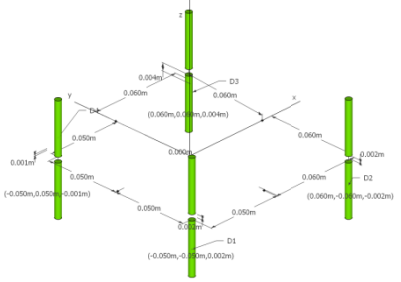
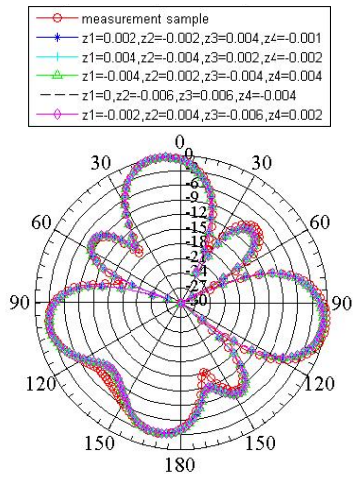
Appendix D: Effects of the Element Spacing and Orientation on the Far-field Pattern of Four Dipole Antenna Arrays

No.	Simulation Model	Variation	Effect to the normalised pattern at theta=90	Observation on the far-field pattern
3	<p>Parallel Dipole with Dipole #1 (D1) displaced along x and y-axis.</p> 	<p>X- and y-values of dipole 1 are shifted by 1 mm from [-0.055 m to -0.059 m]</p>		<ul style="list-style-type: none"> Spacing increment for dipole 3 (D₃) and spacing variation in dipole 1 (D₁) lead to nearly 3 dB increment of the side lobe level in between main lobes (at 45°).

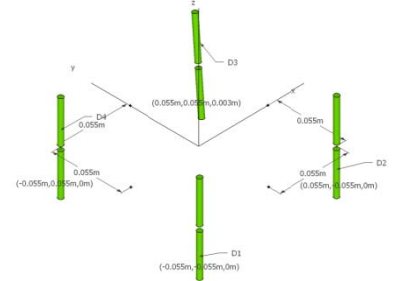
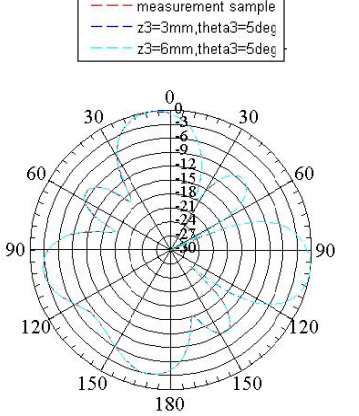
D.5 Effect of Varying the Spacing in Echelon on the Pattern

No.	Simulation Model	Variation	Effect to the normalised pattern at theta=90	Observation on the far-field pattern
1	<p>Parallel dipole with one dipole (D3) displaced in z-direction.</p> 	<p>z_3 is varied from 0m to 0.005m by 0.001m step</p>		<ul style="list-style-type: none"> It is observed that even when one of the dipoles (in this case, dipole 3) is staggered by 5 mm, the far-field pattern remains the same as in the measurement sample.
2	<p>Parallel dipole with two dipoles (D2 and D4 displaced in x, y-direction) while others (D1 and D3) displaced in z-direction</p> 	<p>z_1 values (dipole 1) are varied from 0m to 0.007m by 0.002m</p>		<ul style="list-style-type: none"> A 3 dB change is observed at the side lobes at angles 145° and 305° in comparison with the measurement sample. The increment of side-lobe level is largely due to the spacing between D2 and

Appendix D: Effects of the Element Spacing and Orientation on the Far-field Pattern of Four Dipole Antenna Arrays

	<p>3 Parallel dipole with four dipoles displaced in z-direction.</p> 	<p>z-values of all dipoles are varied while the x- and y-values are fixed.</p>		<p>D4 increased to 0.12m apart.</p> <ul style="list-style-type: none"> A large difference is observed that deeper nulls are formed approximately at angles of 25°, 65°, 125° and 290°. It is due to the spacing variation in parallel and in echelon. All lines except red-circle line overlap each other even though the spacing of dipoles is varied in echelon.
--	---	--	--	---

D.6 Effect of Varying the Spacing (Skewed) on the Pattern

No.	Simulation Model	Variation	Effect to the normalised pattern at theta=90	Observation on the far-field pattern
1	<p>Three parallel dipoles and another dipole (D3) slanted and displaced in z-direction.</p> 	<p>Angle of D3 is slanted at 5° and shifted along the z-axis by about 3 mm and 6 mm.</p>		<ul style="list-style-type: none"> It is observed that the far-field patterns are similar in this case.
2	<p>Two parallel dipoles and other two (D2 and D4) slanted.</p>	<p>Dipole 1 and dipole 3 is in parallel position. Dipole 2 is shifted to</p>		<ul style="list-style-type: none"> It is observed that the far-field pattern when θ_2 and θ_4 are slanted is similar to the pattern of the

Appendix D: Effects of the Element Spacing and Orientation on the Far-field Pattern of Four Dipole Antenna Arrays

		<p>0.001 m and its angle (θ_2) is slanted at 2°, while the angle of D4 (θ_4) is slanted at 4°.</p>		<p>measurement sample.</p>
<p>3</p>	<p>Three parallel dipoles and one dipole (D3) slanted by 5° step.</p>	<p>The slanted angle for dipole 3 (D_3) is increased from 5° to 20° with a step of 5°.</p>		<ul style="list-style-type: none"> It is observed that the far-field pattern is almost similar except that the nulls are slightly less pronounced as the slanted angle increases. This is because the mutual impedance between dipole 3 and other elements varied considerably.